L-Università ta' Malta
Faculty of Engineering

DOCTOR OF PHILOSOPHY

The PQ8 Architecture: Deploying Picosatellite Constellations from a Single Launch

DANIEL CUMBO

Supervised by:

PROF. ING. MARC ANTHONY AZZOPARDI

A dissertation submitted in partial fulfilment of the requirements for the degree of Doctor of Philosophy

by the

Faculty of Engineering

May 2025

L-Università ta' Malta

FACULTY/INSTITUTE/CENTRE/SCHOOL Faculty of Engineering

DECLARATION OF AUTHENTICITY FOR DOCTORAL STUDENTS

(a) Authenticity of Thesis/Dissertation

I hereby declare that I am the legitimate author of this Thesis/Dissertation and that it is my original work.

No portion of this work has been submitted in support of an application for another degree or qualification of this or any other university or institution of higher education.

I hold the University of Malta harmless against any third party claims with regard to copyright violation, breach of confidentiality, defamation and any other third party right infringement.

(b) Research Code of Practice and Ethics Review Procedure

I declare that I have abided by the University's Research Ethics Review Procedures. Research Ethics & Data Protection form code ENG-2022-00036.

☒ As a Ph.D. student, as per Regulation 66 of the Doctor of Philosophy Regulations, I accept that my thesis be made publicly available on the University of Malta Institutional Repository.

□ As a Doctor of Sacred Theology student, as per Regulation 17 (3) of the Doctor of Sacred Theology Regulations, I accept that my thesis be made publicly available on the University of Malta Institutional Repository.

□ As a Doctor of Music student, as per Regulation 26 (2) of the Doctor of Music Regulations, I accept that my dissertation be made publicly available on the University of Malta Institutional Repository.

□ As a Professional Doctorate student, as per Regulation 55 of the Professional Doctorate Regulations, I accept that my dissertation be made publicly available on the University of Malta Institutional Repository.

Abstract

Over the past decade, demand for nano- and pico-class satellites has surged, driving up costs and competition for launch opportunities. CubeSat launches, once easily accessible, have become prohibitively expensive for small institutions, especially when considering constellation deployment. Although the PocketQube standard offers a lower cost alternative, its adoption has been limited and its cost benefits modest, primarily due to launch integration limitations, debris mitigation and trackability concerns. To address these challenges, this work proposes the PQ8 Architecture: a novel deployment model for pico-scale satellite constellations that reduces launch costs by up to 87 %, simplifies integration, and enables the simultaneous deployment of multiple satellites.

The research is divided into three key components. First, the structural design is developed to accommodate eight PocketQube-sized satellites within a 1U CubeSat frame, while remaining scalable. The design is evaluated using finite element analysis and mechanical testing, including modal analysis, vibration, shock, and static load tests, all in accordance with ECSS launch qualification guidelines.. Second, constellation dispersal is addressed through tailored differential drag control algorithms. This approach calculates separation velocities and timing to achieve in-plane phasing, accounting for the operational parameters introduced by the PQ8 form factor. Two case studies with orbital simulations validate the method's effectiveness and scalability. Third, a novel disengagement mechanism is presented, in which magnetorquer coils are reconfigured to act as synchronized electromagnetic actuators. The circuitry is validated through simulation and bench-top testing, and actuator forces are confirmed via finite element analysis. Overall separation dynamics are then demonstrated using a pendulum testbed to emulate near-free-body translational and rotational disengagement behaviour.

Together, these contributions, structural innovation, coordinated dispersal, and integrated separation, form a robust and cost-effective platform for small-satellite constellations. The PQ8 Architecture significantly lowers the barriers to entry and enables missions that would otherwise be financially or logistically infeasible.

Acknowledgements

First and foremost, I would like to express my deepest gratitude to my supervisor, Prof. Ing. Marc Anthony Azzopardi, without whom this research would not have been possible. He not only introduced satellite systems design to the university but also sparked my interest in the field during my undergraduate studies. I am especially thankful for his steadfast support, insightful feedback, and patient guidance throughout this journey.

I would also like to acknowledge my fellow members on the ASTREA team. Thank you for your dedication and hard work on the various aspects of satellite design that intersected with this project. Through your collective efforts, the dream of building not only the country's first satellite but one with a novel and ambitious architecture was kept alive year after year.

The journey toward completing a PhD thesis is long, arduous, and often solitary. I could not have come this far without the unwavering support, love, and sacrifices of my family. I have nothing but gratitude for both my mother and father, who have sacrificed so much for both me and my siblings – thank you for having my back, the constant encouragement, emotional strength and countless hours spent listening to my frustration. To my siblings, thank you for your quiet strength and steady presence throughout this journey. Whether through a well-timed distraction, a word of encouragement, or simply understanding when I wasn't at my best, you helped me stay grounded. Finally, a special mention to my nephew, whose laughter and energy were a joyful reminder of what truly matters.

This degree was carried out following the award of the Tertiary Education Scholarships Scheme (TESS) Scholarship 2021. The research was partly funded through the TESS Scholarship.

The research was also partly through projects ASTREA and QUASAR. ASTREA is financed by Xjenza Malta, through FUSION: The R&I technology Development Programme 2019. QUASAR is also funded by Xjenza Malta, through the FUSION R&I: Space Upstream Thematic Programme of 2023.

Table of Contents

List of Figures

List of Tables

Nomenclature

The following list of acronyms and symbols was used throughout this work. Since the work covers multiple domains, and the most common symbol was used per domain, some may have more than one meaning. For further clarity, the symbols in this list are divided into their respective domain.

Acronyms:

ADC	Analogue-Digital Conversion
ADCS	Attitude Determination and Control System
ASIC	Application Specific Integrated Circuit
CAD	Computer Aided Design
CDS	CubeSat Design Standard
CFD	Computational Fluid Dynamics
COMM	Communications Subsystem
COTS	Commercial off-the-shelf
DAC	Digital-Analogue Conversion
DET	Direct Energy Transfer
DM	Disengagement Mechanism
ECSS	European Cooperation for Space Standardisation
EM	Electromagnetic
EMI	Electromagnetic Interference
EML	Earth-Moon Lagrange Point
EMR	Electromagnetic Radiation
EPS	Electrical Power System
ERF	Error Function
ESR	Equivalent Series Resistance
FEA	Finite Element Analysis
FFT	Fast Fourier Transform
FOSU	Factor of Safety Ultimate
FOSY	Factor of Safety Yield
FPGA	Field Programmable Gate Array
GPS	Global Positioning System
HRM	Hold-and-Release Mechanism
LEO	Low Earth Orbit
LISA	Laser Interferometer Space Antenna
LSP	Launch Service Provider
MPPT	Maximum power-point tracker
MPTT	Maximum power transfer theorem

OBC	On-board Computer
PSD	Power Spectral Density
PWM	Pulse width modulation
QSS	Qualification Shock Spectrum
RAAN	Right Ascension of the Ascending Node
RMSE	Root mean square error
SDR	Software Defined Radio
SEE	Single Event Effects
SEFI	Single Event Functional Interrupt
SEU	Single Event Upset
SMA	Semi-major Axis
SRP	Solar Radiation Pressure
SRS	Shock Response Spectrum
STK	Satellite Tool Kit
TID	Total Ionising Dose
TLE	Two-Line Element (Data)
TRL	Technology Readiness Level
VLEO	Very Low Earth Orbit

Differential Drag:

A	projected surface area
a	Acceleration
α	Energy accommodation coefficient
β	Ballistic Coefficient
c_D	Drag coefficient
E	Kinetic Energy
F	Force
m	Mass
ρ	Atmospheric density
q	Mean dynamic pressure
s	Molecular speed ratio
σ	Momentum accommodation coefficient
t	Time
θ	Angle of incidence
v	Velocity

Satellite Dispersal:

a	Semi-major axis
θ	Separation angle
k	Deployment stage index
n	Total number of satellites in the constellation
S	Generic Satellite symbol
E	Energy

v	Orbital velocity

Disengagement Mechanism:

a	Acceleration
α	Damping factor
β	Earth's Magnetic Field
C	Capacitance
d	Radial displacement
E	Energy
F	Force
I	Current
L	Inductance
M	Mutual Inductance
N	Number of turns
P	Power
Q	Charge
R	Resistance
r	Coil radius
T	Temperature
τ	Torque
U	Stored Energy
μ	Permeability
V	Voltage
W	Work done
ω	Frequency
z	Axial displacement

1 INTRODUCTION

This thesis presents the systems-level design of a novel *many-in-one* satellite platform, the PQ8 Architecture: a satellite that is deployed as a single unit and splits into a constellation of smaller satellites. It covers key areas including structural design, differential drag-based dispersal, a reusable disengagement mechanism, dynamic modelling of the disengagement process, and supporting circuit design. Together, these components form an integrated solution for scalable, low-cost satellite constellation deployment. This chapter introduces the research rationale and motivation, outlines the proposed architecture and its objectives, highlights related projects at the University of Malta, and defines the unique contributions of this work.

1.1 Research Motivation

Satellite constellations are becoming increasingly central to modern space applications, supporting missions in Earth observation, global communications, navigation, and scientific research. However, launching multiple satellites into orbit is expensive and logistically complex, requiring the coordination of various launches and synchronising orbital plane insertions.

Large-scale constellations with strong commercial backing, such as SpaceX's Starlink, benefit from dedicated launches tailored to their mission-specific parameters. For example, the FORMOSAT-3/COSMIC mission launched its entire six-satellite constellation on a single dedicated vehicle by mounting them on an intermediary vehicle [1]. This vehicle, equipped with propulsion to enable controlled deployment and precise orbital phasing, adds additional development and deployment costs, making the

deployment method financially untenable for most academic or small-scale projects. A dedicated Falcon 9 launch to low Earth orbit (LEO) is projected to cost approximately $3,125 per kilogram in 2025, with annual increases estimated at 2.82% [2,3].

In contrast, smaller-scale satellites, particularly CubeSats and PocketQubes, typically rely on rideshare opportunities, resulting in lower total costs per launch. However, this reliance imposes constraints on launch schedules, orbital parameters, and the number of satellites that can be deployed simultaneously. It also introduces cost unpredictability, as rideshare prices fluctuate between missions. For example, the PlanetScope constellation, composed of over 130 3U CubeSats, required multiple launches across different vehicles, including Falcon 9, Electron, and PSLV [4]. Launch costs per kilogram for smaller satellite classes are also disproportionately high: in 2025, prices were estimated at approximately $6,500 per kilogram for CubeSats and increasing to $25,000 per kilogram for a PocketQube [5,6].

Apart from costs, another key challenge, specifically for rideshare missions, lies in the lack of control over the initial orbital parameters. Rideshare launches often struggle to synchronise orbital plane insertions, resulting in initial misalignments that require corrective manoeuvres post-deployment [7]. This prolongs phasing times and typically necessitates the use of onboard propulsion - an impractical solution for mass and volume-constrained platforms such as CubeSats and PocketQubes [8]. As a result, constellation developers are frequently forced to accept suboptimal configurations.

Despite these persistent issues, summarised in Figure 1.1, there has been limited effort in both academia and industry to address constellation deployment from a satellite architecture perspective. Most solutions have focused on either improving launch vehicles or developing external deployment infrastructure. However, despite advances in these areas, overall deployment costs have not significantly decreased [3].

To address these challenges, there is a need for a satellite architecture that tackles not only the constraints of launch logistics but also the limitations of early deployment. Such an architecture should remain compatible with standard rideshare opportunities, leveraging existing launch infrastructure, while significantly reducing the cost and complexity associated with deploying multiple satellites into orbit. By rethinking the deployment problem from a satellite architecture perspective, rather than from the viewpoint of launch vehicles and deployers, it becomes possible to conceive solutions that are better aligned with the constraints and ambitions of small satellite constellations.

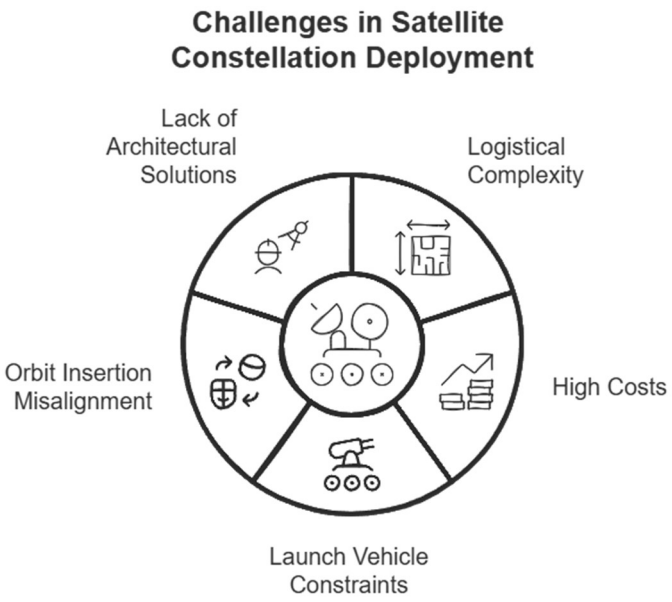

Figure 1.1: Constellation Deployment Challenges

1.2 The Proposed Architecture

This thesis presents a solution to the PocketQube constellation deployment challenge by building on the original "8-in-1" configuration concept presented by Prof. Twiggs at the ESA Vega Maiden Flight First Workshop in 2008 [9]. The proposed approach introduces an architecture in which a primary satellite divides into eight smaller satellites, referred to as the PQ8 Architecture. This architecture addresses deployment constraints by subdividing a standard 1U CubeSat, measuring $10 \times 10 \times 10$ cm³, into eight smaller satellites, each measuring $5 \times 5 \times 5$ cm^3 – roughly the size of a PocketQube. It thus leverages existing CubeSat launch infrastructure while benefiting from the reduced development costs associated with PocketQubes. This innovative approach enables the deployment of a constellation of at least eight, and up to 24, picosatellites from a standard 3U CubeSat deployer, reducing the cost per PocketQube to approximately $3,125 per kilogram, or roughly 12.5% of the current average price.

A PQ8 satellite is therefore a 1U CubeSat that is hierarchically assembled from eight PQ1 satellites. The integrated structure conforms to the CubeSat Design Standard Rev. 14.1, including all associated mechanical, interface, and deployment requirements [10]. This ensures that a PQ8 satellite can be launched using any standard rideshare service compatible with CubeSat deployments.

The deployment strategy begins with the PQ8 maintaining its 1U form factor. Following an initial disengagement manoeuvre, the satellite separates into two PQ4

satellites that are phased relative to one another. Each PQ4 then divides into two PQ2 satellites, also undergoing phasing. Finally, the PQ2 units each separate into two PQ1 satellites, completing the whole sequence and resulting in eight independently functioning spacecraft. These staged configurations are illustrated in Figures 1.2(a) through 1.2(d).

The smallest unit in the PQ8 system is the PQ1 satellite. Internally, each PQ1 houses four core subsystems and a payload, implemented as individual PCBs arranged in a stacked configuration. This modular structure provides clear functional separation of standard subsystems, including the Electrical Power System (EPS), Attitude Determination and Control Subsystem (ADCS), On-Board Computer (OBC), and Communications (COMMs).

To realise this architecture, the following design questions must be addressed:

1. How are the eight PQ1 satellites mechanically integrated to form a unified PQ8 satellite?
2. Can the integrated PQ8 satellite withstand the mechanical loads associated with launch?
3. How are the PQ1 satellites disengaged from the structure in a controlled and repeatable manner?
4. What mechanism or process governs their physical dispersion following separation?
5. How is the target constellation configuration achieved without active propulsion?

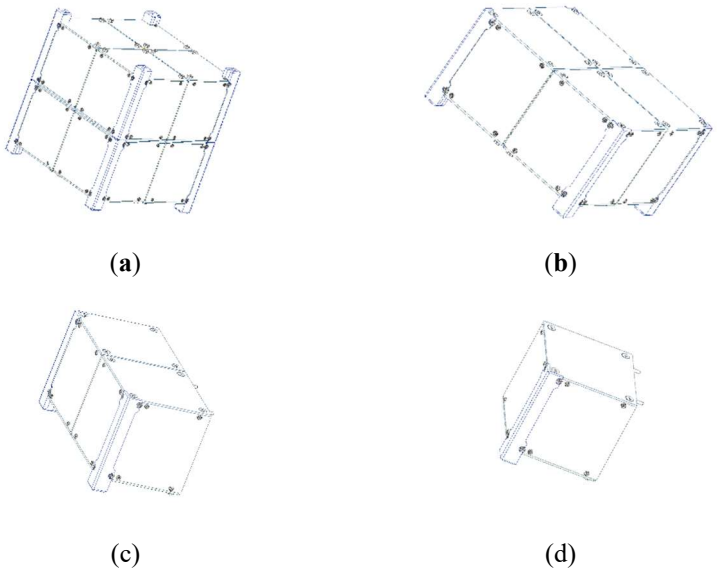

(**a**) (**b**)

(c) (d)

Figure 1.2: (a) PQ8 Satellite (b) PQ4 Satellite (c) PQ2 Satellite (d) PQ1 Satellite

This proposed architecture offers a single-launch solution to the challenges of small satellite constellation deployment by assembling multiple satellites into a single platform and separating them in orbit through a hierarchical disengagement sequence. The disengagement sequence itself imparts a tuneable change in velocity, or Δv, at each separation event, which can be harnessed to enhance constellation dispersal. When combined with differential drag control, this enables passive constellation phasing without the need for onboard propulsion.

The proposed method targets PocketQube-scale satellites. It introduces a new architectural solution that increases the number of deployable PocketQube-sized satellites within the same mass and volume constraints by leveraging existing CubeSat infrastructure. By doing so, an entire constellation can be launched simultaneously, eliminating the need for multiple coordinated launches to populate the orbital plane. As a result, scheduling and logistical complexity are significantly reduced, whilst the need for post-deployment orbit corrections is effectively removed.

1.3 Research Rationale

The motivation for this research stems from the observation that existing methods for deploying PocketQube constellations are both expensive and logistically complex. These challenges are primarily due to the lack of volumetric optimisation in current PocketQube deployment architectures. Rather than addressing the problem at the satellite level, most research and industry efforts have focused on improving the deployer itself. This thesis shifts the focus from deployment hardware to satellite architecture by reimagining how PocketQube-sized satellites can be volumetrically packed within a CubeSat-standard deployer.

PocketQubes were selected as the target satellite class due to their inherent advantages in size, cost, and compatibility with existing commercial electronics. With a volume roughly equivalent to a modern mobile phone, PocketQubes share a scale regime with other small satellite standards, such as CubeSats and ThinSats. This enables the use of commercial off-the shelf (COTS) components from the mobile industry, as well as electronic hardware developed for these alternative satellite platforms. Miniaturising further would require the development of application-specific ICs (ASICs), which would counteract the goal of reducing costs. Whilst larger satellites are heavier and thus more

expensive to launch. Therefore, the PocketQube platform was deemed the most practical and economically viable solution for the proposed architecture.

The decision to pursue an architecture in which specifically *eight satellites* are integrated into a single unit was driven by both technical and strategic considerations. From a deployment perspective, the design had to remain compatible with existing CubeSat infrastructure to be realistically adoptable. Developing a new deployment standard would not only have added complexity, but also introduced a significant barrier to adoption within an industry that favours standardisation and heritage. The CubeSat standard, particularly the 1U form factor, offered a natural volumetric fit for eight 1p PocketQube-sized satellites, whilst still allowing for scalability.

The PQ8 Architecture concept represents a novel contribution to constellation architecture, as there is currently no documented research on a system deployed in the proposed manner. That is, a single unit composed of multiple fully functional satellites that deploys into orbit as a single satellite and hierarchically separates into a constellation, without the need for additional hardware, such as intermediary vehicles, that become redundant after deployment.

This absence of precedent raises several open questions, as discussed in the previous section, which form the basis of this research. The challenges these questions present justify the need for a complete architectural investigation, from basic concept and modelling through to physical validation.

1.4 Engineering Methodology

As the proposed research is an aerospace systems project with an inherently interdisciplinary nature, a concurrent engineering approach was adopted. The project was divided into three domains for concurrent development: structural design, orbital mechanics for in-orbit injection and constellation dispersal, and actuator design for the disengagement mechanism.

Given the novelty of the architecture, a traditional linear design process was deemed unsuitable. Instead, each of the three core domains was developed in parallel to an initial level of maturity, with frequent integration checkpoints to evaluate consistency and compatibility across the system. This approach ensured that constraints emerging from one domain could be identified early and reflected in the others. The first phase of the project was therefore exploratory, aiming to establish the feasibility of each subsystem

independently: confirming that a CubeSat could be structurally divided into eight PocketQube-sized units, that differential drag could achieve constellation dispersion, and that the disengagement mechanism functioned as conceptualised. Following the exploratory stage, these components were refined iteratively with the results of each domain influencing the rest.

This approach was essential in managing the complexity of the systems engineering project. By allowing each domain to develop together, design dead ends that might have emerged under a sequential approach were avoided. It also reinforced the importance of early cross-domain verification, where minor assumptions in one domain can cascade into significant constraints in another. The experience highlighted the value of iterative, system-oriented thinking.

1.5 Aims and Objectives

The overarching objective of this research is to investigate architectural approaches for reducing the launch cost and logistical complexity of satellite constellations composed of PocketQube-class spacecraft. In particular, the work explores whether combining multiple small satellites into a single launchable unit, followed by controlled in-orbit injection and dispersal, can provide a viable alternative to conventional multi-launch or multi-deployer deployment strategies.

The aim of the research is, therefore, to demonstrate the feasibility of the PQ8 Architecture as one possible implementation of such an aggregated launch and deployment approach, comprising a many-in-one satellite system that is launched as a single spacecraft and undergoes a staged sequence of in-orbit disengagement and dispersal.

To achieve this aim, the research pursued the following objectives:

System Design:

1. To design a satellite structure that integrates eight PocketQube-sized satellites into a 1U CubeSat-compliant form factor.
2. To develop a disengagement mechanism capable of delivering controlled separation impulses.
3. To ensure compliance with current CubeSat standards (Rev 14.1), [10], and European Cooperation for Space Standardisation (ECSS) standards.

Modelling and Analysis:

4. To assess the structural integrity of the PQ8 satellite under expected launch loads through finite element simulation.
5. To model the electrical, magnetic, and kinematic behaviour of the disengagement mechanism, including energy conversion and impulse delivery.
6. To evaluate orbital dispersal dynamics and demonstrate that the staged separation sequence can produce phasing through differential drag and Δv.

Validation and Integration:

7. To verify the consistency of the derived models of the disengagement mechanism through experimental testing.
8. To iteratively refine system components through a concurrent engineering approach, accounting for cross-domain constraints and interactions.
9. To demonstrate overall system feasibility through simulation, experimentation, and system-level analysis.

Consequently, this thesis represents a systems-level engineering research and development effort encompassing satellite structural design, orbital mechanics, electronics engineering, and physics-based modelling. As such, the goals are structured to advance the technological maturity of the system components, with specific aims and objectives for each system mapped to corresponding European Space Agency (ESA) Technology Readiness Levels (TRLs), as shown in Figure 1.3.

The minimum target for all subsystems is TRL 3, which would demonstrate that the PQ8 Architecture is, in fact, feasible. Additionally, specific TRL goals for the core domains of the project were set out as follows:

- Satellite Structure**:** TRL 7,
- Disengagement Mechanism: TRL4
- Constellation Dispersal Strategy: TRL3

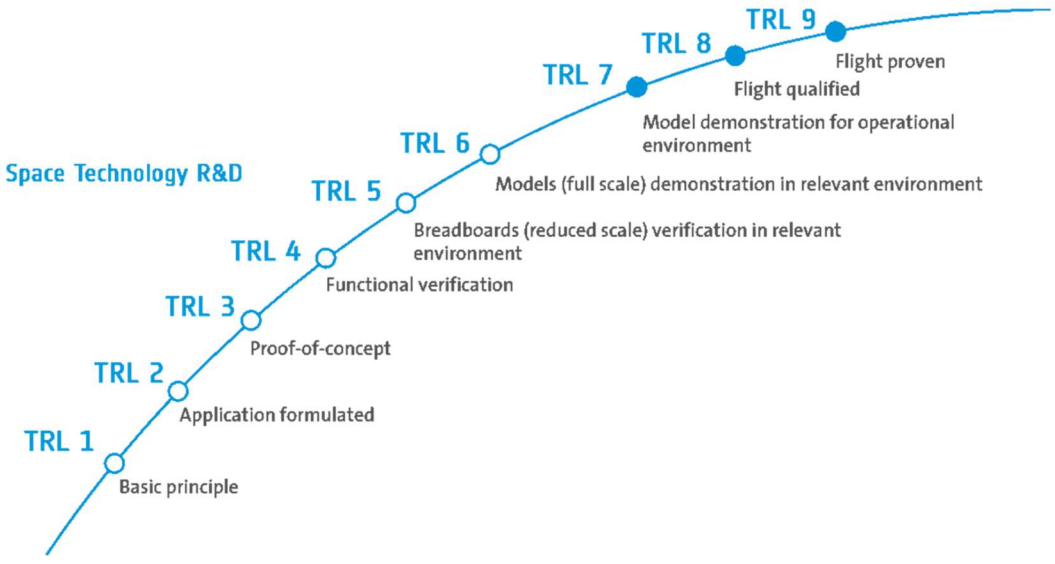

Figure 1.3: ESA Technology Readiness Levels [11]

1.6 Success and Failure Criteria

In addition to the aims, objectives, and TRL targets, the success and failure criteria are defined in Table 1.1 to provide benchmarks against which the outcomes of this research can be evaluated.

Table 1.1: Success and Failure Criteria

Area	Success Criteria	Failure Criteria
Overall Architecture (PQ8)	A complete PQ8 system architecture is defined, integrated, and shown to be physically realisable within CubeSat geometric, mass, and interface constraints.	Architecture cannot be integrated or assembled within CubeSat constraints due to geometric, mass, or interface incompatibilities.
Structural Subsystem (PQ1/PQ8 Frame)	Structural design is shown, through analysis and testing, to withstand representative launch loads with required margins as defined by applicable launch environment standards. PQ1-scale testing successfully routes out major structural weaknesses and validates modelling assumptions.	Structural design fails to demonstrate survivability under representative launch loads with required margins, or exhibits failure modes in PQ1-scale testing that invalidate the structural concept.
Disengagement Mechanism	The disengagement mechanism is shown to achieve controlled physical separation in laboratory testing, and its behaviour is consistent with analytical and simulation-based predictions within acceptable uncertainty.	The mechanism fails to produce physical separation, or demonstrates behaviour fundamentally inconsistent with analytical or simulation predictions.
Dispersal Method	The dispersal method is analytically and numerically demonstrated to enable separation growth consistent with orbital mechanics and differential-drag modelling.	Analytical or simulation results show the dispersal method cannot produce meaningful or controllable post-release separation.
Modelling and Validation	Simulation models of separation dynamics are shown to be physically consistent and supported by experimental trends and sensitivity analysis.	Models produce results that contradict experimental behaviour or physical principles with no defensible explanation.
Technology Readiness Level Targets	Evidence supports: PQ1 structure at TRL 7, disengagement mechanism at TRL 4, and dispersal method at TRL 3, using appropriate test or analysis environments.	Claimed TRLs are not supported by appropriate test, analysis, or environmental relevance.

1.7 Mission Design Envelope

Since this research is fundamentally a proof-of-concept study, the PQ8 Architecture is not designed to fulfil the requirements for any particular mission. Instead, all design decisions, modelling, and experimental demonstrations are referenced to a bounded mission envelope intended to represent a realistic upper-bound operating scenario for CubeSat deployment and PocketQube-class satellite operation. This envelope aims to provide sufficient constraint to justify design choices whilst retaining generality for broader applicability.

The baseline mission envelope adopted for this research is defined as follows:

- **Perigee Altitude:** An initial perigee altitude of 500 km is adopted as the reference case. At higher altitudes, differential-drag induced relative motion becomes increasingly weak, making dispersal inefficient. In addition, such altitudes are generally unrealistic for PocketQube-class missions due to radio link-budget limitations, debris mitigation requirements, and tracking constraints. Lower altitudes are more typical for PocketQube missions, often 450 km or below. Nevertheless, 500 km represents a conservative, worst-case condition for differential drag and therefore provides an upper-bound design case.
- **Eccentricity:** Eccentricity is limited to a maximum of 0.01. This reflects typical values observed in historic rideshare CubeSat deployments and avoids highly eccentric orbits, which complicate constellation phasing and separation analysis.
- **Inclination:** Inclination is not constrained.
- **Right Ascension of the Ascending Node (RAAN):** RAAN is not constrained, as it does not materially affect the separation and dispersal dynamics investigated in this research.
- **Argument of Perigee:** Argument of perigee is not constrained for the same reason as RAAN.

1.8 System-Level Requirements

The PQ8 architecture is governed by the system-level specifications listed in Table 1.2. These specifications define what the integrated system is required to achieve, in addition to the detailed requirements of each individual subsystem. More specific requirements are presented within the chapters where the relevant subsystems and analyses are presented. In addition, a consolidated set of detailed requirements, including those for elements not developed as part of this thesis but required for completeness, is provided in Appendix C.

Table 1.2: Top level system specifications

Specification	Definition	Relevant Chapters
Geometric Specification	The integrated PQ8 system shall conform to CubeSat external envelope and deployer interface standards.	3
Mass and Mass-Property Specification	Total system mass shall be compatible with PocketQube deployer limits. Centre of mass shall lie within a bounded region around the geometric centre. Principal moments of inertia shall limit post-release angular rates to safe values.	3
Launch Environment Specification	The system shall survive representative quasi-static, vibration, and shock loads defined by applicable CubeSat, ESA and User Manual requirements with required safety margins.	3
Functional Disengagement Specification	The system shall provide defined mechanical and electrical interfaces for disengagement. The disengagement event shall produce physical separation under laboratory conditions representative of early-orbit release, with behaviour consistent with analytical and simulation predictions.	3, 5, 6
Power and Energy Specification	All disengagement and control functions shall operate within PocketQube-class power and energy budgets.	3

1.9 Novel Contributions

This research presents the PQ8 Architecture as a novel systems-level approach to satellite constellation deployment, targeting the PocketQube-class platform. Developing this architecture required rethinking conventional design approaches, leading to novel contributions across structural, mechanical, electrical, and orbital subsystems. These contributions collectively enable a scalable deployment strategy that addresses key challenges in pico-satellite constellations.

The core contributions of this research are as follows:

- PQ8 Structure Design**:** Development of a satellite structure that enables eight PocketQube-class satellites to aggregate into a single 1U CubeSat form factor, while remaining compliant with standard CubeSat launch interfaces and structural requirements. The structure was validated through finite element simulation and experimental testing.

- Constellation Dispersal Algorithms**:** Formulation of generalised algorithms for constellation phasing, which calculate the required Δv values and associated disengagement timings for optimal constellation phasing of satellites deployed from a many-in-one configuration.
- Dual-Use Magnetic Actuator Design**:** Design of a dual-purpose actuator and driver circuit that repurposes magnetorquer coils to deliver high-current pulses for mechanical disengagement.
- Synchronised Electromagnetic Separation Mechanism**:** Implementation of a coordinated electromagnetic deployment method in which synchronised pulses across multiple actuator devices produce reliable and repeatable satellite separation events.

1.10 Satellite Systems Projects at UoM

Satellite research at the University of Malta began in 2015 with the Master's dissertation of Cachia, which focused on the design of a pico-satellite platform [12]. This early work provided a high-level conceptual design for a PocketQube-class satellite and evaluated its feasibility for a proposed scientific mission, UoMBSat-1.

The UoMBSat-1, illustrated in Figure 1.4, mission concept was developed collaboratively by Camilleri (University of Birmingham) and Cachia (University of Malta) [13][14]. The mission's primary scientific objective was to measure electron density in the topside ionosphere using a miniaturised ionospheric impedance probe designed by Camilleri [13]. Cachia's contribution in [14] involved the development of the satellite platform. This foundational work catalysed a series of undergraduate and postgraduate projects focused on key subsystems, including EPS, ADCS, COMMs, thermal analysis, and propulsion.

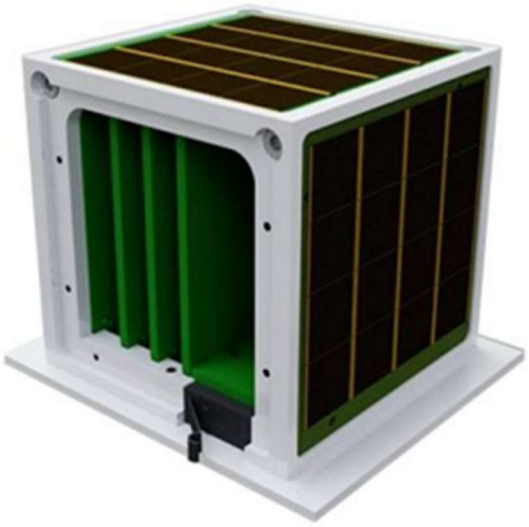

Figure 1.4: UoMBSat-1 PocketQube Concept [13]

While the PQ8 Architecture presented in this thesis is an independent project, it builds upon technologies and insights developed through these earlier efforts. Several subsystem designs have been adapted or evolved to meet the specific requirements of the PQ8 platform. The following subsections provide a brief overview of relevant prior research, highlighting their integration into or influence on the PQ8 Architecture.

1.10.1 Electrical Power Generation, Supply and Distribution

In addition to the platform outlined in [12], Cachia provided significant contributions to the EPS. These included the design of an analogue maximum power point tracking (MPPT) circuit, selection and testing of Li-ion batteries, and the development of a top-level EPS architecture. These elements were partially integrated into the PQ8 EPS, subject to modifications aligned with the system's new constraints.

To validate the performance of the analogue MPPT design, illustrated in Figure 1.5, Cachia benchmarked its efficiency against two alternatives: a Direct Energy Transfer (DET) topology and the commercial LTC3105 IC by Linear Technology. Under simulated PocketQube rotation conditions of 100 °/s, the analogue MPPT achieved an efficiency of 86%, outperforming the LTC3105 (81.7%) and the DET topology (77.4%). Although Cachia's contributions outperformed commercially available ICs, the physical size of the circuitry was too large and thus unsuitable for the PQ8 Architecture. However, the LTC3105 proved to be a viable alternative.

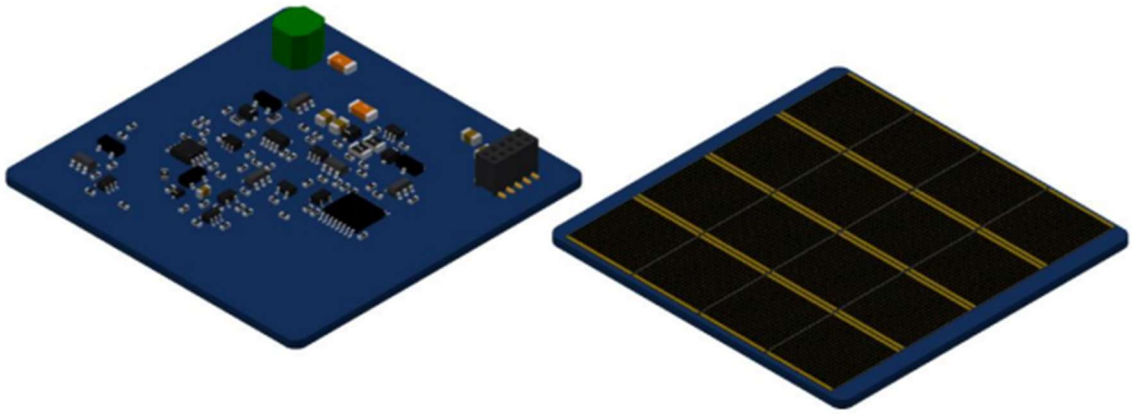

Figure 1.5: MPPT and Solar Panel for the UoMBSat-1

For energy storage, Cachia tested two Li-ion battery topologies: pouch-type cells and cylindrical cells. The pouch-type cells exhibited superior performance at ambient and low temperatures but suffered a 2.8% capacity loss after 24 hours in vacuum. In contrast, the cylindrical cells, were slightly less efficient during ambient testing but showed no degradation in vacuum conditions. This is likely due to their geometry, which limits the expansion of the cell under vacuum. As a result, the PQ8 EPS adopts the cylindrical cells tested by Cachia in a 2P1S configuration, each rated at 650 mAh, 43 × 13 mm in size, and weighing approximately 12 g.

For the EPS topology, Cachia had proposed regulated 3.3 V and 5 V buses, as well as unregulated subsystem outputs. Belazi further developed this design in [15], who removed the 5 V. This modified design was adopted for the PQ8 Architecture, though each sub-circuit was re-engineered to better fit the platform's mass, volume, and thermal constraints.

1.10.2 Attitude Determination and Control

Debattista's Master's thesis, contributed the ADCS subsystem, illustrated in Figure 1.6 for UoMBSat-1, incorporating magnetometers, a gyroscope, and accelerometers, with sensor fusion performed via an Extended Kalman Filter [16]. Attitude control was achieved using three reaction wheels (one per axis) and six magnetorquers, planar PCB coils mounted on each external face, used mainly for detumbling and reaction wheel desaturation. This subsystem was directly carried forward into the PQ8 Architecture with only minor modifications. In particular, the magnetorquer coils and their drivers were revisited to support their additional role in the disengagement mechanism, as discussed in later sections.

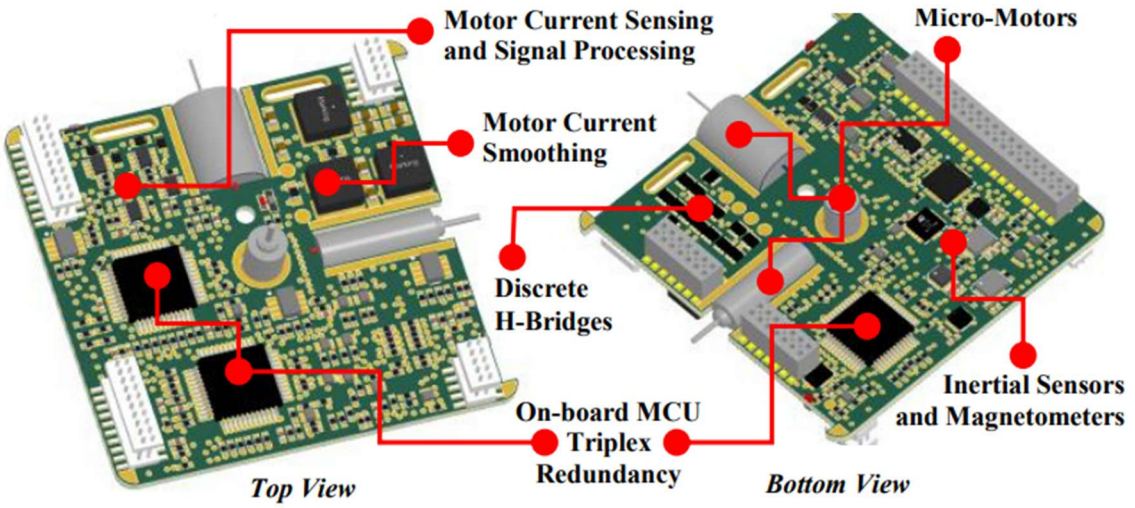

Figure 1.6: UoMBSat-1 Attitude Control Subsystem [17]

1.10.3 Radio and Telemetry

Vassallo developed the communications subsystem for UoMBSat-1 in [18], based on a software-defined radio (SDR) architecture operating within the 435–438 MHz amateur band. The design combines a hardware front-end, responsible for filtering, amplification, and frequency conversion, with a dedicated transceiver for modulation and demodulation. Signal processing, error correction, and encoding were implemented in software using the SEcube Multi-Chip Module. Its low size and power footprint make it highly suitable for PQ-class platforms. The SDR design was adopted in the PQ8 system, with minor modifications to the printed circuit board (PCB) layout. The resulting layout is illustrated in Figure 1.7. The system operates on a compact 42 × 42 mm PCB and maintains an average power draw of 75 mW, peaking at 1.6 W during transmission.

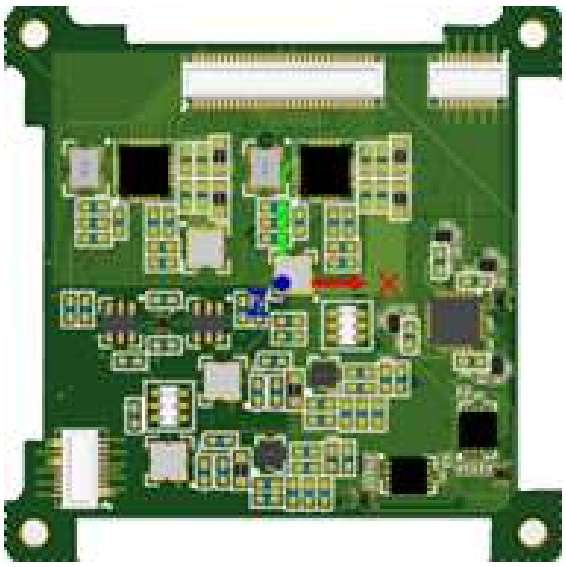

Figure 1.7: PQ8 Communications Subsystem

1.10.4 From the UoMBSat-1 to the PQ8 Architecture

The PQ8 Architecture aims to reduce the cost and complexity of launching multi-picosatellite constellations by introducing a scalable, many-in-one deployment method. This thesis focuses on three core areas of development: structural design, disengagement mechanism design, and mission-level deployment strategy. While it builds upon the foundational work of UoMBSat-1, the PQ8 system required significant architectural changes.

Notably, the structure of UoMBSat-1 could not be reused, as the PQ8 concept requires internal subdivision into eight units and imposes new mechanical constraints. This affected the dimensions and stacking arrangement of the subsystem PCBs, prompting a complete redesign of the structure. Additionally, the disengagement mechanism introduced by this research has no precedent in UoMBSat-1 and was developed from first principles.

The majority of the PQ satellite subsystems, excluding the EPS, were adapted from prior work carried out at the University of Malta. The EPS underwent further development to accommodate the additional requirements introduced by the disengagement mechanism.

1.11 Structure of Thesis

This thesis is organised into eight chapters, as summarised below:

Chapter 2 reviews prior work across four thematic areas: small satellites and constellation deployment strategies, dispersal methods, deployable systems and structural design. The first two sections examine constellation deployment and dispersal methods, with a particular focus on differential drag control derived from first principles. Next, a review of deployable systems assesses existing technologies, and highlights the need for a new solution that meets the PQ8 requirements. Finally, the structural section focuses on industrial standards, specifications, and user manuals, which provide the applicable testing methodologies and safety criteria for space-flight qualification. In this final section, standards and specifications relevant to all space systems are favoured over academic sources that tend to be narrower, focusing on specific structures. The chapter concludes by identifying key research gaps in each area as they relate to the PQ8 Architecture.

Chapter 3 establishes the physical and operational context of the PQ8 system. It details the structure design, material selection, and mass and power budgets. The chapter then presents simulation-based structural qualification, including finite element analyses for quasi-static loads, modal frequencies, and shock events. These are followed by physical vibration and shock testing. The chapter concludes with a summary of structural and power-related constraints, which inform the subsequent design stages.

Chapter 4 develops the dispersal methodology used to achieve constellation phasing. The method is generalised to be applicable across satellite form factors and scales. It introduces two algorithms that work in tandem to define the required Δv range and disengagement timings through differential drag control. The feasibility and scalability of the approach are demonstrated through two case studies.

Chapter 5 serves as a background chapter that consolidates the system-level requirements and constraints associated with the disengagement mechanism. These include structural, thermal, electrical, volumetric, and timing-related limitations, as discussed in previous chapters. Subsequently, the chapter focuses on the design and modelling of the disengagement mechanism. It begins by analysing the force generation equations, then develops a dynamic model capturing the electrical-to-kinetic energy conversion process. This is followed by the design of the coil driver circuitry, including the coil design based on supercapacitor-coil pairing performance. The chapter concludes with a failure analysis of the electrical circuits, identifying mitigations implemented within current constraints and suggestions for future improvements.

Chapter 6 presents the simulation and experimental validation of the disengagement mechanism. It includes LTSpice simulations for circuit performance, Ansys Maxwell simulations for magnetic force and eddy current modelling, and MATLAB simulations of the dynamic system. This is followed by benchtop testing to verify circuit functionality and two pendulum-based test campaigns to demonstrate the disengagement dynamics.

The final chapter, Chapter 7, summarises the research findings and outlines how each of the stated objectives was met. It provides the concluding remarks for each primary research domain and offers recommendations for future work.

2 BACKGROUND AND LITERATURE REVIEW

This chapter provides a comprehensive background and review of the literature relevant to the design and feasibility of the PQ8 concept. The discussion begins by examining the development and adoption of small satellite form factors, specifically CubeSats and PocketQubes, and their role in supporting distributed missions and constellations. This is followed by an analysis of constellation deployment strategies and the key challenge of post-deployment dispersal, with a focus on passive methods suitable for propulsion-less satellites.

Subsequently, the chapter examines the mechanisms available to initiate the separation of multiple satellites from a single platform. This includes an assessment of existing deployment technologies and the limitations they present when scaled to the PQ8's form factor. A novel electromagnetic actuation concept, based on repurposed magnetorquers, is introduced as a potential solution.

Finally, the structural design requirements necessary to support launch survivability, deployment compatibility, and mechanism integration are reviewed. This includes references to applicable standards, such as the CubeSat Design Specification (CDS) and the European Cooperation for Space Standardisation (ECSS).

Through this review, the chapter aims to identify the key technological gaps addressed by the PQ8 Architecture and to justify the design direction adopted in the subsequent chapters of this thesis.

2.1 Small Satellites and Constellations

2.1.1 The Conception of CubeSats and PocketQubes

The emergence of small satellite standards, particularly CubeSats and PocketQubes, has transformed access to space over the past two decades. The CubeSat standard, introduced in the early 2000s by Professor Robert J. Twiggs (Stanford University), was intended as an educational platform to enable hands-on experience in satellite design [19]. The original 1U CubeSat concept specified a mass of approximately 1 kg, however subsequent revisions of the CubeSat standard (Revision 14.1) permit a mass of up to 2 kg [20].

Despite early perceptions of CubeSats as platforms primarily limited to student and amateur developers, the standard has seen substantial adoption over time. By 2012, more than 100 CubeSats had been launched [21]. By 2021, this number had grown to over 2,300 CubeSats, with non-academic missions accounting for more than two-thirds of all deployments [22]. This widespread adoption demonstrated the utility of the CubeSat form factor for low-cost missions. However, it also led to increased competition for launch slots, drove costs up and effectively pushed smaller academic developers out of the space. Launch costs for the first CubeSats, with masses of approximately 1 kg, were initially estimated at around $30,000 per satellite [23]. However, reported launch costs for CubeSats flown shortly thereafter were closer to approximately $40,000 per kilogram .[24]. By the mid-2010s, CubeSat rideshare costs were reported to reach values of up to $50,000 per kilogram [25]. Today, advancements in launch capabilities, particularly through rideshare programs like SpaceX's, have helped reduce the average cost to around $13,000 per 1U, although this figure remains highly dependent on mission profile, integration requirements, and the launch provider [2].

To mitigate these cost increases, Prof. Twiggs proposed the PocketQube (PQ) standard in 2009. A 1p PocketQube is a cube measuring 5 × 5 × 5 cm, with approximately one-eighth the volume and one-fourth the mass of a 1U CubeSat, as illustrated in Figure 2.2. In theory, a single 1U CubeSat volume could be replaced by up to eight PocketQubes [26]. While the PQ standard offered clear benefits in terms of miniaturisation, its deployment has remained limited. As of the time of writing, fewer than 100 PocketQubes

Figure 2.1: UWE-4 CubeSat [27]

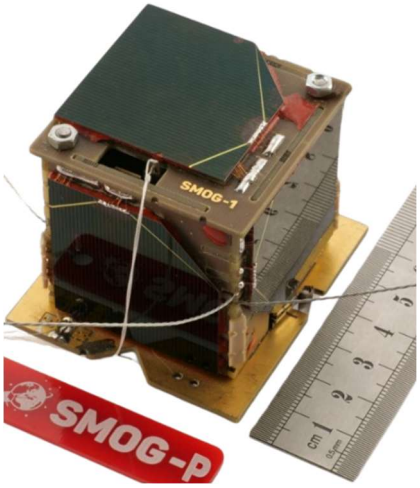

Figure 2.2: SMOG-P PocketQube [28]

have been launched globally [22]. The limited adoption of PocketQubes was driven primarily by regulatory constraints related to space debris mitigation and object trackability, as well as by launch integration barriers.

The very small dimensions of PocketQubes pose inherent risks for space-object tracking system. Empirical analyses of PocketQube tracking data indicate increased uncertainty and higher covariance between successive NORAD two-line element (TLE) data sets [29]. In turn, this results in degraded orbit-prediction fidelity and increased uncertainty for collision-risk estimation. Additionally, when considered alongside international space-debris mitigation frameworks, these tracking limitations impose additional constraints on PocketQube mission design. Particularly because designers must conform with IADC and UN COPUOS debris-mitigation guidelines, whereby the spacecraft must not remain in orbit past a bounded orbital lifetime [30]. This typically necessitates either operation at lower orbital altitudes or the adoption of end-of-life disposal strategies to facilitate rapid orbital decay.

These adoption barriers can be partially mitigated through careful orbital selection. Bouwmeester et al. show that, when accounting for worst-case non-operational behaviour and current debris-mitigation expectations, PocketQubes are best suited to circular low-Earth orbits below 500 km, with an optimal operational regime between 300 and 400 km altitude [29]. In this range, the natural orbital decay results in post-mission lifetimes in the order of approximately five years, aligning with space-debris mitigation guidelines. For missions requiring longer operational lifetimes, Bouwmeester et al. note that active drag management or propulsion-based orbit maintenance become necessary.

These factors have hindered the realisation of the standard's cost-saving potential, leading to the per-kilogram launch costs of a PocketQube being four times more expensive than those of a CubeSat.

Consequently, these costs undermines the core motivation behind the PocketQube standard and necessitate a different approach to improve the viability of this class of satellite and one that is more closely aligned to the original concept of the PocketQube. That is, the concept of subdividing the volume of a single 1U CubeSat among multiple independent users and thereby enabling cost sharing and reduced barriers to entry. This deployer-sharing philosophy formed the basis of the original eight-in-one PocketQube concept was also a key motivator for the ThinSat program, which sought to retain this cost-sharing and accessibility advantage while mitigating the operational and deployment limitations encountered by PocketQubes [31].

Both CubeSats and PocketQubes are governed by dedicated mechanical and operational standards that ensure compatibility with their respective deployers. The CubeSat Design Specification (CDS) defines the mechanical envelope, mass constraints, and interface requirements for CubeSats [20]. Adherence to this specification ensures compatibility with standard CubeSat deployers, such as the Poly-Picosatellite Orbital Deployer (P-POD), illustrated in Figure 2.3, or similar alternatives but also facilitates integration and qualification processes across launch providers.

Similarly, the PocketQube Standard outlines the design requirements for PocketQubes, including dimensions, mass limits, and deployment interfaces. PocketQube deployers include the Morehead-Rome Femto Orbital Deployer (MRFOD) and the Albapod v2, illustrated in Figure 2.4, among others [32].

The PQ8 Architecture subdivides a 1U CubeSat into eight PocketQube-sized satellites. These eight satellites are conceptually PocketQubes but are mechanically modified to assemble into a single 1U CubeSat that is fully compatible with standard CubeSat deployers. This approach improves deployer utilisation efficiency, reduces launch costs, and enables new constellation strategies. As such, the limitations of existing PocketQube deployment methods are a central concern of this work.

Figure 2.3: P-POD [33]

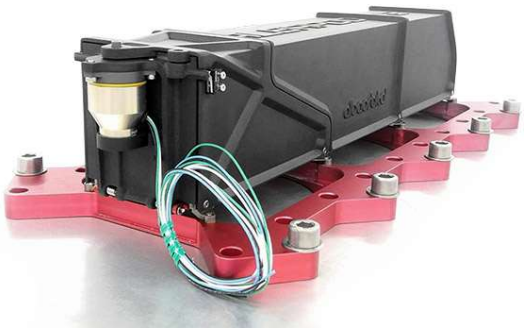

Figure 2.4: AlbaPod [34]

2.1.2 Small Satellite Constellations and Their Deployment

The adoption of small satellites has coincided with a growing interest in satellite constellations, distributed groups of satellites operating cooperatively to deliver enhanced performance, spatial coverage, or redundancy. While large-scale constellations such as Starlink and OneWeb are among the most visible examples, they are not representative of the scale or budget of typical small satellite missions. Their satellites, though technically "small" compared to traditional spacecraft, weigh several hundred kilograms and are supported by dedicated launch campaigns.

More pertinent to the PQ8 Architecture are CubeSat-scale constellations such as QB50, Planet Labs, and Alba Orbital. The QB50 mission, for instance, sought to deploy 50 CubeSats in a “string-of-pearls” configuration to perform atmospheric research at altitudes near 380 km [35,36]. QB50 was initially planned to be deployed via a single launch and using a sequential deployment strategy, whereby the satellites would be released in 4 to 6 minute intervals. This aimed to reduce the risk of collision and promote spatial separation. However, due to launch-related logistical issues, deployment of the constellation required multiple launch campaigns, undermining the intended single-launch architecture [37].

Similar challenges were encountered by Planet Labs, whose Earth observation constellation now consists of more than 130 CubeSats. Due to the absence of dedicated launches for small satellites, Planet Labs relied heavily on rideshare opportunities aboard a diverse set of launch vehicles [4]. This distributed launch approach, while operationally

successful, introduced long deployment timelines, scheduling uncertainties, and substantial integration overheads.

Literature describing the deployment of PocketQube constellations remains limited. To date, there is no clear evidence of any fully deployed, operational PocketQube constellation comparable in scale or maturity to CubeSat constellations. This is largely attributable to the relative immaturity of PocketQube technology, which is still undergoing validation in terms of reliability, regulatory acceptance, and launch integration [38]. The most prominent example of a multi-satellite PocketQube deployment is the FOSSASAT initiative, which consists of a series of open-source satellites developed to demonstrate low-cost space access and basic Internet-of-Things (IoT) functionality [39]. Similar to CubeSat constellations, the FOSSASAT satellites were also deployed using a distributed launch approach, with missions spread across multiple launches rather than a single coordinated deployment.

In summary, the reliance on multi-launch strategies presents persistent challenges for small satellite constellation developers, including:

- Disproportionate cost per satellite,
- Fragmented mission timelines,
- Increased complexity in coordinating orbital phasing,
- Reduced flexibility, particularly for time-sensitive space missions.

These challenges highlight the need for alternative architectures that decouple constellation deployment from multi-launch dependency. The PQ8 Architecture directly addresses this problem by integrating eight PocketQubes into a single satellite compatible with CubeSat deployers. Once in orbit, the satellites disengage hierarchically until all the units in the constellation are functioning independently. Although advancements in orbital deployers allow for large amounts of PocketQubes to be launched simultaneously, they fail to reach the volumetric optimisation and cost reductions promised by the PQ8 Architecture.

2.2 Constellation Dispersion Strategies

Once all the satellites are deployed into orbit, the next step is dispersal. That is the positioning of the satellites relative to one another to achieve the desired constellation configuration. This configuration can either be in-plane, where all the satellites share the same orbital plane (string-of-pearls), or cross-plane, where the satellites' orbital planes

are phased, providing greater spatial coverage. Satellite phasing can be achieved through propulsion, if available, or by leveraging natural perturbations. Multiple factors, including satellite size, available power, mission lifetime, orbital altitude, and the required phasing precision, govern the choice of dispersal strategy.

For large satellites equipped with propulsion systems, dispersal is often achieved by controlled thrust manoeuvres. A notable example is the FORMOSAT-3/COSMIC mission, which deployed six satellites using an intermediary vehicle, called a *pellet*. The satellites were individually ejected at planned intervals, using onboard propulsion to modify their orbits and induce phasing through differential nodal precession [1]. However, this method is not feasible for satellites in the pico- or nano-scales due to the significant mass, volume, and energy demands of propulsion systems.

For architectures constrained by size and energy, such as PocketQubes, passive dispersal mechanisms offer a viable alternative. These techniques utilise natural orbital perturbations, such as atmospheric drag, Earth's oblateness (the J2 effect), and solar radiation pressure (SRP), to achieve satellite separation over time. Differential nodal precession, driven by the J2 effect, enables RAAN separation between satellites placed in orbits with different altitudes or inclinations. Whilst atmospheric drag can be exploited to create velocity differentials between satellites by varying their ballistic coefficients, allowing for phasing along the same orbital path. Similarly, solar radiation pressure can be used for in-plane phasing, but through the reflection of solar energies rather than drag. Depending on the selected method, these effects can be exploited to produce differential variations in orbital parameters, including the true anomaly, RAAN, or inclination.

Numerous satellite missions have demonstrated the viability of passive dispersal. For example, the GRACE mission used differential drag to maintain precise in-plane formation, and FORMOSAT-3/FORMOSAT-3/COSMIC capitalised on the J2-induced nodal precession to phase satellites across multiple orbital planes [40]. These case studies demonstrate the practical applicability of passive mechanisms in achieving effective constellation deployment without the need for propulsion, a key consideration for the PQ8 Architecture. The following sections provide an in-depth exploration of the existing literature on passive dispersal, with an emphasis on differential atmospheric drag, nodal precession, and SRP-based methods, each evaluated in terms of their suitability for the PQ8 Architecture.

2.2.1 Atmospheric Drag and Lift

Atmospheric drag and lift arise from momentum exchange between a satellite and the residual atmosphere at orbital altitudes. As molecules collide with the satellite surface, the resulting change in momentum generates aerodynamic forces, drag acting in the direction of velocity, and lift acting perpendicular to it. These forces can be expressed as accelerations through Eq. 2.1 and 2.2, respectively:

$$\overrightarrow{\mathrm{a}_D} = \frac{1}{2}\, c_D\, \rho\, \frac{\mathrm{A}}{m}\, \vec{\mathrm{v}}\, \hat{\mathrm{v}} \qquad \text{(Eq. 2.1)}$$

$$\overrightarrow{\mathrm{a}_L} = \frac{1}{2}\, c_L\, \rho \frac{\mathrm{A}}{\mathrm{m}}\, \vec{\mathrm{v}}\, \hat{n} \qquad \text{(Eq. 2.2)}$$

Where A is the projected surface area, m is the satellite mass, ρ is the local atmospheric density, c_D *and* c_L are the drag and lift coefficients, respectively, $\vec{v}$ is the satellite's velocity vector, and $\hat{n}$ is a unit vector normal to the surface. The direction of lift depends on the satellite's attitude and can, in theory, be used to induce cross-track motion [41].

Although, in principle, atmospheric lift could enable differential out-of-plane motion for constellation phasing, this approach poses serious challenges. Generating meaningful inclination change via lift requires significant control authority and surface area, both of which are not feasible solutions for small satellites. Although, in principle, atmospheric lift could enable differential out-of-plane motion for constellation phasing, its application is constrained by practical limitations. Achieving meaningful inclination change via aerodynamic lift would require levels of control authority and surface area incompatible with the scale and dimensional constraints of the PQ8 architecture. Consequently, this perturbation is not considered in this study.

2.2.2 Differential Drag

Differential drag is a practical and effective strategy for passive constellation dispersal. It enables along-track formation control and constellation phasing by modulating atmospheric drag through changes in satellite orientation or the deployment of drag-enhancing surfaces. This technique is especially well suited to missions with strict size, mass, and power constraints that preclude traditional thruster-based manoeuvring. In addition to formation-keeping, differential drag has been successfully employed for collision avoidance, constellation reconfiguration, and passive rendezvous operations.

Its utility has been demonstrated in multiple operational missions, some examples include NASA's Cyclone Global Navigation Satellite System (CYGNSS), ORBCOMM's constellation, Planet Labs' Flock and The Aerospace Corporation's AeroCube-4 [42–45]. More recently, its use has been extended to periodic rendezvous missions, as illustrated by Jeon et al. in the design of a CubeSat coronagraph system [46].

NASA's CYGNSS, Figure 2.5, mission, launched in 2016, deployed eight propulsion-less microsatellites to measure GPS signal reflections for tropical cyclone wind retrieval, relying exclusively on differential drag for constellation phasing and maintenance [47]. Differential drag control enabled operators to gradually phase the satellites for uniform topical coverage. However, the effectiveness of differential drag was severely constrained by a higher-than-planned orbital altitude, unexpectedly low solar activity (resulting in reduced atmospheric density), and mission operations that limited the use of high-drag modes during key observation periods. These challenges delayed the intended phasing timeline by over two years. Nonetheless, CYGNSS validated differential drag as a viable, if operationally sensitive, strategy for non-propulsive orbit control, demonstrating its potential for distributed satellite missions in low Earth orbit under constrained mass and power budgets.

The ORBCOMM constellation, Figure 2.6, comprising 36 low Earth orbit satellites, was one of the first commercial systems to operationalise atmospheric differential drag for constellation management [43,48]. Along-track phasing was achieved by adjusting the orientation of the satellites' solar arrays to vary drag levels, based on weekly planning cycles. These attitude changes were typically performed during eclipse periods to avoid interfering with power generation. While differential drag was the primary mechanism for maintaining relative spacing, the system also incorporated occasional propulsion manoeuvres for drift correction and station keeping, forming a hybrid control approach. ORBCOMM's successful long-term operation demonstrated the feasibility and effectiveness of drag-based methods for large constellation management, influencing later satellite networks that adopted similar strategies.

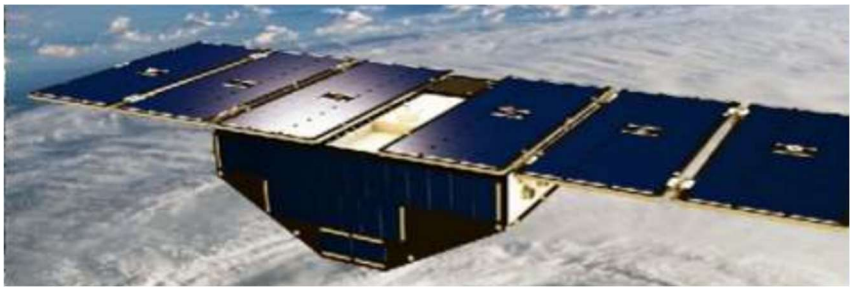

Figure 2.5: CYNSS Microsatellite [42]

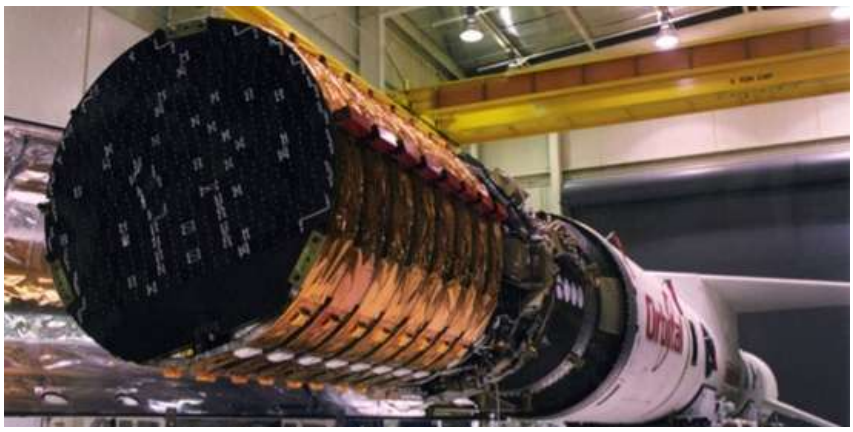

Figure 2.6: A stack of eight ORBCOMM Satellites on Pegasus [43]

AeroCube-4, as shown in Figure 2.7, developed by The Aerospace Corporation under the SMC/XR initiative, was a 1U CubeSat weighing approximately 2.2 kg that demonstrated several novel spaceflight technologies [45,49]. Among its key features were deployable solar panels designed to enable modulation of the satellite's ballistic coefficient. By opening or closing these panels, AeroCube-4 could vary its effective drag area, allowing differential drag-based formation control without the need for propulsion. This capability was supported by a three-axis attitude control system, which provided an absolute pointing accuracy of approximately 1°, enabling precise orientation adjustments for controlled drag modulation. AeroCube-4 served as an early proof-of-concept for passive formation flying among small satellites, illustrating how simple mechanical adjustments and robust ADCS can support orbital phasing strategies in propulsion-less platforms.

The Flock constellation by Planet Labs represents one of the most significant applications of differential drag control in commercial Earth observation [44]. Consisting of over a hundred 3U CubeSats deployed from the International Space Station and various rideshare launches, the Flock satellites used attitude-induced drag modulation to phase themselves into operational configurations. Phasing was achieved by alternating each satellite between high-drag and low-drag attitudes, as illustrated in Figure 2.8. A

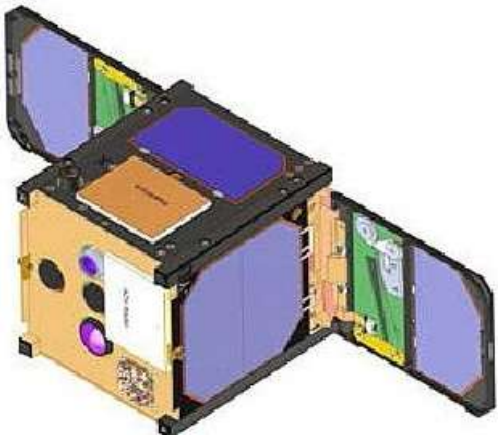

Figure 2.7: AeroCube-4 [49]

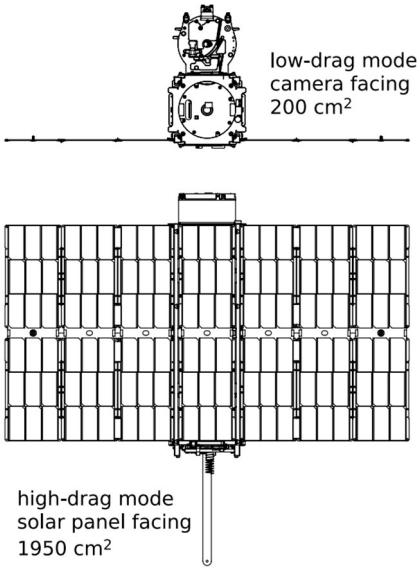

Figure 2.8: Planet Labs Drag Modes [44]

centralised ground-based controller estimated relative drift, assigned final constellation slots, and generated command sequences to coordinate satellite reorientation.

Although the available drag authority was lower than expected due to atmospheric variability and unmodeled system effects, this methodology allowed the controller to adapt dynamically, enabling successful convergence to target configurations. The method proved scalable from small to large fleets and demonstrated that high-precision constellation phasing could be achieved passively, with minimal impact on satellite lifetime.

Despite the successful application of differential drag across several missions, these missions reveal important limitations of the technique. The CYGNSS mission, for instance, was inserted into an orbit at a higher altitude than planned, resulting in reduced atmospheric densities and thus exceeding the predicted phasing times. Similarly, Planet Labs' Dove satellites experienced slower separation rates than expected, due to the inaccuracies in atmospheric models, an issue that introduces significant inaccuracies in drag calculations. These cases highlight the sensitivity of differential drag strategies to both the ambient atmospheric density, which is influenced by solar activity, and the accuracy of orbit insertion provided by the launch vehicle.

2.2.3 Differential Drag Control

Central to differential drag manoeuvring is the concept across the illustrated examples, is the ballistic coefficient, β, which determines a satellite's susceptibility to atmospheric drag. It is defined as the ratio of satellite mass to the product of its projected area and drag coefficients, as given in Eq. 2.1 and shown in Eq. 2.3:

$$\boldsymbol{\beta = \frac{m}{A c_D}} \qquad \text{(Eq. 2.3)}$$

Satellites with a higher ballistic coefficient experience smaller drag accelerations than those with a lower ballistic coefficient. Consequently, differential drag control is typically implemented as a binary modulation scheme, in which satellites alternate between two aerodynamic configurations. Through attitude control, each satellite is oriented to produce either a maximum or minimum projected area relative to the velocity vector, corresponding to the maximum and minimum ballistic coefficients, β_{Max} and β_{Min}, respectively. These discrete states produce a differential acceleration along the orbital track, which constitutes the control authority available to the system for managing relative motion within the constellation.

This differential acceleration forms the basis of the control authority available for orbit phasing and formation management. Over time, various advanced strategies have been developed to optimise this control. These include linear programming, Lyapunov-based adaptive controllers, linear-quadratic regulators (LQR), and convex optimisation techniques, as well as hybrid approaches that combine drag modulation with limited propulsion or lift control [50–54]. Such strategies span both centralised and decentralised architectures, with some leveraging inter-satellite communication and differential nodal precession to extend control beyond the along-track direction.

The differential drag control model developed by Planet Labs is of particular interest due to its simplicity and demonstrated effectiveness in orbit. Their approach, presented in [44], provides a straightforward yet robust formulation that has been successfully applied to large-scale CubeSat constellations and is readily scalable to other form factors. In this model, a discretised set of Cartesian position and velocity vectors of the satellites in the constellation is converted into separation angles, θ, and their rate of change, $\dot{\theta}$, with respect to a designated reference satellite over a 24-hour period, k.

The separation angles experience acceleration due to the application of differential drag, with the magnitude given by Eq. 2.4.

$$\ddot{\boldsymbol{\theta}}_{\boldsymbol{k}} = \frac{\mathbf{3}\boldsymbol{q}_{\boldsymbol{ref,k}}}{\bar{\boldsymbol{a}}_{\boldsymbol{ref}}}\left(\frac{\mathbf{1}}{\boldsymbol{\beta}_{\boldsymbol{Min}}} - \frac{\mathbf{1}}{\boldsymbol{\beta}_{\boldsymbol{Max}}}\right) \quad \text{(Eq. 2.4)}$$

Where $\beta = m/sc_D$, $\bar{a}_{ref}$ is the mean semi-major axis of the reference satellite and $q_{ref,k}$ is the mean dynamic pressure over the discretised period k given by $q_{ref,k} = \frac{1}{2}\overline{\rho v^2}$. This angular acceleration serves as the control variable, providing either acceleration or deceleration between a satellite and reference pair. It is controlled through the ADCS commands using a binary control scheme, in which the satellites orient themselves to align with either $\beta_{Max}\ and\ \beta_{Min}$. Effectively, this splits the phasing time of the two satellites into an acceleration period and a deceleration period, denoted by $\Delta t_a and\ \Delta t_b$. Minimising the sum of these two periods yields the optimal phasing time.

Foster et al. also provide an analytical solution for phasing in, albeit for the case of two satellites, or a satellite-reference pair [44]. Where, considering the case of a two-satellite system, with initial relative motion $\left[\theta\ \dot{\theta}\right]_0^T$ and the desired final relative motion $\left[\theta\ \dot{\theta}\right]_f^T$, then $\Delta t_a and\ \Delta t_b$ are given analytically by Eq. 2.5 and 2.6.

$$\boldsymbol{\Delta t_B} = \frac{\boldsymbol{\Delta\dot{\theta} - \ddot{\theta}_A \Delta t_A}}{\ddot{\boldsymbol{\theta}}_{\boldsymbol{B}}}, \text{ and} \quad \text{(Eq. 2.5)}$$

$$\left[\frac{1}{2}\ddot{\theta}_A\left(\frac{\ddot{\theta}_A}{\ddot{\theta}_B} - 1\right)\right]\Delta t_A^2 + \left[\dot{\theta}_0\left(\frac{\ddot{\theta}_A}{\ddot{\theta}_B} - 1\right)\right]\Delta t_A + \left[\Delta\theta - \frac{\Delta\dot{\theta}}{\ddot{\theta}_B}\left(\dot{\theta}_0 + \frac{1}{2}\Delta\dot{\theta}\right)\right] = 0 \quad \text{(Eq. 2.6)}$$

Where $\ddot{\theta}_A = \ddot{\theta}$, $\ddot{\theta}_B = -\ddot{\theta}$, $\Delta\theta = \theta_f - \theta_0$ and $\Delta\dot{\theta} = \dot{\theta}_f - \dot{\theta}_0$. The solution is the $\Delta t_a and\ \Delta t_b$ that provide positive, real roots for the given relative motion and angular acceleration.

A critical limitation of differential drag control lies in its reliance on accurate estimation of the ballistic coefficient, β, which in turn depends on the drag coefficient, c_D. While satellite mass and projected area can be determined with high precision, the drag coefficient is far more complex to quantify. It is influenced by a combination of satellite geometry, surface materials, and the molecular composition and density of the surrounding atmosphere, all of which vary with altitude, solar activity, and orbital conditions. As such, the following section explores the physical principles governing drag

in the free molecular flow regime and presents established models used to estimate c_D under varying gas-surface interaction conditions.

2.2.4 Calculating the Drag Coefficient

This complexity necessitates a detailed understanding of the gas–surface interactions that govern aerodynamic forces in low Earth orbit. For satellites operating between 150 and 500 km, these interactions occur in the free-molecular flow regime, where traditional viscous flow assumptions no longer apply [55]. In this regime, drag arises from individual molecular impacts rather than collective fluid behaviour, requiring specialised models and assumptions to accurately characterise the drag coefficient, as illustrated in Figure 2.9.

In the free-molecular regime, two primary interactions govern satellite drag. The first is the ramming interaction, which occurs when particles impinge along the satellite's velocity vector. The second involves particles arriving from random directions due to thermal motion. However, when the satellite's orbital velocity far exceeds the thermal motion of atmospheric particles, a condition known as hyperthermal flow, the second component becomes negligible.[56]. To confirm hyperthermal flow, the molecular speed ratio, s, is evaluated through:

$$s = \frac{v_{body}}{v_m}$$

Where v_{body} is the satellite's orbital velocity with respect to the atmosphere, and v_m is the most probable molecular speed, dependent on atmospheric temperature$T$, molecular weight M, and gas constant R and given by Eq. 2.7:

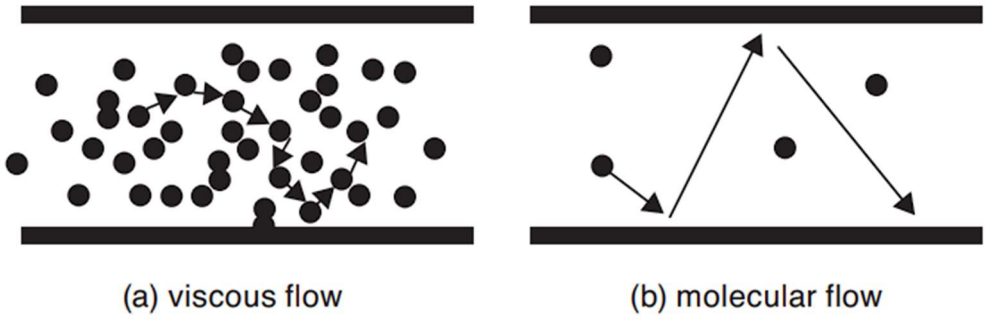

Figure 2.9: Viscous Flow vs Molecular Flow. Reproduced from [57].

$$\boldsymbol{v_m = \sqrt{\frac{2RT}{M}}} \qquad \text{(Eq. 2.7)}$$

Ballance et al. showed that speed ratios greater than 5 are sufficient to classify the flow as hyperthermal [56]. Furthermore, at altitudes below 700 km, this condition is consistently met [58].

Under this condition, the total aerodynamic force on the satellite can be expressed as the sum of momentum exchanges between incident atmospheric particles and the satellite surface:

$$F_T = \sum N_i m_{m_i} \Delta v_{m_i}$$

where N_i is the number of incident molecules, m_m is the mass of the molecule and Δv_m is the change in velocity upon interaction.

However, the momentum exchange depends on how these molecules are re-emitted, particularly whether they are reflected specularly, diffusely or in a quasi-specular manner. Traditionally, most coefficient of drag calculations are built upon two assumptions [55]:

1. Molecules lose almost all energy when striking the satellite surface,
2. Molecules are reemitted with a diffuse angular distribution.

The validity of these assumptions depends on the energy accommodation coefficient, α, which determines if a molecule is deflected and the type of deflection:

$$\alpha = \frac{E_i - E_r}{E_i - E_w}$$

where $E_i \; and \; E_r$ are the average kinetic energies of incident and reemitted molecules, respectively, and $E_w \; is \; the$ average kinetic energy of the molecules reemitted from the satellite at a velocity corresponding to the surface temperature.

The value of α depends on gas species, surface material, temperature, cleanliness or contamination of the surface, and the velocity of impact. In LEO, atomic oxygen dominates the residual atmosphere, and its reactivity with surface materials significantly influences accommodation and, by extension, drag [55]

Deflection dynamics further refine drag behaviour. Molecules may deflect normally or tangentially to the surface, characterised by the momentum accommodation coefficients, $\sigma_n \; and \; \sigma_t$ [59]. Full momentum accommodation corresponds to diffuse reflection ($\sigma_n = \sigma_t = 1$), corresponding to an energy accommodation coefficient of $\alpha = 1$. In contrast, zero accommodation leads to specular reflection ($\sigma_n = \sigma_t = 0$) [55]. Any value in between these extremities results in a quasi-specular reemission. Empirical studies have shown that the energy accommodation coefficient typically falls between the two extremes, indicating a mix of diffuse and quasi-specular reemission of particles. For instance, research conducted on the Space Shuttle observed the scattering of atomic oxygen incident on a carbon surface at energies of 5 eV. The findings revealed that 98% of the reemission was diffuse, with the remaining portion being quasi-specular, at an altitude of 225 km [60].

Adsorption effects, i.e. the process where molecules bind to the surface of the satellite, also play a role. Clean surfaces tend to reflect particles more specularly, whereas contaminated surfaces (e.g., with oxidised films) encourage diffuse scattering and higher drag. Long-duration missions may therefore exhibit evolving drag coefficients due to ongoing adsorption and changes in surface composition [61]. External CubeSat surfaces are typically covered in solar cell assemblies, including cover glass made from materials such as quartz, sapphire, or cerium-doped glass, alongside anodised aluminium rails. The exact material properties and their evolution must be considered in drag modelling.

Sputtering, the ejection of surface atoms due to high-energy particle collisions, is negligible in this context. In LEO, atmospheric particle energies range from 0.5 – 6 eV, well below the 20 eV threshold generally required for significant sputtering [61].

Understanding these surface and flow-dependent interactions is essential to accurately modelling drag. The energy accommodation coefficient directly informs momentum transfer and, by extension, the effective drag coefficient. However, calculating the drag coefficient from these physical principles requires precise knowledge of gas-surface interactions and access to specialised experimental equipment. It is therefore beyond the scope of this work. Fortunately, several well-established models have been developed to estimate drag coefficients in the free-molecular regime. The following section introduces three such models, including those created by Sentman, Schamberg, and Moe et. al, each based on distinct assumptions about surface accommodation, angular reemission, and energy transfer mechanisms.

2.2.4.1 Sentman's Model

In Sentman's model, the gas-surface interaction is assumed to be entirely diffuse, with the reflected molecules having a Maxwellian velocity distribution. The assumption results in a reasonably accurate estimation for VLEO altitudes, with a range of 150 – 300 km, where the reflections are predominantly diffuse [61]. However, this accuracy degrades at higher altitudes. Through his model, Sentman derived the drag coefficients for various shapes. The most pertinent of which is that of a flat plate with a molecule striking the surface at an angle β, given by Eq. 2.8:

$$\boldsymbol{c_d A_{ref}} = \frac{\boldsymbol{P}}{\sqrt{\boldsymbol{\pi}}} + \boldsymbol{\gamma Q Z} + \frac{\boldsymbol{\gamma v_r}}{\boldsymbol{2 v_i}} (\boldsymbol{\gamma}\sqrt{\boldsymbol{\pi}}\boldsymbol{Z} + \boldsymbol{P}) \qquad \text{(Eq. 2.8)}$$

Where:

$$\gamma = \cos(\beta), P = \frac{1}{s} e^{-\gamma^2 s^2}, Q = 1 + \frac{1}{2s^2}, Z = 1 + ERF(\gamma s)$$

V_r and V_i are the most probable speed of the molecule and the speed at which it strikes the surface, respectively. *ERF* is the Gauss error function. The two speeds are related through:

$$\frac{v_r}{v_i} = r = \sqrt{\frac{E_r}{E_i}} = \sqrt{\frac{2}{3}\left[1 - \alpha\left(1 - \frac{E_s}{E_i}\right)\right]}$$

Although the model is reasonably accurate at lower altitudes, as the altitude increases, so does the specular component of the reflection, and thus the accuracy diminishes.

2.2.4.2 Schamberg's Model

Schamberg's model estimates the coefficient of drag, with the assumption of hyperthermal molecular, by employing the reflection law, in which:

$$\cos(\theta_r) = \cos^{\mathrm{v}}(\theta_i), v \gg 1$$

where θ_i and θ_r are the angles of the incident and reflected molecular beams, respectively, the term v describes the nature of the reflected beam, whereby $v = 1$ describes a diffuse reflection, $v = \infty$ describes a specular reflection, and any value in between describes a quasi-specular reflection. Therefore, unlike Sentman's model,

Schamberg's model can represent the specular component of the reemission. Since it assumes hyperthermal flow, the model is only valid for altitudes up to about 700 km.

The drag coefficients for various shapes and angles of attack, derived through Schamberg's model, are shown in

Figure 2.10, where r represents the ratio $\frac{v_r}{v_i}$.

2.2.4.3 Moe & Moe Model

Through their research, Moe et al. demonstrated how combining Sentman's and Schamberg's methods can be used to estimate the drag coefficient across a broader range of physical situations [62]. They suggest employing Sentman's model to compute the diffuse component of the drag coefficient, $c_{D_{Diffuse}}$, while using Schamberg's model for the specular component, $c_{D_{Specular}}$. For the latter, they additionally recommend utilising Goodman's model, in [63], for estimating the energy accommodation coefficient, as indicated by Eq. 2.9.:

$$\boldsymbol{\alpha = \frac{3.6u\sin(\theta)}{1+u^2}} \qquad \text{(Eq. 2.9)}$$

Shape	Drag coefficient (based on projected area perpendicular to direction of motion)	
	Diffuse re-emission	Accommodated specular reflexion
Flat plate (normal to flow)	$2(1+\frac{2}{3}r)$	$2(1+r)$
Flat plate at incidence θ	$2(1+\frac{2}{3}r\sin\theta)$	$2(1-r\cos 2\theta)$
Sphere	$2(1+\frac{4}{9}r)$	2
Cylinder perpendicular to flow	$2(1+\frac{\pi}{6}r)$	$2(1+\frac{1}{3}r)$
Cone of semi vertex angle ψ with vertex forwards and axis parallel to flow	$2(1+\frac{2}{3}r\sin\psi)$	$2(1-r\cos 2\psi)$

Figure 2.10: Drag Coefficients for various shapes using Schamberg's Model [58].

where θ is the angle of incidence, and u is the ratio of the mass of the incident molecule to that of the reflected molecule. The total drag coefficient would then be the sum of the two components as shown in Eq. 2.10:

$$\boldsymbol{\alpha c_{D_{Total}} = f c_{D_{Diffuse}} + (1 - f) c_{D_{Specular}}} \qquad \text{(Eq. 2.10)}$$

where f describes the fraction of the drag coefficient that is diffuse, which is determined empirically.

2.2.4.4 Summary of Coefficient of Drag Estimation

The accurate estimation of the drag coefficient, c_D, is a critical yet inherently uncertain component of differential drag control. It depends on multiple coupled variables: the composition and structure of the residual atmosphere, the surface material and condition of the satellite, and the nature of the gas–surface interaction. In the free-molecular flow regime relevant to low Earth orbit, these interactions become highly sensitive to accommodation phenomena that are difficult to measure or predict. While deriving c_D from first principles requires detailed experimental setups beyond the scope of this work, several analytical and semi-empirical models provide practical alternatives.

The Sentman model offers reliable estimates for diffuse reemission at very low altitudes, while Schamberg's model accounts for quasi-specular reemission and is valid up to about 700 km. The Moe & Moe approach synthesises both models, using a weighted combination modulated by empirical accommodation coefficients. These models form the basis for practical aerodynamic modelling in orbit and are used in the present work to support differential drag simulations and performance prediction.

In the context of this work, the estimation of c_D represents the most significant source of uncertainty in calculating the ballistic coefficient and, by extension, in predicting the performance of differential drag-based dispersal. Nevertheless, the use of well-established models provides a sufficiently robust basis for simulation and design iteration.

2.2.5 Nodal Precession

Nodal precession refers to the secular change in the Right Ascension of the Ascending Node (RAAN) due to the oblateness of Earth, or the J2 perturbation. The equation for nodal precession, Eq. 2.11, with semi-major axis *a,* inclination *I* and

eccentricity *e*. Nodal precession is relevant to constellation dispersal as it results in a shift in the orbital plane. Consequently, the use of differential nodal precession can be employed to achieve passive out-of-plane phasing of a constellation.

$$\dot{\Omega}_{J2} = -\frac{3}{2} \cdot n \cdot cos(i) \cdot J_2 \cdot \left(\frac{R_E}{a(1-e^2)}\right)^2 \qquad \text{(Eq. 2.11)}$$

2.2.5.1 Differential Nodal Precession

The concept of exploiting differential nodal precession as a passive method for constellation dispersal was first proposed and patented by King and Beidleman in 1993, specifically for implementation in the FORMOSAT-3/COSMIC mission [1,64]. As shown in Figure 2.11, the constellation comprised six disc-shaped microsatellites mounted on an intermediary deployment platform referred to as a *pellet*.

Following launch, the pellet used onboard propulsion to reach a parking orbit with a semi-major axis greater than that of the target operational orbit. Each satellite was then sequentially ejected and employed its propulsion system to reduce its orbital altitude. Because nodal precession rates are altitude-dependent, the resulting differences in semi-major axis allowed each satellite's RAAN to drift relative to the others. To achieve the desired spacing, each subsequent satellite was released only after a RAAN separation of 30°, a process that spanned 20 months.

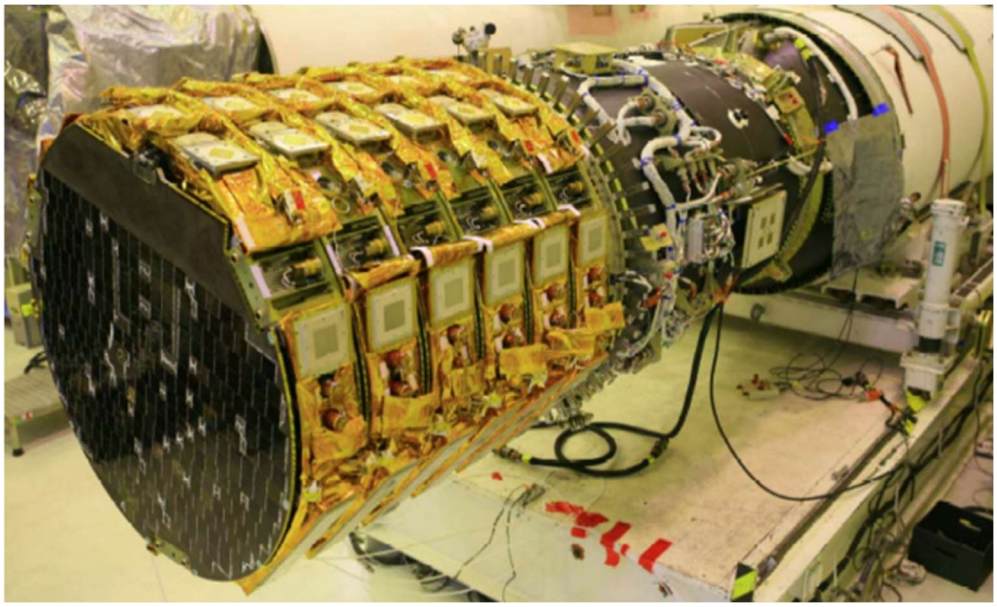

Figure 2.11: Six FORMOSAT-3 satellites on a pellet in a Minotaur launch vehicle [1].

While this approach successfully demonstrated passive RAAN phasing, it relied heavily on propulsion systems both at the carrier and satellite levels. This poses a significant limitation for nano- and pico-satellite missions, where mass, volume, and power constraints preclude onboard propulsion, rendering such a deployment architecture impractical for platforms like the PQ8.

Within this context, Leppinen investigated the feasibility of leveraging differential nodal precession for constellation deployment in a study at a CubeSat scale based on real orbital data from three small satellites: Delfi-C3, AAUSAT-2, and CanX-2 [65]. He noted that these satellites, despite being launched into similar initial orbits, exhibited differing rates of RAAN drift and altitude decay due to variations in mass and ballistic coefficients. The compiled RAAN and altitude data are shown in Figure 2.12.

Through simulation, Leppinen demonstrated that a six-satellite constellation with evenly spaced RAAN separations of 30 ° could be achieved using only passive means, within a time frame of approximately 4 to 5 years. His analysis further indicated that optimal initial deployment altitudes fall within the range of 600 to 800 km. At lower altitudes, excessive atmospheric drag accelerates orbital decay before sufficient RAAN drift occurs. At higher altitudes, drag becomes too weak to induce meaningful altitude differentials, reducing the differential precession effect.

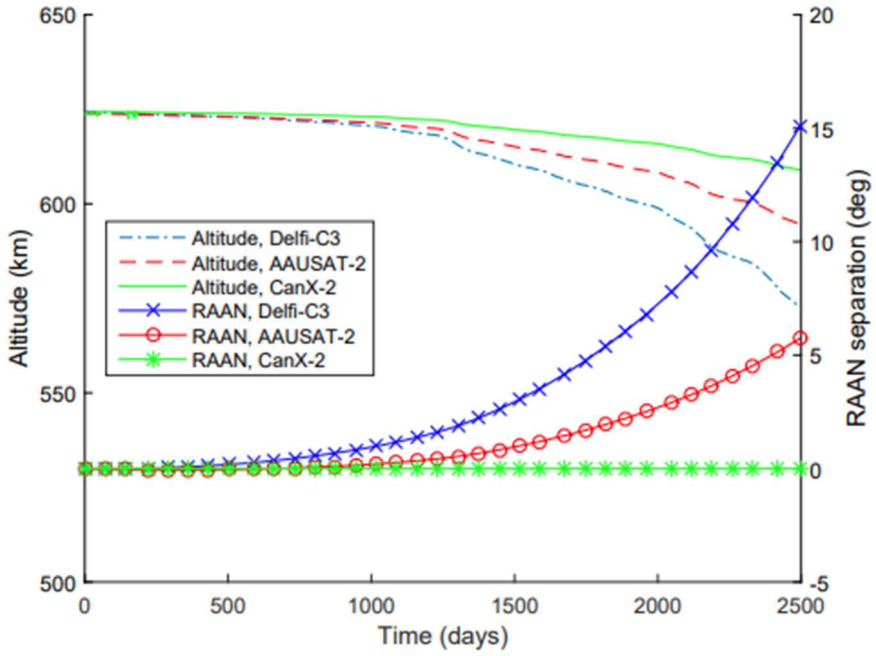

Figure 2.12: RAAN and Altitude Data for Delfi-3, AAUSAT-2 and CanX-2 [65].

Importantly, Leppinen's approach involved 3U CubeSats equipped with deployable drag sails to enhance the differential drag effect. In contrast, the PQ8 satellites considered in this work are significantly smaller and do not employ drag sails. As a result, the effectiveness of differential precession for PQ8 will be more limited, and the optimal altitude window is likely to shift downward. Additionally, the extended timelines associated with RAAN phasing must be weighed against the limited operational lifetime of PocketQube-class satellites.

Although differential nodal precession offers a compelling passive mechanism for out-of-plane constellation phasing, its practical implementation remains constrained by satellite size, the availability of drag-enhancing surfaces, and the required timeframes for phasing. As such, its applicability to PQ8 remains primarily theoretical unless paired with additional mechanisms for altitude separation.

2.2.6 Other Passive Dispersal Methods

In addition to atmospheric drag and nodal precession, several other orbital perturbations offer potential mechanisms for passive constellation dispersal. These include differential SRP and third-body gravitational effects. While less commonly employed, both mechanisms have been proposed or demonstrated in specific mission contexts and merit consideration within the broader framework of passive satellite phasing strategies.

Differential SRP becomes a potentially exploitable control mechanism at altitudes where atmospheric drag is minimal, typically above 600 km, where its influence is no longer dominated by aerodynamic perturbations. It operates analogously to differential drag, modulating satellite acceleration by varying the projected area and optical properties (e.g., reflectivity and absorptivity) of surfaces oriented toward the Sun. Varma et al. in [66] demonstrated, through both analytical and numerical studies, that SRP can be leveraged to achieve constellation phasing, even in the presence of perturbations such as the Earth's J2 effect. Differential SRP can be employed for in-plane phasing through adjustments to the semi-major axis and eccentricity, or for limited out-of-plane control by exploiting its influence on inclination and RAAN.

An alternative class of passive dispersal strategies involves third-body gravitational influences. One notable proposal by Chase et al. in [67] exploits the Earth-Moon Lagrange Point 1 (EML-1) as a staging location for constellation deployment. In

this approach, satellites are launched to EML-1 aboard carrier vehicles that then enter Halo orbits, a class of stable, three-dimensional orbits around the Lagrange point that balance gravitational and inertial forces. From these orbits, each carrier performs a return trajectory to low Earth orbit using aerobraking or aerocapture to lower its velocity and achieve orbital insertion. This technique offers the potential for rapid and controlled deployment of large satellite groups, with simulations showing full constellation placement in as little as 20 days [7]. Although the initial complexity and required energy budget are significantly higher than those of conventional deployment methods, the EML-1 strategy circumvents the need for differential phasing post-insertion.

These alternative approaches open up new possibilities for passive satellite dispersal. However, their suitability for a constellation depends on the needs of the particular mission and satellite properties like orbital altitude, available external surface areas and the selected deployment method. The following section summarises the techniques reviewed together with their strengths and limitations, as well as their applicability for the PQ8 Architecture.

2.2.7 Summary of Passive Constellation Dispersal Methods

Three primary passive methods for constellation dispersal were examined in this chapter: differential drag, differential nodal precession, and differential SRP. Each mechanism relies on natural orbital perturbations to induce separation between satellites but differs significantly in applicability depending on altitude, mission duration, and satellite capabilities.

Table 2.1 compares constellation deployment and dispersal strategies reported in the literature, together with the proposed PQ8 aggregated-launch approach, to illustrate its intended position within the existing design space.

Table 2.1: Comparison of constellation deployment and dispersal mechanisms

Strategy	Mission / Study	Scalability	Deployment Controllability	Cost efficiency	Complexity	Key limitations
Propulsive Maneuvers	FORMOSAT-3 / COSMIC	Moderate	High	Low	High	Requires propulsion Mass, volume, and power prohibitive at pico/nano scale
Differential Drag	CYGNSS, Planet Labs Flock, ORBCOMM, AeroCube-4	High	Moderate	High	Low	Sensitive to atmospheric density and drag-coefficient uncertainty
Differential Nodal Precession (J2)	FORMOSAT-3, Leppinen (CubeSat studies)	Moderate	Low	Moderate –high	Low	Requires altitude separation Phasing times exceed PocketQube lifetime
Differential SRP	Varma et al.	Moderate	Low– moderate	Moderate	Low	Ineffective at low altitudes where atmospheric drag dominates
Third-body/ Lagrange-point	EML-1 concept	High	High	Low	High	Requires propulsion at carrier level High energy and mission complexity
PQ8 (Proposed)	This work	High	Moderate	High	Moderate –high	Increased mission-level coordination and low-TRL maturity

Differential drag emerges as the most viable option for the dispersal method. The method has been successfully demonstrated on numerous missions, including CYGNSS and Planet Labs' Dove constellations. The technique requires no additional onboard equipment, with the control scheme achievable through existing ADCS hardware. However, its effectiveness relies on the accurate estimation of the satellite's drag coefficient, which in turn, depends on accurate and real-time data on atmospheric conditions at the orbit altitude.

Differential nodal precession, in contrast, provides a mechanism for out-of-plane phasing by exploiting variations in RAAN drift caused by the Earth's oblateness. While theoretically passive and continuous, this method requires significant differences in semi-major axis, which are difficult to achieve without propulsion. Leppinen's analysis of

small satellite orbits showed that achieving meaningful angular separation via this method could require 4 to 5 years, far exceeding the operational lifespan of most pico- or nanosatellites. As such, it is considered impractical for missions with constrained lifetimes and no propulsion capability.

Differential solar radiation pressure is a viable alternative for constellation phasing at altitudes above 600 km, where atmospheric drag becomes negligible. Similar in principle to differential drag, SRP-based control relies on modulating the projected surface area exposed to a perturbing force, in this case, solar radiation rather than residual atmosphere. When carefully designed, SRP strategies have been shown through simulation to enable both in-plane and out-of-plane phasing by leveraging differences in semi-major axis, eccentricity, inclination, or nodal precession. However, at lower altitudes, atmospheric drag overwhelmingly dominates perturbative forces, rendering SRP several orders of magnitude weaker and thus ineffective for practical control. Consequently, SRP is not a competitive dispersal mechanism for satellites operating in very low to low Earth orbit. Still, it may be considered for higher-altitude missions with appropriate surface-area-to-mass ratios and attitude control capabilities.

In conclusion, while each method offers unique benefits, differential drag remains the most appropriate passive dispersal strategy for low-altitude, propulsion-less constellations. Its effectiveness depends primarily on controlling the ballistic coefficient, and as such, modelling drag interactions remains a central focus for ensuring reliable phasing performance.

2.3 Disengagement Mechanisms

Dispersal is but one challenge for the PQ8 architecture. Before dispersal, a disengagement method is required to physically separate the many-in-one satellite system into smaller satellites. Due to the novelty of the architecture, technologies that are a direct analogy to the disengagement mechanism remain absent from the literature. However, to address this gap, insights can be drawn from existing studies on satellite deployables, which share similarities in their design principles and operational requirements.

2.3.1 A Framework for Deployment Mechanisms

A deployment mechanism typically follows a generalised framework comprising five sequential stages: stowage, restraint, actuation, guidance, and locking or latching [68]. The stowage stage reduces the mechanism's volume to fit within the designated payload envelope of the launch vehicle or deployer, while also protecting it from the mechanical stresses encountered before and during launch. The restraint stage ensures the mechanism remains immobilised during launch, preventing any unintended motion or premature deployment due to launch-induced loads.

Deployment begins with the actuation stage, where a device imparts motion onto the deployable, moving it from the stowed configuration to the deployed configuration. This is achieved in tandem with the guidance device, which regulates the path of the moving elements as well as their speed. Once fully deployed, the final stage is initiated, whereby a locking device secures the deployable in its deployed configuration.

This framework can be adapted to fit the context of the PQ8 Architecture. Stowage is analogous to the PQ8 satellites being held in the many-in-one configuration within the CubeSat deployer. Restraint ensures that, once deployed into orbit, the many-in-one satellite remains as a single unit until the actuation device initiates disengagement. Guidance mechanisms can be used to ensure that the satellites follow a precise trajectory during disengagement, in order to reduce the risks of collision due to rotations. Locking mechanisms are not applicable, however, as the satellites become physically decoupled following post-separation.

2.3.2 Restraint Devices

Restraint devices are essential in ensuring that the disengagement mechanism remains secure and immobile during the high dynamic loads experienced throughout launch. A review of restraint approaches provides the foundation for identifying a suitable solution for the PQ8 architecture. However, this review excludes restraint mechanisms that require pyrotechnics for release, as they are not compatible with the CDS.

2.3.2.1 Burn Wire

Burn wire mechanisms consist of a heating element, typically a nichrome wire or a carbon resistor, that severs a retaining wire or cord, as illustrated in Figure 2.13 [69]. Activation is achieved electronically, allowing for precise and reliable release timing. These mechanisms offer several advantages, including low mass, cost-effectiveness, and high reliability [70]. As they involve minimal moving parts, the risks of mechanical failure are significantly reduced. Additionally, it simplifies integration in miniaturised systems like PocketQubes. Burn wire systems also provide high holding forces within a compact volume, making them well-suited to space-constrained platforms.

However, their compact design can complicate the loading process, where mistakes, if made, can be difficult to detect or correct [68]. Additionally, if polymer-based cords are used as the restraint element, the cutting process may release smoke or particulates that risk contaminating sensitive surfaces, such as solar arrays.

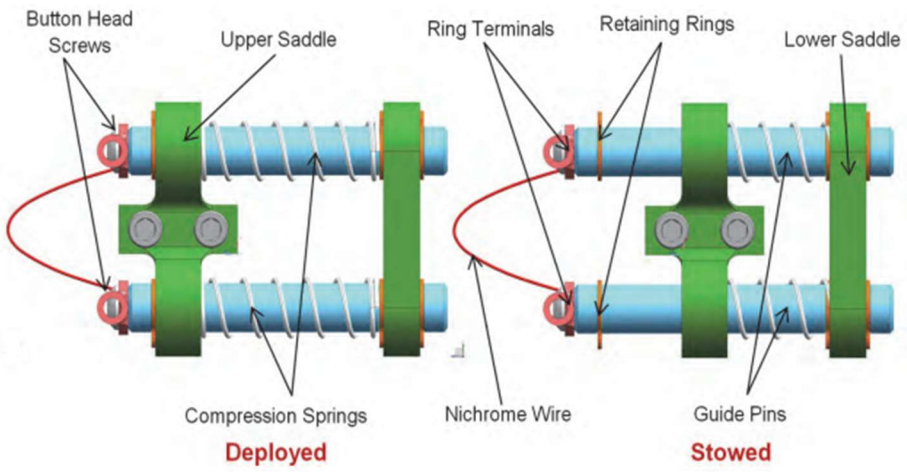

Figure 2.13: Example of a Burn-Wire Mechanism [71]

2.3.2.2 Electro-mechanical Latches

Electro-mechanical latches use active motors or linear actuators to mechanically secure or restrain deployable components in place. These mechanisms are often employed in applications requiring high precision and reliability. For instance, an electro-mechanical latch incorporating a piezoelectric linear actuator was developed for the European Space Agency's (ESA) Laser Interferometer Space Antenna (LISA), a mission designed to detect and measure gravitational waves [72]. The primary advantages of electro-mechanical latches include their precise, controlled operation, along with reusability and programmability. However, their relatively large size and weight can pose challenges in space-constrained satellite systems.

2.3.2.3 Shape Memory Alloys (SMA)

Shape Memory Alloys (SMAs) are specialised materials that, after being deformed at low temperatures, return to their predefined shape upon heating to a critical transition temperature, as illustrated in Figure 2.14. This distinctive thermomechanical behaviour makes SMAs attractive for use as restraint mechanisms in space systems, particularly because they can be actuated electrically via Joule heating. In addition to their unique actuation capability, SMA-based mechanisms are typically simple in design, compact in form, reliable in operation, and, in many cases, reusable - features that align well with the stringent requirements of space applications. [73].

On the other hand, SMAs require precise thermal management and tend to be relatively slow when compared to different mechanisms. The main issue of SMAs is the requirement of maintaining appropriate thermal conditions [74].

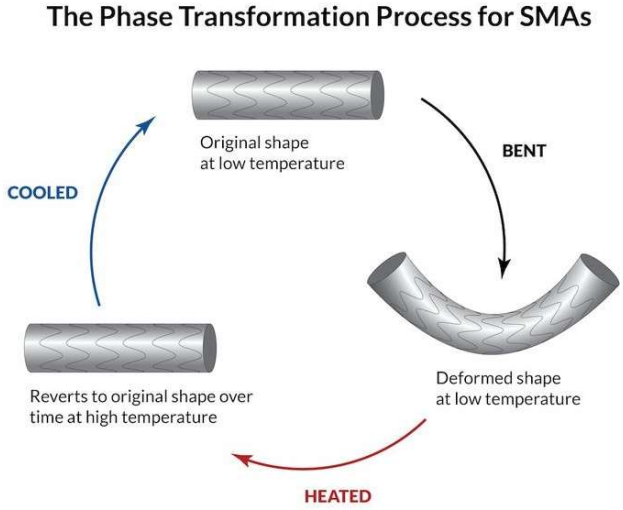

Figure 2.14: SMA Transformation Process [75]

2.3.2.4 Release Nuts

Release nuts, Figure 2.15, are devices comprising a segmented nut or threaded interface that is securely held together by a secondary restraining element, such as burn wires, latches, or SMAs [76]. Upon activation of the restraining element, the segments disengage, enabling the release of the nut or threaded interface.

These mechanisms are typically employed in applications requiring high preload retention due to their strength and reliability in securing deployable components. However, their use necessitates precise preload measurement during assembly, as the release forces are directly coupled to the applied preload [68]. Furthermore, the release nut is not a complete solution and requires additional restraining elements, thereby inheriting the associated complexities and limitations of those supplementary components.

2.3.2.5 Clamp Bands

Similar to release nuts, clamp bands secure a satellite or deployable component using a flexible material, such as Kevlar, that is wrapped around the payload or its interface, as illustrated in Figure 2.16 [77]. The tension in the flexible band provides the necessary restraint to hold components firmly in place. As with release nuts, the release process is initiated by activating a secondary restraint mechanism. Clamp bands are commonly employed to secure satellites to the launch vehicle and are favoured for their ability to withstand high loads.

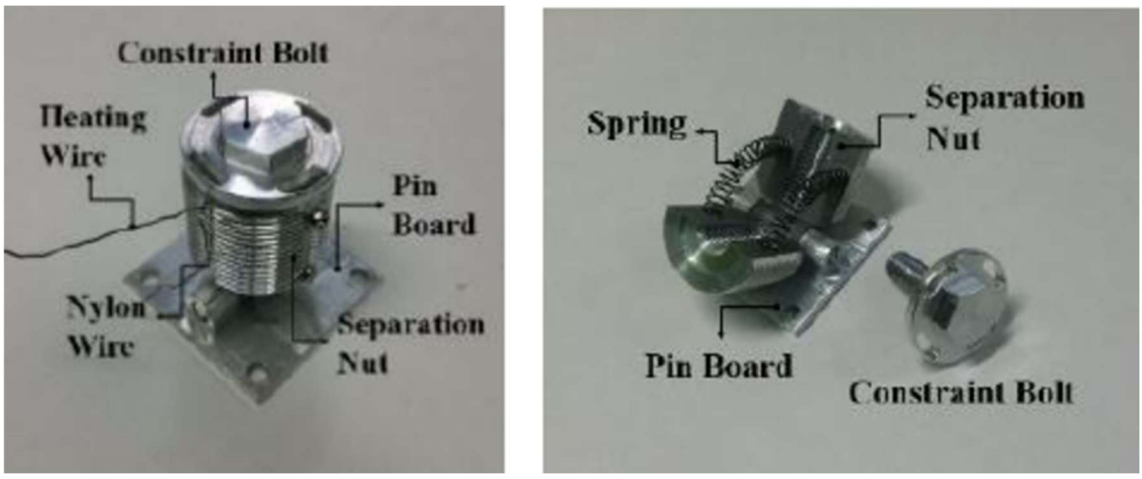

Figure 2.15: Release Nuts Example [78]

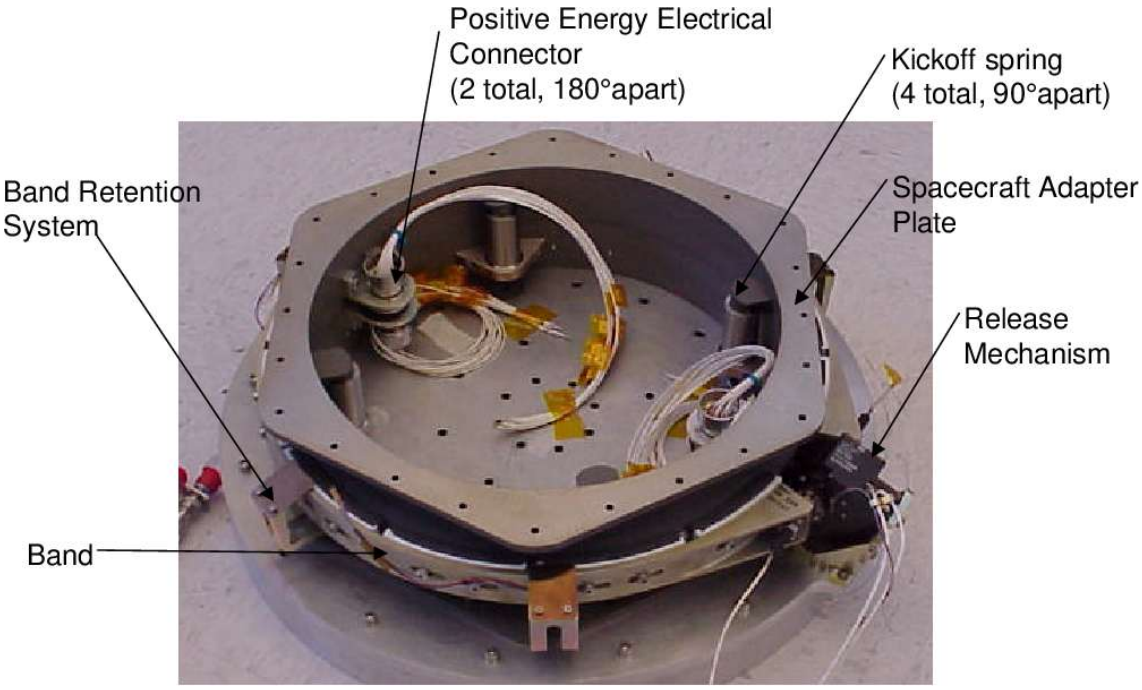

Figure 2.16: Clamp Bands Example [79]

Their inherent flexibility allows them to conform to a variety of payload geometries while also providing effective shock damping. However, a notable limitation of clamp bands is their relatively large size, which poses challenges for miniaturisation and makes them unsuitable for small-form-factor satellites such as PocketQubes.

2.3.2.6 Permanent and Semi-Permanent Magnets

Permanent magnets are employed for their capability of passively generating an attractive force. These components offer a simple, reliable, and energy-efficient means of implementing a restraint mechanism [80]. Although their magnetic properties, and thus this force, can vary with temperature, most permanent magnets remain thermally stable within the operational range typically encountered in low Earth orbit (LEO). Nevertheless, prolonged exposure to elevated temperatures may degrade their effectiveness as restraint elements.

Despite their energy efficiency, the passive magnetic fields generated by these magnets are of concern in satellite design, particularly because their interaction with Earth's magnetic field results in a continuous disturbance to the satellite's attitude. Counteracting this disturbance requires additional power, and, if it becomes too great, compromises the ADC's capability of maintaining the desired attitude [80]. Consequently, the use of permanent magnets in satellites requires careful consideration to ensure that the net magnetic dipole is very small, ideally zero, along all three axes [81].

2.3.2.7 Interference Fits

Interference fits function similarly to permanent magnets in that the deployment mechanism must overcome a retaining force to initiate release [68]. In this case, the retaining force arises from friction between tightly mating components. This approach was employed and successfully demonstrated in the deployment of the drag sail on the AeroCube-3 mission [82].

Interference fits offer a simple, lightweight, and passive restraint method that can be seamlessly integrated into the satellite's structural design, making them an attractive alternative to permanent magnets, particularly for magnetically sensitive satellite systems. The primary challenge associated with interference fits lies in their dependence on precise manufacturing tolerances to achieve the desired frictional force. If the fit is too loose, the mechanism risks premature release; if too tight, deployment may be inhibited altogether [68].

2.3.2.8 Hook-and-Loop Devices

The hook-and-loop mechanism functions by interlocking small, thin hooks and plastic loops to provide restraint. These mechanisms offer a lightweight and straightforward solution, making them particularly appealing for space applications. Release can be achieved by applying an external force to separate the hooks from the loops, or, in specific designs, by melting the adhesive layer to disengage the restraint. Their viability was demonstrated in a CanSat platform, as illustrated in Figure 2.17 [69], where they provided reliable restraint while mitigating vibrational stresses. This makes Hook-and-Loop mechanisms well-suited for low-load applications in space environments. Their main advantages include their simplicity, energy efficiency, lightweight design and reusability. Their main advantages include simplicity, energy efficiency, lightweight design, and reusability, making them ideal for applications where minimal complexity and mass are crucial. However, Hook-and-Loop mechanisms have notable limitations, including limited load capacities, which restrict their use in high-stress applications, and thermal sensitivity, which can affect their performance under extreme temperature variations.

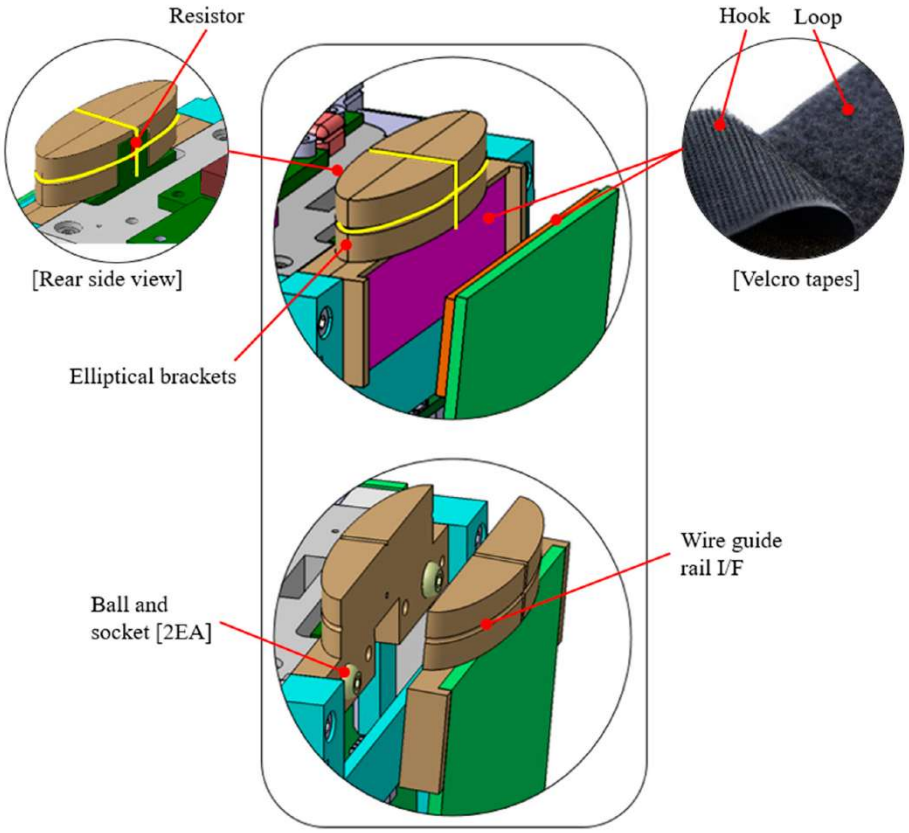

Figure 2.17: Hook and Loop Mechanism on CanSat Platform [83]

2.3.3 Actuation Devices

The actuation device is responsible for initiating motion following release from the restraint mechanism, imparting the necessary force or velocity to transition a deployable or satellite into its deployed state. In the PQ8 architecture, actuation plays a critical role in generating the required disengagement velocity to ensure the controlled and reliable separation of the eight PQ1 satellites.

A range of actuation technologies is available in the context of satellite deployment, including strain energy devices (e.g., springs), electric motors, momentum exchange devices, SMAs, gravity gradient mechanisms, and pyrotechnic actuators [68]. Each of these systems presents specific advantages and trade-offs depending on mission requirements, system complexity, and integration constraints.

However, the PQ8 architecture imposes unique constraints that render most of these technologies unsuitable. Unlike conventional deployables, the PQ1 satellites are not tethered or mechanically linked post-release. As such, actuation must be both self-contained and non-reversible, ensuring that each satellite separates cleanly and independently without requiring sustained control or connectivity. Pyrotechnic actuators,

while capable of generating large impulsive forces, are typically avoided in CubeSat-class systems due to safety concerns, shock loading, and integration complexity. Similarly, systems involving motors, SMAs, or momentum exchange require more space, power, or structural coupling than the PQ8 design can accommodate.

Given these constraints, spring-based actuators emerge as the most viable solution. They offer compactness, passive operation, predictable force profiles, and compatibility with the self-contained disengagement architecture required by PQ8.

Spring-based systems use strain energy stored in a spring, primed before launch, which is translated to kinematic motion once the restraint mechanism is released [68]. Various types of springs (such as compression, conical, extension, torsional, etc.) have been extensively used in space applications due to their significant flight heritage, reliability, customizability, availability, and cost-effectiveness. These attributes make them a versatile and practical choice for the deployment mechanism.

One notable disadvantage of spring-based systems is the non-constant force-displacement relationship, which can lead to variability in performance unless constant-force springs are specifically used. Nevertheless, this limitation can be effectively mitigated through detailed modelling and comprehensive terrestrial testing, ensuring their reliability in space environments.

2.3.4 Suitable Devices for the PQ8 Architecture

Following the five stages for disengagement introduced in Section 2.3.1, the primary design considerations for the PQ8 architecture lie in the stowage, restraint, and actuation stages. In this context, stowage and restraint are effectively unified, serving to securely house and immobilise the satellites until disengagement. Guidance is then a derivative function of the successful execution of these prior stages, ensuring controlled and precise satellite separation. The locking/latching stage, by contrast, is not applicable, as the satellites are fully detached post-disengagement.

To assess the suitability of reviewed mechanisms for the PQ8 architecture, it is essential to consider the specific operational and physical constraints of the system. These constraints significantly influence the selection and integration of appropriate technologies. Table 2.2 summarises the key requirements derived from CubeSat standards and mission-specific considerations. It should be noted that this list is not exhaustive, as

Table 2.2: Requirements for Disengagement Mechanism

Type	Description	Source
Pyrotechnics	Device cannot make use of pyrotechnics.	CDS 14.1
Stowage	Satellite cannot be restrained by the deployer.	CDS 14.1
Debris	Device cannot include ejectable material.	CDS 14.1
Solar Cells	Device should not introduce risks that impact solar cell performance.	Operational
Actuation	Device should impart the satellite with a disengagement velocity.	Operational
Miniaturisation	Device should be physically small due to space constraints.	Operational
Synchronisation	Device should be easily synchronisable.	Operational

further factors such as release precision, material compatibility, and geometric/kinematic disengagement guides are addressed in subsequent design-focused chapters.

The miniaturisation requirement is particularly stringent, imposed by two key factors: the limited internal volume of each 5 × 5 × 5 cm^3 PQ1 satellite and the architectural need for multiple disengagement interfaces across the PQ8 unit. These constraints exclude larger restraint technologies such as electromagnetic latches, clamp bands, and release nuts due to their size and complexity when scaled down.

Synchronisation represents another critical constraint. In the PQ8 configuration, the mechanism is distributed across multiple satellite interfaces. Any asymmetry in release timing can produce imbalanced forces across the satellite faces, introducing unwanted rotational dynamics that elevate the risk of collision. Mechanisms that do not guarantee uniform release timing are therefore problematic in this context.

Among the technologies reviewed, two commonly used systems present particular challenges: **S**MAs and burn-wire devices. Both rely on thermal activation and are therefore sensitive to orbital temperature gradients. These gradients can create desynchronised activation across different satellite faces, undermining the consistency required for reliable deployment. As such, they are not considered suitable for the PQ8 configuration and are excluded from further consideration.

Consequently, the viable set of restraint mechanisms narrows to permanent magnets, interference fits, and hook-and-loop systems. Each of these offers potential compatibility with both miniaturisation and synchronisation requirements. For actuation, spring-based systems emerge as the most feasible option due to their simplicity, compact form factor, and passive operation.

However, existing literature and standards indicate that while these technologies meet many individual requirements, they do not collectively resolve the challenge of achieving a compact, precisely triggerable, and synchronised disengagement system for the PQ8 architecture. In particular, a gap remains in enabling coordinated triggering that satisfies both volumetric constraints and system-level compatibility.

This unresolved intersection of constraints, as derived from the surveyed technologies and design standards, motivates the investigation of alternative actuation principles. In particular, electromagnetic-based release and actuation technologies offer characteristics, such as electronically controlled triggering and reduced sensitivity to thermal gradients, that warrant closer examination in the context of highly synchronised, miniaturised disengagement systems.

2.3.5 Summary of Existing Disengagement Mechanisms

Disengagement mechanisms follow a five-stage framework comprising stowage, restraint, actuation, guidance, and latching or locking. The review focuses primarily on restraint and actuation devices, as they form the core of hold-and-release mechanisms. Restraint technologies examined include burn wires, electro-mechanical latches, SMAs, release nuts, clamp bands, permanent and semi-permanent magnets, interference fits, and hook-and-loop devices. Each was assessed in terms of reliability, volume efficiency, operational simplicity, and compatibility with small satellite constraints.

Table 2.3 compares the restrain and actuation mechanisms reported in literature, together with the proposed PQ8 disengagement mechanism. This comparison highlights that mechanisms suitable for PocketQube-scale systems must balance miniaturisation, low power demand and synchronised release, a combination that is not fully addressed by existing disengagement approaches.

Burn wires offer compact and reliable performance but pose contamination risks and loading challenges. Electro-mechanical latches provide precision and reusability but are bulky. SMAs are compact and reusable but slow and thermally sensitive. Release nuts and clamp bands offer high load capacity but are unsuitable for miniaturised systems. Magnets and interference fits provide passive restraint without power, though magnets can interfere with ADCS and demagnetise at high temperatures. Hook-and-loop mechanisms are lightweight and straightforward but limited by low load capacity and thermal sensitivity.

Table 2.3: Comparison of restrains and actuation mechanisms

Mechanism Class	Reliability	Miniaturization	Synchronous operation	Power demand	Key limitations
Thermal Release Mechanisms	High	High	Low	Moderate	Thermally driven desynchronization, Potential contamination
Electromechanical Systems	High	Low	High	High	Excessive size, mass, and power for PocketQubes
Pyrotechnic Systems	Very high	Moderate	High	Low	Safety, shock loading, CDS incompatibility
Passive Mechanical Restraint	Moderate	High	Moderate	Low	Sensitive to tolerances and preload variability
Magnetic Restraint	Moderate	High	Moderate	Low	ADCS disturbance
PQ8 (Proposed)	Moderate –high	High	High	Low	ADCS disturbance, Requires precise mechanical symmetry and coordination

Actuation technologies include pyrotechnics, springs, motors, momentum exchange devices, SMAs, and gravity-gradient systems. Most are unsuitable due to safety, complexity, power, or coupling requirements. Spring-based systems are identified as the most viable actuation approach due to their passive operation, compactness, and established use in space applications.

Finally, the reviewed mechanisms show that while several restraint and actuation technologies meet individual requirements such as miniaturisation and synchronisation, none fully address the need for a compact, triggerable, and coordinated disengagement system. This highlights a gap in existing solutions and motivates the need for further development in this area.

2.3.6 Electromagnetic Release Systems

Electromagnetic release and actuation systems form a broad class of mechanisms in which mechanical constraint or motion is generated, modulated, or removed through controlled electromagnetic forces. These systems are widely employed across robotics, industrial automation, and automotive applications, where precise timing, repeatability, and electrically controllable behaviour are required for safety-critical or high-cycle operations.

Electromagnetic actuation arises from the interaction between electric currents and magnetic fields, producing force through one or more of the following mechanisms:

1. Magnetic attraction or repulsion, typically between ferromagnetic elements and energised coils,
2. Lorentz-force effects, where current-carrying conductors experience force in a magnetic field,
3. Magnetic circuit modulation, in which energising or de-energising a coil alters the net holding force within a magnetic latch or restraint.

When applied within release mechanisms, electromagnetic actuation is typically employed in one of two architectural forms. In the first, the electromagnetic element itself provides the primary restraining force, requiring continuous coil energisation to maintain constraint. Release is then achieved by de-energising the actuator, allowing separation through external mechanical forces.

In the second, electromagnetic actuation is used as a triggering or enabling element, where coils are energised on command to either nullify the effect of a permanent magnetic restraint, as discussed in Section 2.3.4, or to actively counteract a retaining force, thereby initiating release.

In both cases, electromagnetic actuation enables electrically commanded, rapidly switchable restraint or release, with actuation timing governed primarily by electrical and magnetic response. Unlike burn-wire or pyrotechnic devices, these mechanisms are in principle reversible and may support repeated engagement and disengagement, subject to system-level constraints on power availability, thermal limits, and fault tolerance.

Electromagnetic actuation concepts appear in the small-spacecraft literature primarily in the context of magnetic capture, latching, and docking, where low shock and tolerance to relative misalignment are desirable. A representative example is provided by Bridges et al. in the STRaND-2 programme, which investigates nanosatellite rendezvous

and docking using a coil-based electromagnetic docking interface [84]. The study details the electromagnetic design of the docking mechanism, including coil geometry, drive current, and resulting power demand, and reports experimental validation using a ground-based air-bearing testbed representative of nanosatellite docking dynamics.

A related application of electromagnetic actuation in space is presented by Redah et al. within the TAMARIW project, which develops an active electromagnetic docking system for a 3U CubeSat [85]. In contrast to STRaND-2, where electromagnetic forces are central to the docking interface, the TAMARIW architecture employs electromagnets primarily to provide controlled capture and alignment during docking. Structural retention is subsequently achieved through mechanical latching mechanisms, such as compliant leaf-spring designs.

Beyond docking and capture applications, electromagnetic actuation has also been investigated specifically as a separation mechanism for small spacecraft. Yunhan et al. propose an electromagnetic separation system for a spherical satellite architecture, in which electromagnetic coils are used to actively generate a repulsive magnetic force between mating elements at the separation interface, converting an electrically commanded current pulse directly into separation impulse [86]. The study demonstrates that electromagnetic repulsion can be exploited to achieve low-shock, electrically synchronised separation, while also identifying practical constraints related to coil sizing, peak current demand, and magnetic field interactions that are intrinsic to electromagnetic separation concepts.

From a system-level perspective, electromagnetic actuation offers high synchronisation capability, as multiple release elements may be triggered by a common electrical command, with timing dispersion dominated by driver electronics and coil inductance rather than environmental factors. This contrasts with burn-wire and SMA mechanisms, where release timing is governed by thermal time constants and material variability, leading to greater dispersion. Spring-based systems inherit the timing characteristics of their trigger mechanisms, while motor-driven releases are limited by control-loop latency, startup dynamics, and mechanical backlash. As a result, electromagnetic actuation provides superior determinism where coordinated or near-simultaneous release is required.

In the context of the PQ8 architecture, these characteristics highlight why electromagnetic actuation is of interest for disengagement, where synchronised triggering

is a system-level concern. However, the stringent volumetric, power, and magnetic cleanliness constraints imposed by PocketQube-class platforms mean that these advantages do not directly translate into a resolved implementation. While electromagnetic actuation has been demonstrated in small-spacecraft applications, the majority of published work focuses on docking interfaces, where electromagnetic forces are employed for capture, alignment, or retention, with comparatively few examples using electromagnetic systems as the triggering or actuation element for release or disengagement. This gap between demonstrated electromagnetic docking concepts and their application as compact, synchronised release mechanisms motivates the system-specific design exploration presented in the subsequent chapter.

2.4 Structural Design Standards for Satellite Systems

Unlike the preceding sections, which primarily draw on academic literature to explore constellation dispersal, disengagement mechanisms, and mission architectures, this section reviews aerospace standards and technical documentation. This shift reflects the nature of satellite structural design, where compliance with rigid deployment constraints and mechanical load tolerances is condensed to a well-defined set of requirements and testing methodologies based on decades of industry experience. Accordingly, the structural review draws on specifications from the European Cooperation for Space Standardisation (ECSS), the CubeSat Design Standard (CDS), and the user manuals of prospective launch vehicles. These sources provide the foundational criteria that inform the mechanical design, qualification, and verification processes of the PQ8 satellite architecture.

2.4.1 ESA Standards and Guidelines

The European Cooperation for Space Standardisation (ECSS) provides a comprehensive framework for satellite structural design, articulated through an extensive set of standards and handbooks. These documents address a wide range of engineering domains, including software, hardware, PCB design, thermal management, materials, and mechanical systems, thus offering systematic guidance for the development and qualification of space systems. While many of these standards will be cited in context throughout this thesis, a select few warrant detailed discussions here due to their direct relevance to the structural verification of the PQ8 satellite.

The ECSS-E-ST-32C standard outlines mechanical system requirements, specifying procedures for the application of vibration, shock, and acoustic load testing [87]. It is complemented by ECSS-E-HB-32-26A, a handbook designed to ensure the repeatability and reliability of test results through practical recommendations on test execution [88]. When used in tandem, these documents provide a solid foundation for accurate satellite load analysis, ensuring that mechanical qualification is based on correctly applied launch loads and appropriate safety margins.

An essential conceptual tool introduced by these standards is the Load Analysis Cycle, depicted in Figure 2.18. This iterative process guides the sizing of structural elements to ensure compliance with launch load conditions. It reflects the dynamic interaction between structural geometry and the loading environment. Within the PQ8 development process, this methodology underpins the structural design workflow: *Payload Design* defines the functional configuration; the *Element and Integrated Systems Model* corresponds to the CAD representation of the satellite; and *Load Analysis* refers to the finite element analysis (FEA) conducted on the model. This approach, integral to the PQ8 Architecture, is elaborated further in Chapter 3: The PQ8 Structure.

Safety margins are assessed according to guidelines defined in ECSS-E-ST-32-10C, which prescribes safety factors based on both the heritage and the qualification method employed [89]. These factors are applied to the limit loads, defined by the launch vehicle, to determine the ultimate loads used in structural verification. The recommended values are summarised in Figure 2.19. For instance, a safety factor of 1.6 is applied on yield loads for qualification by analysis, while a lower factor of 1.25 is required for qualification via dedicated mechanical testing. Some launch vehicle providers offer their safety factor specifications. In the case of discrepancies between ECSS and provider requirements, the larger value is adopted in this work.

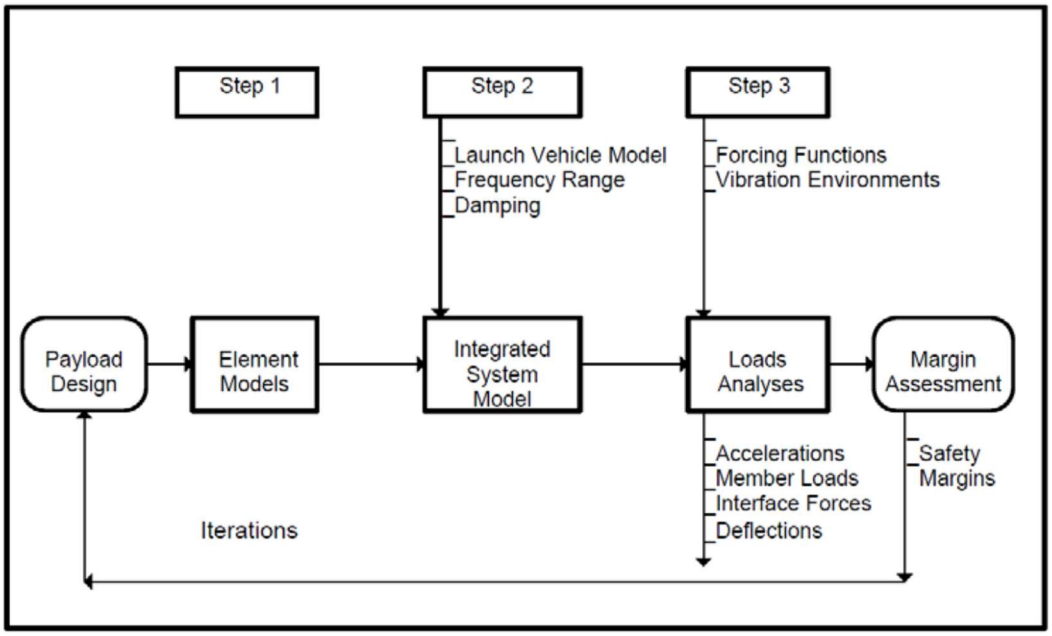

Figure 2.18: Load Analysis Cycle [87]

Option	Design Factors of Safety	
	Yield	Ultimate
1) Ultimate test of dedicated qualification article (1.25 x limit)	1.0	1.25
2) Proof test of all flight structures (1.1 x limit)	1.1	1.25
3) Proof test of one flight unit of a fleet (1.25 x limit)	1.25	1.5
4) No structural test	1.6	2.0

Figure 2.19: Mechanical Load Safety Factors [90]

Limit loads and safety factors are also supplied in launch vehicle user manuals, and can vary significantly from one vehicle to another. The PQ8 structure should ideally be qualified to withstand the worst-case scenarios across multiple platforms, thereby ensuring its compatibility across a broader range of vehicles.

2.4.2 Launch Loads

Launch loads refer to the mechanical forces exerted on a satellite while it is secured within the launch vehicle fairing during ascent. These loads can be categorised into four primary types: quasi-static loads, random vibration loads, acoustic vibrations and shock loads.

As the launch vehicle accelerates through the atmosphere during its ascent, the satellite experiences quasi-static loading. This loading is represented as tension, a positive load, and compression, a negative load, acting along both the longitudinal and lateral axes

of the satellite structure. Quasi-static loads are expressed in units of gravitational acceleration, *g*. The quasi-static load factors for the Arianespace Vega C, in a single launch configuration, are illustrated in Figure 2.20.

Launch vehicle user manuals also include sinusoidal vibration test specifications, which offer simplified approximations of the low-frequency transient effects during ascent. These sinusoidal-equivalent loads are typically expressed as acceleration amplitudes, in g, plotted against frequency, in Hz. An example of such a specification for the Arianespace Vega C is shown in Figure 2.21 for the Arianespace Vega C. Compliance with these requirements ensures that no part of the satellite structure resonates with launch-induced vibrations, where resonance could otherwise cause structural damage, either to the satellite or to adjacent payloads. During early development, modal analysis is performed on the satellite to verify that its natural frequencies exceed the stiffness requirement, typically around 100 Hz.

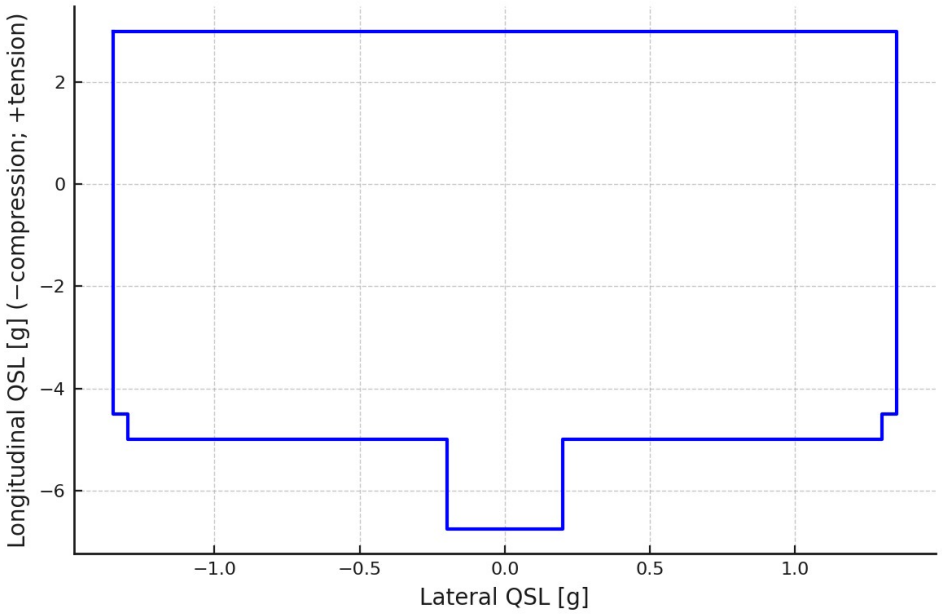

Figure 2.20: Arianespace Vega C acceleration limit load factors. Reproduced from [91]

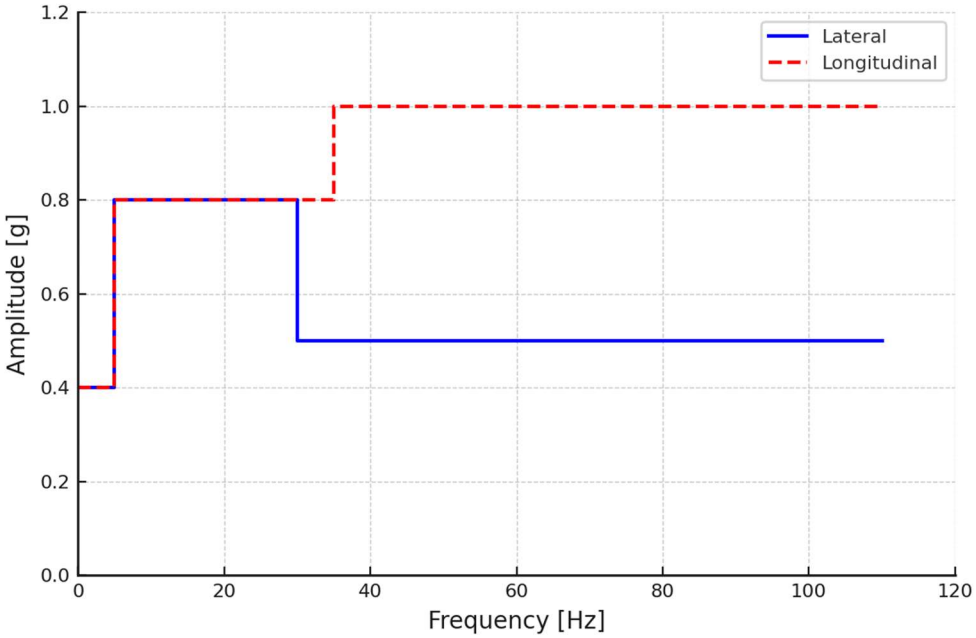

Figure 2.21: Arianespace Vega C sine-equivalent vibrations. Reproduced from [91]

Acoustic loads originate from high-intensity sound pressure waves generated by pyrotechnic events, such as stage separation, which cause vibrations in the satellite structure. These loads are defined as the sound pressure level (SPL), expressed in dB, and are specified for discrete octave centre frequencies. Figure 2.22 shows the acoustic noise spectrum under the Arianespace Vega C.

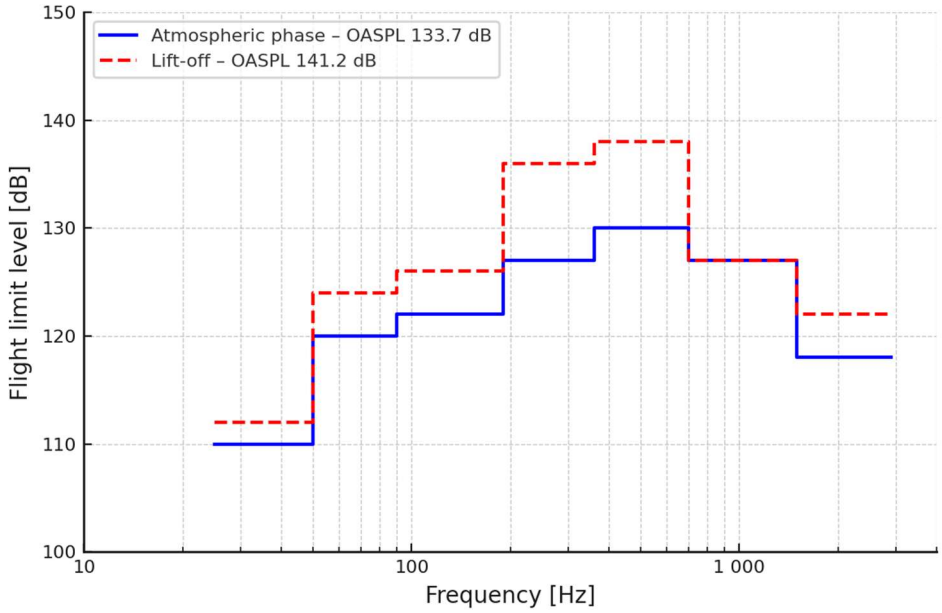

Figure 2.22: Arianespace Vega C acoustic noise spectrum. Reproduced from [91]

Random vibration loads arise from rocket engine operation and aerodynamic interactions during ascent. However, their primary source is the intense acoustic

environment surrounding the satellite. As a result, random vibration testing is often grouped with acoustic load testing [92]. These vibrations tend to be negligible at lower frequencies, making them a less critical factor in structural design. In most cases, meeting the stiffness requirements established by the sinusoidal-equivalent dynamics is sufficient to ensure structural integrity.

Shock loads, like acoustic vibrations, are caused by pyrotechnic events, including fairing and stage separation. Unlike continuous vibrations, these loads occur as high-intensity, transient impulses that propagate through the vehicle structure and deployer systems. Shock loads are described in terms of their acceleration levels over specified frequency bands. The corresponding envelope shock response spectrum (SRS) for the Arianespace Vega C is shown in Figure 2.23.

It is important to note that the magnitude and nature of these mechanical loads vary significantly across launch vehicles. Each provider specifies its envelope of quasi-static, vibration, acoustic, and shock environments, as documented in the respective user manuals. To ensure robustness and cross-compatibility of the PQ8 Architecture, publicly available data from the Ariane Vega C, Ariane 6, and Falcon 9 user manuals were collated and are summarised in Table 2.4 [91,93,94]. This table consolidates the most demanding load conditions across the platforms, providing a conservative baseline for structural design and qualification.

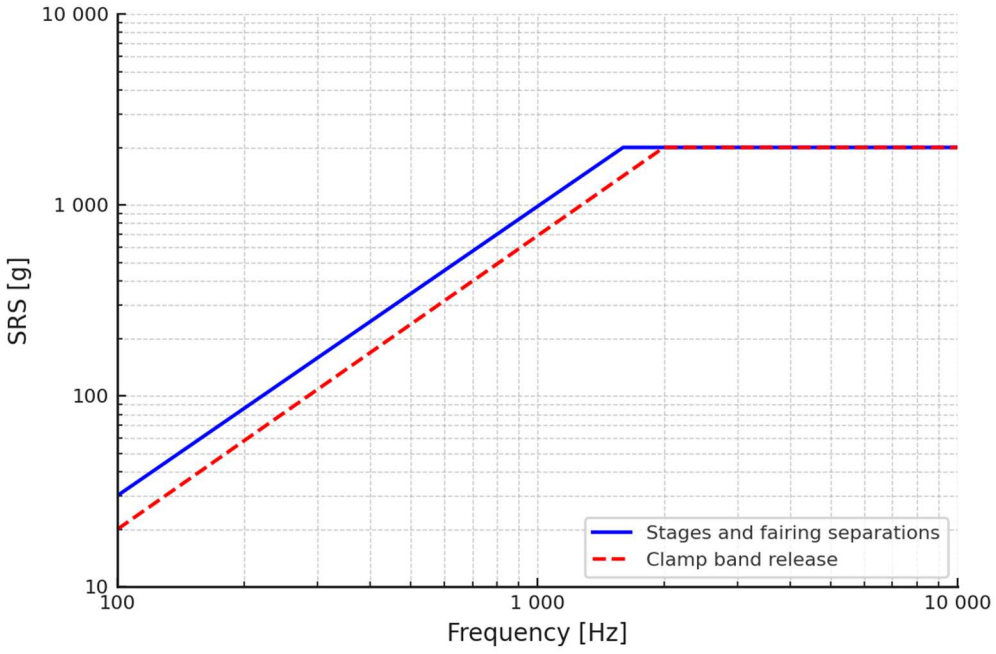

Figure 2.23: Arianespace Vega C SRS. Reproduced from [91]

Table 2.4: Worst Case Launch Loads from Various Launch Vehicles

Quasi-Static Loads (g) (+ = tension ; - = compression)			
	Longitudinal		
Max Value	-7*/+3*		±2**
Sine-Equivalent Dynamics			
Longitudinal direction			
Frequency Band (Hz)	1 - 5	5 - 35	35 - 110
Sine Amplitude (g)	1***	1***	1*
Lateral direction			
Frequency Band (Hz)	1 - 5	5 - 30	30 - 110
Sine Amplitude (g)	0.8***	0.8***	0.5***
Acoustic Vibrations (reference: 0 dB = 2 x 10–5 Pa)			
Centre Frequency (Hz)	Lift-off** Level (dB)		Atmos. Phase* Level (dB)
31.5	128		110
63	131		120
125	135.2		122
250	133.6		127
500	130.2		130
1000	126		127
2000	120		118
OASPL(1) (20 – 2828 Hz)	141.2*		133.7*
Duration	3 Seconds		55 Seconds
Shock Loads			
Frequency (Hz)	100 - 1600		1600 - 10000
Response (Q = 10) (g)	30 - 2000		2000

* From Ariane Vega C User Manual [91],

** From Flacon 9 User Manual [94]

*** From Ariane 6 User Manual [93]

2.4.3 CubeSat Standard

The CubeSat Design Standard (CDS) defines a set of requirements governing the mechanical and electrical interfaces, as well as general operational guidelines, for CubeSat-class spacecraft [10]. Adherence to these specifications is essential for ensuring compatibility with standardised deployment systems such as the Poly-Picosatellite Orbital Deployer (P-POD). While the electrical and operational aspects of the CDS will be discussed in the relevant subsystem chapters, the mechanical specifications are particularly pertinent here, as they define the structural envelope and material constraints for the PQ8 satellite.

With respect to geometry, a single-unit CubeSat (1U) is approximately cubic, with nominal dimensions of $10 \times 10 \times 10$ cm³. The precise dimensional tolerances are

detailed in Appendix A: CubeSat Dimensions. In terms of mass, the standard imposes an upper limit of 2 kg for a 1U unit.

Material selection is also constrained under the CDS. The satellite's structural frame must be constructed from approved aluminium alloys, typically 7075, 6061, 6082, 5005, or 5052, due to their favourable strength-to-weight ratios and compatibility with launch requirements. Furthermore, the standard imposes restrictions on surface finish, particularly for the deployer interface rails, where the surface roughness must not exceed 1.6 μm. This ensures reliable deployment and reduces the risk of mechanical interference during launch separation events.

2.4.4 Summary Of Structural Design Standards

Although this section does not engage with academic literature in the conventional sense, the absence of such sources underscores the novelty of the PQ8 concept. At present, no existing constellation architecture has been launched in a manner that resembles the PQ8 configuration, specifically, as a single deployable structure designed to disengage into multiple operational units. As a result, there is no established body of research or precedent addressing the structural design and qualification of such a system. Instead, this section has relied on authoritative aerospace standards, particularly those issued by the ECSS, the CDS, and launch provider documentation, to define the structural requirements and constraints applicable to the PQ8 Architecture. These standards serve as the foundation for the subsequent design and verification processes presented in Chapter 3.

2.5 Conclusion and Research Direction

This chapter has reviewed the state of the art in small satellite constellation deployment, passive dispersal methods, disengagement mechanisms, and structural design standards. Across all domains, the PQ8 Architecture introduces a novel integration of established concepts, yet lacks precedent in literature.

Current constellation deployment strategies rely heavily on multi-launch campaigns, which introduce cost inefficiencies, coordination challenges, and limited flexibility. The PQ8 approach addresses these constraints by launching eight PocketQubes as a single CubeSat compatible with standard deployers, followed by orbital disengagement and dispersal.

Among passive dispersal strategies, differential drag emerged as the most viable option for low Earth orbit missions without propulsion. However, its effectiveness depends heavily on accurate drag modelling under free-molecular flow, which remains a significant source of uncertainty.

The review of disengagement technologies identified a clear gap: no existing solution offers a compact, triggerable, and synchronised mechanism tailored to the coordinated release of multiple small satellites. This shortfall directly motivates the design of a custom mechanism suitable for the PQ8 form factor and operational requirements.

Finally, the structural design section, based entirely on ECSS, CDS, and launch provider documentation, reflects the absence of prior structural designs for satellites that divide into independent spacecraft post-launch. The PQ8 configuration introduces unique verification challenges not yet addressed in existing literature.

In summary, this review establishes the originality of the PQ8 Architecture. It identifies three primary research needs: (1) a deployment model that avoids multi-launch dependency, (2) a novel disengagement mechanism for coordinated multi-satellite release, and (3) structural design and qualification methods for a many-in-one satellite platform. The remainder of this thesis addresses each of these areas through design, simulation, and experimental validation.

3 THE PQ8 SATELLITE OVERVIEW

The PQ8 satellite architecture presents a tightly integrated mass, volume and power-constrained platform designed to host eight independent PocketQube-satellite satellites in a single 1U CubeSat frame. This chapter provides a comprehensive overview of the satellite's mechanical structure, material configuration, mass and power budgets, and the validation activities undertaken to ensure launch survivability and subsystem compatibility.

The structural design serves as the primary enabler for the satellite's novel deployment architecture. A combination of mission requirements, environmental loads, and CubeSat specification limits drove key decisions regarding geometry, internal partitioning, and material selection. These were validated through numerical simulation and experimental testing to ensure mechanical integrity under the expected quasi-static and dynamic loads of launch.

In parallel, the satellite's power system was developed based on surface area availability, orbital lighting conditions, and the performance of commercial triple-junction solar cells. The resulting generation capacity imposed strict constraints on subsystem operation. This chapter defines the power envelope within which all onboard systems must operate and, more pertinently, the power available for the disengagement mechanism.

The design effort adopted a concurrent engineering approach, whereby structural layout, volume allocation, and both mass and power budgets were developed iteratively and refined throughout the project lifecycle. As subsystems matured, interdependencies between mechanical and electrical constraints were revisited to ensure compatibility. The

values presented in this chapter reflect the final consolidated budgets at the end of the design phase.

The remainder of the chapter presents the structural configuration and subsystem integration strategy, details the material and mass breakdown, outlines the power generation and consumption profile, and concludes with both simulated and experimental validation of structural performance.

The work presented in this chapter is the result of both original efforts conducted as part of this research and collaborative contributions from the wider project research group. The following elements were developed independently as part of this doctoral research:

- Electrical Power System (EPS) architecture and sizing,
- Solar panel mechanical and electrical design,
- Structural design of the PQ8 carrier and PQ1 units,
- Mechanical integration strategy of subsystems within the PQ8 architecture.

The following subsystems were developed by project collaborators and are included for system-level completeness:

- On-Board Computer (OBC),
- Attitude Determination and Control System (ADCS),
- Communications subsystem,
- Battery cell selection and characterisation testing.

Where applicable, these externally developed subsystems are referenced and acknowledged, and their interfaces with author-developed subsystems are defined to ensure consistency with the overall system design.

Additionally, system-level verification and validation activities were similarly divided between original work and collaborative testing efforts. The following analyses and tests were conducted as part of this research:

- Finite Element Analysis (FEA) of the PQ8 structure using Autodesk Inventor NASTRAN
- Vibration and shock testing of the PQ1 satellite units

The following analyses and qualification tests were conducted by other members of the research group and are referenced where relevant:

- Independent PQ8 structural FEA using Ansys,
- Thermal cycling and thermal shock testing,
- Electromagnetic radiation (EMR) compatibility testing,
- Magnetic cleanliness testing,

- Total Mass Loss (TML) and outgassing testing.

These complementary activities provided cross-validation of the system design while ensuring compliance with applicable small-satellite qualification practices.

3.1 Structural Design

3.1.1 Design Requirements

The structural design of the PQ8 satellite was developed in accordance with the CubeSat Design Specification (CDS Rev. 14.1), European Cooperation for Space Standardisation (ECSS) guidelines, and environmental constraints drawn from candidate launch vehicles. These design constraints were used to establish a bounded and traceable set of requirements for structural configuration, material selection, and mechanical qualification. A summary of the key specification requirements is provided in Table 3.1.

Table 3.1: Specification Requirements for PQ8 Structure

Type	Requirement	Reference
Shape/Dimensions	As per drawings in Figure 3.1	CDS Rev. 14.1 [10]
Weight	Up to 2 kg	CDS Rev. 14.1[10]
Material (Structure)	Aluminium (7075, 6061, etc)	CDS Rev. 14.1[10]
Material (Guide Rail)	Aluminium, Anodised, 1.6 µm Roughness	CDS Rev. 14.1[10]
Launch Loads	Loads from Table 2.2 Safety Margins from Figure 2.19	ECSS-E-ST-32-10C [89] Ariane Vega C Manual [91] Ariane 6 Manual [93] Falcon 9 Manual [94]

The mechanical loads used in analysis and testing were derived directly from launcher documentation. These included quasi-static acceleration levels, sinusoidal vibration profiles, and shock response spectra for the Ariane Vega C, Ariane 6, and Falcon 9 systems. For each load type, the most severe value was used to define a composite worst-case envelope, ensuring structural resilience across all plausible launch environments considered. Safety margins were applied in accordance with both ECSS-E-ST-32-10C and launch vehicle user manuals, with distinct values for qualification by analysis and qualification by testing.

To guide structural development, the ECSS Load Analysis Cycle, Figure 2.18, was followed. This iterative process ensures that the structure survives all specified

launch environments with appropriate safety margins while avoiding unnecessary overdesign. In parallel, a concurrent engineering approach was adopted to manage subsystem-level mass and power budgets. Structural and assembly decisions were continuously updated based on evolving figures from subsystem prototyping and real-world testing, ensuring that budget allocations remained grounded in physical results rather than assumptions.

These requirements defined the boundary conditions for the structural concept. They informed every downstream decision, including the internal layout, subsystem packaging, fastener placement, and material choices discussed in the following sections. Although internal modifications were introduced to meet mission-specific requirements, the external geometry remained fully compliant with the CubeSat 1U specification, including guide rails and deployer interface constraints, as shown in Figure 3.1.

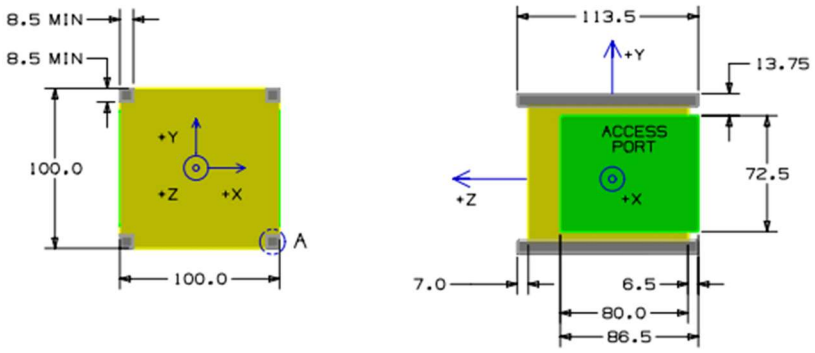

Figure 3.1: CubeSat Standard Interfaces (Reproduced from [10])

3.1.2 Technical Specifications

This chapter addresses the structural configuration of the PQ8 satellite and establishes the mass and power envelopes within which all subsystems must operate. While detailed requirements, budgets, and analyses are presented in their respective sections, it is useful to first summarise the system-level technical specifications that bound the design space considered in this chapter. These specifications define the allowable ranges for geometry, mass, structural performance, and power availability, and provide traceability between high-level requirements and the detailed design and validation activities that follow.

Table 3.2 summarises the principal system-level technical specifications relevant to Chapter 3. More detailed and subsystem-specific specifications are presented

in later sections of this chapter and in subsequent chapters and are collated in Appendix C. Meanwhile, the specifications presented here define the boundary conditions for the structural concept, mass allocation, and power generation strategy presented in this chapter. All subsequent design choices and validation activities are traceable to one or more of these system-level specifications.

Table 3.2: PQ8 system-level technical specifications

Domain	Specification	Value / Range	Source / Rationale	Relevant Section
Structure	External geometry	1U CubeSat compliant	CubeSat Design Specification Rev. 14.1	3.1
Structure	Maximum system mass	≤ 2 kg (PQ8)	CubeSat Design Specification Rev. 14.1	3.1, 3.1.5
Structure	First natural frequency	> 100 Hz	Typical deployer requirement	3.3
Structure	Launch environment	Worst-case envelope from LVs	Ariane, Vega, Falcon manuals + ECSS	3.1, 3.3
Structure	Safety margins	ECSS-defined values	ECSS-E-ST-32-10C	3.1
Mass	PQ1 target mass	250 g incl. 10% margin	System allocation	3.1.5
Mass	Mass contingency	10%	ECSS guidance	3.1.5
Power	Orbit altitude	350–500 km quasi-circular	Mission definition	3.2
Power	Illumination fraction	60–63% per orbit	Orbit geometry	3.2
Power	Average orbital power available	~288 mW	Power budget	3.2
Power	Disengagement energy allocation	32 mWh per orbit	Disengagement requirement (Chapter 5)	3.2

3.1.3 PQ1 Internal Layout and Subsystems

The PQ8 satellite was designed to accommodate eight smaller satellites, PQ1s, within the volume of a standard 1U CubeSat. Each of these satellites is intended to operate independently and carries its subsystem for power, control, communication, and payload functions. In addition to supporting clustered operation during launch, the structure had to enable the clean separation of all eight PQ1 satellites while maintaining mechanical integrity and compliance with CubeSat deployer standards. A complete subsystem block diagram for the PQ1 is shown in Figure 3.2.

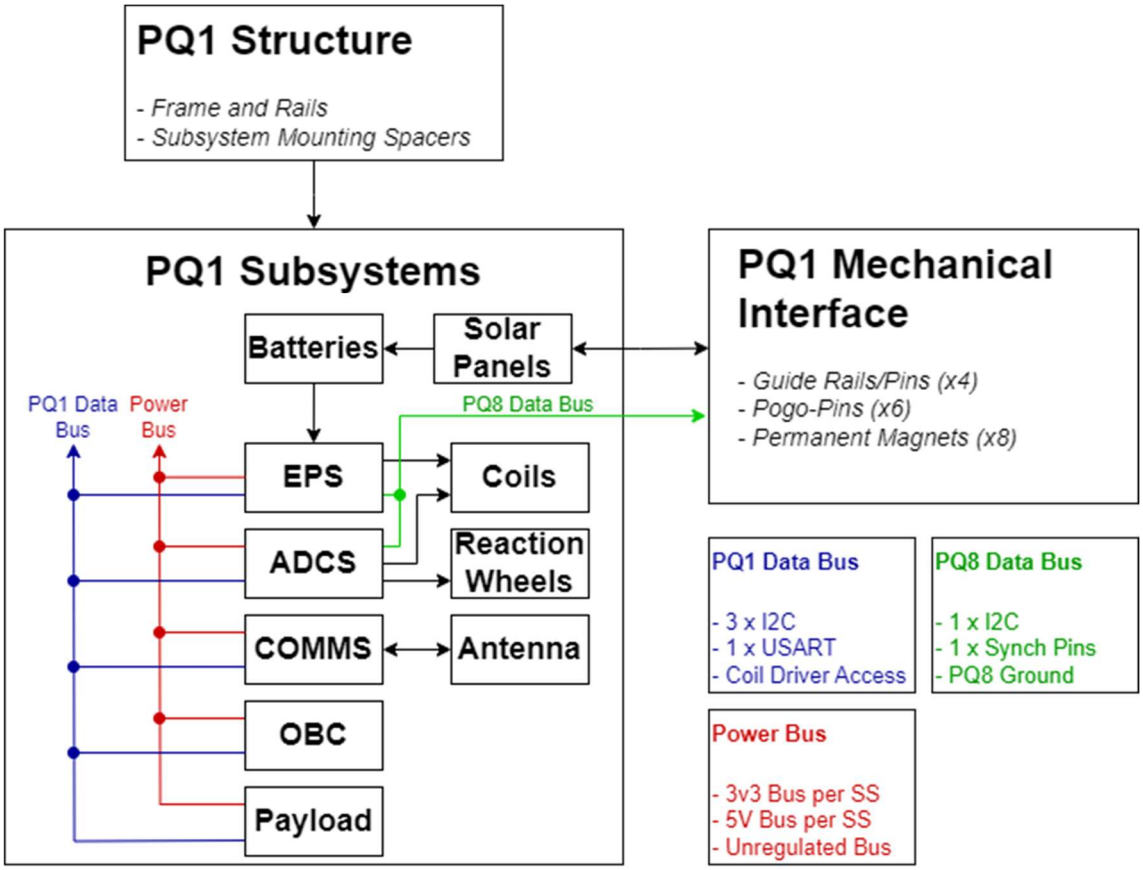

Figure 3.2: PQ1 Subsystem block diagram

This configuration was achieved by dividing the internal volume of the CubeSat in two steps: first horizontally, then vertically. The result is eight equal volumes arranged in a symmetric layout, forming the PQ1 satellites of the PQ8 architecture. This geometric division provides a predictable and centred centre of mass, assuming identical PQ1 units.

To implement the PQ1 satellite arrangement and support the internal subsystem stack, the load-bearing structure includes a machined top frame, bottom frame, guide rails, and a battery clamp. These aluminium components define the boundaries of the internal volumes, provide mounting points for subsystem electronics, and ensure compatibility with the CubeSat deployer. The main structural elements are shown in Figure 3.3.

While the horizontal and vertical division established the PQ1 layout, it introduced a structurally weak region at the centre of the frame. To address this, high-carbon chrome steel (GCr15) guide pins were incorporated into the central area. These serve both as alignment features and as load-bearing elements, restoring rigidity at the point of greatest mechanical vulnerability and ensuring consistent alignment during integration and separation.

The internal electronics are arranged in a vertical stack located in the lower half of the structure. From bottom to top, the PCBs are ordered as follows: EPS, ADCS, OBC, Radio, and Payload. The stack is constrained using stainless steel (SAE 304) corner spacers, and vertical bolts pass through all layers to maintain alignment. PCB spacing was determined based on subsystem-specific requirements: 4 mm between the EPS and ADCS to allow connector clearance, 6 mm between the ADCS and OBC to accommodate the reaction wheel and motor, and 2.5 mm between the remaining boards. The assembled stack is shown in Figure 3.4.

Above the EPS lies the battery compartment. The batteries are fixed to the top frame using a machined aluminium bracket, matching the batteries profile, and secured with two M3 screws. Routing slots in the bracket allow power and coaxial cables to pass cleanly around the internal stack, avoiding interference with the ADCS components.

The structure is enclosed by six external panels, including five supporting solar cells and one allocated for the antenna. These panels are mounted at each corner using screws. One of the solar panels includes a debug port used during assembly and testing for battery charging and in-system programming. While the antenna board is structurally integrated into the satellite, its design is not covered in this work. The structure assembly and complete assembly of the PQ1 satellite are illustrated in Figures 3.5a and 3.5b, respectively.

Electrical grounding is implemented using a single-point grounding approach. The structure is electrically connected to the EPS PCB through the mounting bolts and spacers, while all subsystem PCBs are interconnected through their respective data and power connectors. This approach follows standard ECSS practices to minimise the risk of ground loops and electromagnetic interference.

Eight PQ1 satellites are then assembled into a PQ8 Satellite, as illustrated in Figure 3.6. In its final configuration, the PQ8 satellite is equivalent to a 1U CubeSat, as illustrated in Figure 3.7.

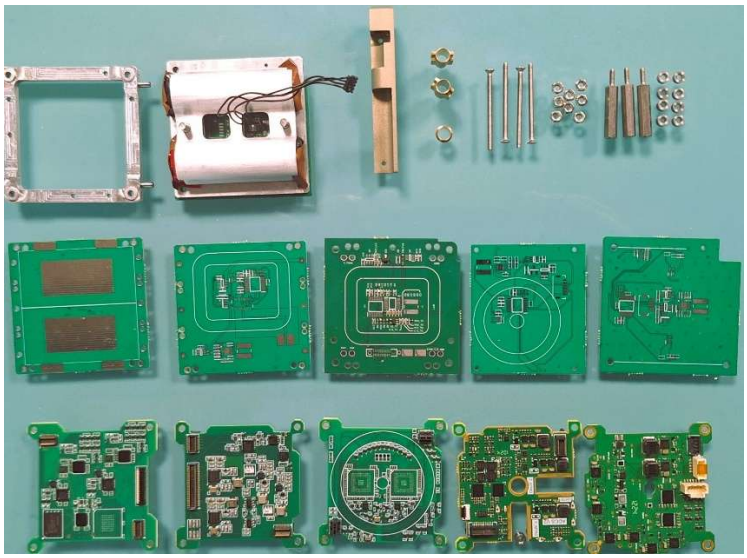

Figure 3.3: PQ1 parts and frame assembly

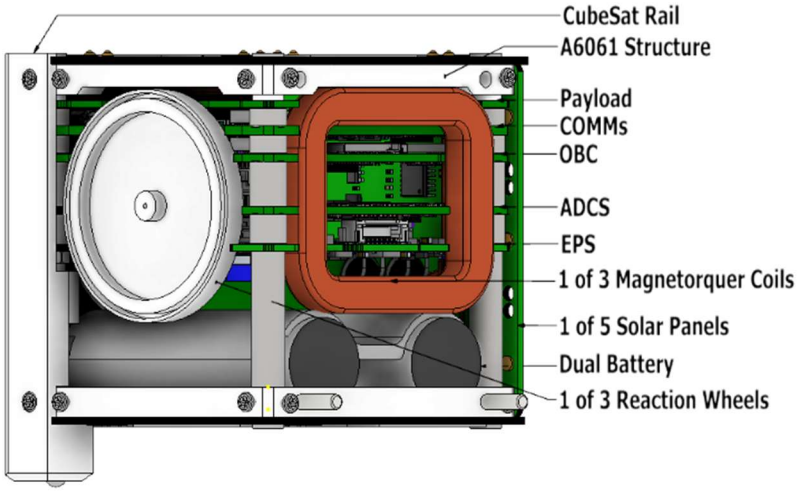

Figure 3.4: PQ1 internal stack-up

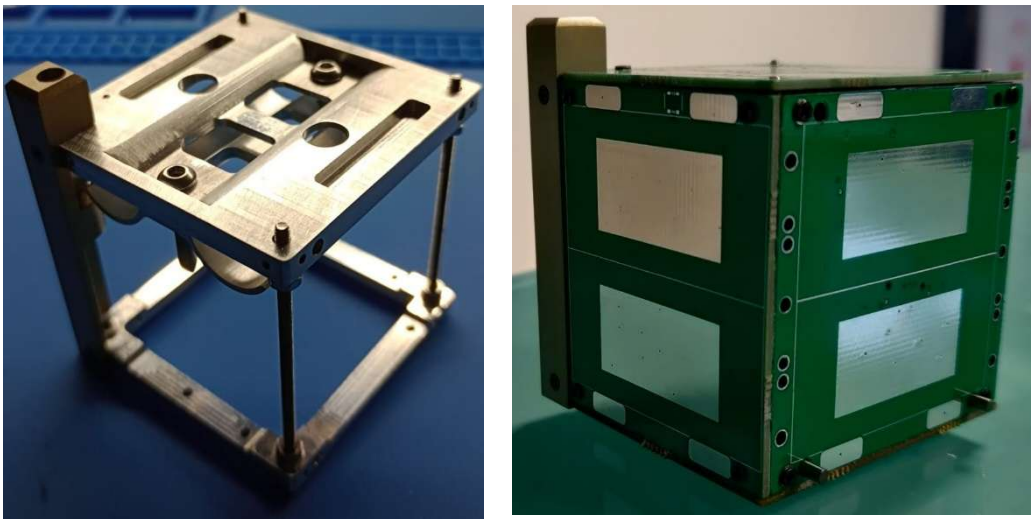

(a) (b)

Figure 3.5: Assembled PQ1: (a) Frame (b) Complete

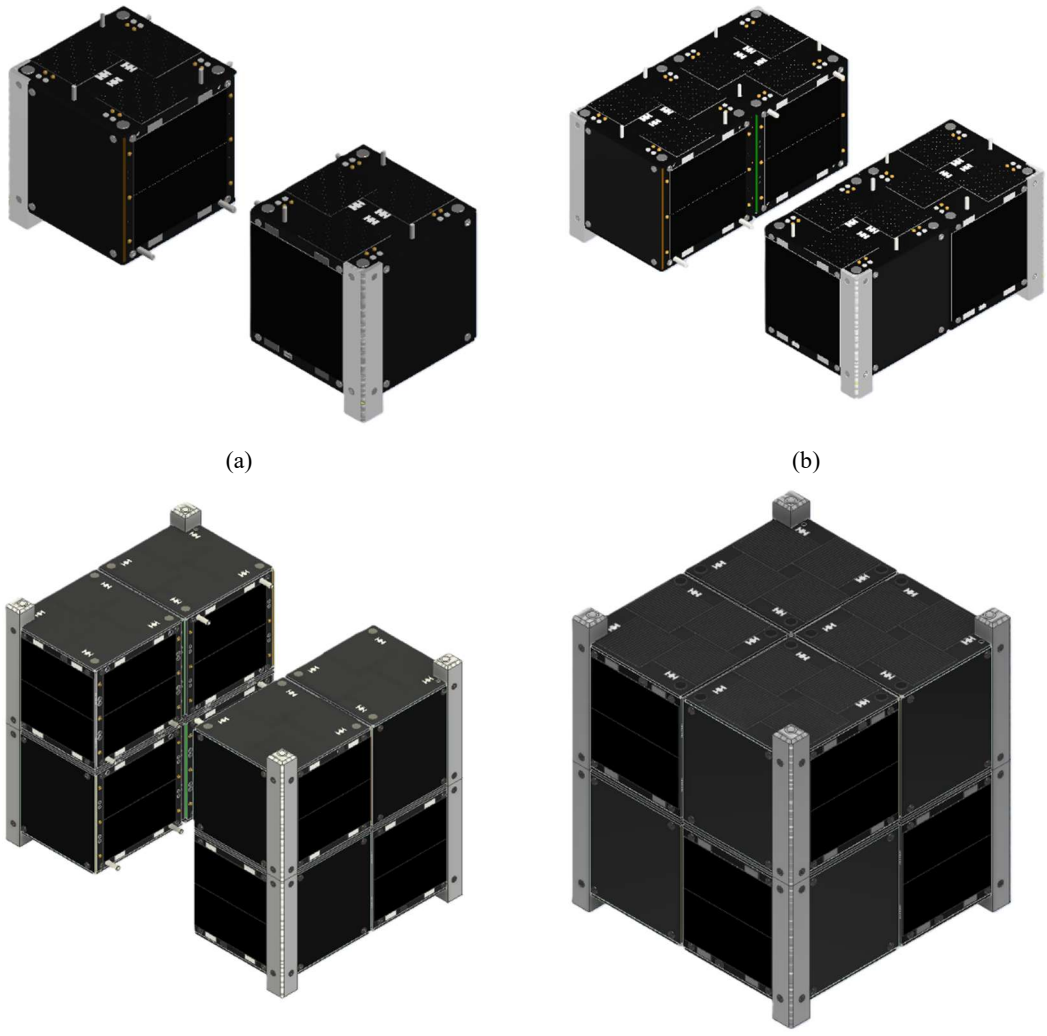

Figure 3.6: PQ8 Assembly: (a) PQ1 to PQ2 (b) PQ2 to PQ4 (c) PQ4 to PQ8 (d) PQ8

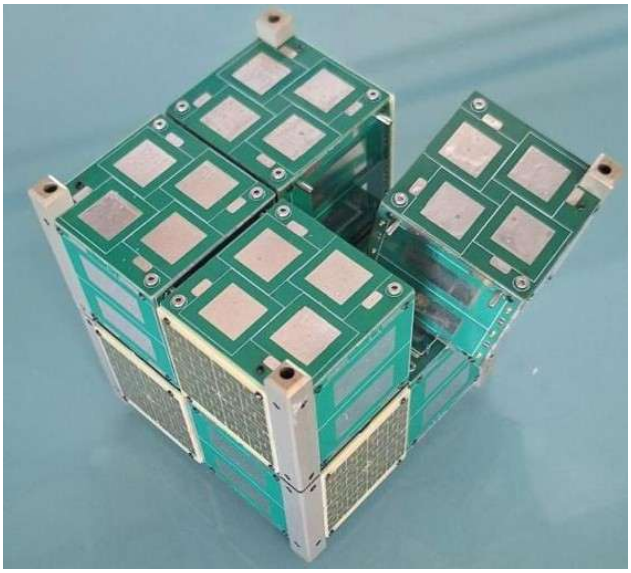

Figure 3.7: Photo of a PQ8 Satellite

3.1.4 Design Approach for Structural Components

The structural design of the PQ8 satellite followed the ECSS Load Analysis Cycle, which prescribes an iterative process of requirement definition, structural modelling, analysis, and redesign until compliance with all mechanical and environmental constraints is achieved. Rather than selecting a single concept through a trade study, the structure evolved through successive iterations, each driven by the results of finite element analysis and by compliance with predefined performance criteria.

The initial structural concept consisted of an aluminium frame using aluminium 6061 for the majority of components, selected for its machinability and compatibility with CubeSat standards. Minimum practical wall thicknesses were adopted to reduce mass while maintaining manufacturability. This baseline model was subjected to modal, linear static, and shock response spectrum analyses using the worst-case launch environment derived from candidate launch vehicles listed earlier in this chapter.

Early analysis revealed three dominant issues:

1. Stress concentrations around internal partition interfaces,
2. Stress concentration at the rails of the satellites,
3. Reduced stiffness at the geometric centre of the structure, where the horizontal and vertical divisions of the PQ8 intersect.

These results triggered the first design modification, in which local wall thicknesses were increased in high-stress regions and central guide pins were introduced to provide load paths across the structurally weakest zone.

Subsequent iterations were governed by a hierarchical response strategy. When analysis results violated predefined criteria, the design response followed the sequence:

- Geometric stiffening through local thickening,
- Material escalation in critical components.

For instance, when structural rails and other highly loaded components approached allowable stress limits under aluminium 6061, these elements were selectively upgraded to aluminium 7075, while non-critical components retained aluminium 6061 in order to constrain mass growth. Each material substitution was followed by re-analysis of the updated configuration, and this iterative process was repeated until all structural and system-level requirements were simultaneously satisfied.

3.1.5 Materials and Fabrication

The structural components of the PQ8 satellite were fabricated from a combination of aluminium and stainless steel. The top frame, bottom frame, battery clamp, and internal walls were machined from aluminium 6061, selected for its balance of strength, machinability, and compatibility with CubeSat standards. The guide rails, which were expected to experience higher loads, were machined from aluminium 7075. Detailed drawings of the satellite structure are provided in *Appendix A*.

Fasteners and spacers used throughout the internal stack were fabricated from stainless steel (SAE 304) to ensure mechanical strength and to avoid magnetic interference with the ADCS. The guide pins, positioned at the central intersection of the PQ1 layout, were manufactured from high-carbon chrome steel (GCr15) to provide local reinforcement at the structurally weakest points. Figure 3.8 illustrates a materials map of the PQ8 Structure.

Non-bonded contact surfaces, primarily the guide pins and their respective guide holes, were designed to have different materials. That is, aluminium 6061 for the guide-holes (part of the top and bottom frames) and GCr15 for the guide pins. This reduces the risk of cold-welding and is recommended by the ECSS standards. As an added measure, and to minimise friction during disengagement, the guide pins are coated with a dry lubricant, specifically polytetrafluoroethylene (i.e. PTFE/Teflon).

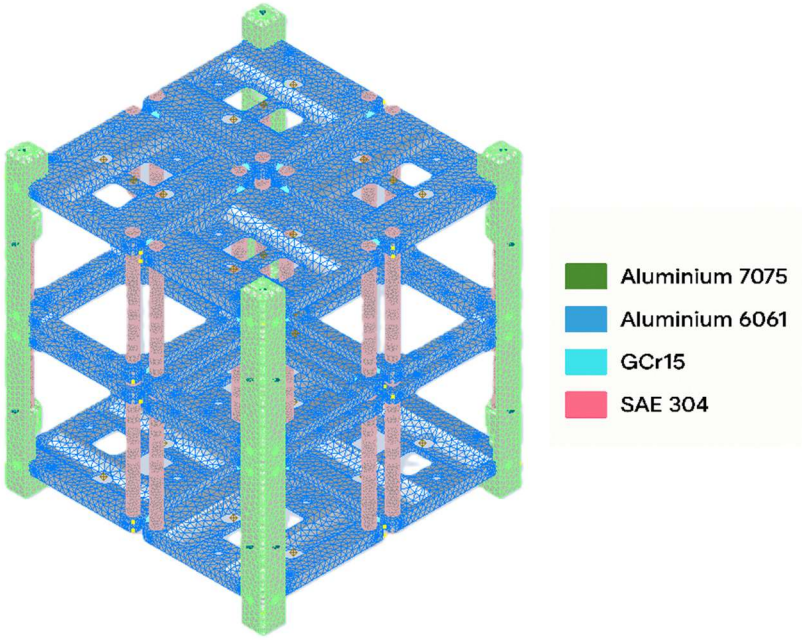

Figure 3.8: Materials Map of PQ8 Structure

Surface finishing was applied selectively and as required by specifications. In particular, the guide rails were anodised for deployer compatibility, while other surfaces were left as-machined and deburred. Additionally, the rails were finished to a surface roughness of 1.6 µm to minimise friction during deployment from the deployer. General dimensional tolerances followed ISO 2768-Medium, with a tighter tolerance of ± 0.1 mm applied to precision features such as fastener holes and guide pin interfaces.

Environmental compatibility was considered where feasible. Outgassing was primarily a concern for adhesives, epoxies and connectors used in minor assembly. Low-vapour-pressure compounds, such as Torr Seal, were selected accordingly. While a complete vacuum compatibility assessment was not undertaken, the approach reflects a conscious alignment with space-readiness practices, limited only by the availability of suitable COTS components at this scale.

All parts were CNC machined, following design verification using 3D printed parts. Machining residues and handling oils were removed using isopropyl alcohol. However, cleanroom procedures were not followed, as this was not a flight model.

3.1.6 External Interfaces

The PQ8 satellite structure is enclosed by six external panels, including five solar cells and one antenna. All panels are mounted using corner screws and are not considered primary structural elements. Their main functions are to support power conversion, house the antenna, and enclose the satellite. While not designed as load-bearing components, the panels contribute to overall enclosure rigidity and help protect internal components from the external environment.

The PQ8 design includes internal mechanical and electrical interfaces between adjacent PQ1 satellites, illustrated in Figure 3.9. These interfaces enable clustered communication and power routing prior to separation. Each PQ1 satellite is aligned mechanically using guide pins and is held in position by permanent magnets. Electrical connectivity is provided by spring-loaded pogo-pins, which transfer both power and I²C communication between neighbouring satellites during clustered flight. Additionally, one of the solar panels includes a debug port, as illustrated in Figure 3.10. This port provides access for battery charging and in-system programming during assembly, integration, and testing.

The permanent magnets are arranged in pairs with opposite poles facing outward at the solar panel surfaces. This configuration produces a net-zero magnetic moment, with respect to Earth's magnetic field and about the satellite's centre of mass. Additionally, the pogo-pins, made of brass, press against unplugged gold-plated vias on the opposing surface. This reduces the contact area of the interface, thus reducing the risk of cold welding. The spacing of both the magnets and the pogo-pins, with respect to their counterparts on the mating surfaces of the adjacent PQ1s, is an essential parameter for the disengagement mechanism. The effect of which is illustrated in Chapter 7.

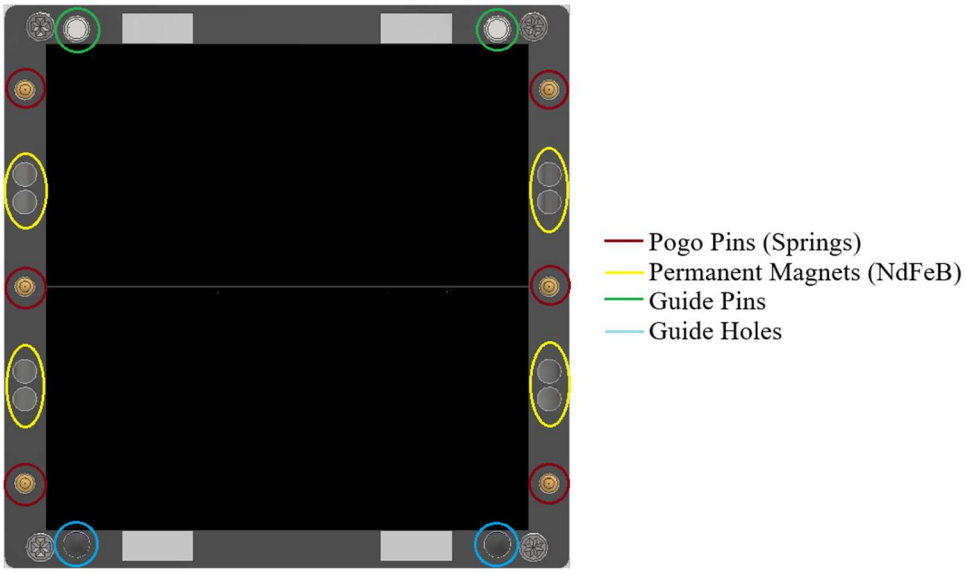

Figure 3.9: PQ1–PQ1 interface

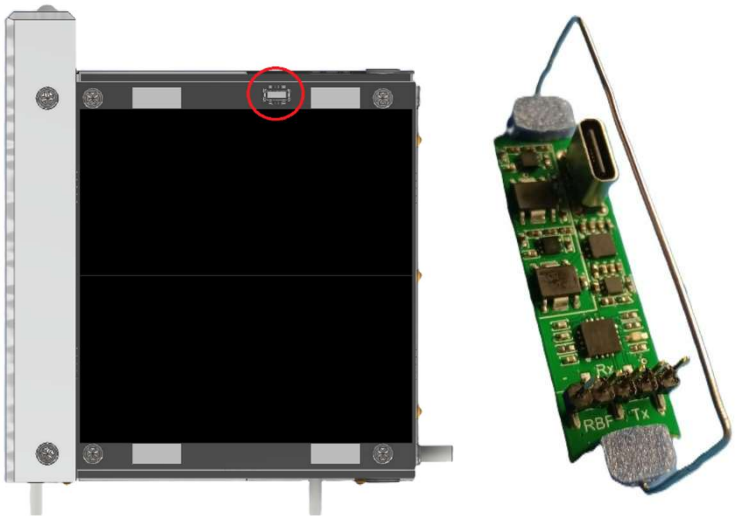

(a) (b)

Figure 3.10: PQ8 Debug Port (a) Connector (b) Debug Port PCB

These internal interfaces are passive and self-aligning, simplifying integration and ensuring consistent contact until the moment of separation. The combined mechanical and electrical design allows the PQ8 to operate as a single coordinated unit during launch and early mission phases before dispersing into eight PQ1 satellites.

3.1.7 Concurrent Engineering Approach for Budgets

Unlike the structural design, which involved discrete geometric and material changes between iterations, the mass and power budgets were managed using a concurrent engineering approach. In this framework, subsystem designs evolved in parallel, with regular reconciliation against system-level mass and power limits.

For mass, a target of 250 g per PQ1 satellite, including a 10 % contingency, was established based on the overall PQ8 system limit of 2 kg. Initial mass allocations were assigned to each subsystem based on heritage designs and preliminary component selections. As subsystems matured through prototyping and testing, these allocations were continuously updated using measured component masses rather than estimates.

When the total mass approached or exceeded the target, corrective action was taken through rebalancing rather than complete redesign. Priority was given to preserving mass in mission-critical subsystems, particularly the structure and ADCS. This process continued until the consolidated mass, including contingency, satisfied the system-level requirement.

Power budgeting followed a similar logic. The available power envelope was fixed by the worst-case target orbit geometry envelope, panel area, solar cell performance, and EPS efficiency. Subsystems were therefore required to operate within this envelope rather than competing to define it. Initial power allocations were based on nominal operating modes and were continuously refined as the design matured.

In this way, decision making for mass and power was driven by continuous optimisation under fixed system-level constraints, rather than by discrete concept selection. The concurrent engineering approach ensured that subsystem-level refinements remained compatible with overall system feasibility throughout the design lifecycle.

3.1.8 Mass Budget

The total mass of a single PQ1 satellite within the PQ8 configuration is approximately 250 g, including a 25 g contingency margin. This allocation ensures compliance with the PQ8 system-level limit of 2 kg for the full 1U CubeSat, in line with the CubeSat Design Specification. The structure contributes a total of 37 g, with a significant portion attributed to the machined aluminium frame. The breakdown by subsystem and component is summarised in Table 3.3.

Table 3.3: PQ1 Mass Budget

Subsystem	**Component**	**Mass [g]**	**Mass [g]**	**Comments**
Structure	Rail	4	37	Structural, Aluminium 7075
	Bottom Frame	4		Structural, Aluminium 6061
	Top Frame	9		Structural, Aluminium 6061
	Battery Clamp	6		Structural, Aluminium 6061
	Bolts + Nuts	4		Structural, Stainless Steel
	Spacers			Between subsystems, Aluminium
	Screws	2		For external PCBs, Stainless Steel
	Guide Pins			GCr15
	Connectors	6		Power, Data
EPS	Solar Cells	10	70	
	Solar Cell PCBs	25		4 layers, 1mm
	Batteries	25		2 x 650 mAh LI-ION Batteries
	EPS PCB	5		4 layers, 1mm
	EPS Components	5		All ICs, passives, etc.
Comms	Antenna	N/A	20	
	Antenna PCB	12		
	RF parts	5		All ICs, passives, etc.
	Comms PCB	5		4 layers, 1mm
	Coaxial Cable	1		
	RF Micro-Connector	1		
ADCS	Magnetorquers	45	77	3 Coils of 15 g each
	Motors	5.4		DC Micro motors 1.8 g each
	Reaction Wheels	16.2		3 reaction wheels of 5.4 g each
	ADCS PCB	5		4 layers, 1mm
	ADCS Components	5		All ICs, passives, etc.
OBC	OBC Components	5	10	All ICs, passives, etc.
	OBC PCB	5		4 layers, 1mm
Disengagement	Supercapacitor	3.5	3.5	
Payload	Payload Components	5	10	All ICs, passives, etc.
	Payload PCB	5		4 layers, 1mm
Contingency			25	
		Total	**250**	

3.2 Power Generation and Regulation

The ADCS subsystem has the highest individual mass at 77 g, driven by the three 15 g magnetorquers and three 5.4 g reaction wheels. Additional contributions come from the micro motors, ADCS PCB, and associated electronics. The EPS accounts for 70 g, primarily from the solar cells and the two 650 mAh Li-Ion batteries, the latter representing the single largest mass within the EPS. The remaining EPS mass includes the 8-layer subsystem PCB and the solar cell PCBs. The disengagement system adds 3.5 g, corresponding to the supercapacitors.

The communications subsystem contributes 20 g, including the antenna PCB, RF circuitry, the coaxial cable, and the antenna itself. Both the Payload and OBC subsystems consist of a PCB and associated electronics only, each with an allocated mass of 10 g.

A 25 g contingency margin, equal to 10% of the total mass, was included to account for additional harnessing, adhesives, component tolerances, and unaccounted components. This margin ensures the PQ1 remains comfortably within the mass constraints of the PQ8 Architecture.

The PQ8 satellite uses five solar panels to generate electrical power for all onboard functions. Power is distributed via the EPS, which provides both a regulated and an unregulated supply line. This section outlines the generation assumptions, conversion efficiencies, and allocation of available power, with emphasis on the requirements of the disengagement system. The topology of the power generation and distribution system is illustrated in Figure 3.11.

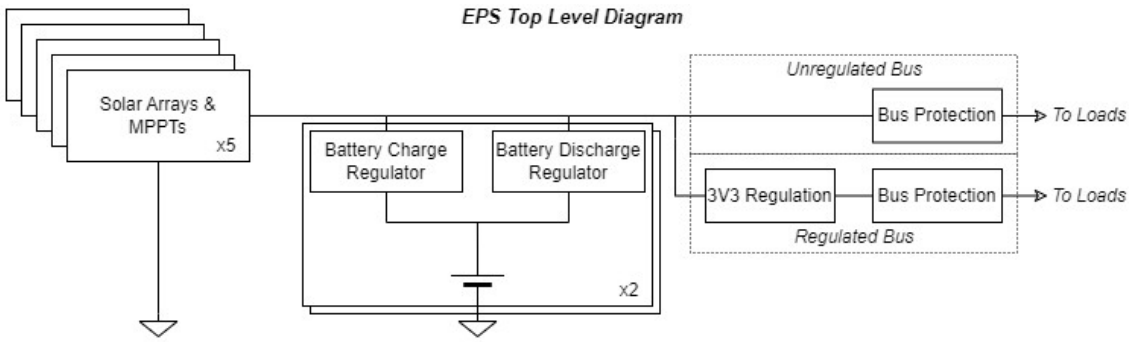

Figure 3.11: Electrical power system topology

The target orbit is quasi-circular, at altitudes between 350 km and 500 km. The corresponding orbital illumination fractions, ranging from approximately 60 – 63%, are computed assuming a worst-case Sun–orbit geometry in which the orbital plane is aligned with the Sun–Earth direction (i.e. near-zero β-angle), resulting in maximum eclipse duration per orbit. The power generation estimates throughout this section are therefore based on these worst-case illumination conditions. An irradiance of 1367 W/m² at AM0 is assumed throughout the calculations.

Multiple space-grade triple-junction solar cell types were evaluated for integration on the five external panels, including models from CESI, DHV, and AzurSpace, as well as a mixed configuration. Each option yields a different power output due to variations in cell efficiency, fill factor, and panel coverage. A total surface area of approximately 16 cm² was available per panel, with each supplier achieving a different fill factor due to the variation in cell form factor. Additionally, the nominal efficiency varied depending on the supplier. Power generation estimates for each configuration are summarised in Table 3.4. These values assume that the satellite rotates slowly in orbit, allowing all panels to be illuminated over time.

A theoretical upper-bound case, shown in Table 3.4, assumes maximum supplier-reported efficiency and a 100 % fill factor. While not physically realizable, this case is included to provide a reference for comparing the relative impact of fill factor and solar cell technology across the subsequent scenarios. In practice, a mixed solar assembly approach was selected, using a combination of CESI and AzurSpace cells. This strategy improved sourcing flexibility and reduced overall cost while maintaining the same effective fill factor.

Table 3.4: Solar cell average orbital power by supplier

Cell Supplier	Area Fill Factor (%)	Stated Efficiency(AM0) (%)	Power (mW)
Theoretical	100	30.0	503
DHV	53	28.0	250
CESI Cell 1	75	29.0	384
CESI Cell 2	75	28.0	371
AzurSpace	100	29.1	504
Lightricity	75	30.0	389
Mixed Cells	100	29.0 / 29.1	501

Power harvested from the panels is regulated by the EPS, which includes a maximum power point tracker for each panel (MPPT), charge/discharge regulation, and voltage conversion. Subsystems draw from either the regulated or unregulated supply, depending on their design. The disengagement mechanism, in particular, operates from the unregulated bus within the voltage range of 3.3 V to 4.1 V. A breakdown of EPS efficiencies, along with the safety margins applied at each stage, is presented in Table 3.5.

Table 3.5: EPS Efficiency Table

Parameter	Value
Power Extraction (MPPT)	82%
Charge/Discharge Efficiency	90%
Delivered Efficiency	98%
Average Power Regulator Efficiency	90%
Fraction of Power Regulated	23%
Fraction of Power Unregulated	77%
10% Safety Margin	90%
Overall Efficiency	65%

A detailed subsystem power budget is given in Table 3.6, with average and peak values allocated to each circuit group. Of particular note for this work is the disengagement mechanism allocation of 20 mW average power per orbit (or 32 mWh), based on the available energy per orbit for the magnetorquer operation. Its circuitry and operational context are described in Chapter 5.

Table 3.6: PQ1 Power Budget

Subsystem	Components	Operation /orbit (%)	Mean Power (mW)	Peak Power (mW)	Orbit Avg. (mW)
EPS	EPS Processor	-	-	35	10
Comms	Radio: Beacon	10	100	100	10
	Radio: Tx	1		1500	1.5
	Radio: Rx	40		435	174
	Comms Processor	27	-	35	9.5
ADCS	RWs (x3)	100	35	45	35
	MTs (x3)	14	150	300	21
	Sensors	100	7	7	7
	Motor Signal	100	10	10	10
	ADCS Processor	-	-	35	10
OBC	Processor	10	128.7	128.7	12.9
Payload	Processor	-	-	-	-
			Average Orbital Power (mW):		**288**

These allocations include margin allowances to reflect ECSS guidance and design best practices. Combined with EPS efficiency and expected orbital conditions, the power budget confirms that all mission-critical systems, including the disengagement mechanism, can be supported throughout the mission lifecycle.

3.3 Structure Finite Element Analysis

Modal, linear static, and shock/response analyses were performed on the structure using Autodesk Inventor NASTRAN, based on launch load environments derived from Ariane 5, Vega, Vega-C, and Falcon 9 variants, as collated in Table 2.4.

These launch vehicles were selected as they collectively represent a significant proportion of contemporary CubeSat and nanosatellite launch opportunities, encompassing both commercial rideshare missions and European institutional launch systems. Since 2021, between 55 – 75% of nanosatellites have been launched aboard Falcon 9, making it a representative mechanical environment for generic CubeSat structural design [95]. Although the Ariane and Vega families are not typically used for commercial CubeSat rideshare deployments, they were included to ensure compatibility with European launcher environments and to account for potential future institutional missions or collaborative opportunities.

Other commonly used launch vehicles, including PSLV, Antares, and Soyuz, were not included in the analysis. PSLV was excluded due to the limited public availability of detailed mechanical environment specifications, while Antares primarily supports ISS deployment missions. Soyuz was excluded due to current programmatic and accessibility constraints.

Modal analysis was performed to evaluate the natural frequencies of the satellite structure, with the requirement that the first structural mode exceed 100 Hz, consistent with typical CubeSat deployer stiffness requirements.

Shock Response Spectrum (SRS) analysis was used to assess the response of an idealised system subjected to high-frequency transient shocks, identifying peak response accelerations across a range of natural frequencies. This analysis is essential to evaluate whether structural resonances may be excited by pyrotechnic events such as stage separations, and whether the resulting accelerations exceed the qualification limits. Finally, linear static analysis was performed to ensure structural integrity under sustained quasi-static loads representative of launch acceleration and gravity-induced effects.

3.3.1 Factors of Safety

Safety factors ensure the structural integrity of the satellite during launch under conditions that account for uncertainties in loading, manufacturing tolerances, and material properties. The European Cooperation for Space Standardisation (ECSS) provides baseline margin requirements for structural qualification, as detailed in [89]. However, launch service providers often specify more conservative safety margins, tailored to their specific launch environments and heritage practices.

In this thesis, two sets of safety factors are considered, each aligned with different qualification methods:

1. FEA-Based Safety Factors (Qualification by Analysis): These higher safety margins are used in the linear static analysis and shock response analysis. They account for modelling uncertainties and are consistent with analytical qualification practices where no direct hardware testing is performed.
2. Test-Based Safety Factors (Qualification by Testing): Applied in the shock and vibration testing sections, these factors are slightly lower but are paired with physical testing. They reflect the increased confidence gained through experimental validation and are aligned with ECSS and LSP test qualification methodologies.

The distinction between these safety factor sets ensures that both analytical predictions and physical test conditions conservatively bound the real-world loads expected during launch. The factors of safety for yield and ultimate stress, FOSY and FOSU, respectively, are presented in Table 3.7.

Table 3.7: Factors of Safety for Structural Components

Test	FOSY (Test)	FOSU (Test)	FOSY (Analysis)	FOSU (Analysis)
Sin Vibration	1.25	1.25	1.25	2
Linear Static	1.25	1.25	1.25	2
Shock Analysis	1.41	1.41	1.41	2

3.3.2 Idealisation

As the accuracy of the FEA analysis is dependent on the quality of the mesh, the model has been simplified to only include the frame of the satellites. Other objects, such as batteries and subsystem PCBs, are represented by point masses and connected to the

model as they would connect in actuality. This, therefore, introduces the assumption that the subsystems are rigid bodies of uniform mass density.

Rigid Body Element type 2 (RBE2) is used for the batteries, which assumes no deformation and that all degrees of freedom are independent from the connector node on the battery clamp. For the subsystem idealisations, Rigid Body Element type 3 (RBE3) is used, which distributes the force caused by the mass to the spacers without adding stiffness.

3.3.3 Meshing

To increase analysis performance, three element sizes were defined to create either coarse, fine or very fine meshing with sizing of 1 mm, 0.5 mm and 0.1 mm, respectively. Coarse elements were used on larger parts of the structure that do not experience large loads. Fine meshing was used on smaller parts and areas that are expected to experience large loads, such as the rails, guide pins and spacers. Finally, very fine meshing was used on areas of high stress, such as any corners or necks in load paths. A total of 1.5×10^6 tetrahedral elements were used, with the vast majority being of good quality. Only 0.02 % of the elements were of poor quality with a skew greater than 70°, but none greater than 83°. Since none of these poor-quality elements were located at high-stress areas or on the surfaces of the structure, the mesh was deemed acceptable for the analysis.

3.3.4 Static Loads Analysis

For the static load analysis, two distinct subcases were defined to account for variations in stowing configurations. In the first subcase, a longitudinal acceleration of ± 7 g is applied along the satellite y-axis, while a lateral acceleration of ± 2 g is applied along the x-axis. In the second subcase, the satellite is rotated such that the longitudinal acceleration is applied along the x-axis and the lateral acceleration along the y-axis. This approach ensures that the structural analysis captures the loading conditions associated with different possible orientations during launch vehicle integration.

The results corresponding to both subcases are presented in Figure 3.12. Mesh convergence was enabled for this analysis, whereby the mesh is progressively refined in regions of localised stress concentration, and the solution is iteratively recomputed until the maximum stress value converges to within 5 %.

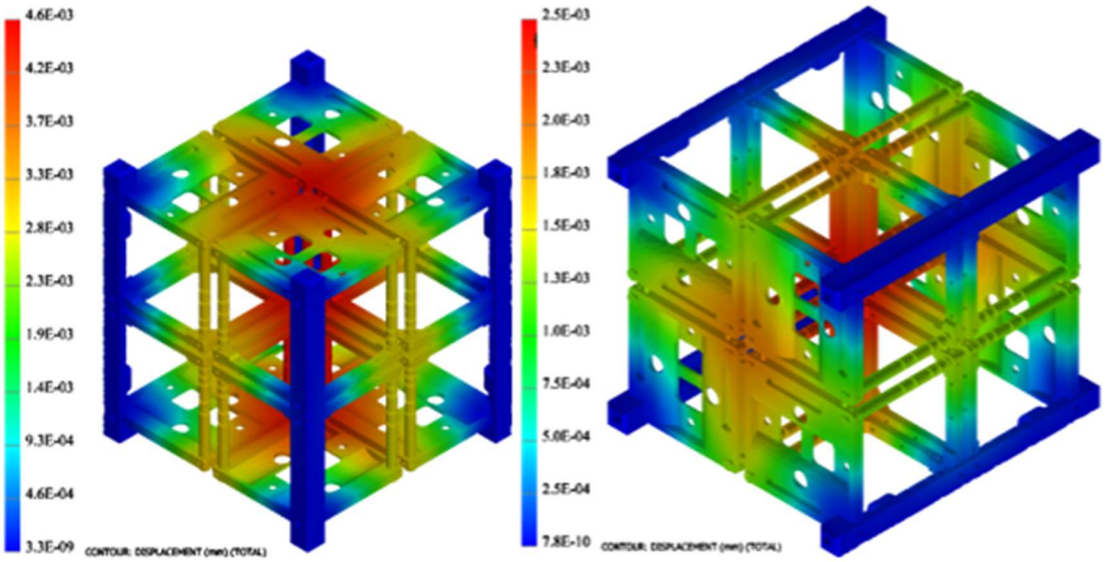

Figure 3.12: Linear Static Analysis Output Displacement in mm.
Left: Subcase 1. *Right:* Subcase 2.

In the first subcase, the analysis yielded a maximum displacement of 4.6 µm and a peak von Mises stress of 14 MPa, with stress concentrations primarily located at the subsystem spacers. In the second subcase, the maximum displacement was reduced to 2.5 µm, while the peak von Mises stress remained below 11 MPa, localised in the same region. The decrease in both stress and displacement observed in the second configuration is attributed to the increased support surface area offered by the rails when the satellite is oriented with the longitudinal acceleration acting along the x-axis.

Considering all cases, the minimum safety factor was about 34, confirming that the structure can withstand the expected quasi-static loads without yielding or excessive deformation. The load levels applied should apply to the Vega-class launchers, Falcon 9, Ariane 6 and PSLV.

The observed minimum factor of safety of approximately 34 under static load conditions reflects the inherently conservative design margins introduced at earlier stages of structural development. The structure was primarily dimensioned to meet dynamic and shock loading requirements, which are more demanding than the quasi-static loads experienced during launch. As such, the static load case represents a less critical scenario, resulting in comparatively low stress levels and consequently high safety margins

3.3.5 Modal Analysis

The modal analysis results are presented in Figure 3.13. Modal analysis was conducted with boundary conditions applied to simulate the PQ8's constrained state within a P-POD. The resulting modal frequency plot showed that the first modal frequency of the structure was 860 Hz, which satisfies the requirement that the fundamental mode be above 100 Hz as specified by most launch providers. This confirms that the structure is sufficiently stiff and unlikely to couple with low-frequency launch vehicle vibrations during ascent.

Since the goal of the modal analysis was to assess the natural frequency of the structure, idealised representations were used for the internal components. However, for qualification, these also need to be considered. Supplementary to the work presented here, Grech, in [96] performed a modal analysis on the PQ1 satellites, including all internal structures. In his results, Grech observed that with the internal components, the first modal frequency is reduced to approximately 184 Hz, localised at the reaction wheels. This value remains greater than the 100 Hz minimum requirement set for the PQ8 Satellites.

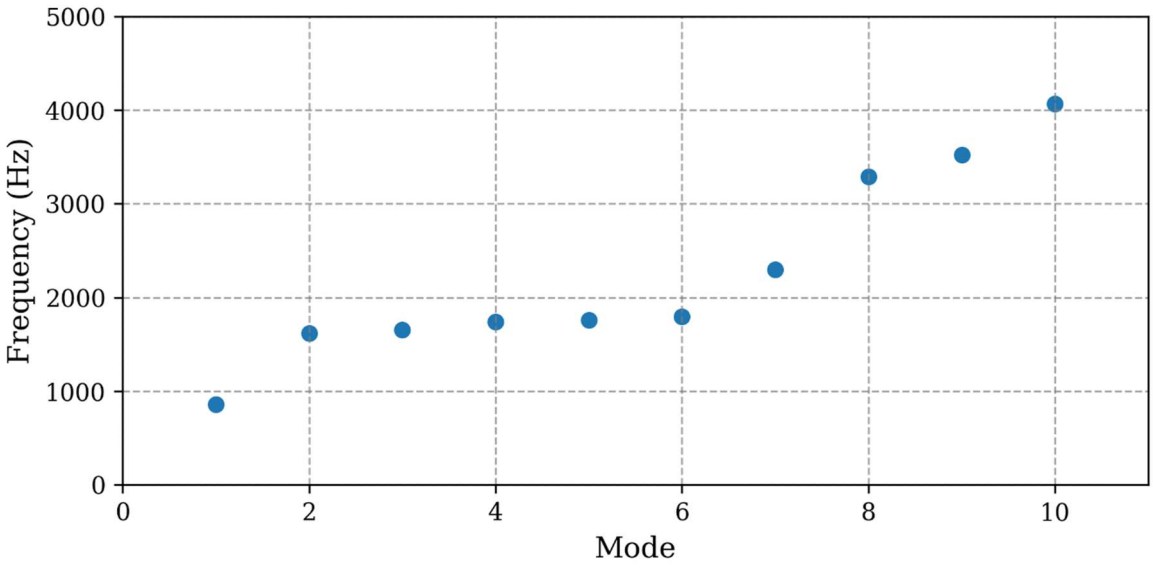

Figure 3.13: PQ8 Modal Analysis Results

3.3.6 Shock/Response Spectrum

Shock response analysis was conducted using a standard Shock Response Spectrum (SRS) approach. A Q-factor of 10 was used throughout the analysis, corresponding to a damping ratio of approximately 5 %, which is typical for aerospace structures and consistent with ECSS recommendations for SRS evaluation [89]. Despite satisfying both static and modal requirements, this analysis revealed several areas of concern. Safety factors under shock excitation varied notably across launch vehicles, underscoring the structure's sensitivity to the high-frequency, transient nature of specific launcher shock profiles. Among all vehicles analysed, the Vega-class launchers (Ariane Vega and Vega C) induced the most critical stress concentrations due to their high shock loads, particularly in the subsystem spacers and guide pins.

Under Vega-class shock loads, the subsystem spacers experienced peak Von Mises stresses of approximately 220 MPa, yielding a minimum safety factor of 1.09. Although this suggests survival under actual flight conditions, it falls short of the minimum 1.25 safety factor required for qualification by both testing and analysis, as stipulated by the ECSS standards and launch service provider guidelines, as in Table 3.7. The guide pins exhibited the next lowest margin, with a peak stress of 361 MPa and a corresponding safety factor of 1.15, also below the threshold. All other components maintained safety factors greater than 2.0, as illustrated in Figure 3.14.

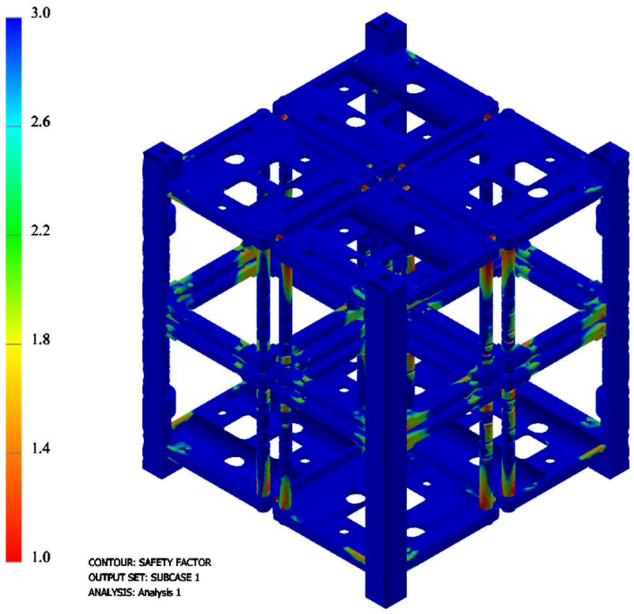

Figure 3.14: Ariane Vega C Shock Load Safety Factors

In contrast, the structure demonstrated satisfactory performance under shock profiles from Ariane 5, Ariane 6, Falcon 9, and PSLV. The Falcon 9 series produced a minimum safety factor of 1.41 in the subsystem spacers, associated with a peak stress of 170 MPa, as illustrated in Figure 3.15. Once again, the guide pins exhibited the next lowest margin, with a peak stress of 287 MPa and a corresponding safety factor of 1.45. All other structural elements retained safety factors exceeding 2.0, confirming the structural adequacy for these launch environments. A total displacement of 0.6 mm was observed for this load case, localised at the centre of the satellite.

Attempts to mitigate the shock-induced stress concentrations by replacing the most affected components with stiffer materials resulted in only partial improvements. While these substitutions increased the local safety factors in the modified spacers and guide pins, the elevated stiffness altered the dynamic response of the structure, redistributing the shock energy and shifting critical stress concentrations to other components, particularly at mechanically coupled interfaces. This is a known limitation in high-frequency transient loading environments, where increased stiffness can reduce local deformation but exacerbate stresses elsewhere.

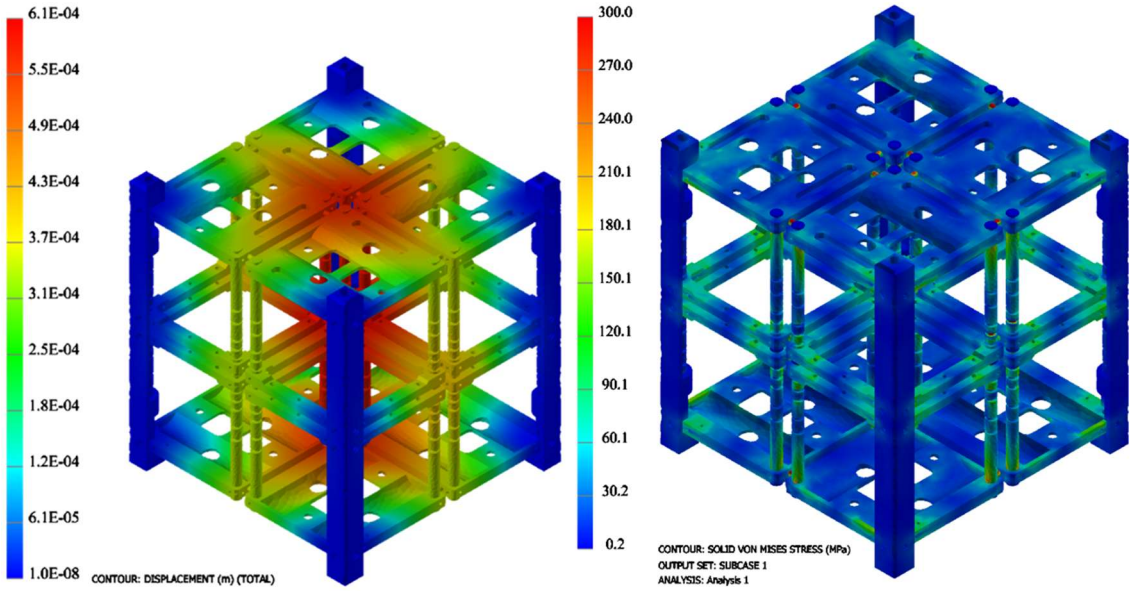

Figure 3.15: Displacement due to shock in m (Left) Von Mises Stress in MPa (Right)

Moreover, the mass and volume penalties introduced by the material upgrades conflicted with the strict constraints of the satellite's form factor and launch mass budget. As a result, a full-system compliance strategy based solely on material substitution was deemed impractical. Considering these trade-offs, and in alignment with broader mission requirements, Vega-class launchers were excluded from the list of compatible vehicles. The final structural configuration was instead tailored to meet the shock qualification criteria of Ariane 5, Ariane 6, Falcon 9, and PSLV, for which the required safety margins were maintained without requiring substantial structural redesign.

Similar to the modal analysis, Grech also performed shock response analysis for the PQ1 structure, including internal components, in [96]. The results confirm the capability of the structure to withstand the launch loads within the margins of safety. However, Grech highlights that, with the current design, the reaction wheels act as "shock-sponges", leading to excessive loads on the motor shaft. Grech recommends extending the motor shaft such that it becomes supported by the PCB parallel to the reaction wheels, as illustrated in Figure 3.16. This change brings the loads and safety factors to within qualification levels.

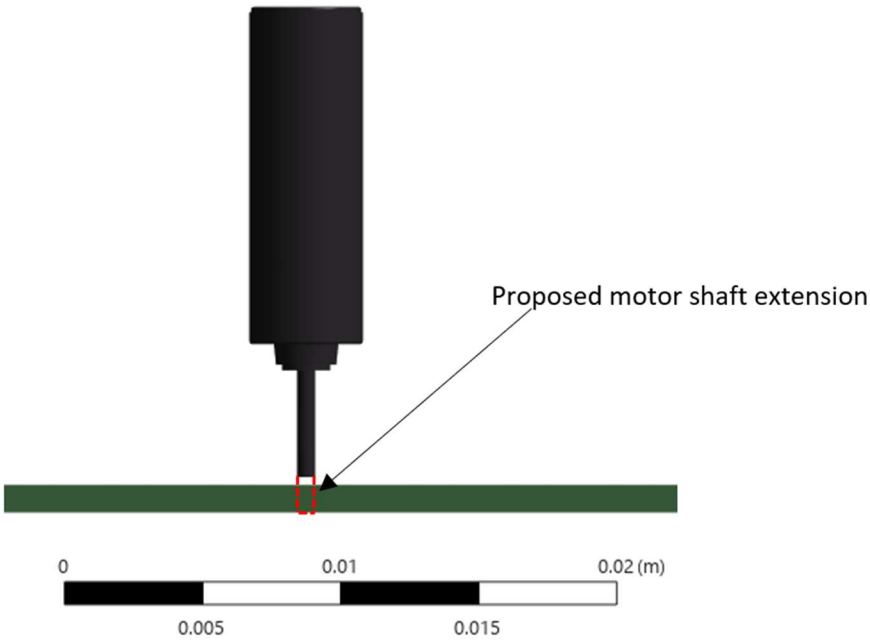

Figure 3.16: Proposed solution by Grech for reducing shock loads on motor shaft [96]

3.3.7 Summary of Structural Analysis

Finite element analysis was conducted to evaluate the structural integrity and dynamic response of the satellite under representative launch conditions. The simulations were performed using Autodesk Inventor NASTRAN, incorporating load profiles from multiple launch vehicles, including Ariane 5, Ariane Vega, Vega C, PSLV, and Falcon 9 variants. Three types of analyses were carried out: modal, linear static, and shock response spectrum analysis.

Modal analysis was used to determine the natural frequencies of the structure under boundary conditions representative of the satellite's constrained state within a CubeSat deployer. The first modal frequency of the structure was found to be 860 Hz, well above the commonly required 100 Hz minimum threshold specified by many CubeSat deployers. This confirmed that the structure is sufficiently stiff and unlikely to resonate with low-frequency launch vibrations. Additional modal studies from related work by Grech on the PQ1 scale model showed similar compliance, with the lowest mode at 183.52 Hz located at the reaction wheels.

Linear static analysis was conducted to verify the structure’s ability to withstand quasi-static loads encountered during launch. Two load subcases were evaluated to account for alternate stowing orientations, with the direction of longitudinal and lateral accelerations reversed in each. In both cases, mesh convergence was achieved with less than 5% deviation in stress values. The maximum displacements observed were 4.6 μm and 2.5 μm for the first and second subcases, respectively, with corresponding von Mises stresses well below material yield limits. The minimum factor of safety in this analysis exceeded 30. This unusually high value is attributed to the structural overcapacity introduced to satisfy more stringent dynamic and shock conditions, as well as the effectiveness of the load distribution paths and stiff frame geometry, which collectively reduce stress under static loads.

Shock response analysis was performed using the shock response spectrum (SRS) method to evaluate how the structure responds to high-frequency transient events, such as stage separation or pyrotechnic activations. This analysis revealed that the most severe loading environment occurred under the Vega-class launchers, which induced critical stress concentrations in the subsystem spacers and guide pins. The lowest safety factors under these conditions were 1.09 and 1.15, respectively, below the ECSS and launch provider threshold of 1.25 required for qualification. Attempts to mitigate this

through the use of stiffer materials led to the redistribution of stresses into other components and increased mass penalties, making such solutions impractical. Consequently, Vega-class vehicles were excluded from the set of compatible launchers. In contrast, all other launchers evaluated, including the Ariane 5, Ariane 6, PSLV, and Falcon 9, demonstrated acceptable safety margins above 1.4, with all components maintaining safety factors greater than 2.0 except for the spacers and guide pins, which were within qualification limits.

It is worth noting that, although the current structural configuration does not meet the shock qualification thresholds for Vega-class launchers under standard hard-mount integration, this limitation may be overcome through the use of deployers equipped with soft-stow technology. These systems incorporate shock isolation features which significantly attenuate the transmitted shock loads to the payload. By mitigating the high-frequency content responsible for the critical stress concentrations observed in this study, soft-stow deployers could enable compatibility with Vega-class launch vehicles without requiring structural redesign. Therefore, if launch availability or mission requirements necessitate the use of Vega-class platforms, integration via a soft-stow deployment system represents a viable mitigation strategy.

Together, these simulations confirm that the structure meets mechanical qualification requirements for most targeted launch environments and highlight areas for potential reinforcement should compatibility with Vega-class vehicles be reconsidered in future iterations.

3.4 Mechanical Testing

3.4.1 Sine Equivalent Dynamics Testing

Sine vibration testing serves as a critical step in validating the structural integrity and modal behaviour of space-bound systems under quasi-static loading and low-frequency dynamic environments typical of launch. In this campaign, sine sweep tests were conducted in accordance with the ESA ECSS-E-ST-10-03C standard to replicate the deterministic vibrational loads imposed by the launch vehicle. The objective was to ensure structural survivability within the expected input spectrum and at a factor of safety of 1.25.

The test configuration consisted of a fully assembled PQ1 satellite in a custom-made aluminium enclosure, with the unit mounted on a Bruel & Kjaer V650 Medium Force

Shaker, see Figure 3.17. The aluminium enclosure mimics how the PQ1 satellite is constrained when integrated in a PQ8 satellite in a P-POD. That is, the PQ1 is supported from the rail and guide pins only, as shown in Figure 3.18.

A swept-sine input was applied from 5 to 110 Hz at a constant logarithmic rate of 2 oct/min along each principal axis (X, Y, and Z), matching the sinusoidal equivalent dynamics of the Flacon 9 launch vehicle. The acceleration was ramped from 0.65 g to 1.25 g, peaking at a frequency of 35 Hz. The 1.25 g acceleration was maintained for the rest of the sweep. Feedback accelerometers were attached to the enclosure to confirm that the required excitation levels have been reached. The profiles for the x- and y-axes are presented in Figure 3.19, and for the z-axis in Figure 3.20.

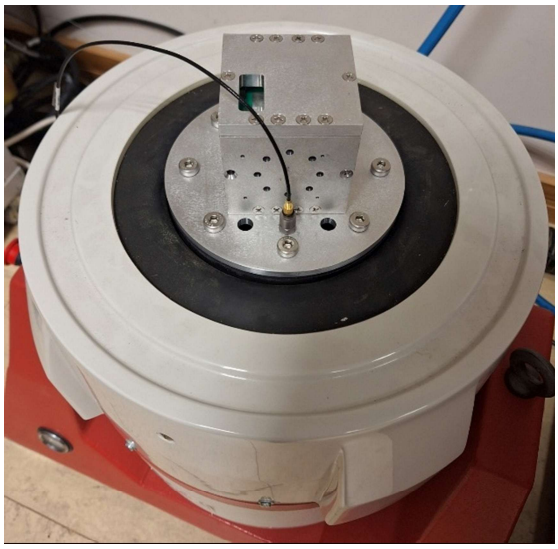

Figure 3.17: PQ1 in enclosure on the Bruel & Kjaer V650 Medium Force Shaker

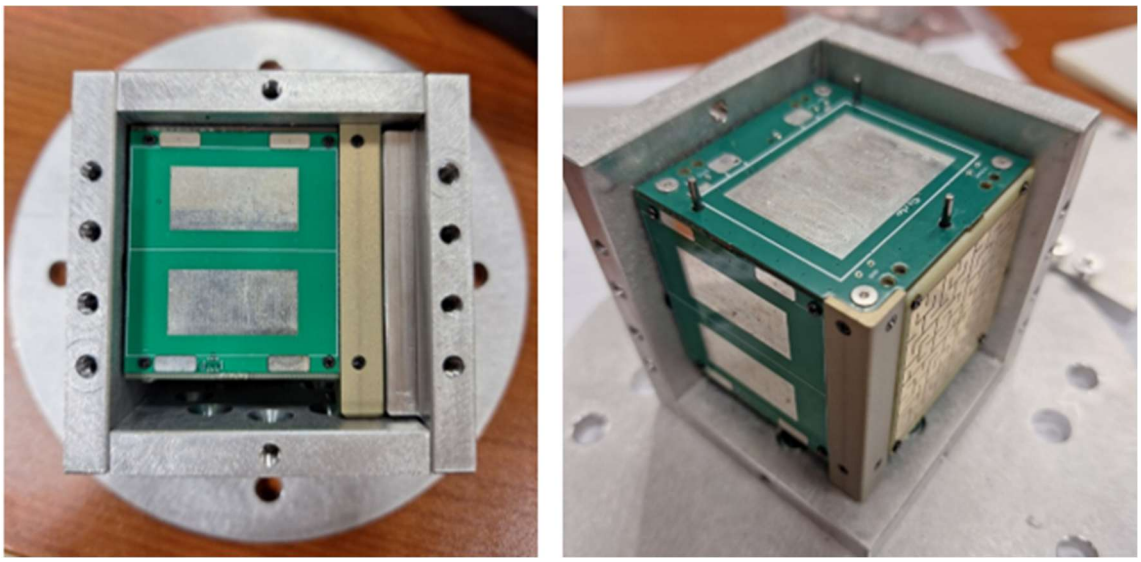

Figure 3.18: PQ1 in aluminium enclosure.

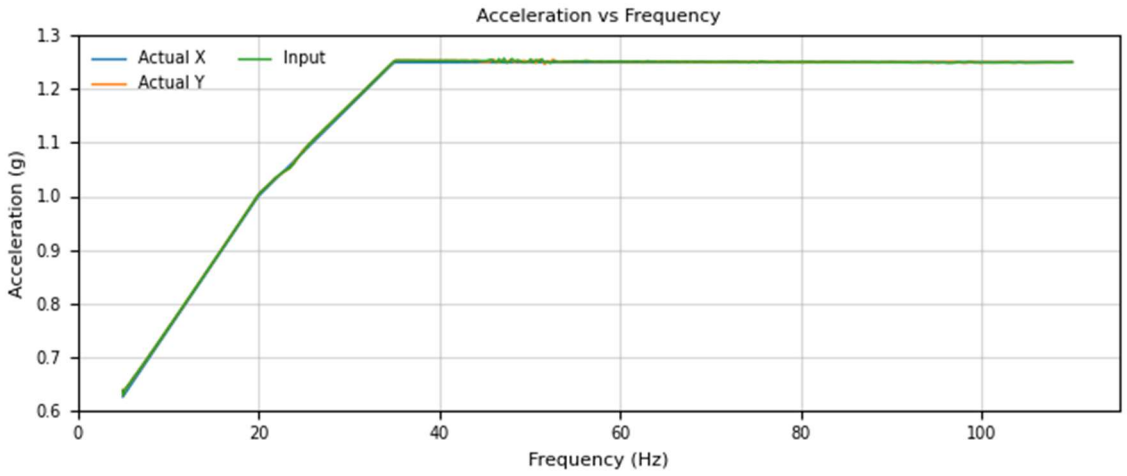

Figure 3.19**:** Vibration profiles for X and Y axis Tests (Symmetric)

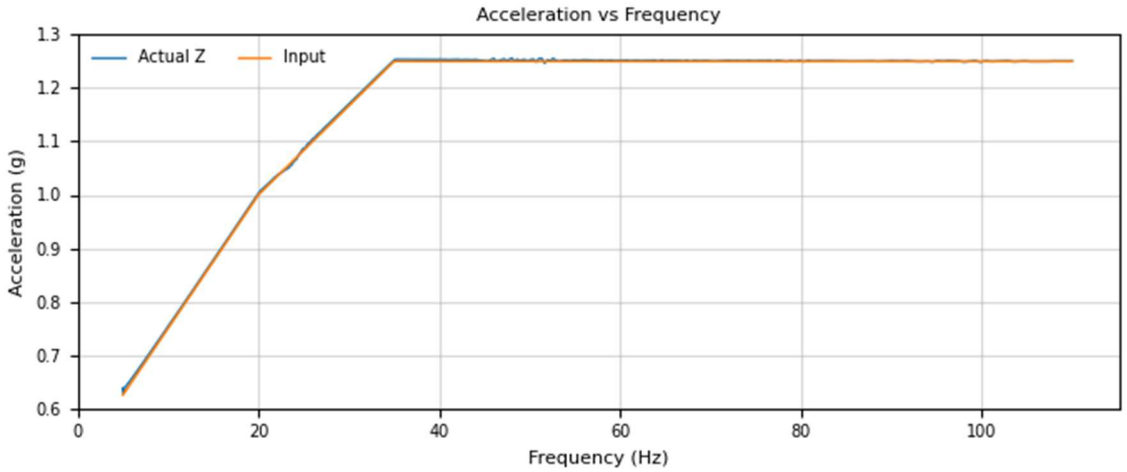

Figure 3.20**:** Vibration profile for Z-axis Test

Post-test inspection of the satellite structure and subsystems presented no signs of deformation or damage, verifying the results of the FEA. Additionally, this qualifies the structure for the Falcon 9 launch vehicle, or similar, under sine equivalent loads.

3.4.2 Mechanical Shock Testing

Shock testing is conducted to replicate the high-frequency, high-acceleration transient loads experienced during critical launch events such as pyrotechnic device activation, stage separation, and deployment of appendages or separation mechanisms. Unlike sine or random vibration environments, which subject the structure to continuous or broadband excitation, shock events are characterised by rapid rise times and short durations, often with spectral content extending into tens of thousands of Hertz. These

conditions pose unique risks to structural interfaces, sensitive components, and materials susceptible to brittle failure or fatigue accumulation.

To replicate the required shock environment, the campaign utilised an Avex SM-105 Shock Test Machine, selected for its ability to produce controlled high-g pulses with a defined frequency content. Figure 3.21. The test aimed to reproduce the Qualification Shock Spectrum (QSS) envelope provided by the launch provider, representative of the most severe shock events expected during mission ascent.

The target SRS was defined as a linearly rising acceleration profile, reaching 1410 g at 1 kHz and remaining flat through 10 kHz, reflecting a conservative worst-case envelope corresponding to the Flacon 9. This spectrum was emulated using a single half-sine pulse of 1000 g peak acceleration and 0.42 ms duration, corresponding to a system response characterised by a Q factor of 10, as shown in

Figure 3.22. This approach was selected to excite the high-frequency modes of the structure whilst remaining within the limitations of the available machinery.

Post-shock inspections and functional testing confirmed the mechanical and electrical integrity of all structural components, with the exception of the x-axis and z-axis motor shafts. Both shafts exhibited physical damage and impaired functionality, as shown in

Figure **3.23** Grech had anticipated this outcome in [96], although his recommendations had not yet been implemented, as the tests were conducted during the

Figure 3.21: PQ1 in enclosure on the Avex SM-105 Shock Test Machine

same timeframe as his analysis. Incorporating these recommendations is expected to introduce minimal design complexity and should mitigate the issue in future iterations of the satellite. No signs of delamination, connector decoupling, or additional structural failure were observed. Functional verification confirmed nominal operation of all other subsystems, including the power distribution unit, communication interfaces, and deployment mechanisms.

This result underscores the critical importance of shock testing in revealing subsystem-specific vulnerabilities that may remain undetected under static or low-frequency dynamic conditions. The test campaign not only validates the structural design under severe transient loading but also yields actionable insights into component-level enhancements needed to ensure complete mission reliability.

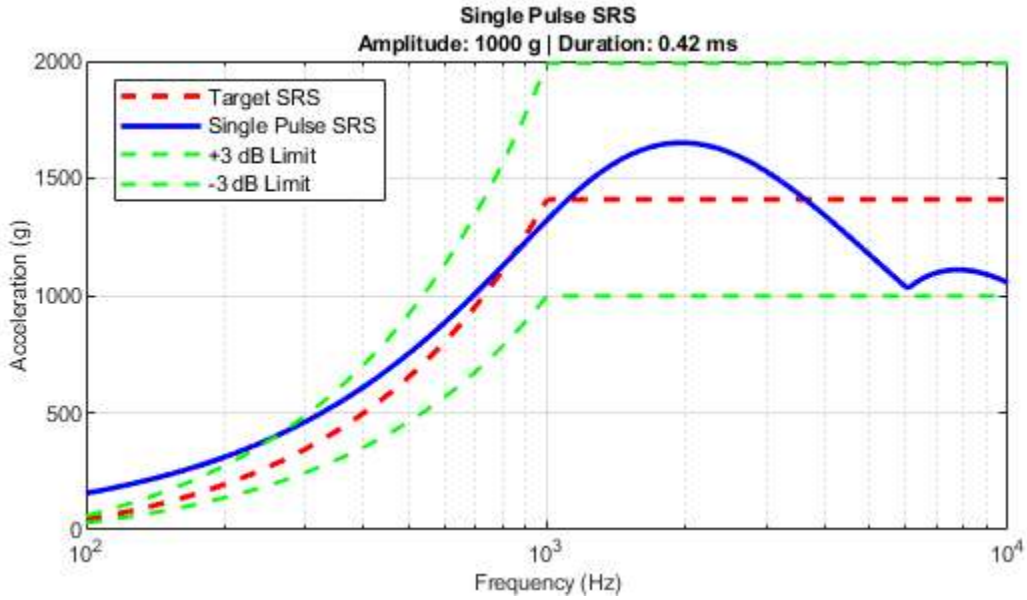

Figure 3.22**:** Shock Response Target profile and the actual profile from half-sine pulse

Figure 3.23: Damage to the motor shaft following shock testing

3.5 Summary and Design Maturity

This chapter has detailed the structural configuration, internal integration, material selection, mass distribution, and power budget of the PQ8 satellite. The structural design is considered mature, having undergone iterative development based on ECSS-compliant load cases and qualification margins. Structural performance was verified through both numerical simulation and environmental testing, including vibration and shock testing under launcher-equivalent conditions.

The mechanical architecture was developed to support the clustered arrangement of eight PQ1 satellites within a 1U CubeSat. All structural features, such as the frame, internal stack, fastener scheme, guide pins, and interface mechanisms, have been implemented in hardware and verified for assembly and alignment. The PQ1-level mass budget is finalised and compliant with the overall 2 kg system-level constraint.

The external surface area, material properties, and mass distribution, constrained by the structural and power designs presented here, are directly relevant to the dispersal strategy described in Chapter 4. These physical parameters define the aerodynamic characteristics and energy availability that govern the behaviour of the satellite cluster during deployment and separation.

Additionally, the power budget defined in this chapter yielded critical design inputs for the disengagement mechanism constraints discussed in Chapter 5. In particular, the disengagement mechanism was allocated a 32 mWh maximum power consumption. This value was derived from subsystem-level energy constraints and corresponds to the energy allocated to the magnetorquer coils per orbit.

Together, these outcomes provide a structurally and electrically viable baseline, enabling subsequent system-level studies of deployment timing, separation control, and mission sequencing. They form the platform on which the PQ8 architecture is built.

From a TRL perspective, the PQ1 structural subsystem has reached TRL 7, having been physically implemented and tested under environmental conditions representative of launch, with hardware-level verification of integration and assembly. Certain aspects of the PQ1 unit may be considered near-TRL 8, as they are finalised and qualified through hardware demonstration. However, the complete PQ8 architecture, involving clustered operation and multi-satellite constraints, remains at a lower TRL and would require additional system-level environmental testing to progress further.

The mechanical test campaign presented in Chapter 3 was designed to verify the structural survivability of an individual PocketQube unit under representative launch vibration and shock environments. This resulted the exclusion of the fully integrated PQ8 satellite. The decision to exclude the full configuration from testing was driven by both risk management considerations and the intended scope of the experimental validation.

Testing the complete PQ8 configuration would have exposed eight fully assembled satellites to high-risk vibration and shock loads in a single campaign. Given the prototype nature of the hardware, this was considered an unacceptable risk, as a single failure during testing could result in the loss of multiple flight-representative units that would otherwise be still valuable for demonstration and further testing. Instead, a single PQ1 satellite was integrated into a custom-designed enclosure that replicates the mechanical boundary conditions of a deployer interface, specifically in terms of contact locations and load introduction paths.

While this approach does not capture the internal load redistribution between multiple PocketQube units in the full PQ8 assembly, it allows the dominant structural elements of an individual satellite, including the fasteners, PCB mounts, and internal supports, to be tested under conservative excitation levels.

The mechanical interfaces and load transfer paths between the eight PocketQube units were instead addressed analytically through structural modelling and finite element analysis, where the integrated PQ8 configuration was explicitly represented. These analyses account for the coupled stiffness and load distribution between units and were used to demonstrate that stress and displacement levels remain within acceptable margins under the applied launch loads.

As such, the experimental campaign and the numerical analyses are complementary. The former validates the structural robustness of the individual PocketQube units under realistic excitation, while the latter assesses the integrated behaviour of the complete PQ8 assembly. Full-scale vibration and shock testing of the assembled PQ8 system is therefore identified as a logical extension of this work and is recommended as part of future qualification activities once the design reaches a higher technology readiness level.

The PQ8 structural subsystem has been fully integrated in hardware, with successful implementation of all internal subsystems, mechanical interfaces, and satellite mounting features. While complete system-level environmental testing has not yet been

conducted, finite element analysis confirms that the structure meets the launch vehicle launch load margins with appropriate safety factors. Based on this physical integration and high-fidelity analytical validation, the PQ8 structural design is assessed at TRL 5. Completion of vibration and shock testing on the integrated PQ8 assembly would be required to advance it to TRL 6 or beyond.

This structural maturity, demonstrated through both hardware integration and simulation, provides strong evidence for the viability of the PQ8 design and establishes a robust foundation for a future test campaign aimed at system qualification and eventual mission integration.

4 THE PQ8 DISPERSAL METHOD

The successful deployment of a satellite constellation relies fundamentally on the ability to exert precise control over the dispersal dynamics of its constituent elements. Differential drag has become an increasingly viable technique for constellation deployment where propulsion systems are absent. However, most existing implementations presuppose an initial spatial separation between satellites, achieved through mechanisms such as staggered ejection timings or pre-defined positional offsets. These conditions facilitate subsequent phasing, but they inherently limit the compactness and integration potential of the initial satellite assembly.

In contrast, the method proposed in this study addresses a distinct scenario in which all satellites are launched as a single, integrated unit occupying a standard orbit. Dispersal is initiated through a staged sequence of mechanical disengagements, after which the satellites employ aerodynamic shaping to induce differential drag forces. These forces enable the satellites to gradually spread apart in a controlled manner. The novelty of this approach lies in its capacity to exploit passive aerodynamic control following a deterministic and hierarchical physical separation process, without reliance on propulsion systems.

This configuration introduces a range of engineering and operational challenges. Chief among them is the requirement for highly controlled disengagement sequencing to prevent collision and ensure consistency in post-separation dynamics. Additionally, the

approach demands accurate characterisation of aerodynamic effects in low Earth orbit (LEO), where atmospheric density varies with altitude, solar activity, and orbital geometry. Furthermore, the initial conditions immediately following each disengagement must be carefully optimised to ensure predictable long-term separation that meets the constellation's spatial requirements.

Traditional constellation deployment architectures typically employ propulsion-based phasing strategies or rely on precise, pre-programmed deployment sequences. While effective, these methods incur penalties in terms of mass, complexity, and cost. Passive dispersal via differential drag presents an appealing alternative by eliminating the need for onboard propulsion. However, its effectiveness is highly sensitive to the configuration of the satellites at the moment of separation and to the control authority available through aerodynamic design.

This chapter presents a comprehensive methodology for achieving effective constellation dispersal under these constraints. The approach integrates a formal problem definition, a mechanical model of the disengagement sequence, aerodynamic parameter estimation, and an optimisation framework to control satellite phasing through differential drag. The methodology is validated through case studies involving small satellite configurations, demonstrating its feasibility for both minimal and moderate constellation sizes. The broader implications of this method are evaluated in the context of deployment efficiency, scalability, and applicability to different mission classes.

4.1 Dispersal Method Requirements and Objectives

The dispersal method presented in this chapter is not developed to satisfy the requirements of a specific mission or application. Instead, its purpose is to demonstrate the feasibility of transforming a single PQ8 satellite into a controlled in-plane constellation under conservative, worst-case initial conditions whilst remaining within the mission envelope listed in Chapter 1. As a result, the validation of the proposed method is framed in terms of feasibility and bounded performance, rather than compliance with mission-specific operational requirements.

In this regard, the dispersal analysis assumes an initial deployment altitude of approximately 500 km in low Earth orbit. While such an altitude is higher than typically selected for differential-drag-based constellation control, it represents the upper bound

commonly quoted by rideshare launch providers and therefore constitutes a conservative case.

At this altitude, atmospheric density, and hence the available differential drag control authority, is reduced relative to lower operational orbits. Successful dispersal under these conditions therefore provides an upper-bound demonstration of feasibility, and thus improved performance is expected at lower altitudes where atmospheric perturbations are stronger.

In terms of target operational lifetime, this study aims to remain in line with current state of the art. Early generations of PocketQube-class satellites were typically limited to very short operational lifetimes, from weeks to a few months, due to immature power systems, limited radiation tolerance of commercial-off-the-shelf electronics, and the difficulty of implementing reliable attitude control and thermal management at extreme miniaturisation scales. As a result, many early PocketQube missions were conceived primarily as technology demonstrations rather than sustained operational platforms.

More recent studies and missions, however, indicate a clear shift toward multi-year capability. Bouwmeester et al. argue that, from both a mission-design and debris-mitigation perspective, an orbital lifetime on the order of five years represents a sensible upper bound for PocketQube-class systems [29]. This supports the selection of an upper-bound operational altitude of approximately 500 km for the PQ8 architecture. It is important to distinguish between orbital lifetime and operational lifetime, where a satellite may remain in orbit for up to five years, it is not necessarily expected to remain fully operational for that entire duration. Nevertheless, this establishes a realistic upper bound for PQ8 system-level specifications.

This trend is reflected in contemporary PocketQube mission planning. The POQUITO PocketQube mission, for example, is being designed for a nominal in-orbit operational duration of approximately 2.8 years, demonstrating that multi-year PocketQube missions are no longer aspirational but are being formally baselined in current projects [97].

Multi-year operational capability has also been demonstrated in flight. The Delft-PQ (3p PocketQube) mission, launched in January 2022, remained operational until its de-orbit in early 2024, achieving nearly two years of sustained in-orbit functionality [98]. This provides clear evidence that PocketQubes are no longer intrinsically limited to

weeks-to-months operational timescales and that operational lifetimes of around two years are already achievable in practice.

Taken together, these developments support the use of a 2 - 5 year operational lifetime as a realistic design envelope for new PocketQube-class satellite missions. Where approximately 2 to 3 years of operation is now being actively targeted and demonstrated, while around five years represents a plausible upper bound as subsystem maturity continues to improve. It is this recent maturation of PocketQube systems that makes extended mission concepts such as PQ8 both feasible and timely, and may explain why architectures of this type have not previously been explored in comparable depth.

In the absence of a mission-specific objective, the target configuration adopted for validation is defined as an equal in-plane angular spacing of eight PocketQube units around a single orbital plane. This configuration represents a worst-case dispersal scenario in terms of both required relative phasing and total separation time. The dispersal method is considered successful if the satellites:

- Achieve positive and controlled relative separation following mechanical disengagement from the PQ8 structure.
- Maintain predictable evolution of relative angular spacing using differential atmospheric drag as the sole control mechanism.
- Converge toward the target evenly spaced configuration within a time frame on the order of weeks to months, which is short relative to a typical LEO mission lifetime of 2 – 5 years.

Based on the above scope, the validation of the PQ8 dispersal method is assessed against the following feasibility-oriented criteria:

- Controlled separation: verification that all satellites disengage and achieve increasing relative angular separation without re-contact or clustering.
- Configuration convergence: demonstration that the constellation evolves toward an evenly spaced in-plane distribution.
- Temporal viability: confirmation that convergence occurs on a timescale compatible with long-duration LEO missions, despite conservative atmospheric conditions.

If these criteria are satisfied under the assumed worst-case conditions, the dispersal concept is considered feasible for a broad range of lower-altitude and less conservative deployment scenarios. The specifications and constraints critical to the dispersal method are collated in Table 4.1.

Table 4.1: Dispersal Method Specifications

Domain	Specification	Value / Range	Source / Rationale	Relevant Chapters
Orbit	Altitude	350 – 500 km	Mission design	Chapter 4
Orbit	Inclination	As per launch	Launch constraint	Chapter 4
Deployment	Initial relative velocity	Simulation Output	Disengagement Mechanism limit	Chapters 4, 7
Lifetime	Operational lifetime	2 – 5 years	PocketQube capability trend	Chapter 4
Propulsion	Onboard propulsion	None	PQ1 design constraint	Chapter 3
Attitude	Attitude control	Magnetorquers + wheels	PQ1 capability	Chapter 3
Mass	PQ1 mass	~250 g	System design	Chapter 3
Volume	PQ1 volume	PocketQube scale	Architecture definition	Chapter 3
Power	Average available power	~288 mW	Power budget	Chapter 3

4.2 Selection of dispersal strategy

A range of potential dispersal strategies were considered for small satellite constellation dispersal, including impulsive separation, onboard propulsion, electromagnetic or tether-based methods, differential drag, and hybrid approaches. These options are compared in Table 2.1 (presented in Chapter 2), based on feasibility within the system-level specifications defined above. The dominant constraints are:

- No onboard propulsion capability,
- Limited power and volume,
- Requirement for long-term passive separation,
- Desire to minimise mechanical and operational complexity.

Under these constraints, most active dispersal methods become infeasible. Onboard propulsion is excluded by mass, volume, and power limits. Continuous low-thrust solutions are incompatible with available energy. Complex mechanical or tether-based systems introduce unacceptable risk and integration burden at PocketQube scale.

Analysis of different passive dispersal methods in the literature review resulting in differential drag as the best candidate solution for the PQ8 architecture. Differential drag, in contrast to propulsive methods, exploits an environmental force that is already

present and requires no additional propellant. It relies only on attitude control, which is already required for mission operation, and scales favourably to very small satellites.

Therefore, the decision logic can be summarised as:

1. Define system-level dispersal constraints (Table 2.1),
2. Eliminate methods incompatible with mass, power, and complexity limits,
3. Select the only method satisfying all constraint.

Following this logic, differential drag emerges as the most viable concept through process of elimination, as opposed to an optimisation study between all viable methods

4.3 Defining The Dispersal Problem

The dispersal problem is formulated within the context of a many-in-one satellite system, wherein a complete constellation is launched as a single, integrated structure and subsequently separated in stages until full deployment is achieved. This formulation does not impose restrictions on the number or size of the constituent satellites but operates under a set of simplifying assumptions to facilitate analytical modelling and scalability. Specifically,

1. Satellites are cube-shaped,
2. Satellites are identical in terms of external surface properties, mass, and shape,
3. Constellation orbit is circular or quasi-circular,
4. Constellation size follows 2^x, where x is a positive real integer,
5. No onboard propulsion,

The first three assumptions ensure that the dispersal behaviour remains scalable and predictable across a range of constellation sizes. The fourth standardises the dynamics of the disengagement process at each deployment stage. The final assumption is not intended to limit applicability, but rather to establish a baseline case from which the efficacy of passive control methods can be evaluated. In practice, the presence of propulsion would relax some of the constraints and provide additional control authority, but would also introduce further complexity in optimisation and design.

4.3.1 Notation and Convention

To ensure consistency throughout the analysis, a standardised notation system is adopted. Satellites and deployment stages are indexed systematically, with Table 4.2 providing a complete summary of the symbols and conventions used.

Table 4.2: Dispersal Notations and Descriptions

Symbol	Description
k	Deployment stage index ($k = 0, 1, \dots, k_{max}$)
n	Total number of satellites. $n = 2^x \; with \; x \in N$
$S_{k,0}$	Reference satellite at stage k
$S_{k,i}$	i^{th} satellite at stage k from $S_{k,0}$ by proximity.
$\theta_{k,i}$	Angular separation between $S_{k,i}$ and $S_{k,0}$

Deployment Stages: Stages are indexed by k, where $k = 0$ at initial deployment when all satellites are combined as a single unit. The current stage increments occur following the disengagement manoeuvre of satellites in the previous stage. Full deployment is reached at $k = k_{max}$, where $k_{max} = \log_2 n$, and n is the total number of satellites.

*Satellite Indexing***:** At each Stage k, one satellite is designated as the reference satellite, denoted $S_{k,0}$. The remaining satellites are indexed based on their initial proximity to the reference satellite: $S_{k,1}, S_{k,2} \dots S_{k,m}$, where $m = 2^k - 1$. By convention, the reference satellite begins in low-drag mode, while the others adjust their drag profiles for phasing.

Angular Separation: Differential drag control is based on angular separation dynamics. The relative position of each satellite in a given stage is defined by its angular separation $\theta_{k,i}$ from the reference satellite $S_{k,0}$, where $i = 1, 2, \dots, m$. The rates of change are denoted by $\dot{\theta}_{k,i}$ (angular velocity) and $\ddot{\theta}_{k,i}$ (angular acceleration).

Disengagement Mechanics: The separation mechanism imparts a differential velocity change (Δv) to the two resulting satellites, with one receiving $+\Delta v$ and the other $-\Delta v$. The satellite experiencing the most consecutive negative Δv instances across stages is designated as the reference. By convention, satellites with odd i values ($i = 1, 3, ...$) receive $+\Delta v$, while even-indexed satellites receive $-\Delta v$.

4.3.2 Disengagement Sequence

For a constellation comprising *n* satellites, deployment begins with a single integrated structure that undergoes a controlled, multi-stage disengagement process to achieve the desired spatial distribution. A stepwise approach minimises collision risks while leveraging aerodynamic forces for passive positioning.

Through k_{max} successive separation events at perigee passes, the system transitions from a many-in-one satellite to a fully deployed constellation. At each deployment stage *k*, every satellite from the previous stage undergoes a disengagement

manoeuvre, increasing the total number of satellites to 2^k until the final configuration of n satellites is reached. Each phase is followed by a controlled phasing period using differential drag to gradually shape the constellation. Figure 4.1 illustrates a three-stage sequence. The disengagement process is outlined as follows:

1. Initial Deployment**:** The satellite system is deployed as a single unit made up of *n* satellites.
2. First Disengagement **(**$k = 1$): Upon reaching the first perigee following the disengagement command, the primary unit undergoes a disengagement manoeuvre. This process results in the formation of two distinct sub-units.
3. First Sub-Unit Phase**:** Following the initial disengagement, the two newly formed sub-units undergo a controlled phasing process, gradually achieving a predefined in-plane separation angle.
4. Subsequent Disengagement Sequences **(** $k = 2, 3, \dots, k_{max}$ **):** Following the phasing process and at the subsequent perigee pass, each satellite from the previous stage undergoes a disengagement manoeuvre, progressively increasing the total number of orbiting satellites to 2^k. Following each disengagement, each sub-unit is phased to a predefined in-plane separation angle.
5. Final Disengagement at **(**$k = k_{max}$): At the last deployment stage, each of the satellites from the previous phase undergoes a final separation, completing the deployment and reaching the total constellation size *n*.
6. Final Phasing and Constellation Formation: With all *n* satellites deployed, one is designated as the reference unit, while the remaining $n - 1$ satellites are phased into their final constellation configuration using differential drag control to achieve the desired spatial distribution with respect to the designated reference.

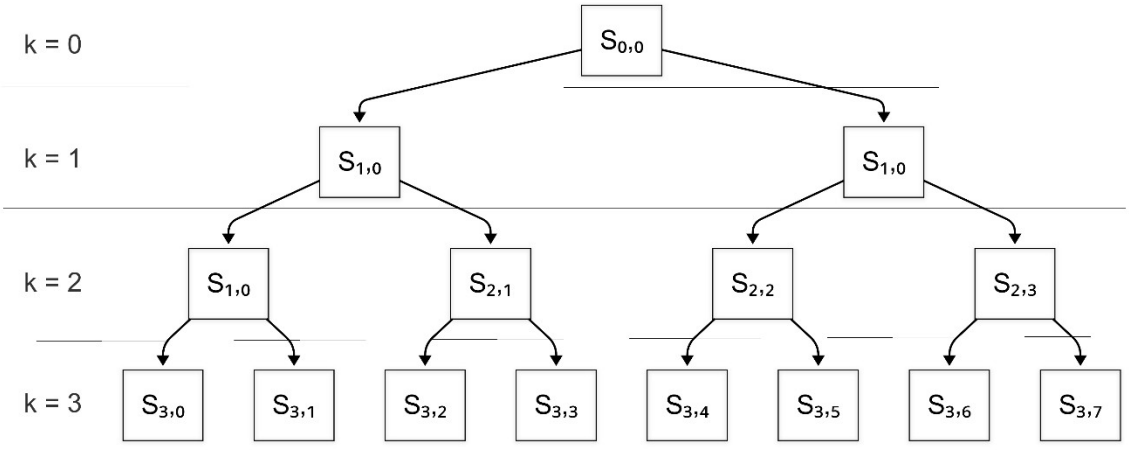

Figure 4.1: Multi-stage Satellite Deployment with $k_{max} = 3$.

For a PQ8 constellation, i.e. $n = 8$ satellites, the deployment follows a $k_{max} = 3$ stage disengagement process, beginning with the initial launch of a PQ8 satellite. At $k = 1$, upon reaching perigee, the primary unit undergoes its first disengagement manoeuvre, splitting into two PQ4 satellites. At $k = 2$, each PQ4 satellite undergoes a second disengagement, resulting in the formation of four PQ2 satellites. Finally, at $k = 3$, each PQ2 satellite undergoes a final disengagement, creating the full set of eight PQ1 satellites.

Following this final separation, a PQ1 satellite is designated as the reference, while the remaining satellites are phased using differential drag control to achieve the desired constellation configuration.

4.3.3 The Disengagement Manoeuvre

The disengagement manoeuvre constitutes a critical step in the staged deployment sequence. At each deployment stage, the parent satellite splits into two smaller daughter units, progressing the system to the next stage of constellation expansion. This mechanical separation imparts a differential velocity, Δv, between the resulting satellites, which serves both to increase their spatial separation and to initiate differential orbital dynamics for subsequent phasing.

Each disengagement applies an equal and opposite velocity increment: one satellite receives a $+\Delta v$, while the other receives a $-\Delta v$, typically along the orbital velocity vector. This alters the orbital energy of both satellites. The one receiving $+\Delta v$ gains energy and transitions to a slightly higher orbit. In contrast, the one receiving $-\Delta v$ experiences a reduction in energy and moves to a slightly lower orbit. Given the inverse relationship between orbital energy and the semi-major axis, this velocity change produces a divergence in mean motion between the satellites, leading to a gradual increase in angular separation over time. To maximise phasing efficiency, the change in orbital energy ΔE must also be optimised, derived from the vis-viva equation:

$$\Delta E = \frac{1}{2}\Delta v^2 + v_0\,\Delta v\cos(\alpha)$$

where v_0 is the orbital velocity at the point of disengagement, and α\alphaα is the angle between the imparted Δv vector and the local velocity vector. A value of $\alpha = 0$ corresponds to a purely tangential disengagement, while $\alpha = \pi/2$ represents a radial separation. Since the term $v_0\ \Delta v\ cos(\alpha)$ dominates, maximum energy change is achieved by performing the manoeuvre tangentially at perigee, where v_0 is at its highest.

This chapter focuses on determining the appropriate Δv magnitudes to meet these objectives under passive control constraints. The physical implementation of the separation mechanism, including how Δv is generated and controlled, and is then presented in Chapter 5. For now, the modelling assumes that the mechanism can deliver consistent and repeatable impulses with alignment precision sufficient to approximate a purely tangential separation. Variations from this ideal are considered in later sections through the analysis of attitude control uncertainty and its impact on the effective along-track component of Δv.

4.3.4 Satellite Dispersal and Phasing

The phasing strategy adopted in this study draws from the model implemented by Planet Labs for their Dove satellite constellation, adapted and expanded here for a many-in-one deployment architecture [44]. The system is modelled by discretising the Cartesian position and velocity vectors of each satellite in the constellation and transforming them into angular separation states relative to a designated reference satellite. The primary quantities of interest are the angular separation, θ, and its first and second derivatives, $\dot{\theta}$ and $\ddot{\theta}$, which describe the relative angular position, velocity, and acceleration over a discretised 24-hour period, k.

Following disengagement, each satellite undergoes differential acceleration due to drag forces modulated by attitude control. The relative angular acceleration experienced between a satellite and its reference is expressed by Equation 4.1:

$$\ddot{\theta}_k = \frac{3q_{ref,k}}{\bar{a}_{ref}}\left(\frac{1}{\beta_{Min}} - \frac{1}{\beta_{Max}}\right) \tag{4.1}$$

where $\beta = m/sc_D$, $\bar{a}_{ref}$ is the mean semi-major axis of the reference satellite and $q_{ref,k}$ is the mean dynamic pressure over the discretised period k given by $q_{ref,k} = \frac{1}{2}\overline{\rho v^2}$. The angular acceleration, $\ddot{\theta}_k$ serves as the control variable, providing either acceleration or deceleration between a satellite and reference pair. It is controlled through the attitude determination and control system (ADCS) commands using a binary control scheme, in which the satellites orient themselves to align with either β_{Max} and β_{Min}, corresponding to low-drag and high-drag mode ballistic coefficients, respectively.

This control strategy effectively divides the phasing period into two intervals: an acceleration phase Δt_a, during which the angular separation increases, and a deceleration

phase Δt_b during which the relative motion is arrested to achieve the desired final separation. The total phasing time is minimised by optimising the duration of these intervals.

Foster et al. also provide an analytical solution for the two-satellite phasing problem in [44], which is directly applicable to each satellite-reference pair in this deployment strategy. For a given pair with initial and final states defined by $\left[\theta\ \dot{\theta}\right]_0^T$ and the desired final relative motion $\left[\theta\ \dot{\theta}\right]_f^T$, then the optimal switching times are given by Equations 4.2 and 4.3:

$$\Delta t_B = \frac{\Delta\dot{\theta} - \ddot{\theta}_A \Delta t_A}{\ddot{\theta}_B} \tag{4.2}$$

$$\left[\frac{1}{2}\ddot{\theta}_A\left(\frac{\ddot{\theta}_A}{\ddot{\theta}_B} - 1\right)\right]\Delta t_A^2 + \left[\dot{\theta}_0\left(\frac{\ddot{\theta}_A}{\ddot{\theta}_B} - 1\right)\right]\Delta t_A + \left[\Delta\theta - \frac{\Delta\dot{\theta}}{\ddot{\theta}_B}\left(\dot{\theta}_0 + \frac{1}{2}\Delta\dot{\theta}\right)\right] = 0 \tag{4.3}$$

Where $\ddot{\theta}_A = \ddot{\theta}$, $\ddot{\theta}_B = -\ddot{\theta}$, $\Delta\theta = \theta_f - \theta_0$ and $\Delta\dot{\theta} = \dot{\theta}_f - \dot{\theta}_0$. The solution is the $\Delta t_a and\ \Delta t_b$ that provide positive, real roots for the given relative motion and angular acceleration.

In a many-in-one system, the total phasing process begins immediately after separation from the launch vehicle at $k = 0$, and continues through each deployment stage ($k = 1, 2, \ldots, k_{max} - 1$). Each stage consists of a disengagement manoeuvre followed by a phasing interval governed by Equations 4.2 and 4.3. The phasing duration of each stage is thus determined by the sequence of initial and final angular states, which evolve recursively based on the disengagement history and aerodynamic control strategy.

Starting from Stage 1, the problem consists of two satellites, $S_{1,0}$ and $S_{1,1}$. The reference satellite will enter low-drag mode first, allowing $S_{1,1}$ to accelerate by some value, $\ddot{\theta}_{1,1}$, until $\left[\theta_{1,1}\ \dot{\theta}_{1,1}\right]_f^T$ is reached. At the next perigee pass, both satellites perform a disengagement manoeuvre, which results in four satellites. This includes $S_{2,2}$ and $S_{2,3}$ that previously formed $S_{1,1}$, as well as $S_{2,0}$ and $S_{2,1}$, which previously formed $S_{1,0}$. This process repeats until the final configuration of *n* satellites is reached. In the final stage, drag configuration is no longer prescribed by convention but instead determined analytically for each satellite using the phasing equations above.

The multiple disengagement pathways from the original unit produce distinct sequences of angular states, resulting in several phasing branches. For example, in an 8-satellite system, four primary branches emerge, each corresponding to a unique disengagement lineage:

- Branch 1:
  - $S_{0,0} \rightarrow S_{1,1} \rightarrow S_{2,3} \rightarrow S_{3,6}$,$S_{3,7}$
  - $S_{0,0} \rightarrow S_{1,1} \rightarrow S_{2,2} \rightarrow S_{3,4}$,$S_{3,5}$
- Branch 2: $S_{0,0} \rightarrow S_{1,0} \rightarrow S_{2,1} \rightarrow S_{3,2}$,$S_{3,4}$
- Branch 3: $S_{0,0} \rightarrow S_{1,0} \rightarrow S_{2,0} \rightarrow S_{3,1}$
- Branch 4: $S_{0,0} \rightarrow S_{1,0} \rightarrow S_{2,0} \rightarrow S_{3,0}$

The phase plots demonstrating these four branches are depicted in Figures 4.2 and 4.3. Solving the phasing times in Branch 1 involves the most complexity, as the initial conditions of each stage are heavily dependent on the final conditions of the previous stage. In Branch 2, this complexity decreases because the solution becomes insensitive to the final conditions of Stage 1 (i.e., $k = 1$). This occurs because, regardless of the time spent phasing $S_{1,1}$, $t_{k=1}$, the initial separation angle of the satellites in Stage 2 will always be zero, with its rate of change determined by the disengagement Δv and the orbital velocity at disengagement.

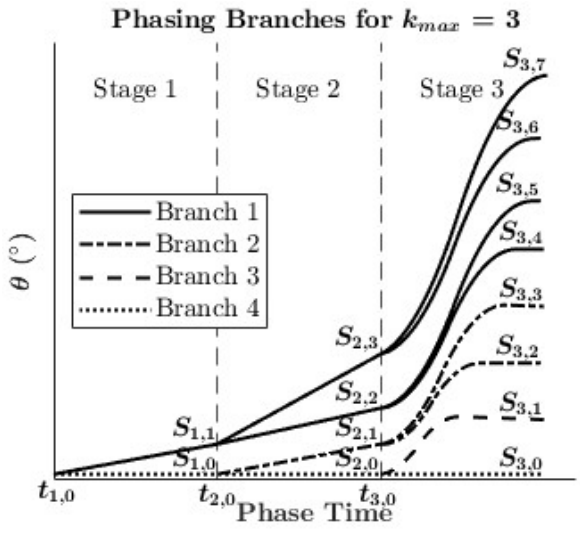

Figure 4.2: Plot showing phasing branches

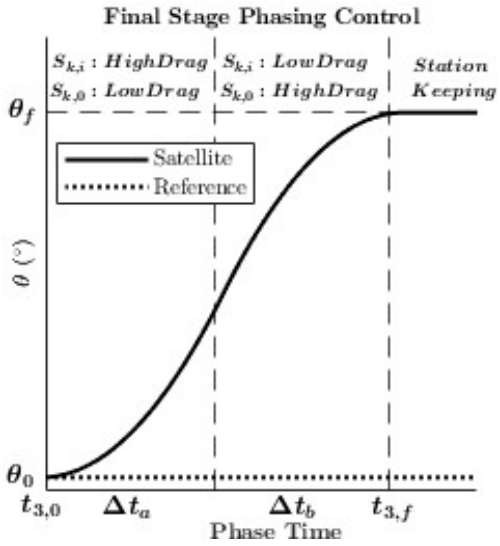

Figure 4.3: Phasing of the final stage satellite

In Branch 3, this insensitivity extends to include the final conditions of Stage 3. Lastly, Branch 4 requires no consideration, as the initial and final conditions are always $[\theta\ \dot{\theta}] = [0\ 0]$ by definition. In other words, the optimal solutions for $S_{3,4-7}$ determines the value of $\theta_{1,1}$, and the optimal solution for $S_{3,2-7}$ determines their respective $\theta_{2,i}$.

As the number of satellites increases, the disengagement sequence becomes increasingly complex. While the fundamental mathematical formulation remains consistent, the computational complexity grows due to the increased number of interactions and constraints that must be resolved. Specifically, the number of cases to analyse follows a logarithmic relationship, increasing with $(1 + \log_2 n)$. This rise in complexity is not primarily due to more intricate mathematical models but rather the greater computational effort required to process and optimise the disengagement sequence efficiently.

4.3.5 The Optimisation Problem

The objective of the optimisation problem is to minimise the total phasing time, $t_{phasing}$, which depends on the time spent in each deployment stage. Since, as shown in Equations 4.2 and 4.3, phasing times are governed by the initial and final relative motion of each satellite-reference pair. The total phasing time is expressed as:

$$t_{phasi} = \sum_{k=1}^{k_{max}} t_k$$

where t_k denotes the phasing time at stage k.

Since the final angular configuration of the constellation is a known mission requirement, the problem is approached in a bottom-up manner. That is, the final conditions at the stage $k = k_{max}$, are specified as $\left[\theta_{k_{max},i}\ 0\right]_f^T$, where θ_{k_{max},i_f} denotes the target angular position of the i^{th} satellite within the range $[0, 360)$.

The initial conditions of Stage k_{max} are determined by the angle at which disengagement occurs in the previous stage, $k = k_{max} - 1$, and the change in the relative motion due to the disengagement Δv. Specifically,

$$\theta_{k_{max},i_0} = \theta_{(k_{max}-1),i_f}\ \ and\ \ \dot{\theta}_{k_{max},i_0} = \dot{\theta}_{(k_{max}-1),i_f} + \Delta\dot{\theta}_{DM}$$

where $\Delta\dot{\theta}_{DM} = f(\Delta v_{DM})$. Consequently, $\left[\theta_{k_{max}-1,i}\ \dot{\theta}_{k_{max}-1,i}\right]_f^T$ represents the final relative motion of the penultimate stage. The recursive nature of this process means that for each stage $k = 2, \dots, k_{max}$ the outcome of the preceding stage directly influences the initial conditions.

For stage $k = 1$, the initial relative motion is determined solely by the disengagement Δv as the initial separation angle will always be zero, therefore $\theta_{1,1_0} = 0$ $and\ \dot{\theta}_{1,1_0} = \Delta\dot{\theta}_{DM}$.

The optimisation thus becomes a cascaded variant of the Foster et al. phasing model, extended to account for the velocity offsets introduced by the staged disengagements. Considering the case of an 8-satellite constellation requiring 3 deployment stages $(k = 3)$, the phasing problem would require solving for the variables collated in Table 4.3.

Each satellite-reference pair at a given stage has its own initial and final state vectors, as well as a unique $\Delta\dot{\theta}_{DM}$. For a known Δv and desired $\left[\theta_{k_{max},i}\ 0\right]_f^T$, the objective is to determine the optimal values of θ_{k,i_f} and $(\Delta t_a, \Delta t_b)_{k_{max}}$, that minimise t_{phasi} across the entire deployment scenario.

Table 4.3: Phasing Problem Variables (*k = 3*)

Variable	Initial Value	Final Value	Comments
$\theta_{1,1}$	0	TBD	Final value is an optimisation variable
$\dot{\theta}_{1,1}$	$\Delta\dot{\theta}_{DM_{k=1}}$	Depends on θ_{1,i_f}	Final value is coupled with $\theta_{1,i}$
$\theta_{2,i}$	θ_{1,i_f}	TBD	Final value is an optimisation variable
$\dot{\theta}_{2,i}$	$\dot{\theta}_{1,i_f} + \Delta\dot{\theta}_{DM_{k=2}}$	Depends on θ_{2,i_f}	Final value is coupled with $\theta_{2,i}$
$\theta_{3,i}$	θ_{2,i_f}	[0, 360)	Final value depends on the satellite slot
$\dot{\theta}_{3,i}$	$\dot{\theta}_{2,i_f} + \Delta\dot{\theta}_{DM_{k=3}}$	0	
$\ddot{\theta}_{1,i}, \ddot{\theta}_{2,i}, \ddot{\theta}_{3,i}$	-		Orbit-dependent, calculated during simulation
$\Delta\dot{\theta}_{DM}$	$f(\Delta v_{DM})$		Calculated during simulation, for different Δv

4.3.6 Other Considerations

The state vector, $\left[\theta\ \dot{\theta}\right]_0^T$, defines the initial relative motion between satellite pairs, where θ_0 represents the initial angular separation and $\dot{\theta}_0$ is its rate of change. The angular separation is determined geometrically from the cross product of the satellites' position vectors, while the angular rate arises from their relative velocities. As demonstrated by the QB50 mission in [36], these values are typically influenced by the sequence and direction of deployment, particularly when multiple satellites are released simultaneously from a deployer.

However, in the context of a many-in-one architecture such as the PQ8, the deployment sequence becomes less consequential unless multiple such units are launched concurrently. Instead, the initial relative motion is primarily governed by the disengagement sequence and the resulting Δv values imparted to each satellite.

Despite this shift in dependence, the orbital parameters at deployment remain critical, particularly due to their impact on atmospheric drag. The effectiveness of differential drag phasing is directly influenced by variations in atmospheric density, which is itself a function of orbital altitude, eccentricity, and solar activity. Lower altitudes and near-circular orbits tend to produce higher mean densities, while high eccentricities or low solar flux reduce the available drag forces. Moreover, solar activity increases atmospheric density at a given altitude, thereby enhancing differential drag.

Consequently, these factors affect the mean dynamic pressure encountered by the satellites, which in turn governs the available angular acceleration $\ddot{\theta}$ for differential drag-based phasing. From a mission design standpoint, the phasing strategy is most effective when systems are deployed into low-altitude, circular orbits during periods of elevated solar activity. These conditions maximise dynamic pressure and minimise phasing time, thereby improving the efficiency of the proposed deployment method.

4.3.7 Problem Summary

In summary, the optimisation of phasing for the proposed deployment architecture requires careful consideration of several interdependent factors: the initial orbit, the disengagement manoeuvre, the differential drag-based dispersal strategy, and the sequential deployment procedure. The initial orbit serves as a mission design variable and is constrained by launch availability and mission objectives. Given a specific initial

orbit, the phasing must be optimised to meet the final angular configuration of the constellation.

The desired final angular states, represented by $\left[\theta_{k_{max},i}\ 0\right]_f^T$, define the constellation's operational configuration. Optimising the deployment process involves determining the disengagement Δv, the angular positions θ_{k,i_f}at intermediate stages, and the corresponding acceleration and deceleration periods $(\Delta t_a, \Delta t_b)_{k_{max}}$, for each satellite. These variables collectively minimise the total phasing time while ensuring a collision-free and energy-efficient dispersal trajectory.

As established in the preceding sections, the phasing problem is inherently recursive: the final conditions at each stage are shaped by the initial conditions and dynamics of the previous one. Therefore, optimisation must proceed in a bottom-up fashion, beginning from the known final configuration and propagating backwards through the deployment tree. This requires identifying the optimal insertion points at stage $k_{Max}$and determining the conditions under which each satellite should disengage and begin phasing. Once the optimal set of intermediate angular states and disengagement velocities is identified, the total phasing time is obtained by summing the durations across all stages.

This formulation captures the entire deployment-dispersal process, providing a deterministic framework that links mission-level parameters to individual satellite control decisions. The following section outlines the specific methodology used to solve this optimisation problem efficiently

4.4 Methodology for Optimising Dispersal

As shown in Table 4.2, the optimisation variables, θ_{k,i_f} (from $k = 1\ to\ k_{max} - 1$) and $(\Delta t_a, \Delta t_b)_{k_{max}}$, increase in complexity with each deployment stage. However, this complexity is mitigated by assumptions regarding satellite uniformity. Specifically, each disengagement stage reduces satellite mass and surface area by half, while the drag coefficient remains constant. As a result, the maximum and minimum ballistic coefficients $\beta_{\mathrm{Max}}\ and\ \beta_{\mathrm{Min}}$ remain unchanged across the early stages, ensuring that the angular acceleration $\ddot{\theta}$ remains constant during those phases.

Given this consistency, satellites with identical orbital parameters will phase at similar rates. However, due to the cumulative effects of disengagement Δv, satellites in

later stages begin with greater relative separation rates. Therefore, initiating disengagements early is favourable, provided sufficient phasing time is available to prevent collisions. This observation significantly simplifies the optimisation problem, reducing it to the identification of the optimal values of $\theta_{(k_{max}-1),i_f}$ and the final-stage timing parameters $(\Delta t_a, \Delta t_b)_{k_{max}}$.

If the assumptions on satellite properties do not hold, the above conclusion remains valid as long as the difference between the inverse ballistic coefficients (see Equation 4.2) does not decrease across stages. Should this difference diminish, an alternative optimisation approach may be required.

The values of $(\Delta t_a, \Delta t_b)_{k_{max}}$ are determined analytically for each satellite-reference pair using Equations 4.2 and 4.3 Since the final angular separations are predefined by the target constellation, the control authority, $\ddot{\theta}$, is updated throughout the simulation, the unknowns reside in the initial conditions at stage k_{max}, which are derived from the preceding stage. This is achieved by generating a set of candidate insertion points for each satellite at the penultimate stage. To resolve this, the phasing problem is reformulated as identifying the set of insertion angles $\theta_{(k_{max}-1),i_f}$ that minimise the total phasing time. These are produced by phasing each satellite to reach discrete angles $\theta \in \{0, \Delta\theta, 2\Delta\theta, \ldots, 360\}$, followed by the application of a disengagement Δv. This process is summarised in Algorithm 4.1, which outputs the corresponding initial relative motions and associated timing data $t_{(k_{max}-1),i}$.

Subsequently, Algorithm 4.2 computes the phasing durations $(\Delta t_a, \Delta t_b)$ for each candidate insertion point using the analytical solution. The optimal combination is the one that minimises the sum of Δt_a, Δt_b and their respective $t_{(k_{max}-1),i}$. This process is repeated for all $n-1$ satellites in the final deployment stage.

The longest of these values defines the final phasing time for the constellation, as it represents the slowest-converging satellite relative to the reference. This value is then used to determine the final phasing segment for the last satellite-reference pair.

For instance, in the case of the PQ8 Architecture, with a system of eight satellites and $k_{max} = 3$, the output will consist of optimal values for $t_{2,1}$, $t_{2,2}$, and $t_{2,3}$, calculated for satellites $S_{2,1}, S_{2,2}$ *and* $S_{2,3}$, covering the critical branches from Section 4.1.4. The largest among them defines the final stage's reference timing.

Algorithm 4.1: Generate Stage $\boldsymbol{k_{max}}$ Insertion Points

1: **Procedure: Generate Stage $\boldsymbol{k_{max}}$ Insertion Points**
2: Propagate $S_{0,0}$ until the first disengagement command.
3: Perform $S_{0,0}$ disengagement manoeuvre to obtain $S_{1,1}$ and $S_{1,0}$
4: **for** $k = 1; k < k_{max} - 1; k$++, **do**
5: Propagate $S_{k,i}$ by t_k and to the next perigee
6: Perform $S_{k,i}$ disengagement manoeuvres to obtain $S_{k+1,j}$
7: end for
8: **for** $i = 1; i < 2^{k_{max}-1}; i$++, **do**
9: **for** $\theta_{(k_{max}-1),i} = 0;\ \theta_{(k_{max}-1),i} < \theta_{(k_{max}-1),i\,max};\ \theta_{(k_{max}-1),i} + \Delta\theta$, **do**
10: Propagate $S_{(k_{max}-1),i}$ until $\theta_{(k_{max}-1),i}$, store $t_{(k_{max}-1),i}$
11: Perform $S_{(k_{max}-1),i}$ to $S_{(k_{max}),j}$ disengagement manoeuvre
12: Calculate $S_{(k_{max}),j}$ initial relative motion (insertion points)
13: end for
14: end for
15: **Output:** $S_{k_{max},j}$ insertion points for every $\theta_{(k_{max}-1),i}$ and associated $t_{(k_{max}-1),i}$

Algorithm 4.2: Calculate Optimal Phasing Times

1: **Procedure: Final Stage Optimal Phase Time**
2: **for** $i = 1; i < n; i$++, **do**
3: Get $S_{k_{max},i}$ Insertion Points from Algorithm 1 Output
4: Get $S_{k_{max},i}$ final angular separation through $\theta_{k_{max},i_f} = 360\left(1 - \frac{1}{n}\right)$
5: **for** number of insertion points, **do**
6: Calculate $(\Delta t_a, \Delta t_b)_{k_{max},i}$ through Equations 4.2 & 4.3
7: Equate $t_{phase,new} = \sum_{k=1}^{k_{max}} t_k$
8: **if** $t_{phase,new} < t_{phase}$
9: $t_{phase} \leftarrow t_{phase,new}$
10 $\theta_{(k_{max}-1),j_f} \leftarrow \theta_{k_{max},i_0}$
11: end if
12: end for
13: end for
14: Compare all $t_{(k_{max}-1),j_f}$, largest value = $t_{(k_{max}-1)}$
15: **Output:** $t_{(k_{max}-1)}$ and $(\Delta t_a, \Delta t_b)_{k_{max},i}$ for $i = 1, 2, \ldots, (n-1)$.

Throughout this process, Δv is assumed constant across all disengagements, scaling proportionally with satellite mass. To determine the optimal magnitude of Δv, Algorithms 4.1 and 4.2 are executed over a range of values. The value yielding the shortest total phasing time is selected as the optimal.

In summary, the optimisation process focuses on minimising the total phasing time, $\sum_{k=1}^{k_{max}} t_k$. Since the ballistic coefficients are constant up to $k = (k_{max} - 1)$, the corresponding phase durations are minimised while ensuring adequate separation. The optimisation thus reduces to identifying the best values for $\theta_{(k_{max}-1),i_f}$ and the final-stage timing parameters $(\Delta t_a, \Delta t_b)_{k_{max}}$, evaluated over a range of Δv values to define the performance envelope of the disengagement mechanism.

4.5 Estimating the Ballistic Coefficients

The ballistic coefficient β is a critical parameter in atmospheric drag modelling and is defined as:

$$\beta = \frac{m}{AC_D}$$

where m is the satellite mass, A the projected surface area, and C_D the coefficient of drag. In the context of differential drag-based constellation phasing, accurate estimation of β is essential, as it directly influences angular acceleration and, consequently, phasing time. While satellite mass and geometry can be measured precisely, C_D introduces the most significant levels of uncertainty.

4.5.1 Theoretical Modelling of Drag Coefficient

The drag coefficient C_D is modelled using the formulation proposed by Moe et al. [61], which accounts for both diffuse and quasi-specular re-emission of incident atmospheric particles. The total drag coefficient is expressed as:

$$c_D = f c_{D,Diffuse} + (1 - f) c_{D,Specular}$$

where f represents the fraction of interactions resulting in diffuse re-emission. In this study, $f = 0.95$ is assumed, consistent with free molecular flow conditions near 500 km altitude.

The diffuse component $c_{D,Diffuse}$ is calculated using Sentman's model for a flat-plate geometry [99]. The total force is then integrated over the surface and flow directions

to obtain the average drag coefficient. For a particle incident at angle β\betaβ, the diffuse drag force per unit area is expressed as:

$$c_d A_{ref} = \frac{P}{\sqrt{\pi}} + \gamma Q Z + \frac{\gamma v_r}{2 v_i} (\gamma \sqrt{\pi} Z + P)$$

where:

- $\gamma = \cos(\phi)$,
- ϕ angle of incidence,
- s is the speed ratio, defined as the satellite velocity relative to the most probable speed of ambient gas molecules,
- v_i is the incident particle velocity relative to the satellite,
- v_r is the most probable velocity of re-emitted particles,
- $P = \frac{1}{s} e^{-\gamma^2 s^2}$,
- $Q = 1 + \frac{1}{2s^2}$,
- $Z = 1 + erf(\gamma s)$, with $erf(x) = \int_0^x \exp(-y^2)\, dy$.

The re-emission velocity v_r accounts for energy exchange between the surface and the incoming particles and is defined as:

$$v_r = \sqrt{\frac{2}{3}} v_i \left[1 + \alpha \left(\frac{E_w}{Ei} - 1\right)\right]^{\frac{1}{2}}$$

where:

- E_i is the average kinetic energy of incident gas particles,
- E_w is the kinetic energy of the re-emitted particles, determined by the satellite's surface temperature,
- α is the energy accommodation coefficient, using Goodman's formula [63]:

$$\alpha = \frac{3.6\, u\, sin(\beta)}{(1+u)^2}$$

with $u = m_{atm}/m_{surface}$, i.e. the ratio of the mass of the incident atmospheric molecule to that of the surface. In this study, the satellite's outer surface is assumed to be composed of solar assemblies, including cover glass, and thus a mean molecular mass of approximately 60 amu is assumed.

The quasi-specular specular component $c_{D,Specular}$ is calculated using the model developed by Schamberg in [100]. In this formulation, a portion of the incident particles

undergo quasi-specular reflection, but with partial accommodation of energy and momentum losses. The quasi-specular drag coefficient for a flat plate is expressed as:

$$c_{D,Specular} = 2(\,1 - rcos(2\theta))$$

where:

- θ is the incidence angle of the particle relative to the surface normal,
- $r = v_{sat}/v_{rms}$ is the ratio of the satellite's orbital velocity to the root-mean-square speed of the ambient gas molecules.

This formulation captures the angular dependence of quasi-specular interactions and allows the drag to vary as a function of satellite orientation, atmospheric conditions and thermal environment.

To compute the drag coefficient across relevant orbital conditions, environmental parameters such as temperature, molecular mass, and atmospheric composition were obtained using the NRLMSISE-00 atmospheric model. These values were derived using the satellite's ephemeris data for representative epochs and orbital altitudes.

The satellite itself is modelled as two flat plates with square cross-sectional geometry held perpendicularly to one another. This simplification enables tractable integration of incidence-angle-dependent drag contributions and is consistent with the geometric configuration of the PQ1, PQ2, PQ4, and PQ8 satellites.

Table 4.4 presents the theoretical ballistic coefficients for the PQ4, PQ2, and PQ1 stages. Two configurations are listed for PQ1. The second entry corresponds to a PQ1 satellite oriented at a 45 ° angle of attack, resulting in the highest ballistic coefficient of the PQ1 configuration, as illustrated in Figure 4.4. This configuration represents the initial baseline design for the final stage of deployment.

However, as demonstrated in the upcoming case studies, the relatively small ratio between the high-drag and low-drag ballistic coefficients in this configuration leads to prolonged phasing times. To address this, an alternative configuration is presented in the first PQ1 entry, featuring a deployable panel that increases the cross-sectional area and raises the ballistic coefficient ratio to 2:1, thereby enhancing differential drag performance.

Table 4.4: PQ8 Ballistic Coefficients

	Maximum		***Minimum***	
Satellite	Ram Surface	β (kg/m^2)	Ram Surface	β (kg/m^2)
PQ4		57.2	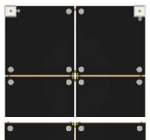	28.6
PQ2		57.2		28.6
PQ1		28.6	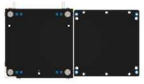	14.3
PQ1*	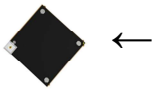	35.7		28.6

**PQ1 with an angle of attack of 45° (Arrow indicates flow direction)*

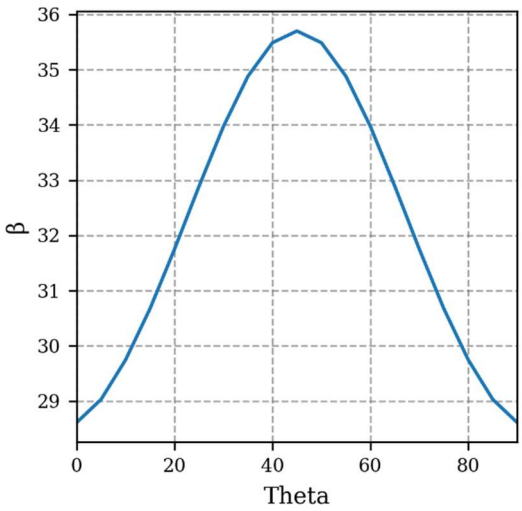

Figure 4.4: Ballistic Coefficient versus angle of attack, theta, for a PQ1 Satellite.

Preliminary attempts were made to validate the theoretical β range using orbit decay data derived from publicly available Two-Line Elements (TLEs). However, the estimation method proved highly sensitive to TLE inaccuracies and insufficiently robust for meaningful analysis. In particular, some results implied drag coefficients as low as 0.5, which are physically implausible for the satellite geometry and altitude considered.

Therefore, the values presented in Table 4.4 correspond to an estimated drag coefficient of 3.48 for a polar orbit at an altitude of approximately 500 km. A review of published literature indicates a broad range of drag coefficients, from 2.3 to 5.5, for satellites of similar shape, size and surface materials, though these are reported under different orbital conditions [44,45]. Additionally, simulations using the ADBSat tool

developed by Sinpetru et al. yield values between 2.86 and 3.03 for the same orbital parameters as those used in Table 4.3 and depending on the chosen drag model [101,102]. Given this variability and the sensitivity of the coefficient to both model assumptions and environmental conditions, it is difficult to identify a universally reliable value. For consistency throughout this work, the model that yielded a coefficient of 3.48 at 0° angle of attack is adopted to provide the nominal references.

4.6 Case Studies

To demonstrate the feasibility of the proposed dispersal method and the impact of disengagement velocity and phase angle selection on optimal phasing times, two case studies are presented. The first case study presents a system of eight PocketQube-sized satellites in an initial configuration resembling a 1U CubeSat. The second presents the case of four 1U CubeSat satellites in a $2 \times 2 \times 1$ initial configuration.

The simulations are performed on MATLAB and make use of the Aerospace Blockset. In both case studies, the initial perigee altitude is 500 km, matching standard rideshare options, with an eccentricity of 0.01. Other orbital elements are set to zero and are summarised in Table 4.5.

The epoch is set during the solar minima of Solar Cycle 25, leading to reduced atmospheric densities and lower differential accelerations, which present the worst-case weather conditions for a dispersal method dependent on drag. For Earth's gravitational model, the EGM2008 spherical harmonic model is applied. Additionally, third-body point masses for the Sun and the Moon are considered. For the atmospheric model, the NRLMSISE-00 atmospheric model is used, with CelesTrak space weather data updated up to 2nd February 2024. The EGM2008 and NRLMSISE-00 models were selected because they were readily available in MATLAB. Additionally, NRLMSISE-00 has become the standard for satellite drag modelling over the last few years [103]. Finally, the effects of Solar Radiation Pressure (SRP) are also simulated, using a dual cone shadow model for eclipse effects.

Table 4.5: Simulation Initial Orbit Setup

Orbital Element	Initial Value
Epoch	1st December 2020
Altitude (Perigee)	500 km
Eccentricity	0.01
Inclination	*Case Study 1:* 90º *Case Study 2:* 63.4º
RAAN	0 º
Arg. of Perigee	0 º
True Anomaly	0 º

4.6.1 Case Study 1: Dispersal of a PQ8 Constellation with Deployable

In the first case study, we examine the PQ8 satellite, and its various configurations as shown in Figure 4.5 (a) to (d). The PQ8 is essentially a 1U CubeSat (10 x 10 x 10 cm^3 with a mass of 2 kg) hierarchically assembled from eight PQ1 satellites. Each PQ1 is formed by slicing the PQ8 in half twice, lengthwise and heightwise, resulting in eight 5 × 5 × 5 cm units, each weighing 250 g, closely resembling a 1p PocketQube.

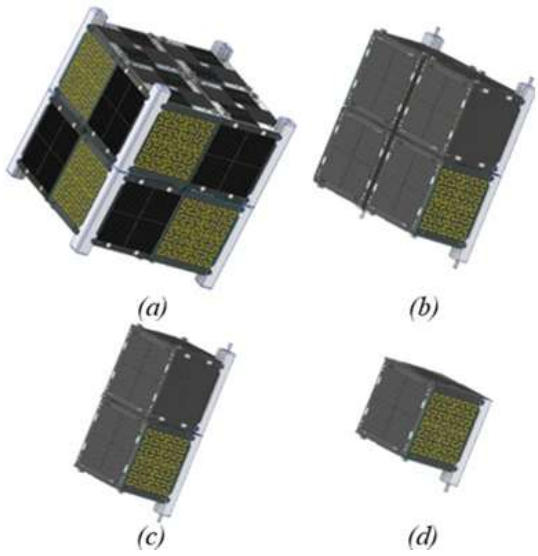

Figure 4.5: (a) PQ8 Satellite (b) PQ4 Satellite
(c) PQ2 Satellite (d) PQ1 Satellite

The deployment sequence follows a staged separation process, forming intermediate configurations: PQ8 → PQ4 → PQ2 → PQ1. The process begins with the PQ8 ($S_{0,0,}$) at $k = 0$, which undergoes an initial disengagement manoeuvre, splitting into two PQ4 satellites ($S_{1,i}$) at $k = 1$. These are phased before further splitting into PQ2 satellites ($S_{2,i}$) at $k = 2$, and finally, eight independent PQ1 satellites ($S_{3,i}$) at $k = 3$.

4.6.1.1 Case Study 1: No Deployables

The initial round of simulations was conducted using the original PQ8 architecture configuration presented in this thesis. In this baseline concept, the high-drag mode satellite was oriented at an angle of attack of 0°, while the low-drag mode satellite was set at 45°. As shown in Figure 4.6, the resulting optimal phasing times exceeded 500 days for a Δv of 0.15 m/s. Attempts to increase Δv led to separation velocities that surpassed the corrective capability of the differential drag controller within the available phasing duration. This caused the relative phase angles to diverge continuously, ultimately compromising formation integrity.

While the simulations confirmed that phasing remained theoretically achievable, the convergence time was impractically long. By approximately 550 days, the satellites were nearing the end of their planned two-year operational lifetime. The primary limitation stemmed from the insufficient difference in ballistic coefficient ratios, which resulted in inadequate control authority for effective phasing. To address this, the original

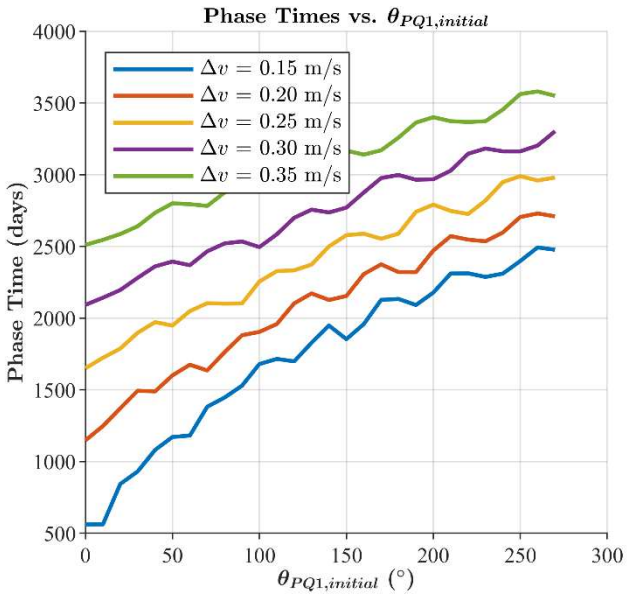

Figure 4.6: Optimal phase times for PQ1 satellites without deployables

concept was revised to incorporate a deployable panel. This addition increased the ballistic coefficient ratio and, more importantly, the difference between their reciprocals as defined in Equation 4.1, thereby enhancing differential drag control and enabling significantly reduced phasing times, as demonstrated in the subsequent sections.

4.6.1.2 Case Study 1: Initial Relative Motion

The initial relative motion between satellites is determined by computing the angle between their position vectors. Depending on the drag configuration, this angle either increases or decreases over time, exhibiting oscillatory behaviour due to orbital variations between apogee and perigee. Figure 4.7 illustrates this behaviour across multiple orbital cycles.

The first and second derivatives of the angular separation yield the relative angular velocity and angular acceleration. To accurately capture the average angular acceleration, values are extracted from extended simulation periods. As shown in Figure 4.7(d), the average converges to a stable value of 0.0103 °/day² after approximately 140 days, despite initial variability.

4.6.1.3 Case Study 1: Disengagement Velocity and Insertion Points

The initial angular velocity of each satellite increases linearly with respect to an increase in disengagement velocity, as illustrated in Figure 4.8. The PQ1s that have experienced multiple positive Δv instances exhibit higher initial separation rates. For example, $PQ1_{7,}$ having undergone three successive positive, shows the highest initial angular velocity. $PQ1_6$, $PQ1_5$ and $PQ1_3$ follow accordingly, while the remainder experienced lower separation rates due to fewer Δv increments.

The insertion points represent the $\left[\theta\ \dot{\theta}\right]_0^T$ values for each PQ1 satellite in the PQ1 phase. These values depend on both the disengagement velocity and the relative positions of the satellites at the time of disengagement, as illustrated in Figure 4.9. The separation rates are grouped similarly to those described by the disengagement velocity in Figure 4.8. Notably, oscillations in the plots highlight the influence of epoch-dependent orbital dynamics.

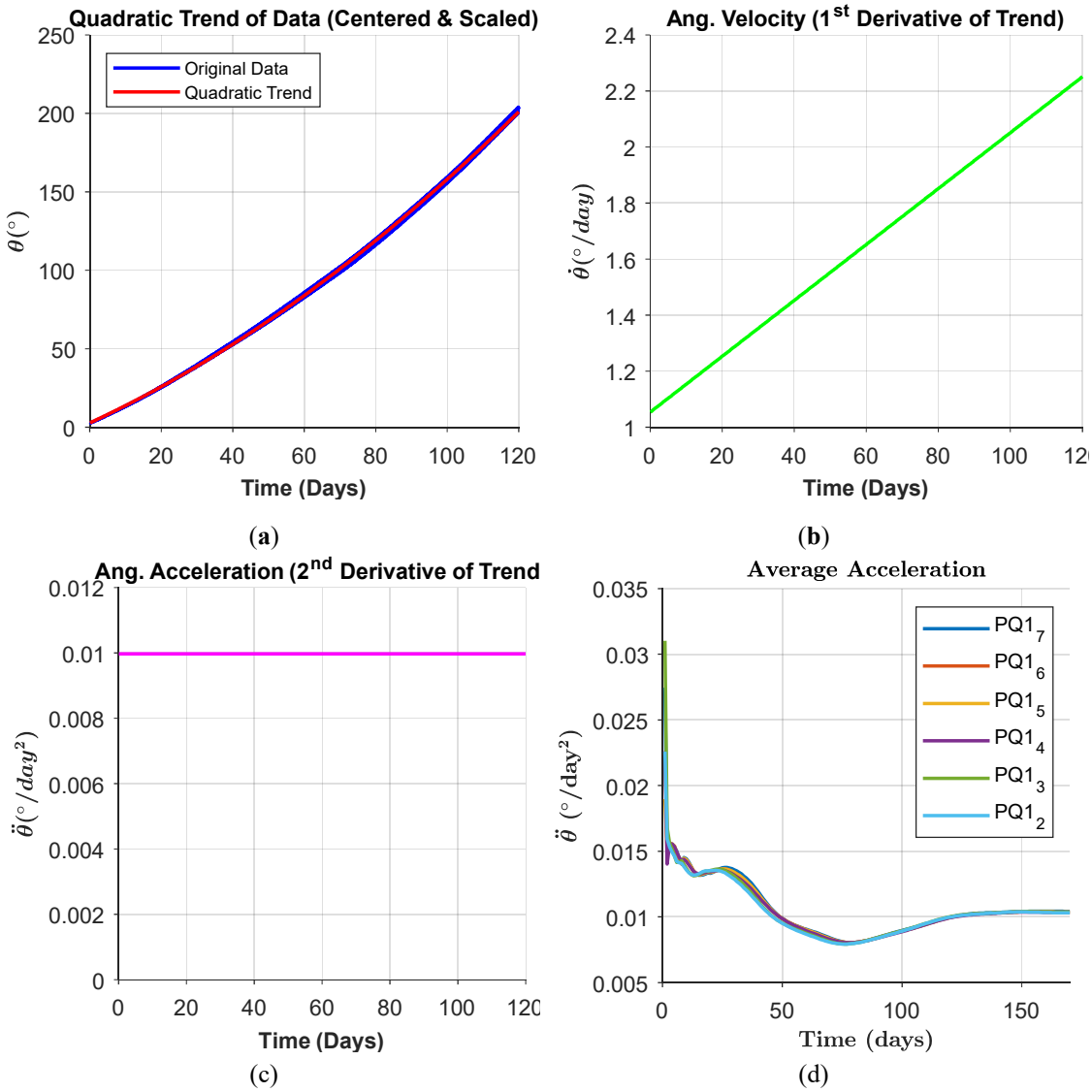

Figure 4.7: (a) PQ Satellite Relative Motion: Relative Angle, (b) Angular Velocity, (c) Angular Acceleration, (d) Average Acceleration

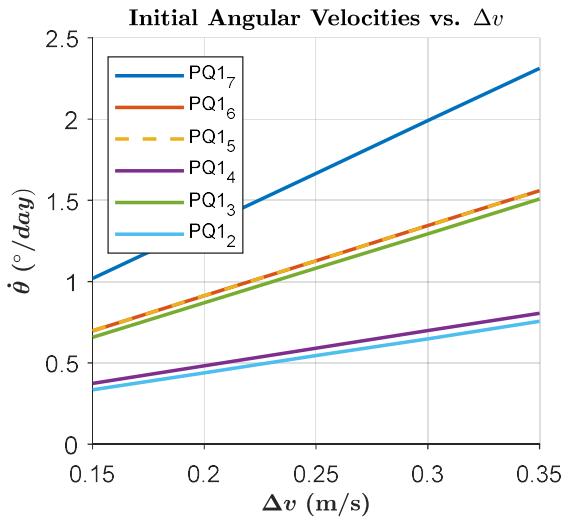

Figure 4.8: PQ1 Initial Angular Velocities

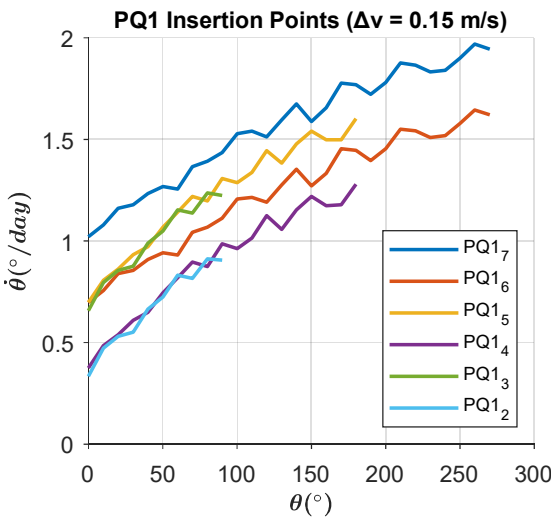

Figure 4.9: PQ1 Insertion Point

4.6.1.4 Case Study 1: Optimal Phase Times

Figure 4.10 illustrates the optimal phase times for $PQ1_7$ across various Δv magnitudes, plotted against the initial angular separation $\theta_{PQ\ ,initial}$. Among these, the plot corresponding to the highest Δv magnitude of 0.35 m/s shows the shortest phase times. All curves begin with a region of low gradient before transitioning into a steeper incline. This initial shallow gradient appears when the reference satellite is the first to adopt the low-drag configuration after disengagement, while the remaining PQ1 remains in high-drag mode. Within the low gradient region, the phasing time is largely insensitive to variations in $\theta_{PQ\ ,initial}$, as reflected by the gentle slope.

However, once $\theta_{PQ\ ,initial}$ exceeds a specific threshold value, $\theta_{PQ1,thresh}$, the gradient steepens significantly. Beyond this point, the reference satellite enters high-drag mode immediately after disengagement, while the counterpart enters low-drag mode, resulting in phase times that are highly sensitive to $\theta_{PQ1,initial}$. At $\theta_{PQ\ ,thres}$, a special condition arises where the acceleration phase is entirely omitted, as the Δv imparted at disengagement alone achieves the peak separation velocity, and only deceleration is needed for optimal phasing.

Since the initial angular rate $\dot{\theta}_i$ is linearly proportional to the disengagement Δv, an increase Δv reduces $\theta_{PQ1,thres}$. For Δv values around 0.4 m/s or greater, the low gradient region disappears entirely. This implies that increasing Δv beyond a certain threshold, Δv_{thres} , ceases to offer viable improvements. For this scenario, Δv_{thres} is approximately 0.4 m/s.

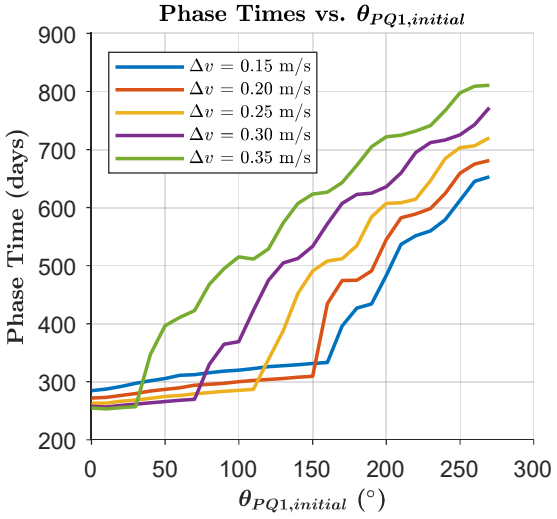

Figure 4.10: Optimal phase times for $PQ1_7$ for various Δv magnitudes

Comparing the plots reveals that increasing Δv, while remaining below Δv_{thres}, yields improved phasing times within the low gradient region. This suggests that optimal phase performance occurs when $\Delta v \approx \Delta v_{\text{thresh}}$, emphasising the trade-off between Δv, total phase time, and the viable range of $\theta_{PQ1,initial}$.

If the optimal Δv ($\Delta v = \Delta v_{\text{thresh}}$) is used, any delay in the PQ2-to-PQ1 disengagement or errors in dispersal rate calculations cause a significant increase in phasing time, as the solution moves into the steep-gradient region. Conversely, for Δv values below Δv_{thresh}, a tolerance window exists in which such delays have minimal impact. This window could be beneficial for accommodating disengagement delays due to collision avoidance or fault recovery manoeuvres, as well as for accounting for modelling uncertainties.

Among the simulated Δv values, 0.35 m/s yielded the shortest phasing time for $PQ1_7$, approximately 255 days. Notably, this value reflects the phasing time of the slowest (i.e., final) satellite, with other satellites achieving their final phase angles earlier, as depicted in Figure 4.11. In these simulations, the total phasing duration was dictated by the time required for $PQ1_7$ to reach its target phase. This observation offers a useful shortcut for future simulations: total phasing performance can be approximated by tracking only the final satellite, denoted $S_{kmax,n-1}$.

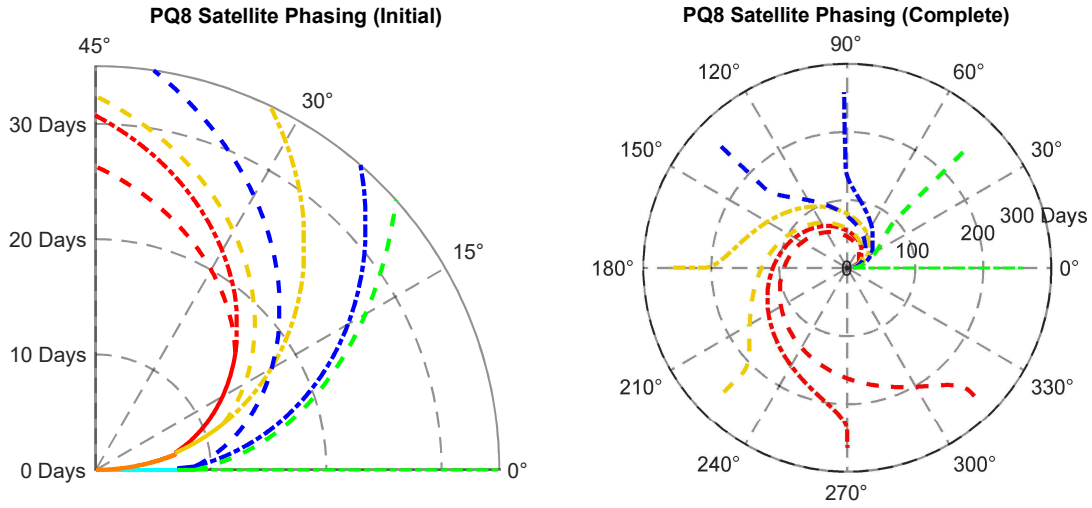

Figure 4.11: (a) Early orbit separation (Note the scaled theta axis) (b) PQ8 Satellite Phasing Polar Plots

To account for drag coefficient uncertainty, a boundary analysis was conducted using literature values ranging from 2.3 to 5.5 [44,45]. Although these values correspond to different orbital conditions, they provide a conservative bracket for the expected variability in phase times. For the minimum drag coefficient, the phase time extends to 311 days at $\Delta v = 0.3$ m/s. With this value, Δv_{thresh} lies between 0.3 and 0.35 m/s, highlighting the sensitivity of the phase times on both the disengagement velocity and drag coefficient values. At the maximum drag coefficient, the phase time shortens to 218 days for the same Δv. Taking this variability into account, the total phase time can be estimated as 255 +56/−37 days.

This analysis assumes ideal attitude control. In practice, Alba Orbital reports that its Unicorn-2 PocketQube achieves a pointing accuracy of approximately 5 ° [104]. In a worst-case scenario where both the reference and active satellites experience this level of pointing error, the ballistic coefficient during the final phase ranges from 14.5 to 29 kg/m². This spread leads to an average angular acceleration of 0.0102°/day² and a corresponding phase time of approximately 256.5 days. The resulting uncertainty in total phase time is ± 1.5 days, relatively minor compared to uncertainties introduced by atmospheric model limitations.

4.6.1.5 Case Study 1: Semi-major Axis Decay and RAAN Drift

Since the system relies on differential drag control, it inherently induces a difference in the semi-major axis between the satellites. This presents two concerns. First, a difference in the semi-major axis leads to a variation in the satellites' mean motion, causing the in-plane phase angle to drift apart. Second, it causes differential nodal precession within the constellation.

The first concern is mitigated by the differential drag control strategy, particularly through the analytical solutions provided in Equations 4.2 and 4.3. These equations are solved to ensure a final angular separation rate $\dot{\theta}$ of zero, which directly correlates with mean motion. Essentially, the differential drag controller reduces the semi-major axis of the higher-altitude satellite at a faster rate than that of the lower-altitude satellites until they converge to approximately the same value. As a result, their mean motions become nearly identical. This effect is illustrated in Figure 4.12, which

Shows the semi-major axis profiles of the leading PQ1 satellite and the reference satellite. Here, the reference satellite, $PQ1_0$, is in high-drag mode, until its mean motion converges with that of $PQ1_7$, which is in low-drag mode.

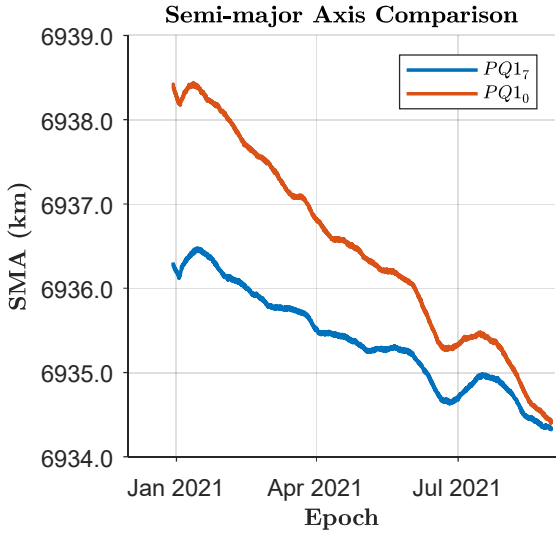

Figure 4.12: Semi-major axis comparison between leading satellite and the reference

The second concern remains valid, as some drift in RAAN between satellites is inevitable when using this method for dispersal. The extent of this drift is strongly influenced by orbital inclination. At high inclinations, particularly near-polar orbits, RAAN drift is minimal and often negligible over typical phasing durations.

However, at lower inclinations, the effect can become more pronounced, with drift reaching several degrees depending on the length of the deployment phase. In general, a shorter phasing period helps minimise this divergence. The degree of RAAN drift that can be tolerated is ultimately mission-dependent. In this context, Falcone et al. proposed a differential drag control scheme that addresses cross-track motion using convex optimisation [52]. If nodal precession poses a concern for constellation geometry or coverage, such schemes can be integrated to help mitigate its long-term impact.

4.6.2 Case Study 2: A 4U CubeSat

In the second case study, a fictitious scenario is considered in which the constellation consists of four 1U CubeSats, collectively referred to as CS4. This scenario is included to illustrate the scalability and general applicability of the proposed dispersal methodology beyond the specific PQ8 implementation. By applying the same analytical framework to a different satellite form factor and unit count, this case demonstrates that the dispersal dynamics are governed primarily by orbital conditions and satellite ballistic properties, rather than by a particular structural standard. The 4 × 1U configuration therefore serves as a representative and familiar reference within the small satellite domain, reinforcing that the PQ8 dispersal strategy constitutes a specific instantiation of a more general approach.

These satellites are initially stacked in a configuration similar to the PQ4 satellite shown in Figure 4.5(b). Each unit, denoted as CS1, has a mass of 2 kg and a deployable panel with an area of 0.01 m^2. Using the same configurations presented in Table 4.4, but scaled for mass and area, yields β_{Max} and β_{Min} of 114.4 and 57.2 $kg.m^{-2}$, respectively, for the CS2 satellites. In the case of the CS1 satellites, the corresponding values are 57.2 and 28.6 $kg.m^{-2}$, respectively.

The deployment strategy begins at the CS4 stage, where the satellite maintains its 4U CubeSat form factor. Its deployment follows a $k_{max} = 2$ stage deployment process, starting with the initial launch of a CS4 satellite at $k = 0$. After an initial disengagement manoeuvre, the CS4 satellite splits into two CS2 satellites, marking the start of the stage $k = 1$ and phased to some degree. The process is repeated one more time, culminating in four CS1 satellites.

4.6.2.1 Case Study 2: Optimal Phase Times

Figure 4.13 illustrates the optimal phase times for $CS1_3$ across various Δv magnitudes relative to $\theta_{CS1,initial}$. The trends closely follow those observed in the PQ8 case study, remaining within a similar range of phase times. This consistency suggests that the proposed algorithms scale reliably across different constellation sizes and configurations. In this case, a Δv magnitude of 0.45 ms^{-1} provided the best phase times of approximately 330 days.

The required Δv magnitude for the disengagement mechanism increased despite the proportional scaling of mass, with Δv_{thres} almost double that of Case Study 1. This increase is attributed to the reduction in the number of disengagement sequences, from the three-stage process in the PQ8 case to the two-stage process in the CS4 study. This trend suggests that as the number of satellites in the constellation increases, the demand on the disengagement mechanism decreases. This outcome is intuitive, as a larger number of satellites results in more Δv instances, distributing the required impulse more effectively. However, when considering Δv_{thres} alongside the collision avoidance

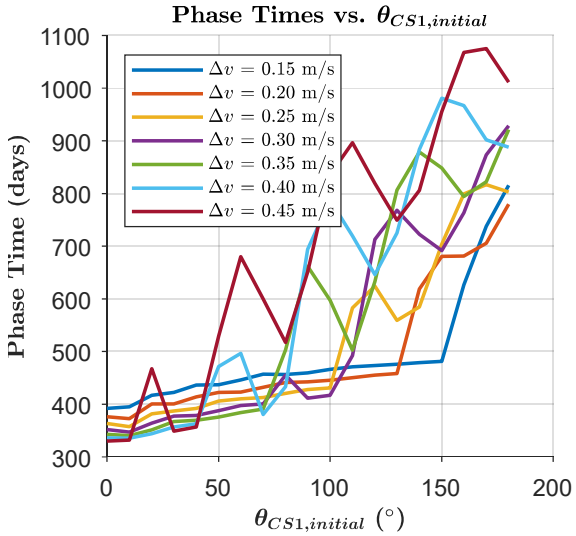

Figure 4.13: Optimal phase times for CS1$_3$

trade-off discussed in the previous case study; it becomes evident that an upper limit exists on the number of satellites in the constellation. Beyond this, Δv_{thresh} falls below the minimum required to prevent collision.

4.6.2.2 Case Study 2: Ballistic Coefficient vs. Phase Times

In both case studies, a single deployable surface was assumed to achieve a ballistic coefficient ratio of 2:1. Increasing the ballistic coefficient, whether through additional deployables or alternative methods, can substantially reduce phase times. For instance, if all four sides of the cube-shaped satellites were deployable, a ballistic coefficient ratio of 5:1 would be achieved, leading to significantly improved phase times, as illustrated in Figure 4.14. Moreover, this benefit could be further enhanced, as the analysis does not consider the potential increase in disengagement Δv. A higher ballistic coefficient ratio raises the Δv_{thresh} value, thereby enabling a greater separation velocity.

Furthermore, although both case studies employed a ballistic coefficient ratio of 2:1, the rate of separation differed due to the absolute values of the ballistic coefficients. The case with the lower β achieved faster phase times than the one with higher β values. This is because differential drag acceleration is not governed by the ratio alone, but more so by the difference in inverse ballistic coefficients. Lower absolute ballistic coefficients yield stronger drag forces and thus faster acceleration rates.

When combined, the effects of differential drag scaling with absolute ballistic coefficients and the cumulative impact of the disengagement Δv lead to significantly reduced phasing times. This suggests that the proposed method is particularly well-suited to constellations composed of a larger number of compact, mass-optimised satellites.

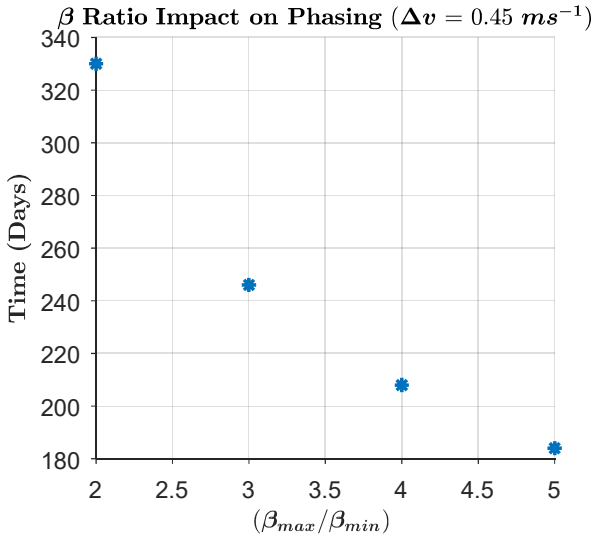

Figure 4.14: Ballistic Coefficient Ratio effect on phase times

4.6.3 Phase Time Sensitivity to Drag Coefficient

The dispersal strategy relies on differential aerodynamic drag to generate relative along-track acceleration between satellites. The drag acceleration acting on a satellite of mass m, drag coefficient C_d, and reference area A, moving at velocity $v$through an atmosphere of density ρ, can be expressed as:

$$a_D = \frac{1}{2}\,\rho\, v^2\,\frac{C_d A}{m}$$

For a satellite pair operating in high-drag and low-drag configurations, the relative along-track acceleration driving orbital phasing is proportional to the difference in their drag accelerations. Introducing the ballistic coefficient, $\beta = m/(C_d A)$, the relative angular acceleration governing in-plane separation can be written as:

$$\ddot{\theta} \;\propto\; \rho\, v^2 \left(\frac{1}{\beta_{min}} - \frac{1}{\beta_{max}}\right)$$

Since the phasing process integrates this angular acceleration over time, the duration required to reach a target angular separation scale approximately inversely with the effective drag coefficient. To first order, a fractional uncertainty in drag coefficient therefore propagates linearly into the predicted phasing time, such that:

$$\frac{\Delta t_{phase}}{t_{phase}} \;\approx\; \frac{\Delta C_d}{C_d}$$

In practice, the drag coefficient of small satellites in low Earth orbit is subject to uncertainty arising from gas-surface interaction effects, surface finish, and attitude-

dependent projected area. These factors introduce variability in the effective ballistic coefficient even for geometrically identical spacecraft.

The sensitivity of the proposed dispersal method to such uncertainty is reflected in the simulation results presented in the PQ8 case study. Variations in effective ballistic coefficient arising from attitude control result in phase-time deviations of approximately ± 1 - 2 days around the nominal value of 255 days. This corresponds to a relative variation of less than 1 %, indicating that moderate uncertainty in aerodynamic parameters does not significantly affect the feasibility or qualitative behaviour of the deployment strategy.

Additionally, a boundary analysis for drag coefficient estimation uncertainty for the PQ8 satellite case study resulted in an increase of 57 days or decrease in 18 days over a nominal value of 255 days, corresponding to uncertainty levels of +22% / −7.1 %.

Larger deviations in phasing performance are expected to arise primarily from uncertainties in atmospheric density and composition, which vary with altitude, solar activity, and geomagnetic conditions and are only approximated by empirical atmospheric models. While higher-fidelity aerodynamic characterisation, such as rarefied-flow computational fluid dynamics or experimental drag coefficient measurements, would reduce uncertainty in C_d, such analyses are considered beyond the scope of the present study. They are therefore identified as future work, appropriate for mission-specific optimisation and progression toward higher Technology Readiness Levels.

4.6.4 Deployment Collision Risk and Operational Constraints

Disengagement of the satellites in the proposed manner introduce early-mission cession risks, particularly during the early phases of separation when relative distances are small and differential drag dynamics have not yet produced meaningful spacing. For the PQ8 architecture, two collision-risk scenarios are identified: the immediate post-disengagement phase, and the first-orbit closest-approach phase driven by orbital dynamics and differential drag.

The highest instantaneous collision risk occurs during the first few seconds following disengagement, when the satellites remain in close proximity and relative velocities are low. During this phase, any residual angular rate increases the likelihood of contact between the disengaged PQ units.

This risk is mitigated through both design and operational measures. First, the ADCS is operated during disengagement to suppress body rates and maintain a near-zero rotation condition. Second, the disengagement pulse is designed to terminate before the guide pins and guide holes lose contact. Consequently, thrust is applied only while mechanical guidance still constrains motion, ensuring that the final stage of separation is dominated by linear translation whilst suppressing rotational dynamics. Once mechanical guidance is lost, the actuation pulse has already stopped, leaving only inertial motion. This sequencing eliminates the possibility of thrust-induced torque during free flight and significantly reduces the probability of lateral collision during the highest-risk period.

A second collision-risk regime occurs after approximately one orbit, when the satellites reach their first natural closest approach as a result of natural orbital dynamics. The magnitude of this minimum separation distance depends primarily on the initial separation impulse, the ballistic coefficients of the deployed satellites, and the atmospheric density at deployment altitude.

To quantify this risk, the closest-approach distance after one orbit was evaluated for the PQ8 and CS4 case studies, at an initial disengagement perigee altitude of 500 km. This distance was computed for the range of disengagement impulse values simulated in the case studies. The altitude represents a conservative, worst-case scenario for differential-drag-driven separation, as atmospheric density is relatively low and drag-induced divergence occurs slowly. At lower altitudes, higher atmospheric density would lead to faster differential-drag evolution and therefore larger early-orbit separations.

Table 4.6 presents the predicted minimum separation distance at the first-orbit closest approach as a function of initial separation impulse for both configurations.

Table 4.6 Distance of closest approach

Impulse (m/s)	distance (m)	
	CS	PQ8
0.45	4.6	-
0.4	4.1	-
0.35	3.6	6
0.3	3.1	5.1
0.25	2.6	4.3
0.2	2.1	3.4
0.15	1.5	2.6

Although both cases were configured with the same nominal ballistic ratio of 2, the absolute ballistic coefficients of the PQ8 satellites are approximately half those of the 4U CubeSat case. As a result, the PQ8 configuration experiences more rapid drag-driven divergence, leading to larger minimum separation distances over the first orbit.

For the 4U CubeSat case, minimum separation distances fall below 3 m for separation impulses of 0.25 m/s and below, reaching approximately 1.5 m at 0.15 m/s. These conditions represent the highest collision-risk regime during early orbital phasing. In contrast, the PQ8 configuration consistently exhibits larger minimum separation distances for equivalent impulses, reaching approximately 2.6 to 6 m over the impulse range.

These results demonstrate that collision risk during early orbital phasing is governed not only by the ratio of ballistic coefficients but also by their absolute magnitude. At the conservative altitude of 500 km, the PQ8 architecture already exhibits more favourable early-orbit spacing. At lower deployment altitudes, where atmospheric density is higher, greater separations than those reported in Table 4.6 can be expected, further reducing early-orbit collision risk.

To ensure that collision risk is minimised, a set of operational constraints is imposed on the deployment sequence:

- Deployment must only occur when the carrier and PQ units exhibit sufficiently low angular rates. The ADCS must be active prior to disengagement and capable of maintaining near-zero rotation throughout the separation event.
- The disengagement pulse duration must be shorter than the time to loss of mechanical guidance. No secondary actuation or attitude manoeuvres may occur until a minimum safe separation time has elapsed.
- Deployment should be scheduled to avoid periods of low atmospheric density. The deployment altitude must be selected such that differential drag is sufficient to increase spacing over the first orbit.
- A minimum acceptable first-orbit closest-approach distance should be enforced through mission planning, placing a lower bound on allowable separation impulse.

Together, these operational constraints ensure that deployment occurs only under conditions that minimise collision probability and ensure predictable early relative motion.

4.6.5 Summary of Results

The case studies presented demonstrate the feasibility and performance of the proposed dispersal method for deploying a single-plane constellation from a single launch, even under suboptimal orbital conditions. The results highlight the significance of carefully selecting the disengagement velocity Δv and the insertion angle $\theta_{initial}$ both of which directly influence phasing times and overall deployment efficiency.

The simulations confirm that by adjusting Δv within a practical range, the phasing time can be significantly reduced while maintaining a sufficient buffer to accommodate operational delays such as collision avoidance or anomaly handling. The identification of a disengagement window governed by a critical angle θ_{thesh} provides further robustness, allowing the system to tolerate timing uncertainties without significant performance degradation.

Moreover, the results validate the applicability of the optimisation framework and associated algorithms in managing the trade-off between phasing performance and design constraints, such as ballistic coefficient ratios, drag configuration, and structural complexity. The addition of deployables was shown to enhance aerodynamic control authority, particularly in the final phase, where slight differences in ballistic coefficients can otherwise lead to excessive phasing durations.

In the case of the PQ8 architecture, the total phasing time was approximately 255 days under nominal conditions and increased only slightly with realistic pointing uncertainties. This indicates that the proposed method is not only analytically tractable but also practically viable for operational missions involving small, mass-constrained satellite platforms.

Collectively, the results demonstrate that passive aerodynamic phasing from a single launch configuration is not only achievable but also scalable, provided that the deployment sequence, disengagement velocities, and drag parameters are optimised holistically.

4.7 Discussion

A novel deployment strategy was introduced, featuring a scalable, many-in-one satellite architecture launched as a single integrated unit and subsequently dispersed through a staged disengagement sequence combined with differential drag control.

Although the disengagement mechanism design is still pending, an analytical framework and supporting algorithms have been developed to identify optimal timing and disengagement velocities for effective in-plane phasing.

The case studies validated this approach under realistic orbital conditions and mission constraints. The simulations confirmed that the algorithm reliably computes optimal phasing times and can accommodate variations in Δv to address operational considerations such as collision avoidance and fault recovery.

The method is notably distinct from established deployment strategies such as those employed by the QB50 mission or Planet Labs [36,44]. Unlike conventional approaches that require post-deployment slot allocation or pre-staged release, the proposed method predefines the full deployment tree and constellation geometry. This removes the need for slot allocation and instead shifts the control focus to the disengagement velocity and timing, both of which are modelled analytically and optimised through simulation.

The main logistical and economic advantage of this architecture lies in the compact, single-unit launch configuration, which enables high packing efficiency and mass optimisation. For example, the PQ8 architecture demonstrated in Case Study 1 can accommodate twice the number of PocketQubes compared to a standard deployer that typically supports four units [26]. However, the extent to which this cost advantage scales with satellite form factor remains to be determined.

The deployment altitude of 500 km was selected to balance mission lifetime with sufficient atmospheric drag for phasing. At higher altitudes, drag forces become negligible, limiting the applicability of passive methods. At lower altitudes, while phasing performance improves, the mission lifetime may fall below acceptable thresholds. In this study, a PocketQube-class satellite operating at 500 km was estimated to have a mission lifetime of approximately two years, well within the typical orbital decay timescales at this altitude.

One of the primary limitations of the approach is the extended phasing duration when the ballistic coefficient ratio is low and no deployables are present. This can be mitigated by increasing the surface area difference between drag modes through additional deployables. However, doing so introduces complexity and potential failure points. Alternatively, relaxing the cube-shaped constraint can improve performance, albeit at the cost of manufacturing and integration complexity. Maintaining both

constraints, uniform geometry and no deployables, may result in suboptimal phasing durations, and at least one must be reconsidered to ensure mission viability.

An essential advantage of the many-in-one strategy is that satellites can begin nominal operations before final constellation geometry is achieved. This is particularly useful for missions that are not highly sensitive to precise spatial configuration during early operations.

Although the presented framework determines the required Δv for optimal phasing, it assumes the disengagement vector is aligned perfectly along the velocity direction. In reality, pointing inaccuracies, either from the mechanism or the ADCS, introduce cross-track components. These deviations are not explicitly modelled in this study but are considered in sensitivity analyses. For example, a 5° pointing error results in negligible cross-track velocity at the magnitudes of Δv used. Still, pointing accuracy must be evaluated case-by-case based on mission geometry and allowable tolerances.

The method introduces added risk due to the multiple disengagements required. This risk scales with constellation size, as each stage adds a potential point of failure. However, failure at any stage does not necessarily compromise the entire mission as undeployed units may still operate as part of a reduced-capability constellation. Collision risk is also elevated immediately after separation, as relative velocities are small. This risk is mitigated through careful tuning of Δv, separation angle, and by leveraging the natural divergence introduced through drag.

The study relies heavily on simulation and on the NRLMSISE-00 atmospheric model, which has known limitations in capturing fine-scale atmospheric variations [103,105]. While real-time updates to model inputs, such as those applied in Planet Labs' operational systems [50], can improve accuracy, uncertainties in drag modelling remain a significant challenge in differential drag control.

The orbital and environmental simulations presented in this work were performed using the MATLAB Aerospace Toolbox and were not cross-validated against independent tools such as GMAT or STK. Cross-validation using GMAT was not feasible, as the publicly available version does not provide access to the NRLMSISE-00 atmospheric model, which was required in this study as it is the only widely used model that explicitly includes anomalous oxygen effects relevant at the considered altitudes. Validation using STK was similarly not possible due to the unavailability of an appropriate license during the research period. Consequently, all simulations were

conducted within a single, internally consistent modelling environment. Future work should address this limitation by performing cross-validation against alternative high-fidelity propagators, either through licensed tools or by implementing equivalent atmospheric models within open-source frameworks.

Lastly, the contribution of the PQ8 architecture to orbital debris is minimal. The small size and low altitude of the satellites result in short orbital lifetimes, and the materials used are designed to disintegrate upon re-entry in accordance with CubeSat standards. The design ensures minimal long-term debris accumulation in LEO.

Although the PQ8 architecture has limitations, particularly in cross-plane deployments, its ability to optimise in-plane formation from a single launch makes it a cost-effective and scalable solution. While attitude-dependent manoeuvres can, in theory, enable orbital plane changes, the required phasing times are often impractically long. In such scenarios, multiple launches remain the preferred option. Nevertheless, the proposed method demonstrates that optimising single-plane deployments can form the building block of more complex, multi-plane architectures.

4.8 Summary and Outputs

This chapter presented a novel satellite deployment and dispersal framework tailored to many-in-one satellite architectures. Unlike traditional deployment strategies that rely on propulsion systems or sequential ejections, this approach leverages the differences in orbital velocities induced by disengagement, supplemented by the natural divergence induced by atmospheric drag and modulated through controlled attitude configurations.

The dispersal process follows a recursive sequence, with each parent satellite separating into two daughter units. This hierarchical approach simplifies system design, supports scalability, and preserves spatial ordering throughout deployment. Assuming uniform satellite properties, the system enables analytically guided control through an optimisation framework that determines insertion angles and phasing intervals to minimise total deployment time.

The methodology incorporates real-world constraints such as pointing inaccuracies, dynamic pressure variability, and uncertainty in ballistic coefficient estimates. To accommodate these uncertainties, it introduces concepts like insertion

windows and critical separation angles that enhance operational robustness and flexibility.

Within the context of this thesis, the chapter demonstrates the feasibility of the PQ8 dispersal method under the proposed deployment strategy. However, to fully implement this approach, a deployable panel must be incorporated into the satellite design to achieve the required differential drag. For the Case 1 deployment scenario, simulations indicate that the PQ8 architecture requires a Δv operating range between 0.2 m/s and 0.4 m/s to enable effective phasing. While 0.4 m/s yields the shortest phase times, it results in a narrow insertion window and reduced tolerance to modelling uncertainties, increasing the risk of extended deployment durations. A more conservative Δv value, such as 0.3 m/s, offers greater robustness and operational flexibility, making it better suited to accommodate real-world variations in drag and pointing performance.

From a TRL perspective, the dispersal methodology presented in this chapter achieves a readiness level of 3, having been validated through simulation incorporating realistic environmental perturbations and system-level constraints. The approach demonstrates analytical feasibility and supports operational robustness through the introduction of critical design constructs such as insertion windows and separation angle thresholds. However, as the deployment strategy relies on differential drag augmentation, requiring a deployable panel mechanism that has not yet been implemented or tested, the method cannot advance beyond TRL 3 without integrated hardware validation and in-orbit demonstration. Nonetheless, this simulation-driven analysis establishes a clear framework for phasing control in many-in-one satellite architectures.

5 DISENGAGEMENT MECHANISM: BACKGROUND

The disengagement mechanism plays a critical role in enabling the controlled separation of satellites following deployment. The following chapters presents a comprehensive study of a novel multi-purpose disengagement system that repurposes the magnetorquer coils to perform disengagement. The system is designed to meet specific performance requirements, primarily the generation of sufficient force and impulse, as defined by the satellite dispersal strategy. Its design must also navigate a number of practical constraints, including limited PCB area on the EPS, volumetric limitations within the satellite structure, and the necessity for reliable dual-mode operation.

This chapter begins by introducing the proposed disengagement mechanism, consisting of spring-loaded pogo-pins, permanent magnets and the ADCS's magnetorquer coils for actuation. This is followed by describing the design space of the mechanism, including the performance requirements and, physical and operational constraints. Finally, the requirements are tabulated together with the design approach adopted.

5.1 Specifications for the Disengagement Mechanism

The disengagement mechanism is a mission-critical subsystem that enables the transition from clustered flight (PQ8, PQ4, PQ2) to independent PQ1 operation. The disengagement mechanism operates within a discrete and well-defined phase of the mission. Whilst in other phases, the same hardware is used for attitude control by the ADCS. Its functional context is illustrated by the mission cycle presented in Table 5.1. To support the mission cycle defined above, the disengagement mechanism must satisfy a set of explicit system-level technical specifications as presented in Table 5.2.

Table 5.1: PQ8 Mission Phases

Phase	Mission Stage	Disengagement Mechanism Role	Key Requirements / Conditions
1	Launch and deployer release	Inactive	Mechanism must survive launch loads and shock without actuation
2	Early orbit stabilisation	Hardware controlled by ADCS	Detumbling and attitude acquisition; disengagement disabled
3	Clustered operation	Hardware controlled by ADCS	Provides attitude control while maintaining mechanical and electrical coupling between PQ units
4	Pre-disengagement arming	Standby for Disengagement Mode	Stable attitude, no critical ADCS manoeuvres, capacitors fully charged, command synchronisation verified
5	Disengagement event	Disengagement Mode	High-current pulse releases restraint and imparts Δv = 0.2–0.4 m/s
6	Post-separation recovery	Hardware controlled by ADCS	Re-establish attitude knowledge and control, suppress residual magnetic fields
7	Nominal constellation operations	Hardware controlled by ADCS	Continuous ADCS support throughout differential-drag phasing and mission operations

Table 5.2: Disengagement Mechanism Specifications

Domain	Specification	Value / Range	Source / Rationale	Relevant Chapter
Function	Primary role	Controlled separation of PQ units	Mission architecture	5
Function	Secondary role	Magnetorquer for ADCS	Reduce dead-weight through dual use.	5
Performance	Separation velocity Δv	0.2 – 0.4 m/s	Dispersal Requirements	4
Power	Mean power for recharge	≤ 20 mW per orbit (32 mWh)	EPS budget	3
Geometry	Coil volume	≤ 26 × 36 × 4 mm	Structural constraints	3
Mass	Coil mass	≤ 15 g per coil	Mass budget	3
Integration	Circuit footprint	≤ 10.5 cm²	EPS PCB area	3
Control	Control signals	≤ 6 pins	ADCS/EPS interface	3
Operation	Dual mode	MT mode and DM mode	Architecture requirement	5
Reliability	Autonomy	MT mode independent of EPS MCU	Fault tolerance	5
EMI	Magnetic disturbance	Must decay rapidly post-pulse	ADCS stability	5

5.2 Selection of Disengagement Technology

Two decision matrices were developed to compare candidate restraint and actuation concepts for the PQ8 architecture. The objective of this trade study is to assess

their suitability for PQ8, where the dominant drivers are miniaturisation within PocketQube-class constraints, implementation across eight interfaces, compatibility with synchronised operation, and reliability. To avoid false precision, all criteria are treated with equal importance and scored using a three-level ordinal scale.

Scoring scale applied to all criteria:

- (1) represents poor suitability, significant limitations or high risk within the PQ8 context.
- (2) represents Moderate suitability, feasible but with notable limitations or sensitivities.
- (3) represents Good suitability, readily implementable with manageable risk within PQ8 constraints.

The 'Restraint' mechanism criteria are presented in Table 5.3, with the presented then forming the decision matrix presented in Table 5.4.

The matrix indicates that restraint concepts such as magnetic restraint score strongly within the PQ8 context due to favourable miniaturisation and high compatibility with coordinated multi-point separation. Mechanisms such as clamp bands and

Table 5.3: Restraint Mechanism Matrix Criteria

ID	Criterion	Definition
R1	Miniaturisation / packaging feasibility	Ability to integrate within the PQ8/PQ1 envelope without excessive mass, volume, or integration complexity.
R2	Multi-interface implementation feasibility	Practicality of implementing the restraint across eight interfaces, including assembly effort, routing, tolerance stack-up, and unit-to-unit consistency.
R3	Synchronised Operation	Compatibility with achieving near-simultaneous separation across all eight interfaces under a single coordinated actuation event. This criterion reflects system-level synchronisation and is not restricted to release-type restraints.
R4	Hold-down reliability under launch loads	Ability to maintain mechanical restraint and contact integrity throughout vibration and shock loading without slip, creep, or loosening.
R5	Release reliability	Probability of clean and complete release when commanded, including avoidance of partial release, hang-up, or residual constraint.
R6	Environmental robustness	Sensitivity to thermal cycling, vacuum conditions, contamination, material aging, and related environmental effects.

Table 5.4: Restraint Mechanism Decision Matrix

Restraint Method	R1	R2	R3	R4	R5	R6	Total
Burn wire	3	2	1	2	2	3	**13**
Electromagnetic latch	1	1	3	3	3	3	**14**
SMA restraint	3	2	1	2	2	3	**13**
Release nut	1	1	1	3	2	2	**10**
Clamp band	1	1	3	3	3	3	**14**
Magnets	3	2	3	3	2	3	**16**
Interference fit	3	2	3	2	1	1	**12**
Hook-and-loop	2	2	3	1	2	1	**11**

electromagnetic latches score well in terms of hold-down integrity and release reliability, but incur a significant miniaturisation and multi-interface implementation penalty at PocketQube scale. Burn wire and SMA-based restraints are attractive from a packaging perspective, but score lower on synchronous release compatibility when scaled across eight interfaces due to routing complexity and the practical challenge of achieving a narrow timing window. Concepts such as release nuts, interference fits, and hook-and-loop exhibit reduced suitability within PQ8 primarily due to limitations in clean release reliability, launch-load robustness, or environmental sensitivity.

The ‘Actuation’ mechanism criteria are presented in Table 5.5, with the presented then forming the decision matrix presented in Table 5.6.

Table 5.5: Actuator Matrix Criteria

ID	Criterion	Definition
A1	Miniaturisation/ packaging feasibility	Ability to integrate the actuation concept within PQ8/PQ1 mass and volume constraints without excessive complexity.
A2	Separation outcome predictability	Ability to generate a consistent and controllable separation impulse across all units.
A3	Synchronised Operation	Compatibility with simultaneous or near-simultaneous actuation across multiple units with minimal timing skew.
A4	Reliability/ repeatability across 8 events	Consistency of actuation performance across eight separations, accounting for tolerances and relevant environmental variation.
A5	Disturbance and re-contact risk	Likelihood of inducing off-axis impulses, attitude disturbances, or immediate re-contact following separation.
A6	Power/ energy feasibility	Peak power and total energy required at the separation event relative to realistic PQ-class EPS capabilities, including any auxiliary release mechanisms.

Table 5.6: Actuation Decision Matrix:

Actuation Method	A1	A2	A3	A4	A5	A6	Total
Springs	2	2	2	3	2	2	**13**
Motors	1	3	3	3	2	1	**13**
Momentum exchange	2	1	1	1	2	1	**8**
SMA actuation	2	3	2	2	2	2	**13**
Hybrid spring–electromagnetic	2	3	3	3	3	1	**15**

The actuation trade study indicates that the hybrid spring–electromagnetic actuation concept offers the highest overall suitability for the PQ8 architecture. This concept combines predictable and repeatable separation dynamics with strong compatibility for multi-unit synchronisation, while mitigating re-contact risk through controlled impulse magnitude. Passive spring-based actuation performs well in terms of reliability and simplicity, but is limited by reduced controllability of separation dynamics and reliance on an auxiliary release mechanism. Motorised actuation provides excellent control and synchronisation but is penalised due to packaging and power constraints at PocketQube scale. SMA-based actuation remains feasible but exhibits reduced repeatability and synchronisation accuracy due to thermal dependence. Momentum-exchange approaches are considered poorly suited to PQ8 due to limited predictability and high implementation risk within the short-timescale disengagement event considered.

5.3 Proposed Solution

As discussed in the literature review (Section 2.3), existing satellite deployable technologies do not offer a complete solution for the PQ8 architecture. The disengagement system can be broadly categorised into three functional mechanisms: restraint, actuation, and guidance. Viable restraint options were narrowed down to permanent magnets, hook-and-loop fasteners, or interference fits, while spring-based mechanisms were identified as the only practical means of actuation. However, actuation remains an open challenge. Crucially, combining the spring actuators with the available restraint options fails to yield a functional system, as none allow for thee controlled triggering of disengagement. This highlights the need for a novel solution tailored to the specific requirements of the PQ8 deployment strategy.

The primary design drivers for developing the new topology are size constraints and reliability concerns. Given the limited volume of the satellite, any design decision

inherently involves trade-offs with other subsystems. In this case, since the disengagement mechanism is mounted on the external surfaces of the PQ1 satellite, it directly competes with solar cells for the available surface area, which are critical for a platform already constrained in power generation capacity. From a reliability perspective, the mechanism must be easily characterisable, reusable (in case of a misfire) and tuneable to ensure consistent and predictable performance during disengagement.

The proposed solution adopts a hybrid approach, combining permanent magnets for restraint, springs for partial actuation, and a novel trigger mechanism that repurposes the magnetorquer coils, as shown in Figure 5.1. Neodymium magnets, arranged in opposing pairs to create a net-zero dipole moment, serve as the primary restraint. These magnets, each 2 mm in diameter, generate tuneable holding forces based on their separation distance and are compact enough to be embedded directly into the solar cell PCBs, enabling straightforward integration and assembly.

Spring-loaded pogo pins partially pre-load the restraint mechanism, contributing to the actuation force required for disengagement, though not sufficient to overcome the magnetic restraint alone. These pogo pins also function as electrical and data connectors between PQ1 satellites when configured in PQ8, PQ4, or PQ2 assemblies.

The trigger mechanism, which operates in tandem with the springs, utilises the existing magnetorquer coils mounted on opposing faces of adjacent PQ1 satellites. By generating a synchronised electromagnetic pulse, these coils produce a repulsive force that overcomes the magnetic restraint and initiates separation. This pulse not only breaks the mechanical hold but also imparts the necessary initial Δv to the satellites. Importantly, as the number of adjacent satellite faces increases through the PQ8 → PQ4 → PQ2 →

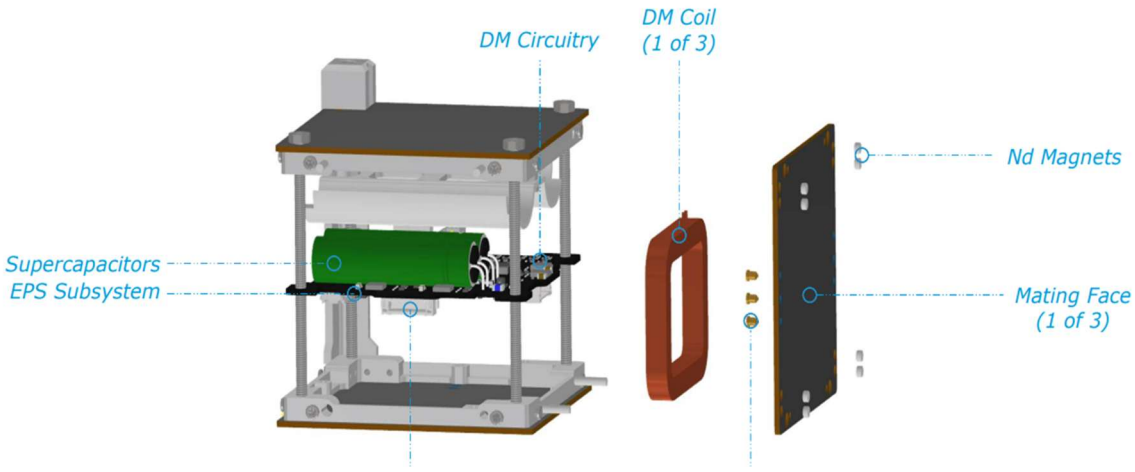

Figure 5.1: Exploded view of Disengagement Mechanism Components in a PQ1 Satellite

PQ1 stages, the number of coils contributing to the disengagement scales accordingly, thus ensuring consistent actuation force across all deployment stages.

The disengagement mechanism must generate sufficient force to achieve clean separation while operating within the system's electrical and volumetric constraints. The target separation velocities dictate the required force and impulse values. Additionally, the design must accommodate several hardware limitations, including minimal available PCB area, limited coil volume, and the requirement for dual-mode operation.

The remainder of this chapter introduces the technical foundation for the disengagement mechanism, including the functional objectives, requirements, and design constraints that influence component selection and integration. It also sets the stage for the detailed modelling of the electromagnetic and mechanical interactions between adjacent PQ1 units, which is essential for developing and validating the dynamic behaviour of the PQ8 disengagement system.

5.4 Performance Requirements

The primary performance requirement of the disengagement mechanism is to deliver a controlled change in velocity (Δv) as defined by the dispersal algorithms presented in Chapter 4. In the PQ8 constellation case study (Section 4.4.1), the desirable Δv values fall within the range of 0.2 to 0.4 ms^{-1}. The lower bound ensures sufficient initial separation to prevent post-release collisions. In contrast, the upper bound reflects a practical performance limit, where exceeding it would result in prolonged phasing times due to increased difficulty in decelerating the satellites from their dispersal trajectories.

To meet this requirement, the disengagement system must provide a sufficient impulse, I_{Sep}, defined as:

$$I_{Sep} = m\Delta v$$

where m is the satellite mass. Assuming a pulse-based trigger, the impulse is given by:

$$I_{Sep} = \int_0^{t_{sep}} F(t)dt$$

where $F(t)$ represents the time-varying disengagement force and t_{sep} is the duration of the impulse. Table 5.7 provides the impulse ranges required for different satellite variants, assuming Δv values from 0.2 to 0.4 ms^{-1}:

Table 5.7: PQ8 Impulse Requirements for $\Delta v = 0.2\ to\ 0.4\ ms^{-1}$

Satellite	Mass (kg)	Impulse (kgm/s)
PQ4	1.00	0.20 – 0.40
PQ2	0.50	0.10 – 0.20
PQ1	0.25	0.05 – 0.10

5.5 Design Constraints

The design of the disengagement mechanism is subject to a series of physical and operational constraints dictated by the satellite's compact form factor, subsystem integration requirements, and dual-functionality objectives. These constraints influence component selection, layout decisions, and control architecture, and must be addressed systematically to ensure reliable system performance without compromising core satellite functions.

5.5.1 Physical Constraints

5.5.1.1 PCB Area Limitations:

The disengagement circuitry must be integrated into the EPS board, which provides limited available space. The total EPS PCB area is 35 cm², of which approximately 70 % is occupied by core EPS components. This leaves only ≈10.5 cm² for the disengagement circuitry. Component height is also constrained:

- On the underside, components must not exceed 2 mm in height to avoid interference with adjacent ADCS PCBs.
- On the top side, the maximum allowable height is 8 mm, constrained by the vertical clearance between the EPS board and the battery harness.

These spatial limitations restrict component selection to compact packages, often with reduced power-handling capacity. Consequently, the circuit must be designed for simplicity, minimal component count, and compatibility with the available footprint.

5.5.1.2 Coil Volume and Mass Constraints:

The magnetorquer/disengagement coils must be accommodated within a designated internal volume of 26 mm × 36 mm × 4 mm. To minimise impact on the satellite's mass budget, each coil is allocated a maximum mass of 15 grams. These constraints govern key coil parameters, including wire gauge, number of turns, and

winding configuration, all of which influence the achievable magnetic force and energy conversion efficiency.

5.5.1.3 ADCS and EPS Interactions

Control of the disengagement coils is shared between the ADCS and the EPS. Due to limited PCB area on the ADCS board, the driver circuitry is hosted within the EPS, while the ADCS retains directional control via a minimal two pins per coil control system, one for each direction.

Additionally, subsystem communication is constrained by the limited number of connector pins, requiring an efficient and fault-tolerant signal allocation scheme. The coil drivers must remain operable independently of the EPS microcontroller state to ensure continued magnetorquer functionality in the event of EPS failure. This necessitates the implementation of a fallback mechanism or default state to maintain baseline attitude control capabilities.

5.5.2 Operational Constraints

5.5.2.1 Dual-Use Requirement:

The disengagement mechanism must function in two distinct modes:

- Magnetorquer Mode (MT mode): Used by the ADCS to generate a controlled magnetic dipole for attitude control (e.g. wheel desaturation and detumbling via B-dot control).
- Disengagement Mode (DM mode)**:** The same coils are pulsed to generate repulsive forces for mechanical separation.

In MT Mode, the coils produce a magnetic moment, M, which interacts with Earth's magnetic field, β, to generate torque, given by (Eq. 5.1):

$$\boldsymbol{T_{MT} = \mathbf{M} \times \beta = m\beta sin(\theta)} \quad \text{(Eq. 5.1)}$$

where, $\mathrm{M} = NIA$, with N is the number of turns, I is the current, A is the coil area, and θ is the angle between the magnetorquer's dipole and Earth's magnetic field. The operating voltage required to generate the target magnetic moment is derived from: (Eq. 5.2):

$$\boldsymbol{V = \frac{\mathbf{M}R_{Coil}}{NA}} \quad \text{(Eq. 5.2)}$$

The ADCS requires a maximum dipole of $74\ mAt$, which constrains the coil resistance, current rating, and number of turns. These requirements introduce trade-offs between the electrical characteristics needed for MT mode and those for DM mode.

5.5.2.2 Energy Source and Current Handling Constraints:

DM mode operation requires a short, high-current pulse to deliver sufficient impulse. However, satellite batteries cannot directly provide the required peak currents due to discharge limitations and power bus stability concerns. To address this, a capacitor-based energy storage solution is employed. This introduces its own constraints:

- The capacitor must store sufficient energy for consistent force output.
- Recharging must not exceed an average power budget of 20 mW per orbit.
- The discharge process must avoid voltage dips or surges on the shared power bus.

As a result, the system must include regulation circuitry for both controlled discharge and safe recharging of the storage elements.

5.5.2.3 Electromagnetic Interference (EMI)

The use of electromagnetic actuation during disengagement introduces the risk of residual magnetic fields, which can interfere with other satellite subsystems, particularly the magnetometer and the attitude control algorithms relying on magnetic field measurements. This interference poses a challenge both during the disengagement event and in the post-separation phase, where precise attitude knowledge and control are required for constellation phasing.

To mitigate these risks, the system must be designed to minimise residual magnetisation and suppress transient magnetic disturbances. This involves selecting materials with low remanence, optimising coil placement to limit stray field coupling, and ensuring that the induced magnetic field decays rapidly after disengagement. The decay behaviour is primarily governed by the coil's electrical characteristics, particularly its resistance and inductance, as well as the configuration of the discharge circuitry.

In addition, timing plays a critical role. The activation of the disengagement pulse must be coordinated to avoid overlap with sensitive ADCS operations or magnetometer readings. This temporal multiplexing reduces the likelihood of sensor corruption or torque calculation errors resulting from residual fields. Effective EMI

management is therefore essential to maintain post-separation stability and ensure proper functioning of the ADCS throughout the satellite's operational timeline.

5.6 Summary of Requirements & Constraints

A summary of the requirements and constraints is listed in Table 5.8. The disengagement system must serve as both a separation actuator (DM mode) and a magnetorquer (MT mode). While disengagement operations are managed by the EPS, magnetorquer functionality is governed by the ADCS. To increase fault tolerance, the circuit must allow autonomous MT mode operation regardless of the EPS controller state. Constraints are primarily driven by the high level of miniaturisation in the satellite platform. These include strict limits on volume, mass, PCB area, control pin count, and power consumption.

Table 5.8: Summary of Disengagement Mechanism Design Requirements

Function	Requirement
DM Mode	Must generate impulse as in Table (Δv = 0.2 – 0.4 m·s^{-1})
MT Mode	Must generate a maximum Torque of 74×10^{-3} At
Circuit Size	Must have a footprint not exceeding 10.5 cm²
Coil Dimensions	Must not exceed 26 mm × 36 mm × 4 mm
Coil Mass	Must not exceed 15 g per coil
Control Signals	Must be limited to 6 control pins
Autonomy	Must operate in MT mode independently of the EPS controller state
Power	Mean power must not exceed 20 mW/orbit (32 mWh)
EMI/EMR	Must not interfere with or damage other circuitry during operation

5.7 Design Approach

With the proposed solution, performance requirements and design constraints established, the development of the disengagement mechanism followed a structured approach aimed at producing a system that maximises force outputs within strict physical, mass, and power limitations. The system was engineered to allow controlled modulation of the disengagement force via capacitor charge levels or discharge pulse duration. The design process was governed by two primary phases: a static force analysis to define

theoretical requirements, and a dynamic model that integrates electrical behaviour, mechanical separation dynamics, and system-level validation.

The first phase focused on a static analysis of the force equations to establish the fundamental relationships between coil current, coil geometry, separation distance, and radial misalignment. These analytical expressions outlined the key geometric and electrical parameters to maximise the forces generated by the coils. The analysis formed the basis for initial sizing and selection of key components, including the disengagement coils and energy storage elements.

The second phase involved the development of a dynamic model to capture the time-dependent behaviour of the disengagement system. This begins with a simplified electrical model of the capacitor discharge circuit, which characterises the coil current profile during separation. This electrical model also informed the selection of suitable supercapacitors, which were evaluated based on their size, energy capacity, discharge capability, and compatibility with the limited PCB footprint.

Once the capacitor parameters were defined, the coil design was optimised to achieve maximum disengagement velocities. Coil characteristics, which include wire gauge, number of turns, and resistance, were selected to maximise the magnetic force while remaining within mass, volume, and power constraints. The coil and capacitor models were then coupled to identify the optimal configuration that satisfies both DM and MT operating requirements.

The final step in the design process involved experimental validation through physical testing. A rigid pendulum setup was used to assess current behaviour and initial force response, while a long pendulum test simulated complete impulse transfer. These tests validated the dynamic model under conditions approximating in-orbit separation and verified that the mechanism operates as intended during disengagement.

The following sections cover the analyses of the force equations, develop the dynamic model and designs the electrical drivers of the disengagement mechanism. First, the force generated by the two coils is assessed, noting the impact of each equation parameter on the resulting forces. Next, the electrical, thermal, interface, friction and kinematic models are developed, describing the different processes that contribute to the resultant forces. These models are then combined to develop six degrees of freedom model that describes the kinematic motion of the satellites during disengagement.

Circuit components are then selected, starting with the selection of the tightly coupled supercapacitors and coil designs. Next, the circuitry is developed consisting of the charging circuitry, series/parallel switch that allows the capacitors to charge at lower voltage, an H-Bridge that allows for bi-directional operation in MT mode, and the H-Bridge gate drivers. Circuit design and component design is highly constrained by volumetric and performance requirements, necessitating the use of COTS components that are not designed for the space environment. Consequently, the chapter is closed of with a theoretical risk and failure mode analysis that highlights possible points of failure, the risk mitigation strategies that are in place and what can be done to further enhance the circuits survivability in space.

5.8 Static Force Equations Analysis

5.8.1 Equations Derivation

Various formulae for calculating the forces induced between two current-carrying conductors have been derived and proposed over the years. These derivations typically build upon Maxwell's formula, which relates the induced force to key parameters such as the mutual inductance between the coils (M), their separation distance (g), and the currents flowing through the coils, I_1 and I_2. The resulting force magnitude is given by Eq. 5.3, which provides the theoretical basis for analysing the repulsive force generated by the magnetorquer coils in the proposed trigger mechanism [106,107].

$$\boldsymbol{F = I_1 I_2 \frac{\delta M}{\delta g}} \qquad \text{(Eq. 5.3)}$$

Historically, the complexity of calculating the induced force has stemmed mainly from the expansion of the term for mutual inductance. Mutual inductance quantifies the coupling between two current-carrying coils and depends on their geometric and spatial configuration. Maxwell's formula for calculating the mutual inductance between two coils, such as that illustrated in Figure 5.2, is given in Eq. 5.4, providing a foundational expression for analysing the electromagnetic interactions in the proposed mechanism.

$$\boldsymbol{M = 4\pi\sqrt{R_1 R_2}\left\{\left(\frac{2}{k} - k\right)K(k) - \frac{2}{k}E(k)\right\}} \qquad \text{(Eq. 5.4)}$$

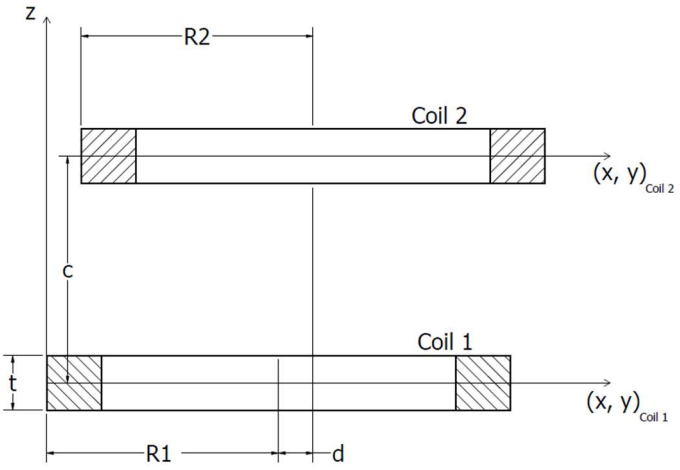

Figure 5.2: Cross-section of coils with misalignment in the xy-plane

where $k = \frac{2\sqrt{R_1 R_2}}{\sqrt{(R_1+R_2)^2+c^2}}$, R_1 *and* R_2 are the radii of the two coils, and c is the separation distance between the centres of the two coaxial coils. $K(k)$ *and* $E(k)$ are the elliptic integrals of the first and second kind, respectively, given by:

$$K(k) = \int_0^{\frac{\pi}{2}} \frac{1}{\sqrt{1-k^2\sin^2\theta}}\, d\theta$$

$$E(k) = \int_0^{\frac{\pi}{2}} \sqrt{1-k^2\sin^2\theta}\, d\theta$$

The solution for Equation 5.4 varies between literature sources due to the different methods used to calculate the elliptic integrals [108]. Various methods of series expansion have been employed to approximate these terms, but this approach is often complex and slow to converge for most practical cases [109]. Alternatively, the formulae and supplementary expressions derived in [109] offer a more efficient means of achieving sufficient accuracy with a moderate amount of computational effort.

That is, the accuracy of these calculations can be enhanced by employing computational techniques, such as the trapezoidal approximation method, to approximate the elliptic integrals more efficiently. Therefore, using the nomenclature of Figure 5.2 and the derivation in [109], Maxwell's equation for the mutual inductance of two filaments is adapted to provide Eq. 5.5:

$$\mathbf{M} = \frac{\mathbf{2\mu_o\sqrt{R_1R_2}}}{\boldsymbol{\pi}} \int_{\mathbf{0}}^{\boldsymbol{\pi}} \frac{\left[\mathbf{1} - \frac{\mathbf{d}}{\mathbf{R_2}}\mathbf{cos(\phi)}\right]\boldsymbol{\psi}\mathbf{(k)}}{\sqrt{\mathbf{V^3}}}\mathbf{d\phi} \qquad \text{(Eq. 5.5)}$$

where μ_o is the permeability of free space, R is the radius of the coils, d is the offset in the *xy-axes* between the centres of the coils, and $\psi(k)$ is given by:

$$\psi(k) = \frac{1}{k}\left[\frac{(2-k^2)}{2}K(k) - E(k)\right]$$

Additionally, k can be rewritten as:

$$k = \sqrt{\frac{4\alpha V}{(1+\alpha V)^2 + \beta^2}}$$

with $\alpha = \mathrm{R}_1/R_2,\ \beta = c/R_1$ and $V = \sqrt{1 + \frac{d^2}{{R_2}^2} - \frac{2d}{R_2}\cos(\phi)}$.

Considering Eq. 5.3 and 5.5, the calculation of the force between two filamentary coils requires computing the derivative of the mutual inductance with respect to the generalised separation distance, g. The separation distance can either be along the z-axis, representing an axial displacement, or on the xy-plane, representing a radial displacement between the coils. Consequently, computing the derivation in either of the two directions results in an axial force or a radial force, respectively.

5.8.1.1 Axial Force

Considering Eq. 5.3 to 5.4, and continuing the derivation in [107] for the case where $g = c$, yields the axial force expressed as:

$$\boldsymbol{F_z = \frac{\mu_o I_1 I_2 \beta}{2\pi\sqrt{\alpha}}\ \Lambda(\phi)} \qquad \text{(Eq. 5.6)}$$

where,

$$\Lambda(\phi) = \int_0^{\pi} \frac{\left[\frac{d}{R_2}cos\phi - 1\right]\phi(k)}{\sqrt{V^5}}\ \partial\phi$$

and,

$$\phi(k) = k\left[\frac{2-k^2}{2(1-k^2)}E(k) - K(k)\right]$$

If the coils are perfectly aligned, i.e. $d = 0$, then Eq. 5.6, as shown in [107], becomes:

$$\boldsymbol{F_z = -\frac{\mu_o I_1 I_2 \beta}{2\sqrt{\alpha}}\ \phi(k)} \qquad \text{(Eq. 5. 7)}$$

The resulting force is opposing when the two currents are flowing in the same direction, which represents a force of separation along the z-axis. In the case of opposing currents, and hence opposing electromagnetic fields, the coils would attract one another.

5.8.1.2 Radial Force

Similarly, following the derivation in [107], but computing for the $g = d$, yields the force in the xy-plane, given by:

$$\boldsymbol{F_{x,y} = \frac{\mu_o I_1 I_2}{\pi\sqrt{\alpha}}\, \Pi(\phi) + \frac{\mu_o I_1 I_2}{4\pi\alpha\sqrt{\alpha}} \Upsilon(\phi)} \qquad \text{(Eq. 5.8)}$$

where,

$$\Pi(\phi) = \int_0^{\pi} \frac{\left[\frac{d}{R_2}\cos^2\phi + \left(1 + \frac{d^2}{R_2^2}\right)\cos\phi - \frac{3d}{R_2}\right]\psi(k)}{\sqrt{V^7}}\, \partial\phi$$

$$\Upsilon(\phi) = \int_0^{\pi} \frac{\left[\left(1 - \frac{d}{R_2}cos\phi\right)\left(\frac{d}{R_2} - cos\,\phi\right)(1 + \beta^2 - \alpha^2 V^2)\right]\phi(k)}{\sqrt{V^9}}\, \partial\phi$$

In the case that the coils are perfectly aligned, i.e. $d = 0$, then Eq. 5.8, as shown in [107], becomes:

$$F_{x,y} = 0$$

Therefore, when the coils are perfectly aligned along the xy-plane, the resulting force is purely axial.

5.8.1.3 Modifications for PQ8 Architecture

Together, Eq. 5.6 and Eq. 5.8 describe the static electromagnetic forces between two filamentary, current-carrying conductors, encapsulating the fundamental physical principles underlying the proposed disengagement mechanism. To achieve the intended functionality, these equations must be adapted and applied to the magnetorquer coils integrated within the PQ8 satellites, in conjunction with the development of suitable driving circuitry. Particularly, the coils in the PQ1 satellites will not be a single loop but will consist of N turns. Consequently, Eq. 5.6 and Eq. 5.8, should be expanded, such that:

$$\boldsymbol{F_{Axial} = \frac{\mu_o I_1 I_2 N_1 N_2 \beta}{2\pi\sqrt{\alpha}}\, \Lambda(\phi)} \qquad \text{(Eq. 5.9)}$$

$$F_{Radial} = \frac{\mu_o I_1 I_2 N_1 N_2}{\pi\sqrt{\alpha}}\,\Pi(\phi) + \frac{\mu_o I_1 I_2 N_1 N_2}{4\pi\alpha\sqrt{\alpha}}\Upsilon(\phi) \qquad \text{(Eq. 5.10)}$$

where $N_1\ and\ N_2$ represent the number of turns for the respective coils. This assumes that by taking the axial separation of the coils with respect to the coil centres, the multi-turn coil can be represented as a single-turn loop carrying an effective current $I_{Approx} = NI_{Actual}$.

Additionally, as these expressions are derived under static assumptions, their applicability must be re-evaluated for dynamic conditions in which both the separation distances along the x, y, and z axes, and the coil currents vary with time. This dynamic reassessment is essential to ensure the reliable operation of the disengagement mechanism under real-world conditions. The electromagnetic forces are inherently time-dependent due to their dependence on circuit current $I_1,\ I_2,\ \beta, V\ and\ k$. The currents I_1 and I_2 vary over time due to the electrical dynamics of the discharge circuit, which governs the current profiles through each coil.

The parameter β is a geometric factor that varies as a function of the separation distance between the coils along the axial direction, while V depends on the radial offset between the coil centres. Both parameters are determined through the relative positions of the coils, and thus influence the magnitude of the generated forces. The coefficient k is a composite term that incorporates both β and V and encapsulates the combined effect of axial and radial offsets on the interaction dynamics.

As disengagement proceeds, both axial separation and radial misalignment increase with time, leading to a dynamic evolution in the axial and radial force components. Capturing this time-varying behaviour is essential for accurately estimating the net impulse transferred to the satellite during separation.

In addition to translational acceleration, the asymmetry introduced by radial misalignment and uneven force application induces a torque τ on the satellite, resulting in angular acceleration α as described by:

$$\tau = I\alpha$$

where I is the satellite's moment of inertia about the relevant axis. These rotational effects reduce the overall energy efficiency of the separation event and must later be corrected by the ADCS, increasing the burden on the power budget.

Mitigating induced torques requires careful alignment of the coil centres with the satellite's centre of mass and a symmetric inertia distribution. However, given the tight mechanical constraints, some degree of misalignment is unavoidable. As such, the disengagement system must be designed to minimise and tolerate induced rotational motion as part of its overall performance strategy.

5.8.2 Equations Analysis

To establish a baseline understanding of the forces involved in satellite separation, the static forms of the axial and radial force equations, Eq. 5.9 and Eq. 5.10, are evaluated across key parameter ranges. The results, shown in Figure 5.3, provide insight into how the generated magnetic repulsion varies with ampere-turns, coil radius, and separation distance.

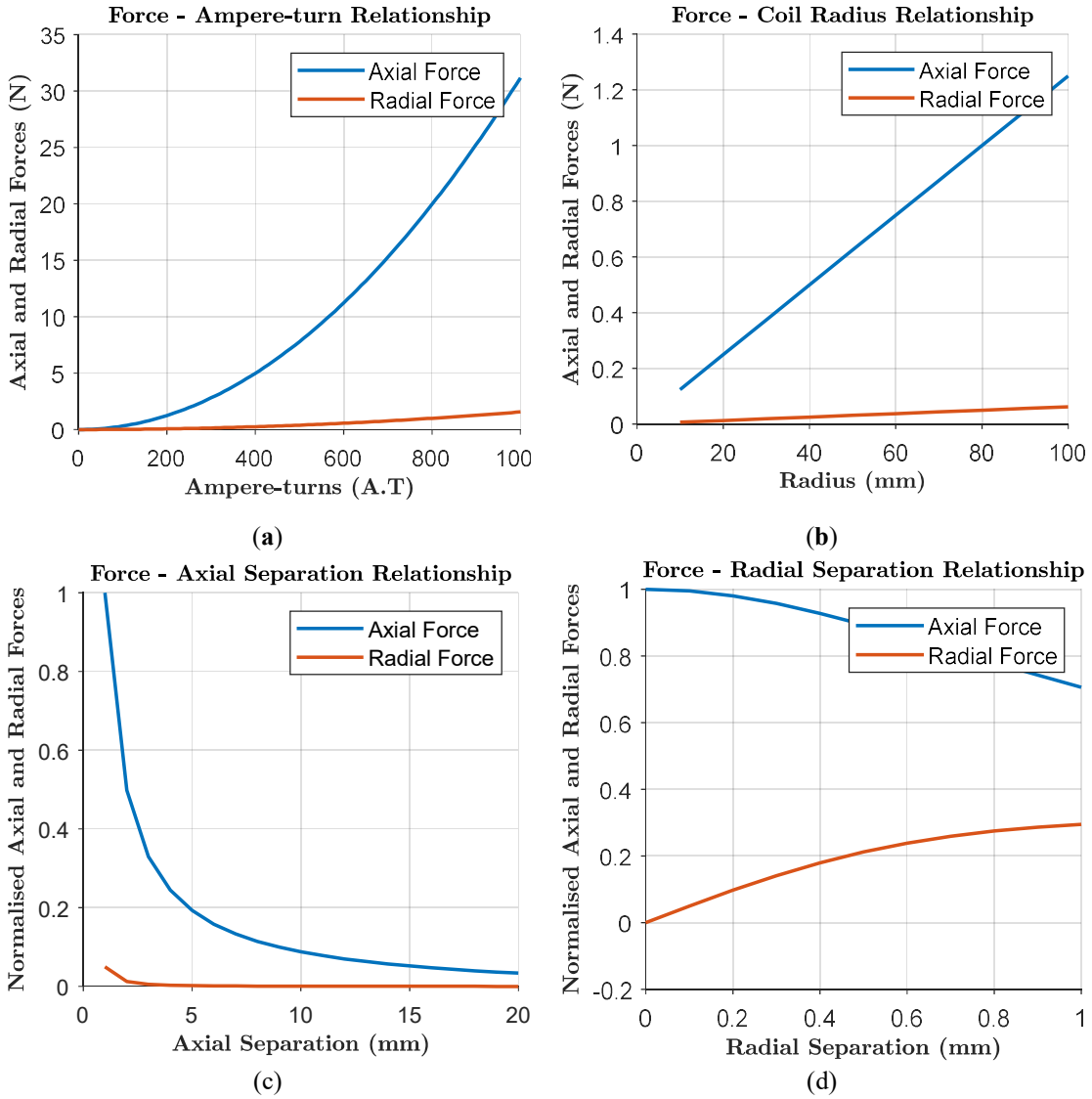

Figure 5.3: Plots for static force analysis: (a) Force vs Ampere-Turns, (b) Force vs Radius (c) Forces vs. Axial Separation (d) Forces vs. Radial Separation

Figure 5.3(a) illustrates the axial repulsive force as a function of ampere-turns. The plot confirms the expected quadratic relationship, as the magnetic force is proportional to the square of the current through the coil windings. This demonstrates the importance of maximising the ampere-turn product, either by increasing current or the number of turns, within the constraints imposed by resistance, heating, and power supply requirements.

Figure 5.3(b) shows the force as a function of coil radius. A linear relationship is observed, indicating that larger coil radii yield proportionally greater magnetic force. Although increasing coil radius is advantageous from a force-generation standpoint, this must be balanced against the volume limitations imposed by the satellite's internal layout.

Figure 5.3(c) presents the normalised axial force as a function of axial separation distance. The force profile approximates the inverse square of distance, highlighting the critical importance of minimising the initial coil separation to ensure an effective impulse transfer during disengagement.

Figure 5.3(d) plots the normalised force against radial separation. The force exhibits an inverse dependence, though the decline is less steep than in the axial case. This suggests that although radial misalignment does degrade force output, its effect is more gradual and can be mitigated through careful mechanical alignment and structural tolerances.

These trends serve as a foundation for coil design and placement strategies. They lead to the following design guidelines:

1. Maximise coil radius for given volumetric constraints,
2. Maximise Ampere-turn magnitude,
3. Minimise the initial distance between the centres of the two coils,
4. Minimise radial misalignment.

By identifying and quantifying the influence of each parameter, the static force analysis informs the selection of coil dimensions and electrical specifications to ensure the disengagement mechanism can deliver the required impulse under nominal conditions. The following section extends this analysis by incorporating dynamic effects, where time-varying current and coil separation are considered within a coupled electromechanical framework.

5.9 Dynamic Force Model

The static force equations assume fixed geometries and steady-state current conditions. However, in practical operation, both the electrical and mechanical parameters evolve during the disengagement event. As the capacitors discharge, the currents through the coils decay. Simultaneously, the coils accelerate away from each other under the influence of the generated repulsive force. The resulting forces are therefore inherently time-dependent and dynamically coupled to the system's motion.

To accurately model this interaction, the system is treated as an energy-conversion process in which stored electrical energy is transformed into mechanical kinetic energy. This energy-based framework enables the integration of circuit behaviour with the kinematic response of the satellites, accounting for the interplay between the evolving current profile and mechanical motion.

5.9.1 Simplified Circuit Model

A simplified electrical model is constructed based on two identical LCR circuits, representing each satellite's coil configuration as illustrated in Figure 5.4. Each circuit comprises a coil with inductance L, series resistance R, and a capacitor bank with capacitance C. To capture the energy transferred from electrical to mechanical domains, an additional time-dependent resistance term, R_Z, is introduced. This term models the effective electrical loss associated with the generation of kinetic energy in the system.

The total energy in the system, U, includes contributions from the capacitors (U_B) and inductors (U_E):

$$U = U_B + U_E = \frac{1}{2}LI_1^2 + \frac{1}{2}\frac{Q_1^2}{C} + \frac{1}{2}LI_2^2 + \frac{1}{2}\frac{Q_2^2}{C}$$

Assuming identical current profiles for I_1 and I_2, and charge storage (Q_1 and Q_2), then:

$$U = LI^2 + \frac{Q^2}{C}$$

and the time derivative of the total energy in the system becomes Eq. 5.11:

$$\boldsymbol{\frac{\delta U}{\delta t} = 2LI\frac{\delta I}{\delta t} + \frac{2}{C}Q\frac{\delta Q}{\delta t}} \qquad \text{(Eq. 5.11)}$$

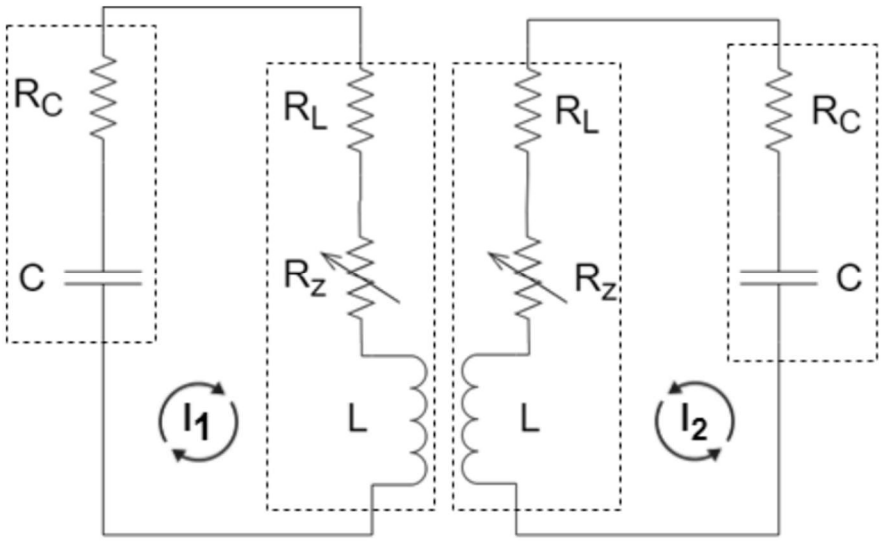

Figure 5.4: Two adjacent LCR Circuits demonstrating disengagement coil circuitry

The electrical energy dissipated in the system is split between conventional resistive losses and energy transferred to mechanical motion through R_Z, given in Eq. 5.12:

$$\begin{aligned} \boldsymbol{\delta U} &= \boldsymbol{-I_1^2 R\,\delta t\; - I_2^2\, R\delta t - I_1^2\, R_z \delta t\; - I_2^2\, R_z \delta t} \\ &= \boldsymbol{-2I^2 R\delta t - 2\, I^2 R_z \delta t} \end{aligned} \qquad \text{(Eq. 5.12)}$$

where $R = R_C + R_L$.

5.9.1.1 Kinetic Energy Equivalence:

In the case of perfect coil alignment and assuming negligible losses, the mechanical work performed by the system is manifested entirely as translational kinetic energy by (Eq. 5.13):

$$\boldsymbol{K.E.} = \frac{\mathbf{1}}{\mathbf{2}}\boldsymbol{mv^2} = \int \boldsymbol{I^2 R_z \delta t} \qquad \text{(Eq. 5.13)}$$

Alternatively, the work performed can be computed from Maxwell's formulation of the magnetic interaction between two current-carrying coils. The axial force is defined as:

$$F_z = I_1 I_2 \frac{\delta M}{\delta z}$$

Integrating over the separation distance z yields the mechanical work (Eq. 5.14):

$$\boldsymbol{W} = \int \boldsymbol{F_Z\, \delta z} = \int \boldsymbol{I_1 I_2\, \delta M} \qquad \text{(Eq. 5.14)}$$

Babic et al. in [107] provide an expression for $\delta M/\delta z$ as a function of coil geometry:

$$\frac{\delta M}{\delta z} = \frac{\mu_o z N_1 N_2}{2r} \Phi(k)$$

Considering $v_z = \delta z/\delta t$, the time derivative of mutual inductance becomes:

$$\frac{\delta M}{\delta t} = \frac{\mu_o z v_z N^2}{2r} \Phi(k)$$

Substituting into Eq. 5.8 and assuming $I_1 = I_2 = I$, yields Eq. 5.15:

$$\boldsymbol{W = \frac{\mu_o N^2}{2r} \int I^2 z v_z \Phi(k)\, \delta t} \quad \text{(Eq. 5.15)}$$

Comparing Eq. 5.13 with Eq. 5.15 allows identification of the equivalent dynamic resistance R_z as Eq. 5.16:

$$\boldsymbol{R_z = \frac{\mu_o N^2}{2r} z v_z \Phi(k)} \quad \text{(Eq. 5.16)}$$

This formulation shows that the mechanical energy conversion can be represented electrically as a variable resistance term dependent on both coil separation and velocity.

5.9.1.2 Differential Equations:

Substituting the time-varying R_z into the total circuit model yields a second-order differential equation for the system, with a time-dependent damping term:

$$0 = 2L\frac{\delta^2 Q}{\delta t^2} + R(t)\frac{\delta Q}{\delta t} + \frac{2Q}{C}$$

where $\mathrm{R(t)} = 2(R + R_z)$. Solving this equation for the current requires either mapping $R(t)$ onto an equation with known analytical solutions or employing a recursive approach using an infinite sequence of exactly solvable equations, each derived from a base equation with established solutions. Consequently, as the analytical solution or base equation is not known, it becomes excessively complex to solve.

However, if it can be demonstrated that R_z remains much smaller than R over the relevant time window, this simplifies to a conventional second-order RLC circuit to Eq. 5.17:

$$\boldsymbol{0 = L\frac{\delta^2 I}{\delta t^2} + R\frac{\delta I}{\delta t} + \frac{I}{C}} \quad \text{(Eq. 5.17)}$$

Having a damping factor $\alpha = R/2L$ and natural frequency $\omega_o = 1/\sqrt{LC}$, similar to a classical second-order RLC circuit. If the circuit is underdamped, $\alpha < \omega_o$, the current has

an oscillatory profile. If overdamped, $\alpha > \omega_o$, the response is non-oscillatory and exhibits a gradual exponential decay.

Solving the second-order differential equation for the overdamped case equates to (Eq. 5.18):

$$\boldsymbol{I(t) = \frac{CV\omega_o^2}{2\sqrt{\alpha^2 - \omega_o^2}} \left(e^{\lambda_1 t} - e_2^{\lambda_2 t}\right)} \qquad \text{(Eq. 5.18)}$$

where $\boldsymbol{\lambda_1 = -\alpha + \sqrt{\alpha^2 - \omega_o^2}}$ and $\boldsymbol{\lambda_2 = -\alpha - \sqrt{\alpha^2 - \omega_o^2}}$. This expression forms the basis for simulating the current profile and, by extension, the evolution of disengagement forces.

The selection and sizing of the capacitor, inductor, and resistive elements are critical for maximising the efficiency of energy transfer from electrical storage to mechanical impulse. For the capacitor, key parameters include the capacitance, equivalent series resistance (ESR), and voltage rating, which govern the total energy available and the rate at which it can be delivered. For the inductor, design optimisation involves selecting the number of turns, wire gauge, and winding configuration to achieve high magnetic force generation within the volumetric and mass constraints of the satellite. The series resistance, arising from both the coils, capacitor ESR and any resistive element in the conduction path, affects current decay and energy dissipation. Together, these parameters determine the temporal profile and magnitude of the disengagement force and ultimately define the mechanism's overall performance and efficiency.

5.9.2 Thermal Model

During disengagement, high current pulses through the coils result in Joule heating, which increases the coil temperature and, consequently, the electrical resistance. This rise in resistance can reduce the effective current and diminish the electromagnetic force produced, especially in systems operating near performance limits. To account for these effects, a thermal model is incorporated to simulate the temperature evolution of the coils and their impact on the electrical domain.

The instantaneous power dissipated in each coil due to resistive heating is expressed as:

$$\boldsymbol{P(t) = I(t)^2 \cdot R(t)}$$

where $I(t)$ is the time-dependent current and $R(t)$ is the temperature-dependent resistance of the coil. The temperature rise is computed using a lumped heat balance model, Eq. 5.19:

$$\boldsymbol{\Delta T(t) = \frac{1}{mc_P}\int_0^t P(\tau)d\tau} \quad \text{(Eq. 5.19)}$$

Here, m is the mass of the coil c_p is the specific heat capacity, which in this case corresponds to copper. This approach assumes uniform temperature distribution within the coil, which is valid for short-duration pulses where temperature gradients can be neglected. The coil resistance at time t is updated as a function of temperature using the linear approximation in Eq. 5.20:

$$\boldsymbol{R(t) = R_o(1 + \alpha\Delta T(t))} \quad \text{(Eq. 5.20)}$$

where R_o is the resistance at ambient temperature and α is the temperature coefficient of resistance for copper. The updated resistance value is fed back into the electrical model at each time step, forming a closed-loop interaction between the thermal and electrical domains. This thermal-electrical coupling allows the simulation to account for resistive degradation of performance under repeated or prolonged activations.

The electromagnetic coils used in the disengagement mechanism are actuated through short-duration current pulses, resulting in transient Joule heating. As the disengagement event occurs over a timescale of milliseconds to seconds and is typically executed only once per satellite, the thermal response of the coils is dominated by transient rather than steady-state effects.

To bound the thermal behaviour during actuation, conservative assumptions were adopted regarding coil resistance, current amplitude, and initial temperature. The resulting temperature rise during a single disengagement pulse was found to be limited and compatible with typical PocketQube thermal environments. Additionally, thermal baseline temperatures were informed by representative PocketQube thermal studies, providing an estimate of the operational temperature range prior to actuation.

A full thermal analysis of the integrated PQ8 system, including radiative coupling between units, conduction paths through structural interfaces, and orbital hot–cold cases, was not undertaken in this work. Such an analysis is highly dependent on final configuration details and mission-specific parameters and is therefore deferred to future work. The present study instead demonstrates that coil heating during disengagement does not constitute a first-order feasibility constraint for the proposed mechanism.

5.9.3 Interface Interaction Models

The mechanical interface between adjacent PQ8 satellites includes pogo-pin springs and neodymium magnets, both of which contribute forces during the initial phase of disengagement. The magnets generate an attractive force that must be overcome to initiate separation, while the pogo-pins provide a preloaded spring force that aids in pushing the satellites apart. Together, these elements define a threshold force that the disengagement coils must exceed to initiate motion.

To accurately capture their influence on the separation dynamics, empirical force–displacement data were obtained through experimental characterisation of the interface components. This data was then fitted and integrated into the simulation model. Figure 5.5 illustrates the measured force responses of both the magnetic and spring elements as a function of separation distance.

When simulating the model, the relative distance between the two satellite bodies is computed at each time step, and the corresponding magnetic attraction and spring repulsion are interpolated from their respective force–distance datasets. This allows the simulation to dynamically evaluate the net interface force at each time-step.

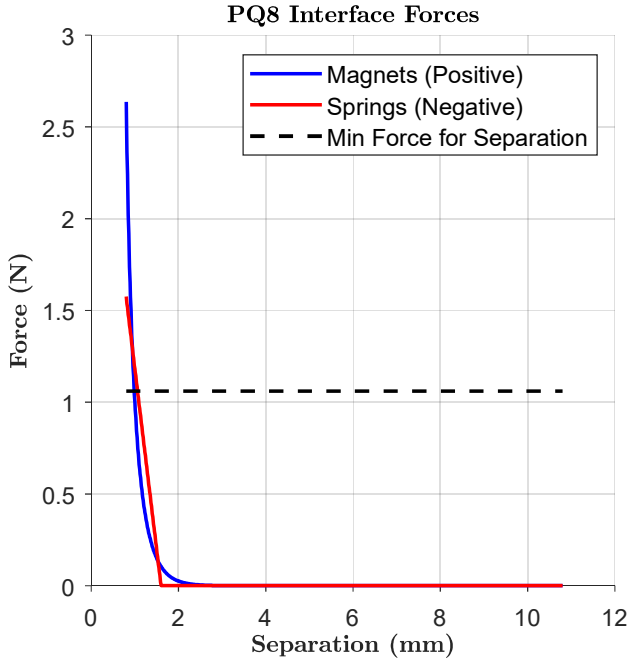

Figure 5.5: Measured PQ8 Interface Forces

5.9.4 Friction Model

Friction acts as a resistive force opposing the relative motion between adjacent satellite bodies during disengagement. In the PQ8 assembly, friction arises primarily from contact between the aluminium 6061 structural frames and the carbon steel guide pins used to maintain alignment between units.

This model assumes a conservative scenario in which no lubrication is applied to the guide pins. As a result, the coefficient of friction corresponds to dry contact between aluminium and steel, yielding a higher frictional resistance than would occur under lubricated conditions.

In the disengagement mechanism context, the normal force that drives friction is not due to gravity but originates from the radial electromagnetic repulsion between misaligned coils. Any lateral offset during disengagement induces a radial component of the repulsive force, which presses the satellite bodies against the guide pins and thereby generates friction. This frictional force at each time step is calculated using Eq. 5.21:

$$\boldsymbol{F_{Frivtion}(t) = \mu F_{Radial}(t)} \quad \text{(Eq. 5.21)}$$

where μ is the coefficient of friction and $F_{Radial}(t)$ is the instantaneous lateral force due to coil misalignment. This force is included in the overall axial force calculation. It acts in opposition to the net disengagement force, thereby reducing the effective linear acceleration and total impulse imparted to the satellite.

5.9.5 Linear Kinetic Model

The linear kinetic model governs the translational motion of the satellite resulting from the net axial force generated during disengagement. It integrates all relevant force contributions, including the electromagnetic repulsion, pogo-pin spring force, magnetic attraction, and friction, to compute the satellite's acceleration, velocity, and kinetic energy over time.

At each simulation time step, the net axial force acting on the satellite is calculated as:

$$F_{net}(t) = F_{axial}(t) + F_{spring}(t) - F_{magnet}(t) - F_{friction}(t)$$

This net force is then used to compute the instantaneous linear acceleration via Newton's second law, Eq. 5.22:

$$\boldsymbol{a(t) = \frac{F_{net}(t)}{m}} \quad \text{(Eq. 5.22)}$$

where m is the mass of the satellite. The linear acceleration is numerically integrated to obtain the velocity profile Eq. 5.23:

$$\boldsymbol{v(t) = \int_{o}^{t} a(\tau) d\tau} \quad \text{(Eq. 5.23)}$$

From the velocity, the translational kinetic energy imparted to the satellite is calculated through (Eq. 5.24):

$$\boldsymbol{\Delta E_{Linear}(t) = \frac{1}{2} m v(t)^2} \quad \text{(Eq. 5.24)}$$

This model provides a direct link between the time-varying force environment and the resulting separation dynamics. It enables the prediction of final separation velocity and impulse, which are critical performance metrics for verifying whether the mechanism meets its dispersal objectives under the imposed constraints.

5.9.6 Rotational Kinetic Model

The rotational kinetic model captures the angular motion induced during disengagement as a result of off-centre force application or structural asymmetries. When the electromagnetic force does not act through the satellite's centre of mass (CoM), a torque is generated, producing angular acceleration and rotation. This rotational motion affects post-separation stability and imposes additional correction demands on the ADCS.

At each simulation time step, the torque about the CoM is calculated using Eq. 5.25 as the vector cross-product of the moment arm and the applied force

$$\mathbf{T(t) = r \times F(t)} \quad \text{(Eq. 6.25)}$$

The corresponding angular acceleration is obtained using the satellite's moment of inertia matrix I, through Eq. 5.26:

$$\boldsymbol{\alpha(t) = I^{-1} \cdot \mathbf{T}(t)} \quad \text{(Eq. 6.26)}$$

Integrating the angular acceleration over time yields the angular velocity and total angular displacement, through Eqs. 5.27 and 5.28, respectively:

$$\boldsymbol{\omega(t) = \int_{0}^{\tau} \alpha(\tau) d\tau} \quad \text{(Eq. 6. 27)}$$

$$\theta(t) = \int_{0}^{t} \alpha(\tau)\, d\tau \quad \text{(Eq. 6.28)}$$

The rotational kinetic energy imparted to the satellite is then given by Eq. 5.29:

$$\boldsymbol{\Delta E_{Rot}(t) = \frac{1}{2}\omega(t)^{\top} I \omega(t)} \quad \text{(Eq. 5.29)}$$

In practice, rotational motion is constrained in the early stages of separation by the guide pins that maintain alignment between adjacent satellites. These pins restrict angular freedom until a minimum separation distance is reached, at which point rotational motion becomes unconstrained. The model incorporates this constraint by suppressing angular acceleration when the axial separation remains below a defined engagement threshold.

5.9.7 Model Integration and Algorithm

This set of interconnected sub-models governs the complete separation kinematics, each responsible for capturing a distinct physical domain relevant to the disengagement process. These include the electrical, magnetic, thermal, mechanical, and kinematic subsystems. Together, they determine the time-varying translational and rotational motion of the separated satellites, as well as the energy conversion dynamics underlying the mechanism's performance.

Figure 5.6 illustrates the overall system model, showing the transformation from capacitor voltage through current, force, motion, and ultimately into translational and rotational kinetic energy. To simulate this process with fidelity, each domain-specific model is integrated into a sequential, time-stepped simulation, showcasing the transformation from capacitor charge voltage, V, to linear and rotational separation, $\Delta\theta \; and \; \Delta v$, respectively.

The simulation begins with the electrical model, which calculates the instantaneous coil currents, I, based on the capacitor voltage, V, and temperature-dependent coil resistance, R_{Coil}. These current values are then used in the electromagnetic

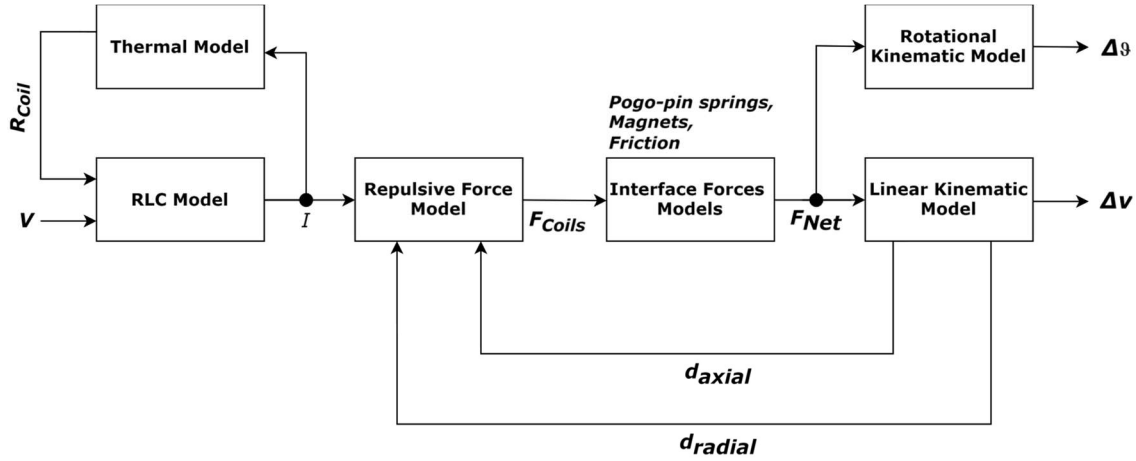

Figure 5.6: Disengagement Mechanism System Model

model to determine the axial and radial forces, F_{Coils}, imparted by the disengagement coils.

The thermal model runs in parallel, computing the coil temperature rise due to Joule heating. The increased resistance is fed back into the electrical model, forming a closed-loop feedback loop between thermal and electrical models. This feedback loop repeats at every iteration, enabling the simulation to account for performance degradation due to heating and its impact on current and force output.

The interface model evaluates additional mechanical forces, including magnetic attraction and the spring preload from the pogo pins. The friction model adds a resistive force component arising from radial misalignment and structural contact with guide pins. These models collectively contribute to the net force, F_{net}, acting on the system at each time step.

This net force is passed into the linear kinetic model, which computes the satellite's instantaneous acceleration, velocity, and translational kinetic energy. Simultaneously, the rotational kinetic model determines torque, angular velocity, and rotational energy due to off-centre force application. If the axial separation remains below the guide pin disengagement threshold, rotational motion is constrained.

By integrating all domains, the simulation produces a time-resolved output of key parameters, including coil current, separation distance, temperature, linear and angular velocities, and kinetic energy. The simulation enables analytical evaluation of the disengagement mechanism's performance under realistic operational conditions and constraints. The algorithm that governs this process is presented in Algorithm 5.1.

Algorithm 5.1: Time-Domain Simulation Procedure

Procedure: Time-Domain Disengagement Model
for $t = 0; t \leq 1; (t + \Delta t)$++, **do**
  if $t \leq Pulse\ Width$
    Calculate Coil Resistance at temperature *T(t)*
    Calculate the coil currents.
    Calculate the change in coil temperature.
    Calculate the Disengagement forces.
    Interpolate the magnetic force and spring force at distance z
    Calculate Friction
    Calculate Net Force through:
    $F_{Net}(t) = F_{Axial}(z) + F_{Spring}(z) - F_{Magnet}(z) - F_{Friction}$
  else
    Set $I(t) = 0, F_{Axial}(t) = 0, F_{Radial}(t) = 0$
    Calculate Net Force, $F_{Net}(t) = F_{Spring}(z) - F_{Magnet}(z)$
  end
  Calculate Torque (Eq. 6.25)
  Calculate angular velocity and acceleration.
  Calculate Rotational Kinetic Energy.
  Calculate linear velocity and acceleration.
  Calculate Translational Kinetic Energy
  Integrate linear acceleration to obtain $z(t)$
  Integrate rotational acceleration to obtain $\theta(t)$
end
Output: $z(t)$, $\theta(t)$, $E_{Linear}(t)$, $E_{Rot}(t)$

5.9.8 Dynamic Model Summary

The simulation provides a comprehensive tool for evaluating the dynamic performance of the disengagement mechanism under realistic operational conditions. By coupling electrical, thermal, mechanical, and kinematic models, it captures the interdependencies that govern energy conversion and motion during separation. The resulting outputs, including separation velocity, rotational motion, and energy partitioning, serve as key performance indicators for verifying compliance with mission requirements and guiding subsequent design decisions.

The force model assumes nominal axial alignment between coils, with radial offset represented through the parameter d_{radial}, which is propagated through the repulsive force block. Other alignment errors, such as angular tilt and combined multi-axis misalignment, are not explicitly modelled in this chapter.

In practice, alignment in all directions is constrained by the mechanical tolerances of the PocketQube platform. Due to the small, dense packaging of the satellite and the use of CNC-machined frames and machine-assembled PCB subsystems, relative

alignment between disengagement components is typically limited to approximately ± 0.1 mm. Larger misalignments would prevent physical assembly of the satellite. Consequently, the assumption of near-axial alignment represents a bounded idealisation, whose validity is governed by manufacturing tolerances.

Radial misalignment is explicitly included in the force model structure, and further uncertainty treatment of alignment parameters is addressed in the subsequent chapter under the uncertainty analysis of simulated parameters.

Mechanical symmetry is implicitly assumed in two respects: symmetry between the disengaging PocketQubes and symmetry in the overall mass distribution of the system. The rotational kinematic model accounts for the satellite's moment of inertia, which is derived from detailed CAD mass modelling. This ensures that the rotational response is governed by a realistic inertial distribution rather than an idealised point-mass assumption.

Symmetry between disengaging units is assumed at the geometric and mechanical interface level. In practice, this is justified by the manufacturing approach: structural elements are CNC-machined, while electronic subsystems are produced using automated PCB fabrication and assembly. As a result, geometric and mass deviations between identical subsystems are expected to be small relative to the overall system scale.

Additionally, magnetic symmetry is also assumed in the repulsive force model, such that coil geometry, winding density, and target properties are treated as uniform and repeatable. Local deviations in winding placement or material properties are not represented at this modelling stage.

Electrical parasitic elements are explicitly included in the RLC model, including wiring resistances, switch resistances, capacitor equivalent series resistances, and temperature-dependent resistance variations. These parasitic directly influence the current waveform that drives the force model.

Magnetic parasitic effects are not comprehensively modelled at this stage. Eddy current losses, leakage flux, fringing fields, and unintended ferromagnetic return paths are not explicitly represented in the repulsive force block. Instead, the force model represents an idealised mapping between current, geometry, and separation distance. Magnetic parasitic effects are investigated separately using finite-element analysis in the following chapter, where their influence is quantified and compared against the analytical model.

Joule heating and temperature rise of the coil are explicitly included through the coupled thermal model, which feeds back into the electrical resistance and therefore alters the discharge current and force profile.

Mechanical friction is included in the interface forces block, representing the dominant resistive mechanical effect during disengagement. However, secondary mechanical losses such as stiction, compliance of structural elements, impact losses during initial separation, and dynamic damping are not modelled explicitly. These effects are assumed to be second-order relative to the primary repulsive force, spring preload, magnetic holding forces, and frictional resistance.

This represents a modelling choice aimed at preserving tractability while capturing the dominant energy pathways during disengagement. The modelling approach in this chapter prioritises structural clarity and physical consistency of subsystem interactions over exhaustive representation of all second-order effects. Idealised alignment, symmetry, and magnetic behaviour are therefore bounded by physical constraints imposed by manufacturing tolerances, assembly feasibility, and component repeatability.

Where assumptions may significantly influence predicted outputs, such as separation force, impulse, disengagement timing, and resulting linear and rotational velocity increments, their sensitivity is addressed in later chapters through uncertainty analysis.

5.9.9 Sensitivity of Disengagement on Key Parameters

The dynamic model allows the influence of key parameters on disengagement behaviour to be examined. In particular, the predicted separation force, impulse, and timing are strongly influenced by coil geometry, material properties, and circuit resistance.

The repulsive force model depends directly on coil geometry through parameters such as number of turns, coil diameter, axial length, and initial air gap. Increasing the number of turns or reducing the effective air gap increases the magnetic field intensity for a given current, thereby increasing peak repulsive force. However, increasing the number of turns also increases coil resistance, which reduces peak current for a fixed capacitor energy. As a result, coil geometry introduces an inherent trade-off between magnetic field generation and electrical efficiency.

Similarly, changes in coil diameter and axial length alter the spatial distribution of the magnetic field and its gradient with respect to separation distance. Since the force is strongly dependent on the axial separation $\boldsymbol{d_{axial}}$, small geometric changes near the initial engagement position can significantly alter the early force-time profile and therefore the time required to overcome magnetic holding force, spring preload, and friction. Consequently, separation timing is particularly sensitive to geometric tolerances that affect the initial field gradient.

Material properties influence both the electrical and magnetic behaviour of the system. The electrical resistivity of the coil conductor, which is temperature dependent, directly affects the discharge current profile and therefore the magnitude and duration of the repulsive force. Higher resistivity or elevated operating temperature reduces peak current and broadens the discharge pulse, reducing peak force while potentially increasing total impulse.

Magnetic material properties, such as permeability and saturation behaviour of nearby ferromagnetic elements, affect field distribution and force efficiency. Although idealised in the analytical force model, finite-element analysis in later chapters demonstrates that deviations from ideal magnetic behaviour can reduce effective force compared to nominal predictions. As a result, separation force predictions are sensitive not only to coil current but also to the magnetic environment created by surrounding materials.

Circuit resistance, including coil resistance, wiring resistance, switch resistance, and contact resistance, directly governs the peak current delivered during capacitor discharge. Since repulsive force scales strongly with current, even modest increases in total series resistance produce a disproportionate reduction in peak force. This primarily affects early-time behaviour, when force must exceed magnetic holding force, spring preload, and friction to initiate separation.

These sensitivities motivate the inclusion of temperature-dependent resistance, friction forces, and geometric separation variables within the Chapter 5 model architecture, and they provide the physical basis for the uncertainty and experimental repeatability analyses presented in subsequent chapters.

5.10 Disengagement Mechanism Circuit Design

The disengagement mechanism requires a circuit capable of delivering high-current, short-duration pulses to the magnetorquer coils, which are repurposed to function as the separation actuators responsible for disengagement. This dual-use system must also support standard attitude control operations, requiring the circuit to operate in two different modes: single, high-current pulse mode, or pulse-width modulated (PWM) low-current mode. This section presents the full design and optimisation of the disengagement circuitry. It covers the selection of capacitors and coils, the development of the charge and discharge circuits, and the implementation of control logic and synchronisation mechanisms.

Figure 5.7 provides a high-level block diagram of the disengagement mechanism circuitry, illustrating the relationships between the energy storage, switching, control, and actuation subsystems. While detailed schematics of the complete DM are provided in Appendix B.

5.10.1 Supercapacitor Selection

The supercapacitor bank serves as the energy reservoir for the disengagement mechanism, responsible for delivering a high-current pulse during actuation. The key parameters influencing capacitor selection include energy density, peak power capability, ESR, and form factor. For the latter, volumetric constraints restrict the available volume for capacitor integration to 40 × 16 × 8 mm³, necessitating balancing between electrical performance and physical size.

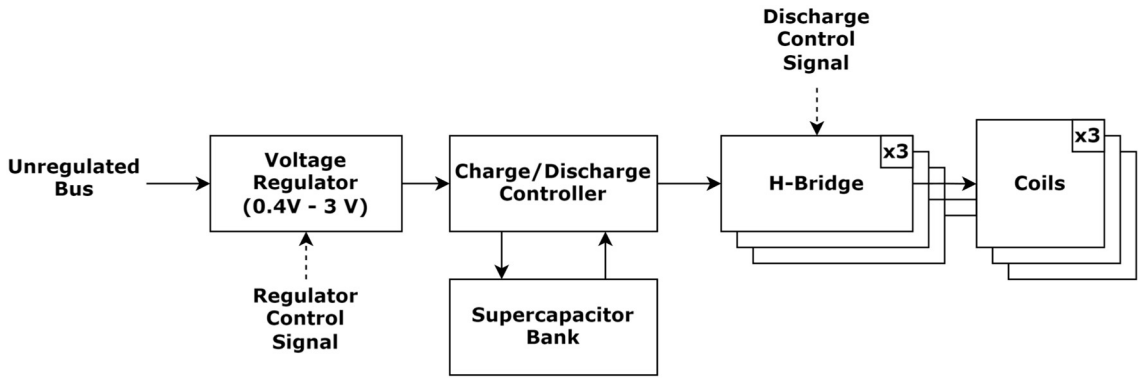

Figure 5.7: Block Diagram of the Disengagement Mechanism Circuitry

The energy stored in a capacitor is proportional to both its capacitance and the square of its operating voltage. Increasing the energy stored is desired as it increases the energy available for disengagement. Therefore, capacitors with higher capacitance and voltage properties are desired. Assessment of available supercapacitors that conform to the satellite's volumetric constraint yielded two categories. The first included high-voltage capacitors, with relatively lower capacitance and higher ESR values. The second category included low-voltage capacitors, with higher capacitance and lower ESR.

Opting for high-voltage capacitors offers the benefit of delivering short, high-current pulses due to the reduced discharge time constant. However, this introduces additional challenges. First, the shorter pulse duration increases sensitivity to synchronization errors between firing events, as small mismatches result in only partial overlap of magnetic fields and thus reducing the net disengagement force. Second, lowering the capacitance increases the risk of underdamping the discharge circuit, leading to oscillatory current profiles. In such cases, the resulting oscillating magnetic field may briefly induce attractive forces during current zero-crossings, particularly if synchronization between coils is imperfect.

Conversely, using low-voltage, high-capacitance supercapacitors results in higher time constants and longer pulses, thereby reducing reliance on precise synchronization. Although the voltage is lower, the ESR is also lower, which may still allow the generation of high current pulses, provided the coil parameters are appropriately matched. This tight coupling between capacitor and coil design adds further complexity to the selection process.

In either case, the trade-offs involved make an analytical determination of the optimal capacitor difficult. At this stage, it could only be concluded that the ideal capacitor for this application must balance three competing factors:

- Sufficient energy and power density to generate the required impulse,
- Low ESR to enable efficient current delivery,
- A capacitance value that avoids underdamping while providing adequate synchronisation tolerance.

Based on an evaluation of electrical characteristics and volumetric constraints, three capacitors were shortlisted as suitable candidates, including both single-unit and series-paired configurations, as shown in Table 5.9.

Table 5.9: Capacitor Shortlist

Device	Max ESR (Ω)	Capacitance (F)	Voltage (V)	Configuration
SCMR22H155PRBB0	0.180	1.5	6	Single
SCCR25E505SRB	0.085	5	3	2 × Series
HV0830-2R7605	0.040	6	2.7	2 × Series

Each of the shortlisted capacitor configurations was evaluated in combination with an optimised coil design tailored to its electrical characteristics. These capacitor–coil pairs were then compared based on their overall disengagement performance. The results of this optimisation process are presented in the following section, where the most effective configuration is selected based on system-level criteria.

The capacitor values listed in Table 5.9 represent nominal manufacturer specifications. In practice, supercapacitors exhibit relatively large component tolerances compared to conventional electrolytic or ceramic capacitors, with typical capacitance tolerances in the range of ± 20 % to ± 30 %, and variation in equivalent series resistance (ESR) between production batches. These tolerances directly influence the discharge dynamics of the disengagement circuit and therefore the achievable impulse and separation velocity.

Capacitance tolerance affects the total stored energy according to $E = \frac{1}{2}CV^2$. A negative tolerance reduces available energy and lengthens the discharge time constant, potentially lowering peak current and resulting electromagnetic force. Conversely, a positive tolerance increases stored energy and peak current, which can improve separation performance but also raises the risk of excessive current flowing through the driver circuitry.

ESR tolerance is equally critical. Higher-than-nominal ESR increases damping and reduces peak current, leading to weaker magnetic repulsion and reduced separation velocity. Lower-than-nominal ESR produces higher peak currents, which may drive the circuit into the underdamped regime. This behaviour is particularly sensitive for high-voltage, low-capacitance configurations, where the discharge time constant is already short and small variations in ESR can strongly affect synchronisation tolerance between adjacent coils.

In this work, the capacitor shortlist in Table 5.9 was evaluated using nominal capacitance and voltage ratings to enable consistent comparison between candidate devices. Component tolerances were not explicitly propagated through the capacitor–coil

optimisation described in Section 5.10.2, and the predicted performance values should therefore be interpreted as nominal estimates. The influence of capacitance and ESR tolerances on discharge dynamics, peak current, and delivered impulse was not systematically analysed as part of this design cycle.

Accordingly, Table 5.9 should be interpreted as defining a feasible capacitor design space that satisfies the geometric and rating constraints, rather than uniquely determining the realised discharge behaviour. In practice, the as-built system performance will depend on the specific device tolerances (capacitance and ESR), the realised coil parameters, and their combined effect on the transient discharge response. Quantifying the sensitivity of disengagement performance to these tolerances is identified as an important area for future refinement of the model and design methodology.

5.10.2 Disengagement Coil Design

The disengagement coils are responsible for generating the repulsive magnetic forces that drive satellite separation. Their design directly affects current handling, force generation, and overall energy transfer efficiency. However, coil design presents a highly coupled problem, whereby the number of turns, wire diameter, resistance, inductance, and geometric dimensions (internal volume of 26 × 36 × 4 mm^3, and an external volume of 30 × 40 × 4 mm^3) are all interdependent..

Two key observations from the static force analysis in Section 5.2 guided the coil design strategy. First, increasing the coil radius within the physical limits of the satellite's internal structure enhances axial force generation. Second, increasing the ampere-turns leads to greater magnetic repulsion for a fixed geometry.

To address the first point, the coil was designed to occupy the maximum available area within the allocated footprint. This resulted in a rectangular coil shape, which does not conform directly to the circular geometry assumed in the analytical force models. To enable meaningful comparison with these models, the rectangular coil was approximated by a circular loop of equivalent area. The effective radius $r_{approx}$is given by:

$$r_{approx} = \sqrt{\frac{lh}{\pi}}$$

where l and h are the length and height of the rectangular coil. This approximation preserved the cross-sectional area relevant to magnetic field generation while allowing force predictions using existing circular-coil equations.

To incorporate multiple turns, the original single-loop force expressions were extended by assuming that the inter-turn spacing is negligible relative to the overall coil radius and that the coil's thickness of 4 mm does not introduce significant variation in the axial force distribution. Under these assumptions, the force can be evaluated at the geometric centre of the coil's thickness and scaled by a factor of N^2, where N is the total number of turns in each coil.

Optimising the ampere-turn product also introduced a tightly coupled design trade-off. Increasing the number of turns improves magnetic force generation but simultaneously raises both resistance and inductance. An increase in resistance also reduces peak current and leads to greater energy loss during discharge, negatively affecting the system's efficiency. Meanwhile, higher inductance can drive the circuit into underdamped operation, resulting in oscillatory current profiles. Using a larger wire diameter helps reduce resistance, allowing for higher current flow, but also limits the number of turns that can be accommodated within the available volume.

However, a greater inductance also enhances mutual coupling between adjacent coils and thus increases the rate of change of mutual inductance as the satellites separate. According to Maxwell's force formulation, this rate of change contributes directly to the generated repulsive force. Therefore, higher coil inductances can potentially improve overall force output.

This interplay indicates that coil parameters cannot be optimised in isolation, as each influences the others through their combined effect on circuit behaviour and force generation. The design must therefore strike a balance between resistance, inductance, wire geometry, and current dynamics. Additionally, since the LCR parameters are tightly coupled, the optimal values for these parameters are relative to the selected supercapacitor.

To identify optimal coil parameters for each candidate capacitor, a numerical optimisation routine was implemented using MATLAB's *fmincon* solver. For each capacitor, the algorithm searched for the wire diameter that maximises the satellite separation velocity Δv, using the time-domain disengagement simulation presented in Algorithm 5.1.

The wire diameter d_w governs the number of turns that can be accommodated within the fixed coil cross-section, which is approximated by Eq. 5.30:

$$\boldsymbol{N = floor\left(\frac{16}{d_w}\right)} \quad \text{(Eq. 5.30)}$$

Once the number of turns is known, the total length of wire L_w is computed by multiplying the average turn length by N. This wire length, in combination with the copper cross-sectional area, A_w, is used to calculate the series resistance through Eq. 5.31:

$$\boldsymbol{R = \frac{\rho L_W}{A_W}} \quad \text{(Eq. 5.31)}$$

where $\rho = 1.68 \times 10^5$ Ω·mm, the resistivity of copper at 20 ºC.

The coil inductance is estimated using an empirical approximation from [110], given by:

$$\boldsymbol{L = \frac{0.8(\text{Radius})^2(\text{N}^2)}{6(\text{Radius}) + 9(\text{Length}) + 10(\text{Depth})}} \quad \text{(Eq. 5.32)}$$

Where $Radius$ is the radius of the disengagement coil in inches, and both $Length\ and\ Depth$ are the given by $\left(\sqrt{N} \times d_w\right)_{Inches}$.

These parameters, resistance and inductance, were then used within Algorithm 5.1 to evaluate the discharge current profile, electromagnetic force, and resulting satellite kinematics for each candidate configuration. The optimiser iteratively adjusts d_w, computes the corresponding coil parameters, and simulates the system response until the wire diameter that yields the maximum separation velocity Δv is found. A flow chart describing the process of finding the optimal coil for each capacitor bank is provided in Figure 5.8.

The optimisation identified an ideal solution using a 0.8 mm wire diameter in combination with the HV0830-2R7605 capacitor bank (6 F, 2.7 V, 80 mΩ ESR). This configuration achieved the highest separation velocity due to low resistance and well-matched damping behaviour, as shown in Figures 5.9 and 5.10.

However, while ideal for disengagement, this coil's low resistance yields excessively high current during the MT mode of operation, resulting in coarse magnetic dipole control. As a compromise, a 0.65 mm wire diameter design (second-best option) was selected to better balance disengagement performance with ADCS requirements. This version provides adequate separation force while ensuring manageable current levels for attitude control. Table 5.8 shows the ideal, compromise and actual parameters of the selected coil. The manufactured coils inside a PQ1 satellite are depicted in Figure 5.11.

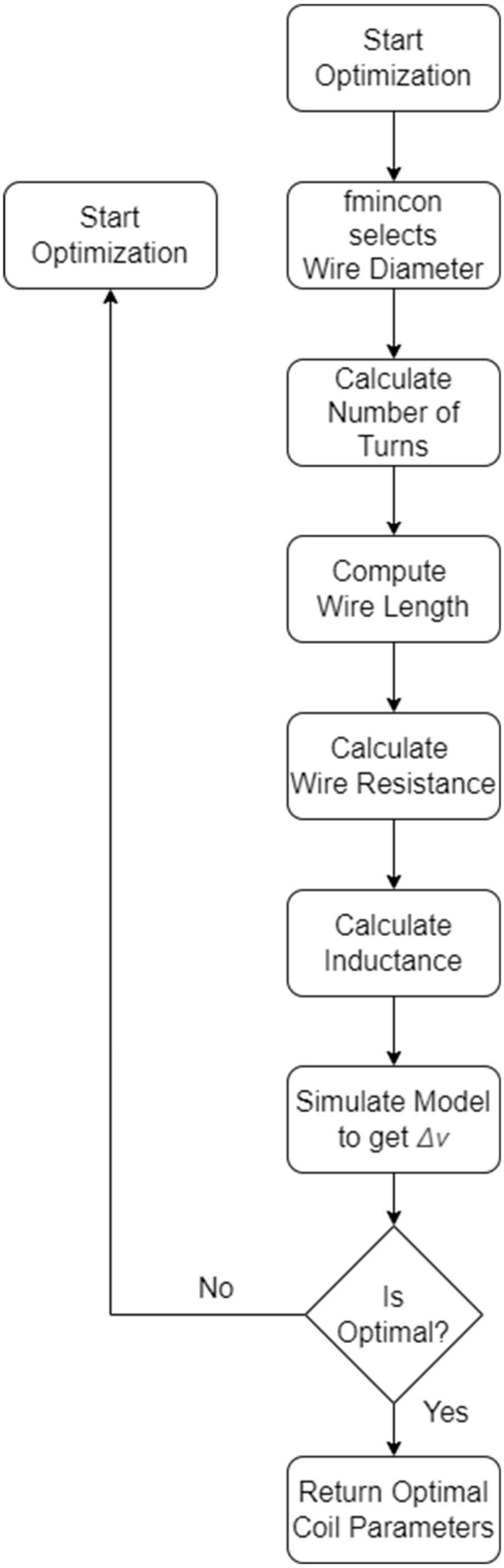

Figure 5.8: Flow Chart of Optimisation Process.

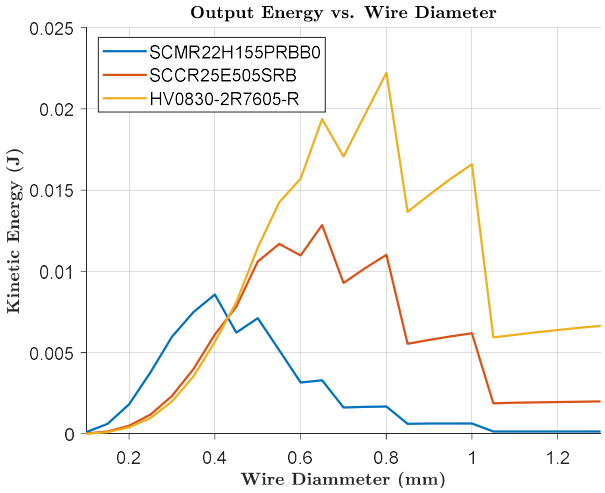

Figure 5.9: Optimal Wire Diameter Comparison

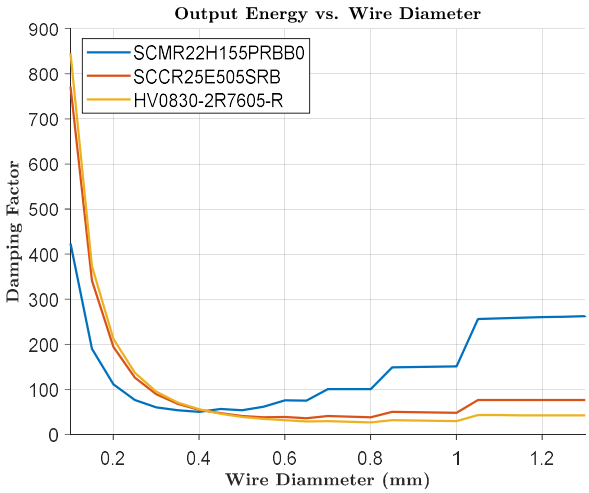

Figure 5.10: Damping Factor at various wire diameters

Table 5.10: Disengagement Coil Parameters

	Wire (mm)	Turns	Resistance (mΩ)	Inductance (μH)	Mass (g)
Ideal	0.85	16	88	11.4	7.5
Compromise	0.65	36	171	55.7	10.1
Actual	0.65	36	171 ± 6	55.7 ± 0.5	11.2 ± 1

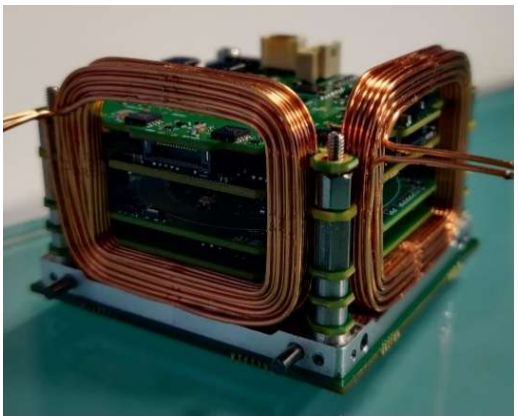

Figure 5.11: PQ1 Satellite magnetorquer/disengagement coils

5.10.3 Charge Circuit

The charge circuit is responsible for replenishing the energy in the supercapacitor bank, ensuring that sufficient voltage is available for both disengagement and magnetorquer operation. This circuit must operate efficiently across a wide voltage range and under strict power constraints, while maintaining compatibility with both automatic and autonomous modes of operation.

5.10.3.1 Step-Down Converter

The charging circuit is supplied from the satellite's unregulated power bus, which operates between 3.0 V and 4.1 V. The output voltage of the charge circuit must be adjustable to support both operational modes:

- In MT mode, a low output voltage (≈ 0.4 V) is required, based on the coil parameters derived in Table 5.8 and Eq. 5.2.
- In DM mode, the capacitors must be charged to their maximum rated voltage (typically 2.7 – 3.0 V) prior to reconfiguration into a series topology.

The circuit must also support a continuous current of at least 2.5 A to accommodate ageing-induced degradation in capacitor capacity and provide redundancy in case direct magnetorquer control is required from the buck converter.

To meet these requirements, the LM3253 synchronous step-down converter was selected. This device supports output voltages from 0.4 V to 3.6 V at currents up to 3 A, and operates at 2.7 MHz to minimise inductor and capacitor sizes. The converter's compact 2×2 mm QFN package and high-frequency switching make it well suited for the satellite's constrained PCB area. The complete circuit is shown in Figure 5.12.

However, a key drawback of high-frequency operation is reduced efficiency at low load currents, particularly toward the end of the charge cycle. In disengagement mode, worst-case efficiency reaches approximately 85%, whereas in magnetorquer mode it may drop to 70% due to extended low-current operation. To mitigate this, efficiency can be improved by charging the capacitors to a higher voltage over a shorter time. For instance, if a final operating voltage of 0.4 V is required, the capacitors may be charged to 0.8 V over approximately 0.7τ rather than being charged directly to 0.4 V over a full 5τ. This approach increases converter efficiency and reduces overall charge time. A similar strategy can be applied to enable operating voltages below 0.4 V, offering the added benefit of improved control resolution by lowering coil current during magnetorquer mode.

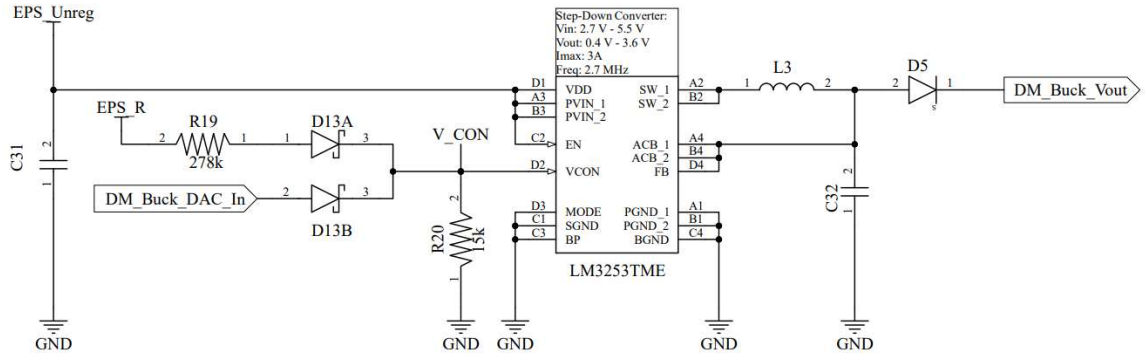

Figure 5.12: Charging Circuit Step-Down Converter

High-frequency operation also introduces challenges related to electromagnetic radiation (EMR), which can interfere with sensitive satellite subsystems. To mitigate these effects, careful PCB layout techniques are employed, including minimising loop areas, optimising ground planes, and strategic component placement to reduce noise coupling.

The converter's output voltage is controlled via an analogue input pin (V_{CON}), which is driven by a DAC output from the EPS microcontroller. The relationship is defined as:

$$V_{Out} = 2.5\, V_{CON}$$

To support autonomous operation in the event of EPS microcontroller failure, a passive hardware fallback is implemented. If no DAC output is provided, a voltage divider consisting of resistors R19 and R20, together with two matched Schottky diodes D13A and D13B , sets V_{CON} to 0.16 V. This ensures a default output voltage of 0.4 V, allowing the coils to remain operational in magnetorquer mode. When DAC output is available, the diodes function as an OR gate, enabling the controller to override the default voltage safely:

$$V_{CON} = \frac{(V_{EPS_R} - V_{FD})R_{20}}{R_{19} + R_{20}} \Rightarrow V_{Out} = 2.5\,(V_{DAC} - V_{FD})$$

This redundancy ensures magnetorquer functionality is maintained even under partial system failure, enhancing reliability and fault tolerance.

5.10.3.2 Series-Parallel Switch

To maximise energy transfer during disengagement while maintaining safe charging conditions, the supercapacitor pair is charged in parallel and discharged in series. This configuration enables efficient charging at a lower voltage and high-current

discharge at an elevated potential, at effectively double the charging voltage. The switching circuitry responsible for this reconfiguration is shown in Figure 5.13.

The circuit incorporates the two selected supercapacitors (C38 and C39), current-limiting resistors (R39 and R40), and a set of three power MOSFETs (Q9, Q10, Q11) governed by complementary control signals: *Series*, *Parallel*, and *Parallel_Inv*. The EPS microcontroller generates these logic signals and includes software-enforced dead time to avoid simultaneous conduction. The switching behaviour is defined as follows:

- When *Series* = LOW and *Parallel* = HIGH, MOSFET Q11 is activated, placing the two capacitors in series for discharge. In this mode, the total voltage across the coil doubles, increasing the peak current delivered during disengagement.
- When *Series* = HIGH and *Parallel* = LOW, Q9 and Q10 conduct while Q11 remains off. This connects the capacitors in parallel, enabling charging at a lower voltage.

To prevent reverse conduction through the MOSFET body diode during series mode operation, a blocking diode (D7) is inserted between the R40 and the positive terminal of the high-side capacitor. While this introduces a slight voltage drop during charging, it is essential for protecting the converter from reverse current during discharge.

Of the three switches, Q11 is the most critical from a performance perspective, as it remains in the discharge path during disengagement. Its drain-source resistance directly influences energy delivery. Since Q11 operates over a gate-source voltage range of 0.4 – 2.7 V (depending on capacitor charge), the selected device must exhibit low threshold voltage and minimal $R_{DS(on)}$ across this range to minimise conduction losses.

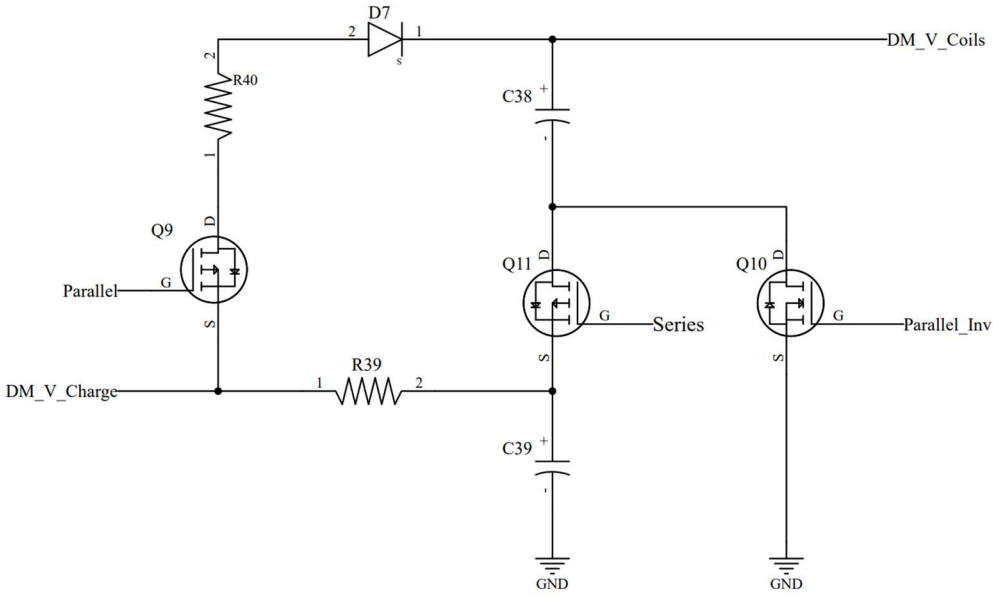

Figure 5.13: Series-Parallel Switching Circuit

The Si8851EDB MOSFET ([111]) was selected for this application due to its favourable characteristics, including a compact footprint and excellent performance in the desired voltage range. Its threshold voltage is approximately 1 V, and under nominal operating conditions (V_{GS} = 3.6 V, ambient = 25 °C), its $R_{DS(on)}$ is approximately 6 mΩ. At lower gate voltages, the on-resistance increases but remains within acceptable limits for short-duration pulses. The on-state characteristics for this MOSFET are provided in Figure 5.14.

MOSFETs Q9 and Q10 are used exclusively during the charging phase, where current levels are lower and timing is less critical. As such, their selection is less constrained, and moderate on-resistance is acceptable, allowing greater flexibility in component sourcing and layout.

This switching configuration enables electrical reconfiguration between parallel and series capacitor arrangements using compact solid-state components. While it introduces additional conduction losses, particularly across the discharge-side MOSFET (Q11) and the blocking diode (D7), it avoids the mechanical complexity and spatial demands of relay-based solutions. The use of commercial off-the-shelf (COTS) MOSFETs does impose limitations with respect to radiation tolerance and long-term reliability in space; as such, these components must be subjected to appropriate environmental testing, including thermal cycling, vacuum compatibility, and radiation exposure, to validate their performance and assess their risk within the mission profile.

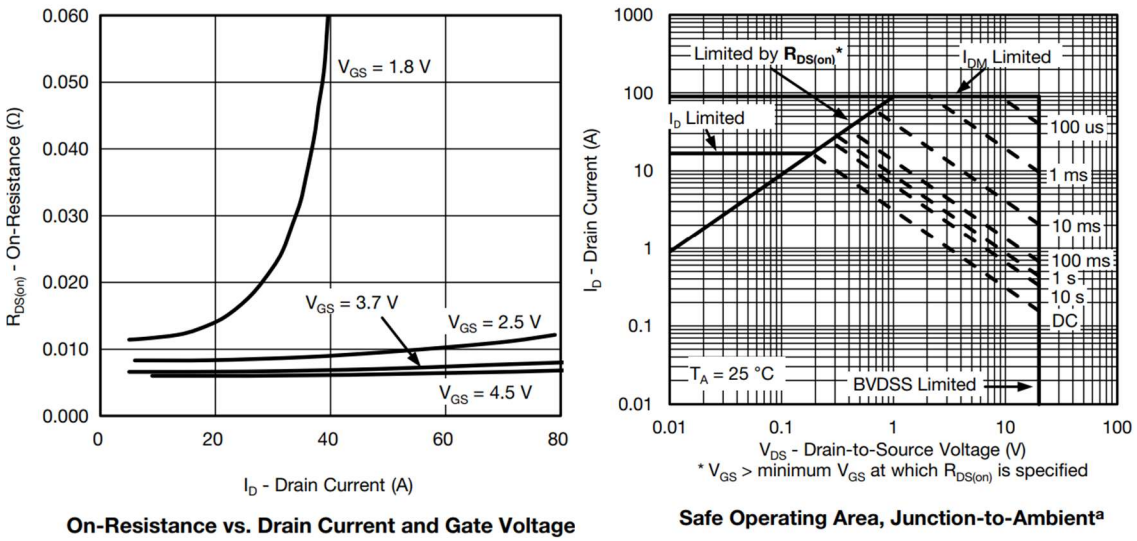

Figure 5.14: Si8851EDB on characteristics [111]

5.10.4 Discharge Circuit (H-Bridge)

The discharge circuit is designed to support both disengagement and magnetorquer operation. The electrical requirements are primarily governed by the disengagement mode, which demands high peak power, whereas the operational requirements are dictated by the attitude control system (ADCS), which requires precise, bidirectional coil actuation.

The power requirements for the discharge circuit are as follows:

- Operating voltage: 0.4 – 6 V
- *Maximum current*: 25 A (for a 100 ms pulse)

Operationally, the system must support bidirectional current flow through the coils to enable magnetic dipole generation in either direction. This necessitates the use of an H-Bridge circuit. Furthermore, given the bi-directional nature of the current path, each coil would typically require two control signals, one per side of the H-Bridge. With three magnetorquer coils, this results in six microcontroller pins and six EPS–ADCS connector lines. To reduce interface complexity, the system is designed such that each coil is controlled using a single trigger signal. This reduces pin allocation burden and operational complexity, at the cost of added hardware complexity.

The complete H-Bridge circuit is presented in Figure 5.15.

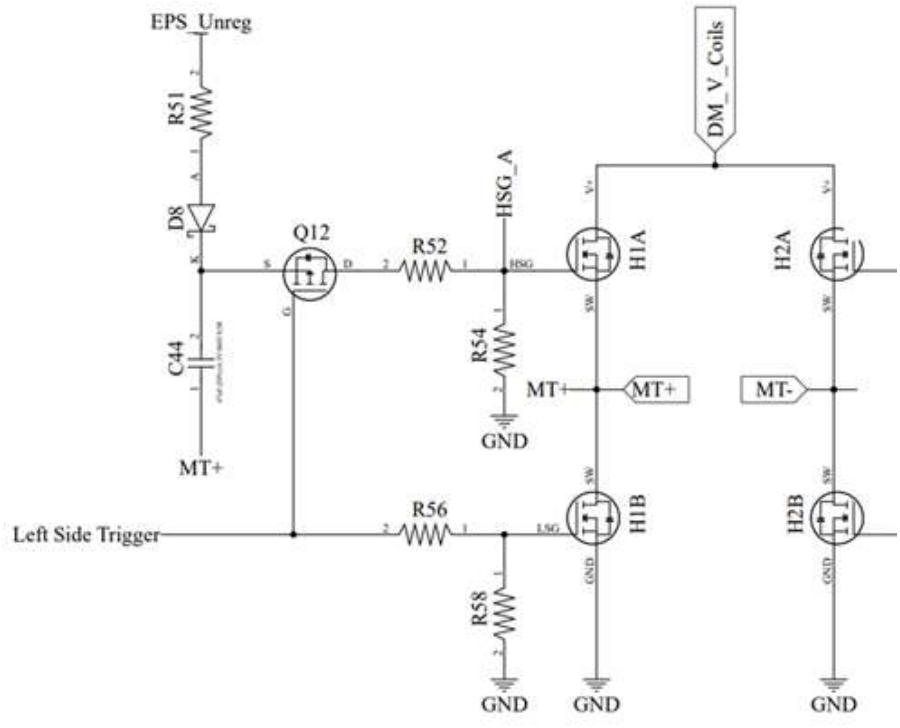

Figure 5.15: Disengagement/Magnetorquer H-Bridge (Left-hand side)

5.10.4.1 H-Bridge Circuit

A MOSFET-based topology was selected for the H-Bridge due to its superior current handling and switching speed characteristics. BJT devices were ruled out as they exhibit higher conduction losses resulting from their collector-emitter saturation voltage $V_{CE(sat)}$, which causes increased power dissipation under high-current operation. Moreover, BJTs are limited by slower switching transitions due to minority carrier storage effects at the base terminal, making them unsuitable for fast switching environments.

MOSFETs, being voltage-controlled devices, provide lower conduction losses through reduced drain–source resistance $R_{DS(on)}$, and faster transitions. Given the miniaturisation and high-power requirements of the system, an n-channel MOSFET topology was selected. Compared to p-channel devices, n-channel MOSFETs offer higher charge carrier mobility, which enables a lower $R_{DS(on)}$ for the same package size and thus improved efficiency in high-power applications.

To support high-side switching in the n-channel configuration, external gate driver circuitry is required to ensure the gate is driven sufficiently above the source voltage. The device selected for this application is the NTTFD2D8N03P1E ([112]), a half-bridge n-channel MOSFET package that integrates two matched power switches in a 3.3 × 3.3 mm footprint. This package meets the current and thermal performance requirements, whilst occupying minimal PCB area, making it well-suited for the miniaturised design requirements of the system.

With gate-source voltages between 3.6 V and 4.1 V, the device is capable of handling a 25 A pulse for up to 200 ms., as illustrated in Figure 5.16. Under these conditions, the current is constrained primarily by $R_{DS(on)}$, rather than thermal limits. Additionally, the expected voltage drop across the MOSFET is approximately 50 mV, corresponding to an on-resistance of around 2 mΩ, which ensures high efficiency in both DM and MT modes of operation.

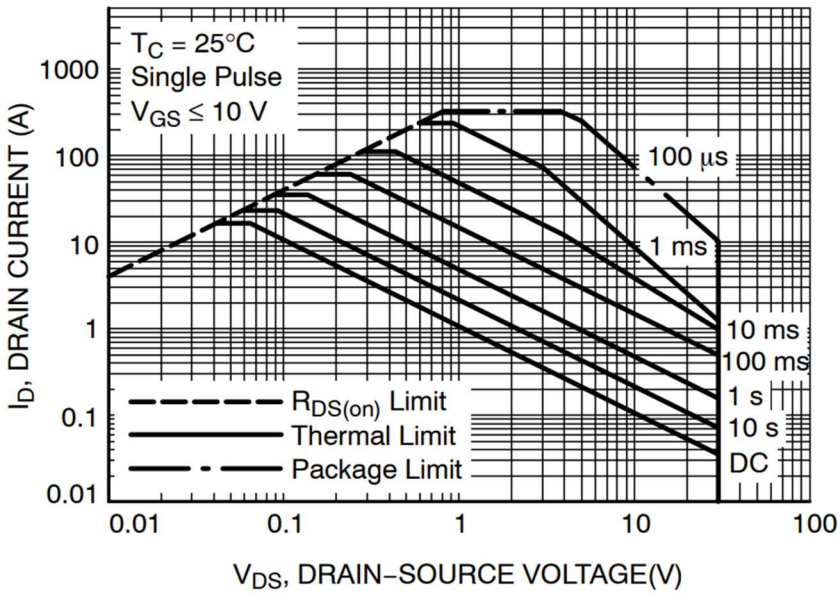

Figure 5.16: NTTFD2D8N03P1E Safe Operating Area [112]

5.10.4.2 Gate Driver Circuit

The gate driver circuits for the H-Bridge consist of R51, D8, and C44 on the left side, and the same circuit mirrored on the right side. During idle conditions, the negative terminal of C44 is held at ground potential through nodes H1B, allowing the bootstrap capacitors to charge via the unregulated bus voltage V_{EPS_UNREG} through the respective resistors and diodes.

Resistor R51 limits the inrush current during capacitor charging to protect the power supply, while diode D8 prevents reverse current flow once the H-Bridge is triggered. During switching, the positive terminals of the bootstrap capacitors may reach voltages approximated by:

$$V_{C34}, V_{C44} \approx (V_{EPS\_UNREG} + V_{DM\_V\_COILS}) > V_{EPS\_UNREG}$$

To ensure the high-side MOSFET remains fully saturated during its conduction interval, the bootstrap capacitance $C_{Bootstrap}$ (referring to the capacitance of C44) must be selected to provide the total charge Q_{Total} over the required on-time. The required capacitance is given by:

$$C_{Bootstrap} = \frac{Q_{Total}}{\Delta V_{Bootstrap}}$$

where $\Delta V_{Bootstrap}$ is the minimum voltage required to sustain operation, given by:

$$\Delta V_{Bootstrap} = V_{EPS\_Unreg_{Min}} - V_F - V_{GSMIN} = 3.3 - 0.125 - 3 = 0.175\,V$$

Whilst, Q_{Total} is determined through the equation:

$$Q_{Total} = Q_{Gate} + \left(I_{LKCAP} + I_{LKGS} + I_{QBS} + I_{LK} + I_{LKDIODE}\right).t_{on}$$

Where:

- $I_{LKCAP} = Capacitor\ Leakage$
- $I_{LKGS} = Gate - Source\ Leakage\ current$
- $I_{QBS} = Bootstrap\ Circuit\ Quiescent\ Current$
- $I_{LK} = Bootstrap\ Circuit\ Leakage\ Current$
- $I_{LKDIODE} = Bootstrap\ Diode\ reverese\ leakage\ current$
- $t_{on} = On\ time\ of\ highside\ switch$

The values for these parameters are listed in Table 5.11. These values yield a total required charge of approximately 5.4 μC, resulting in a minimum required capacitance of 31 µF. Applying a 20% margin for ageing, leakage, and tolerance, a 47 µF bootstrap capacitor is used.

To reduce idle power consumption, the design includes p-channel MOSFETs Q12 and Q13, which isolate the bootstrap charging path when the circuit is not active. In the absence of Q12, an idle current path exists from V_{EPS_UNREG}, flowing through R12, D8, R52, and R54 to ground. This results in an idle current of several milliamps. When considering the right-hand side, the idle current doubles, and across the three H-Bridges on the PCB, it then triples, leading to large and unnecessary power dissipation. The addition of Q12 eliminates this idle path without affecting the timing or function of the bootstrap circuit, improving overall energy efficiency during inactive periods.

Table 5.11: Bootstrap Circuit Total Charge Variables

Variable	Value	Sources
Q_{Gate}	9.5 nC	MOSFET Datasheet
I_{LKCAP}	6 μA	Diode Datasheet
I_{LKGS}	0.1 μA	MOSFET Datasheet
I_{QBS}	16 μA	Simulation
I_{LK}	3μA	Simulation
$I_{LKDIODE}$	2 μA	Diode Datasheet
t_{on}	200 ms	Requirement

5.10.4.3 Trigger Circuit

Each H-Bridge is equipped with a pair of trigger circuits, one for each side. Focusing on the left-hand side, the trigger comprises three pre-biased bipolar junction transistors (BJTs): Q15A, Q15B, and Q14A, along with current-limiting resistors R60 and R62. Figure 5.17 illustrates the schematics of the left-side trigger.

Transistors Q15A and Q15B form a logical OR gate, allowing the EPS or ADCS subsystem to trigger the H-Bridge. The configuration is inverting, requiring an active-HIGH input signal to initiate a coil pulse. This dual-path design enables both autonomous (from the EPS) and commanded operation, while preserving logical separation between subsystems.

Q14A serves to discharge the gate of the high-side MOSFET after the trigger signal is released. To ensure this occurs rapidly and avoids shoot-through currents, resistor R60 is selected to be significantly smaller than R52. As a result, the low-side path disables before the high-side path becomes active, and conversely, ensures that the high-side gate discharges before the low-side gate re-engages. This minimises overlap between conduction states and prevents simultaneous current paths across the supply rails.

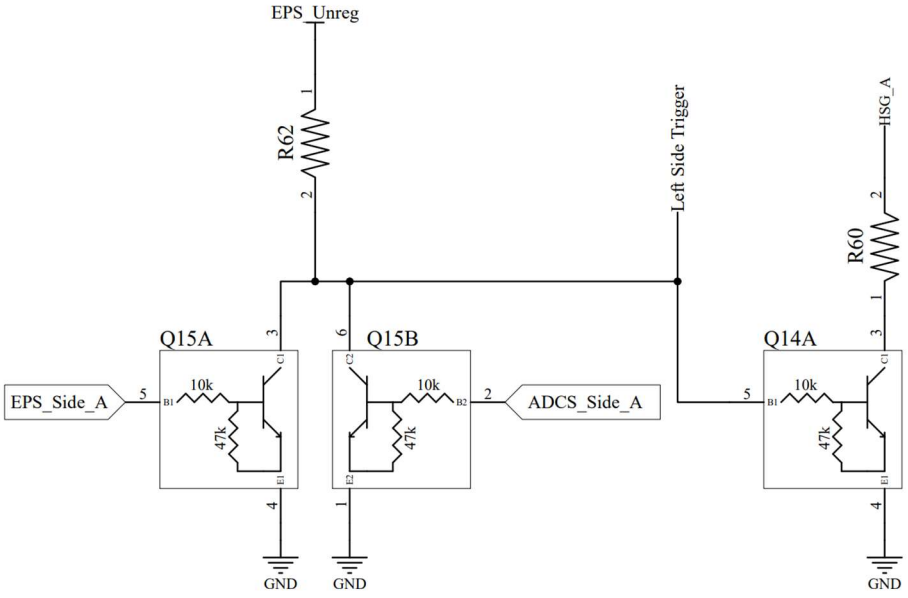

Figure 5.17: H-Bridge Left-Side Trigger

5.10.4.4 Synchronisation

Precise synchronisation of the disengagement pulse across adjacent satellites is critical for efficient energy transfer and uniform force generation. Asynchronous activation leads to two principal inefficiencies. First, any misalignment in pulse timing reduces the overlapping interval between interacting coil pairs, diminishing the effective repulsive impulse. Second, due to the nature of capacitor discharge, the current profile is non-uniform over time. Mismatched timing leads to asymmetric peak currents between the two coils, reducing the net electromagnetic force. Since the repulsive force is proportional to the product of the opposing coil currents, even minor discrepancies can result in a significant performance penalty.

To mitigate these effects, a synchronisation scheme is implemented using the PWM and Input Capture peripherals of the EPS microcontrollers onboard each PQ1 satellite. As illustrated in Figure 5.18, a master satellite generates a PWM signal that is routed to its Input Capture module and simultaneously distributed to the Input Capture modules of all slave satellites. All microcontrollers enter a predefined idle state and wait for the same input event. This approach ensures simultaneous triggering across nodes with minimal latency.

Since the onboard clocks are not inherently synchronised, the maximum timing error is determined by the clock frequency. For a system clock of 80 MHz, the theoretical worst-case synchronisation error is:

$$t_{async_{max}} = \frac{1}{f_{clk}}$$

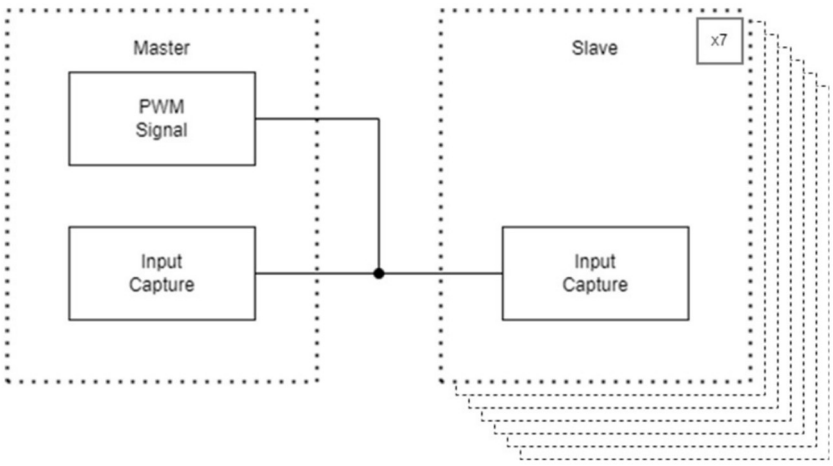

Figure 5.18: Synchronisation Block Diagram

Where f_{Clk} is the microcontroller clock frequency. For a clock frequency of 80 MHz, the maximum asynchronisation time is therefore 12.5 ns. This margin is sufficiently small to ensure that both pulse alignment and peak current matching remain within tolerances for effective disengagement. The assumption holds provided that clock drift due to temperature differences is minimal and that inter-satellite propagation delays are negligible over short distances.

5.10.5 Failure Scenarios and Risk Mitigation

Miniaturisation was a primary design constraint for the disengagement mechanism circuitry, as it had to deliver the required performance within the stringent volume limitations of the PQ1 satellite. To meet these constraints, the design relies extensively COTS components, which are not radiation-hardened or space-qualified. These components are typically much larger and difficult to procure due to trade restrictions.

While the use of COTS components is standard practice in CubeSat and PocketQube missions, it introduces a significant risk of failure when operating in the space environment. This section assesses the impact of space environment factors on the circuitry, outlines the mitigation strategies currently implemented, and identifies potential avenues for further improving reliability.

There are four environmental factors that are of concern: radiation effects, temperature extremes, vacuum environment and electrostatic discharge (ESD). The latter three can be addressed from an architectural perspective, through system-level design choices such as thermal management to cope with wide temperature variations, appropriate venting, or comprehensive grounding and shielding schemes to mitigate ESD. In contrast, radiation effects must be assessed at the component or circuit level, as susceptibility varies significantly between different devices and technologies.

For a satellite and orbit comparable to PQ1, the internal thermal environment is expected to oscillate between –20 °C and 20 °C [113]. Based on this range, automotive-grade components were selected, whilst ensuring that their operating limits remain comfortably within these bounds. However, dedicated thermal analyses have not yet been conducted for the PQ8, PQ4, or PQ2 configurations. This represents an important area for future work, including a detailed thermal assessment of the current circuitry under representative orbital conditions.

For the vacuum environment, the primary concern for the circuitry is the presence of residual trapped air within the satellite. This can result in localised low-pressure regions, where, if the pressure-length product falls within a critical range (approximately 10 Torr.cm), electrical discharges can occur due to plasma formation at relatively low voltages (potentially within a few hundred volts). To mitigate this, the satellite must be adequately vented to prevent the formation of air pockets, and any high-voltage nodes should be sufficiently spaced and insulated to avoid arcing. In the PQ1 architecture, gaps between the external solar panel PCBs facilitate the venting of air trapped between subsystems. Furthermore, the satellite operates at low voltages, with a maximum of 6 V, which is well below the threshold typically required for plasma generation under partial vacuum conditions.

Electrostatic discharge may occur on the satellite due to the accumulation of charge on external surfaces, resulting from interactions with charged particles trapped in the ionosphere and solar wind. This charge build-up can lead to significant potential difference build-up between exposed, electrically isolated materials, increasing the risk of sudden discharges that may damage sensitive components. To mitigate this risk, external surfaces are coated with a conductive material and electrically bonded to the satellite structure, which is then grounded at a single point within the EPS. This single-point grounding strategy ensures a controlled return path for accumulated charge and reduces the likelihood of differential charging across the spacecraft.

Radiation exposure is the dominant reliability concern, particularly ionising radiation due to the electrons, protons and heavy ions that form cosmic rays. The issue arises due to two mechanisms induced by radiation, Total Ionising Dose (TID) and Single Event Effects (SEE), and their impact on semiconductor devices. TID is a gradual and cumulative effect that, for MOSFET devices in particular, generates electron-hole pairs in the gate oxide layer. While the electrons escape, the holes become trapped causing a build-up of charge and shifts their threshold voltages: negatively for n-channels devices, and positively for p-channel. Ultimately this leads to increased leakage current during the standby or off states of the device.

Single Event Effects, on the other hand, are caused by singular, localized ionization events when an energetic particle passes through or becomes lodged in a semiconductor. These events can produce various effects depending on the impacted device. For the disengagement mechanism circuitry, the most critical concerns are Single Event Latch-Up (SEL) and Single Hard Errors (SHE). The former induces the activation

of parasitic *npnp* or *pnpn* structures within CMOS transistors, causing them to latch-up. This can create a low-impedance path to ground, potentially leading to permanent failure, due to excessive current draw. If the device survives, the latch-up can typically be reset by disconnecting the device from all power sources. SHEs are less forgiving as they can cause gate or dielectric rupture or burn-out, leading to the permanent failure of the device.

Given these vulnerabilities, this section presents a component-level analysis of failure modes within the disengagement and magnetorquer circuitry. For each critical element, potential failure mechanisms are identified, their impact on system functionality assessed, and existing mitigation measures reviewed. Recommendations are then proposed to improve robustness against radiation and other environmental factors in future implementations.

5.10.5.1 Buck Converter

Starting with the buck converter, which charges the disengagement capacitors and supports magnetorquer mode, the device is inherently susceptible to TID effects, which may shift internal voltage references or degrade control stability over time. It is also vulnerable to SEE, particularly latch-up or logic upset within its pass-device, internal feedback or soft-start circuitry.

Since this converter is the sole device responsible for charging the capacitor bank, it represents a single point of failure. A fault in the buck converter could result in a complete loss of disengagement capability and prevent magnetorquer operation. Moreover, a malfunctioning converter may induce noise or instability on the unregulated power bus, affecting other EPS or payload functions.

The current design includes several mitigation features. The converter is downstream of the TPS2553 load switch, which provides programmable overcurrent protection and thermal shutdown, and has flight heritage on prior FOSSASAT-1 PocketQube missions [114]. In the event of excessive current draw or anomalous operation, the TPS2553 disconnects the buck converter from the bus. Additionally, the EPS microcontroller continuously monitors the buck output voltage via its internal ADC. If abnormal behaviour is detected at the output, such as voltage drift or failure to reach the setpoint, the circuit is reset in software. In some cases, the control voltage may also be tuned to compensate for any drift in the output of the converter.

To further mitigate this risk, a redundant buck converter could be incorporated in future iterations of the design, configured to activate only in the event of primary converter failure. Alternatively, replacing the COTS regulator with a radiation-hardened device would significantly improve resilience to both SEE and TID effects. One such candidate is the Intersil ISL73006SLH, a space-qualified synchronous buck controller. However, it imposes several trade-offs: its minimum output voltage is 0.6 V, which limits compatibility with low-voltage magnetorquer operation, and its package size, 6.73 × 6.22 mm, is substantially larger than the existing LM3253, potentially exceeding the available PCB area. These modifications may therefore be more appropriate for high-reliability or long-duration missions where radiation tolerance outweighs volume and efficiency concerns.

5.10.5.2 Switching Circuit MOSFETs

The series-parallel switching circuit employs two p-channel MOSFETs (Q9 and Q10) and one n-channel MOSFET (Q11) to alternate the capacitor bank between charge (parallel) and discharge (series) configurations. These devices are directly connected to the supercapacitors, which, when fully charged, store a substantial amount of energy. As such, failure in this circuit is of particular concern, as it could lead to catastrophic electrical failure.

TID degradation in MOSFETs can result in threshold voltage shifts and increased leakage currents, while SEE, such as gate rupture or latch-up, may cause sudden and irreversible failures. For n-channel devices, TID generally causes a negative shift in threshold voltage, increasing the risk of the device remaining permanently on. In contrast, p-channel MOSFET**s** tend to experience a positive threshold shift, potentially preventing them from turning on entirely.

In this topology, a failure of Q9 would prevent the supercapacitors from charging in parallel, while a failure of Q11 would inhibit series operation. Although not directly in the discharge path, the n-channel MOSFET Q10 is connected to the positive terminal of the bottom-side supercapacitor via Q11. If Q10 were to become permanently conducting, due to TID-induced threshold shift or latch-up, and Q11 were simultaneously enabled, a low-resistance path from the bottom capacitor to ground would be formed. This would result in excessive current through both Q10 and Q11, potentially damaging both devices and causing complete loss of charge and discharge functionality. Even if Q11 remains intact, a permanently switched-on Q10 would block the lower capacitor from charging.

At present, the switching circuit lacks hardware-level protection against SEE or latch-up in the MOSFETs. However, two mitigation strategies are recommended for future implementations. First, the supercapacitors should be fully discharged when not in use, before launch and outside of active disengagement periods, to reduce the energy available in case of failure. Second, once disengagement is complete, the supercapacitor bank should be disconnected from the circuit, either through a solid-state switch or a one-time fuse mechanism, allowing the magnetorquers to operate directly from the buck converter. This would minimise long-term exposure of high-energy components to potential fault pathways and limit the risk of catastrophic failure.

Implementing full redundancy in the switching circuit is not straightforward. It would increase system complexity and could itself introduce new points of failure. Furthermore, duplicating the circuit is impractical due to the volume and mass of the supercapacitors, which already strain the available space within the satellite. Similarly, identifying radiation-hardened replacements for all three MOSFETs that meet the necessary electrical and dimensional constraints is unlikely to be feasible. For these reasons, mitigation should prioritise procedural safeguards and post-disengagement isolation, rather than circuit-level redundancy or complete radiation hardening.

5.10.5.3 H-Bridge MOSFETs

The H-Bridge circuit enables bi-directional current through the magnetorquer coils, supporting both DM and MT modes of operation. It uses integrated n-channel half-bridge MOSFETs, which are susceptible to TID-induced threshold shifts and SEE, potentially leading to permanent conduction, loss of polarity control, or unintended current paths. This risk is amplified by the H-Bridge's direct connection to the supercapacitor bank, where a failure could result in uncontrolled discharge and catastrophic device damage. Loss of a half-bridge would lead to loss of both DM and MT functionalities in the axis of failure.

The same recommendations made for the switching circuitry apply here, namely, that supercapacitors should be fully discharged when not in use and isolated from the circuit after disengagement to limit exposure.

Redundancy, while impractical for high-current DM operation, may be feasible for the lower-current MT mode. Since MT requires lower currents, and thus smaller devices, and operates over the mission’s full duration, targeted redundancy could improve robustness. In contrast, DM mode is only needed during the early phase of the mission,

where the likelihood of radiation-induced failure remains low. This prioritisation balances reliability within the strict volume constraints of the system.

5.10.5.4 Gate Driver MOSFET

The gate driver circuit includes p-channel MOSFETs (Q12 and Q13), which suppress idle current by isolating the bootstrap capacitor charging path when the H-Bridge is inactive. These devices are not critical to switching functionality but are essential for ensuring power efficiency when the bootstrap circuitry is idle.

The primary concern is Total Ionising Dose (TID) degradation. A positive shift in threshold voltage may prevent the MOSFET from turning on, which would inhibit charging of the bootstrap capacitor. In this case, the high-side gate driver would become inoperative, resulting in loss of functionality for the corresponding H-Bridge half and disabling bi-directional operation on that axis.

In contrast, a latch-up failure would reintroduce the idle current path that the device was intended to suppress, but bootstrap operation would continue as normal. This condition is not catastrophic and can typically be cleared by resetting the circuit.

Given the failure impact and usage role, redundancy offers limited benefit, as TID-induced threshold shifts are not recoverable and would affect redundant devices similarly. Instead, the recommended mitigation is to select a p-channel MOSFET with demonstrated TID tolerance over the expected mission duration. Devices with published TID test data or those previously used in LEO environments should be prioritised.

5.10.5.5 Trigger Circuit BJTs

The H-Bridge trigger circuitry uses pre-biased bipolar junction transistors (BJTs) to form a logic-level interface that enables control of the discharge and magnetorquer functions. These BJTs serve two primary purposes: acting as an OR gate between EPS and ADCS trigger sources, and rapidly discharging the high-side gate to suppress shoot-through currents during switching transitions.

The main vulnerability lies in TID effects, which can degrade current gain, increase base drive requirements, or prevent proper switching. This may result in failed gate control and asymmetric coil actuation. SEE are less critical for BJTs, as they do not exhibit latch-up behaviour, and any transient disruptions are typically recoverable via circuit reset or re-triggering.

Importantly, redundancy is already embedded in the design. Separate BJTs handle EPS and ADCS trigger inputs, providing dual control paths. Moreover, the BJT responsible for rapid gate discharge is implemented using a dual-transistor package, supports simple hardware redundancy and a second discharge path can be activated by populating an additional resistor. Further supporting the reliability of this design, the specific BJT package used has undergone radiation testing for both TID and SEE effects as part of the RESOLUTE project led by the University of Malta, increasing confidence in its performance under space conditions.

Given the low current levels and the existing redundancy, no further mitigation is strictly required. However, for extended-duration missions or harsher radiation environments, component selection could be further optimised by prioritising packages with published TID performance data or additional flight heritage.

5.10.5.6 Synchronisation Mechanism

Synchronisation of the disengagement pulse is essential to ensure efficient energy transfer and reliable separation. The mechanism relies on coordinated pulse timing across multiple PQ8 satellites, initiated by a master microcontroller and captured by slave microcontrollers via Input Capture peripherals. The trigger signal is generated by the EPS microcontroller, which also manages capacitor charging, discharge initiation, and pulse timing.

The main risk lies in a failure of the EPS microcontroller to issue the disengagement trigger at the correct time. This may be due to internal logic failure, software fault, or radiation-induced effects such as Single Event Upsets (SEU), Single Event Functional Interrupts (SEFI), or latch-up. However, the EPS controller is protected by multiple layers of fault management, including:

- Latch-up protection to shut off power in the event of abnormal current draw,
- Overcurrent protection on all power rails.
- Software watchdog timers to recover from firmware stalls or timing anomalies,
- Hardware watchdog timers in case the software watchdog fails.

If synchronisation fails due to a missed or corrupted trigger, the disengagement sequence would not occur or would be incomplete, as the repulsive force depends on synchronised current pulses in opposing coils. However, this failure mode is non-catastrophic as the satellites remain connected, and not enough impulsive force is

generated for disengagement. The system can be reset, and disengagement re-attempted once the fault is cleared.

Furthermore, the EPS architecture includes a cold-redundant microcontroller, enabling recovery through reconfiguration in the event of primary controller failure. This design ensures that even if one microcontroller becomes permanently unresponsive, the disengagement system retains functional viability. Given these protections and the ability to retry disengagement, synchronisation-related failure is considered recoverable and low-risk. No additional mitigation is required.

5.10.5.7 Summary of Failure Scenarios

This section has presented a theoretical failure mode analysis of the disengagement and magnetorquer circuitry, with a focus on the radiation susceptibility of key COTS semiconductor components. While several risk mitigation strategies are already implemented, such as watchdog-supervised microcontrollers, overcurrent protection, and redundant trigger paths, some subsystems, particularly those involving power MOSFETs, remain exposed to failure under specific scenarios.

For the disengagement function, the overall probability of radiation-induced failure is very low, as the event occurs immediately after deployment, before Total TID effects accumulate. Though SEE remain a concern, especially in regions such as the South Atlantic Anomaly, risk is significantly reduced by ensuring the supercapacitors remain discharged and isolated until disengagement is required. These procedural safeguards minimise the likelihood of catastrophic failure and support a retry mechanism in the event of a transient fault.

In contrast, the magnetorquer function remains active over the longer mission duration, making it more vulnerable to TID degradation and cumulative SEE. However, MT activity is intermittent, primarily required for desaturation events occurring only a few times per orbit. This reduced duty cycle enables the same procedural safeguards as those used for DM mode. Additionally, because current requirements in MT mode are significantly lower, it becomes feasible to implement cold-redundant MT driver circuits using smaller, low-power components. This approach improves long-term reliability without incurring the mass and volume penalties that would accompany complete duplication of the high-power disengagement circuitry.

5.10.6 Theoretical Failure Mode Analysis

5.10.6.1 Failure Definitions

For the disengagement mechanism, failure is defined relative to its two functional roles:

- Primary function: provide a synchronised electromagnetic impulse that separates PQ units with the required relative velocity.
- Secondary function: operate as a magnetorquer for attitude control throughout the mission.

Accordingly, failure is defined as any condition in which:

- Disengagement cannot be executed when commanded,
- Disengagement produces insufficient or asymmetric impulse leading to partial or unsafe separation,
- Disengagement occurs unintentionally,
- Magnetorquer functionality is lost or degraded beyond controllability limits.

Failures are further classified as:

- Catastrophic failures: lead to irreversible loss of disengagement capability or uncontrolled electrical damage.
- Recoverable failures: allow retry, reset, or reconfiguration.
- Degraded failures: allow partial function but with reduced performance or margin.

From a system-level perspective, a disengagement mechanism failure refers to loss of one or both primary functions:

- Failure of disengagement: PQ units remain clustered or separate unpredictably.
- Failure of magnetorquer: long-term attitude control becomes impossible or unstable.

From a sub-system-level perspective, failure includes the failure of individual functional blocks that may or may not propagate to system failure:

- Power conditioning (buck converter),
- Energy storage and switching (supercapacitors, MOSFET network),
- Actuation (H-Bridge and coils),
- Control and synchronisation (microcontrollers, trigger logic),
- Protection and interface circuitry.

Additionally, a sub-system failure becomes a system-level failure only if it removes all functional paths to achieve either disengagement or magnetorquer operation or introduces unsafe behaviour such as uncontrolled discharge.

5.10.6.2 Functional Failure Categories

A functional failure refers to a failure that does not lead to the immediate failure of the mission. At the system level, failure modes can be grouped into four functional categories listed in Table 5.12. The detailed component-level analysis presented in Section 5.10.5 identifies the dominant vulnerabilities. These are collated in Table 5.13.

Table 5.12: System-Level Functional Failure Categories for the Disengagement Mechanism

Category	Failure Type	Description	System-Level Impact
F1	Failure to disengage	Insufficient current, loss of synchronisation, or inability to charge capacitors prevents release	PQ units remain clustered; constellation cannot form
F2	Unsafe disengagement	Asymmetric discharge, uncontrolled firing, or electrical damage during discharge	Partial separation, collision risk, or irreversible hardware damage
F3	Loss of magnetorquer function	Loss of bi-directional coil drive or excessive current preventing fine control	Attitude control lost or severely degraded
F4	Long-term degradation	Radiation-induced drift, ageing, or cumulative damage	Gradual loss of performance, reduced mission capability

Table 5.13: Circuit-Level Failure Mode Analysis

Circuit	Failure Modes	Immediate Effects	Propagates to System-Level?	Recoverable?	Failure Category
Buck converter	TID drift, latch-up, internal logic failure	Capacitors cannot charge; MT mode disabled	Yes	Catastrophic	F1, F3, F4
Switching MOSFET network	MOSFET stuck on/off, latch-up	Cannot switch between charge/ discharge; risk of short circuit	Yes	Recoverable/ Catastrophic	F1, F2, F4
H-Bridge MOSFETs	Half-bridge failure.	Loss of axis control; uncontrolled discharge	Yes	Catastrophic	F2, F3, F4
Gate driver MOSFETs	Threshold shift, latch-up	High-side switching fails or idle current increases	Yes	Degraded	F3, F4
Trigger BJTs	Gain loss, open circuit	Loss of one trigger path	No	Recoverable	F1, F4
Synch. system	Missed or corrupted trigger	Pulses not aligned or not fired	No	Recoverable	F1
Supercaps	ESR increase, capacitance loss	Reduced peak current and impulse	No	Degraded	F1, F4
Coils	Open circuit, resistance increase	Reduced or zero magnetic force	Yes	Degraded/ Catastrophic	F1, F2, F3, F4

5.10.6.3 Combined Failure Mode Summary

The disengagement system exhibits three dominant system-level failure pathways:

1. Loss of power conditioning or switching integrity:
    i. No capacitor charging or unsafe discharge,
    ii. Irreversible loss of disengagement capability.
2. Loss of synchronisation or partial actuation:
    i. Incomplete or failed separation,
    ii. Recoverable through reset and retry.
3. Long-term radiation degradation of control and driver electronics
    i. Gradual loss of magnetorquer performance,
    ii. Degraded but potentially operable mission.

The most critical risks are therefore associated with:

- High-energy switching elements,
- Single-point power conditioning,
- Radiation effects on MOSFET-based circuitry.

Existing mitigation measures, overcurrent protection, watchdog timers, cold-redundant microcontrollers, procedural isolation of capacitors, and trigger redundancy, primarily address recoverable and procedural failures. Catastrophic failures remain dominated by radiation-induced damage to power MOSFETs and the absence of redundancy in high-current paths, which is a direct consequence of volume and mass constraints.

5.11 Conclusion

This chapter presented the complete design and modelling of a dual-use disengagement mechanism tailored to the physical, electrical, and operational constraints of the PQ-class satellite architecture. By repurposing the magnetorquer coils for both satellite separation and attitude control, the system achieves significant reductions in volume and hardware complexity.

The development process followed a structured and iterative approach. A static analysis of published force equations was used to assess the influence of key design parameters, such as coil radius, ampere-turns, and separation distance, on repulsive force generation. These insights informed the sizing and selection of energy storage and actuation components. A dynamic simulation model was then constructed to capture the

coupled electrical, thermal, mechanical, and kinematic behaviour of the system during separation. This model served as the foundation for evaluating candidate coil–capacitor configurations and identifying an optimal design for peak separation performance.

A custom circuit was developed to support both disengagement and magnetorquer modes. This included a reconfigurable series–parallel capacitor bank, high-current H-Bridge discharge stage, gate drivers, trigger logic, and synchronisation mechanisms. However, the system relies on non-space-grade COTS components, particularly semiconductor devices, which are inherently susceptible to radiation effects in orbit. A theoretical failure mode analysis was performed to assess the risks associated with each major subsystem, including the buck converter, switching and discharge MOSFETs, gate drivers, and synchronisation logic. Existing mitigation measures were identified, and further improvements proposed, including procedural safeguards and the implementation of cold redundancy where feasible.

In summary, the disengagement mechanism meets its design objectives through compact, functionally integrated hardware and validated performance modelling. Although it does not employ space-qualified components, the design offers a pragmatic solution for small satellite missions, effectively balancing performance with development constraints and mission risk.

6 DISENGAGEMENT MECHANISM: SIMULATION AND TESTING

This chapter presents the simulation and experimental validation of the dual-purpose disengagement mechanism designed in the preceding chapter. Building on the theoretical modelling and circuit design, the objective here is to evaluate the system's performance across electrical, magnetic, and mechanical domains, and to confirm its suitability for mission deployment. The validation effort spans four key activities. First, LTSpice simulations are used to verify the correct operation of the charge circuit, series-parallel switching network, and H-Bridge discharge path. Second, bench-level circuit tests are conducted to confirm that the hardware behaves as intended under representative electrical conditions. Third, the electromagnetic force model is validated against finite element simulations to ensure its applicability to the non-ideal coil geometries used in the mechanism. Finally, system-level validation is performed through a series of pendulum-based experiments, designed to assess the mechanism's dynamic behaviour during disengagement and its sensitivity to design and alignment parameters. This chapter establishes the accuracy of the developed models, the reliability of the circuit implementation, and the practical feasibility of the proposed separation architecture.

6.1 Circuit Simulation using LTSpice

To verify the electrical functionality of the disengagement mechanism, LTSpice simulations were performed across all central disengagement circuitry. These simulations served to evaluate the transient behaviour of the charge circuit, validate the series-parallel switching circuitry, and assess the current dynamics of the high-current discharge circuit under realistic operating conditions.

6.1.1 Charge Circuit

The circuit was simulated to confirm its ability to charge the capacitor bank when operating in parallel configuration. The control signals were configured such that *Parallel* and *Series* were initially set to LOW, and *Parallel_Inv* to HIGH, activating the parallel configuration. The input voltage was set to a constant 2.7 V.

The simulation results, shown in Figure 6.1, indicate that the supercapacitors reach 99% of the target voltage within approximately 4 minutes, well within a single orbital period (≈ 95 minutes). As expected, the low-side capacitor reaches 2.7 V, while the high-side capacitor saturates at 2.58 V due to the 120 mV forward voltage drop across the Schottky diode. The peak charge current is approximately 880 mA, remaining well within the capabilities of the buck converter.

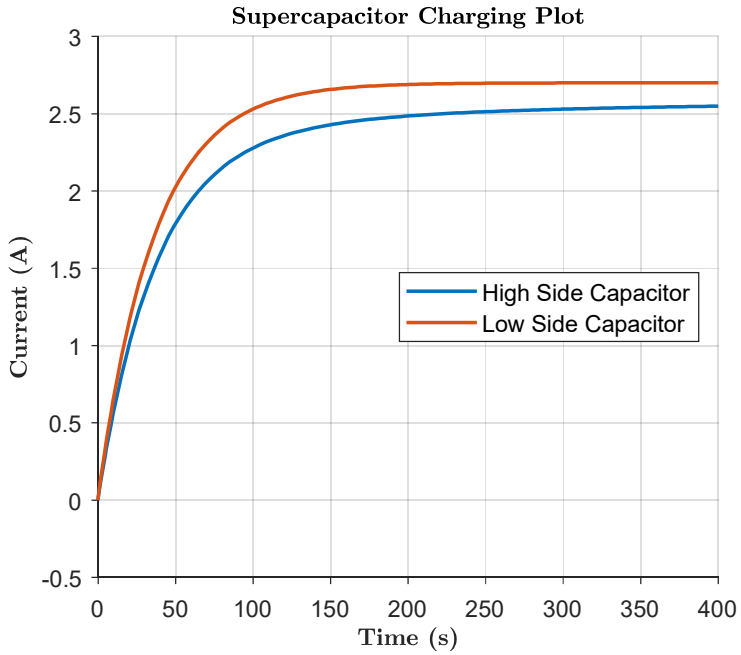

Figure 6.1: Supercapacitor charging plot (LTSpice)

6.1.2 Series/Parallel Switch

To validate the series-parallel switching network, the simulation was extended to ensure that the series configuration reaches the expected voltage levels at disengagement. The system was initially run in charge mode until the capacitors reached full voltage. At t = 500 s, control signals were toggled to enable the series configuration, by setting *Parallel* and *Series* set to HIGH, and *Parallel_Inv* to LOW.

The voltage at the output node, shown in Figure 6.2, transitioned from 2.58 V (parallel mode) to 5.3 V (series mode), reflecting the expected summation of capacitor voltages minus diode losses. The transition was smooth, without ringing or overshoot, and remaining stable for the duration of the 10-second pulse. This confirms both the timing reliability and voltage stability of the switching architecture, supporting its use in the high-current disengagement application.

6.1.3 Discharge Circuit (H-Bridge)

The final simulation involved the discharge path, including the H-Bridge and bootstrap circuitry. The goals of this simulation were to:

1. Validate the intended functionality of the supporting circuitry, specifically the bootstrap mechanism for high-side switching.
2. Observe the current flow dynamics in response to a 100 ms pulse applied across the disengagement coils.
3. Validate the analytical model from Chapter 6.2 against the LTSpice simulation.

The supercapacitors were pre-charged to 5.4 V. Bootstrap capacitors were set to 4.1 V, matching the EPS unregulated bus. Upon triggering, the high-side gate voltage reached ≈ 9.5 V, enabling complete enhancement of the n-channel MOSFET and ensuring low on-resistance operation.

Figure 6.3 confirms stable high-side gate voltage throughout the 100-ms pulse duration, validating the functionality of the bootstrap configuration. Figure 6.4 compares the coil current predicted by LTSpice with that from the analytical RLC model. The current rises to 21 A, then decays to 18.5 A, a characteristic overdamped profile. The analytical model tracks the simulation closely, with a maximum error less than 0.5 %.

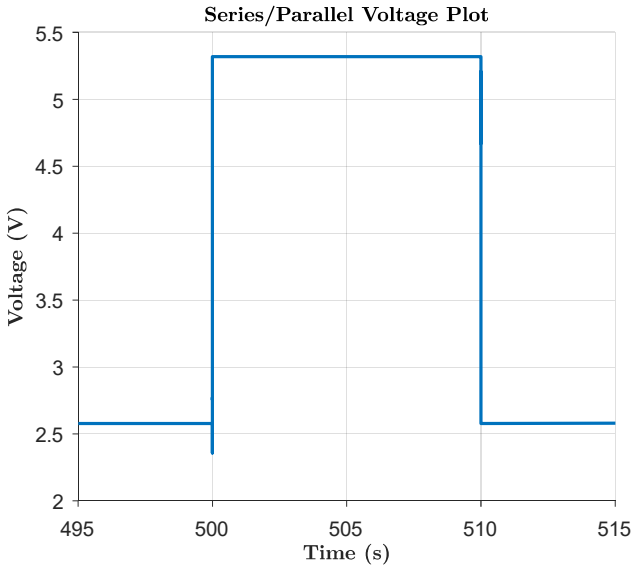

Figure 6.2: LTSpice simulation of series/parallel switch

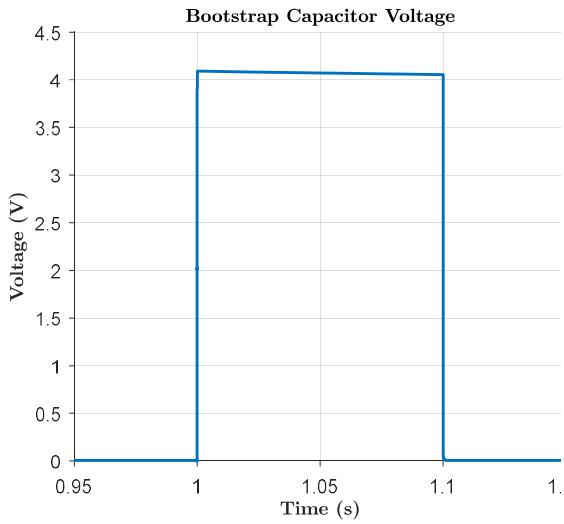

Figure 6.3: Bootstrap Voltage (LTSpice)

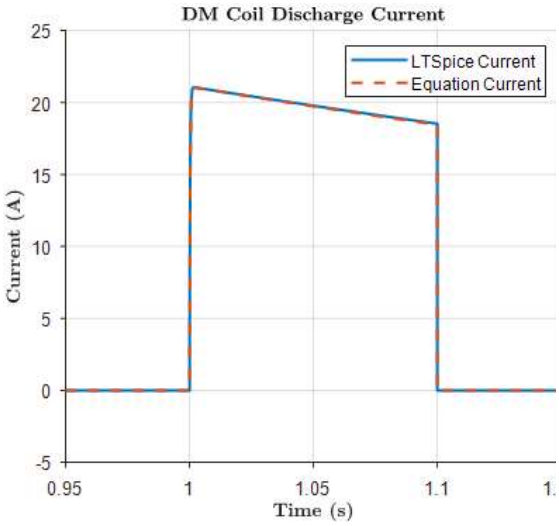

Figure 6.4: DM Current Comparison

6.2 Validation of Force Equations

To assess the accuracy of the dynamic disengagement model, it is first necessary to confirm the validity of the electromagnetic force equations, Eq. 6.7 and Eq. 6.8. The goal is not only to ensure the correctness of the equations, but also to evaluate the assumptions made when adapting them to the geometric and operational requirements of the PQ8 Architecture. The two key assumptions include:

1. The rectangular disengagement coils can be approximated as circular coils of equivalent area.

2. The coils, though multi-turn, can be represented as a single-turn loop carrying an effective current $I_{Approx} = NI_{Actual}$.

Although these approximations are commonly used to simplify force calculations, their influence must be quantified to ensure the fidelity of the model.

6.2.1 Coil Parameters and Setup

The coil configuration used for validation is summarised in Table 6.1. An initial separation of 7.3 mm was selected to replicate the in-satellite stacking configuration, accounting for coil thickness, PCB spacing, and structural clearance. The analytical force model was implemented in MATLAB using a coil radius of 15.3 mm, equivalent to the area of the actual rectangular coil.

Table 6.1: Coil Properties for Ansys Maxwell FEA

Parameter	Value
Number of turns	36
Wire diameter	0.65 mm
Outer Coil Dimensions	26 × 36 × 4 mm³
Current	20 A
Initial Separation Distance	7.3 mm

6.2.2 Field Distribution and Magnetic Interaction

A parametric analysis was set up to calculate the force between the two coils, carrying a constant 20 A current, at varying distances. Two identical coils were placed in coaxial alignment in Ansys Maxwell, and a magnetostatic solver was used to compute the repulsive force as a function of separation. In parallel, the same configuration was simulated in MATLAB using the analytical model.

The magnetic flux density produced by the coils is shown in Figure 6.5. The field is concentrated around the conductor and peaks at ~ 110 mT near the inner coil corners. Field strength drops off rapidly with radial distance, but remains substantial at the coil centre due to geometric superposition.

This visualisation provides critical insight into the spatial distribution of magnetic flux density around the disengagement coils, particularly identifying regions of elevated field intensity. These observations are directly applicable to subsystem PCB

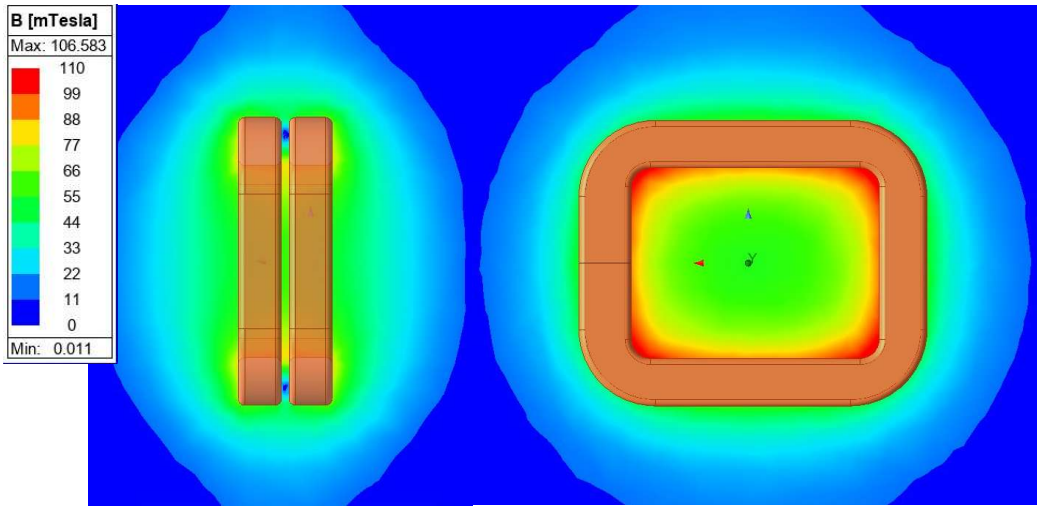

Figure 6.5: Disengagement Coil Magnetic Flux Density (Ansys)

design, where electromagnetic compatibility is essential. The simulation results show that the magnetic flux density decreases sharply beyond approximately 4 mm from the coil surface. To mitigate the risk of electromagnetic interference, eddy current losses or unintended coupling during disengagement, it is therefore recommended to maintain a minimum clearance of 4 mm between the coil face and any conductors or sensitive electronic components.

6.2.3 Force Comparison: Analytical vs. FEA

Figure 6.6 presents the comparison between the analytical and FEA-derived magnetic repulsive forces across a range of axial separations. The results demonstrate strong agreement throughout the operational distance range. At a separation of 10 mm, the analytical and FEA forces differ by less than 2%, confirming that the simplified analytical model adequately captures the dominant electromagnetic behaviour.

Figure 6.7 plots the absolute error between the two methods. At smaller separations, where magnetic coupling is strongest, the analytical model aligns closely with the FEA results, with discrepancies falling within Ansys Maxwell's solver tolerance of 1%. As the separation increases beyond 9 mm, divergence becomes more apparent due to fringe field effects and geometric simplifications not accounted for in the analytical formulation. However, this divergence is not performance-limiting, as the bulk of the disengagement impulse is imparted at smaller separations, where the agreement is strongest.

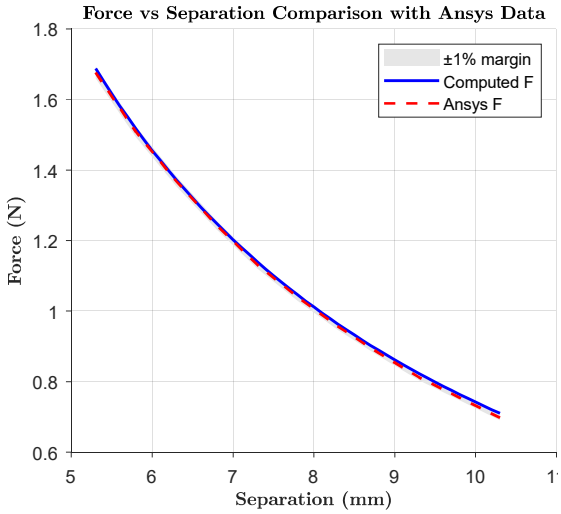

Figure 6.6: Magnetic force comparison (Ansys vs. Analytical)

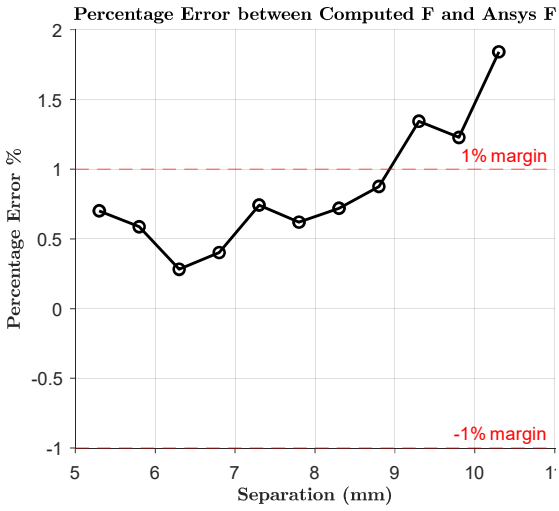

Figure 6.7: Magnetic force comparison error

6.2.4 Eddy Current Loss Analysis

During disengagement, a high-current pulse is applied to the coils, generating strong transient magnetic fields. Although the dynamic disengagement model does not explicitly account for eddy current effects, these can introduce non-negligible energy losses that reduce the net electromagnetic force generated. To quantify these losses, a frequency-domain analysis was performed by combining the results of Ansys Maxwell's eddy current simulations with a spectral decomposition of the coil current waveform.

The current profile generated during a disengagement event approximates a decaying square pulse, characterised by steep rise and fall edges due to the switching circuitry. These transients introduce high-frequency components, which are primarily responsible for inducing eddy currents in nearby conductive materials. To characterise these components, a Fast Fourier Transform (FFT) was applied to the simulated current waveform in MATLAB, yielding the frequency-domain spectrum, |I(f)|, as shown in Figure 6.8.

An eddy current analysis was then conducted in Ansys Maxwell, with the coil and surrounding PCB environment modelled to reflect the actual satellite geometry. A frequency sweep from 1 Hz to 60 Hz was applied using a constant coil current of 20 A to capture eddy current losses, considering up to the 6^{th} harmonic. The resulting power losses, denoted as $P_{(20)}(f)$, are summarised in Table 6.2.

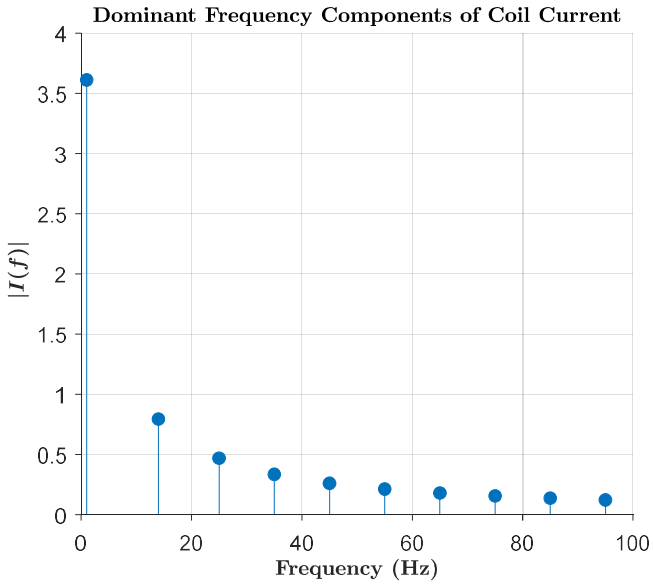

Figure 6.8: FFT of Disengagement Current Pulse

Table 6.2: Ansys FEA results for eddy current losses during disengagement ($\boldsymbol{I = 20\ A}$)

Frequency (Hz)	Eddy Loss (mW)
1	4.8×10^{-3}
15	1.1
25	3.0
35	5.9
45	9.7
55	14.5

To estimate actual power dissipation under the real current profile, the FEA-derived losses were scaled according to the square of the corresponding FFT-derived current magnitudes, assuming linear material behaviour:

$$P_{Actual}(f) = P_{20}(f)\left(\frac{|I_{FFT}(f)|}{20}\right)^2$$

The total eddy current energy loss was then computed by integrating the scaled frequency-domain power over the pulse duration:

$$E_{eddy} = t_{pulse}\sum_{f} P_{Actual}(f)$$

Applying this procedure yielded a total eddy current loss of approximately 1.9 mJ during the disengagement event with a disengagement voltage of 5.4 V.

This energy represents electromagnetic losses caused by eddy currents induced in nearby conductive structures during disengagement, which reduce the effective repulsive force and consequently the resulting Δv. Accounting for this loss in the full kinematic simulation improves model accuracy and helps reconcile discrepancies between the simulated and experimentally observed energy transfer.

6.2.5 System-Level Simulation of Disengagement Model

To evaluate the performance of the disengagement mechanism under realistic operating conditions, the complete dynamic model developed in Chapter 6 (Figure 6.4 and Algorithm 6.1) was implemented and executed using the parameters outlined in Table 6.3. This model integrates the electrical, thermal, mechanical, and kinematic subsystems to simulate the full-time evolution of coil current, repulsive force, separation velocity, temperature rise, and energy transfer throughout the disengagement event.

The simulation outputs are presented in Figure 6.9, showing the time evolution of the electromagnetic force, separation velocity, equivalent resistance R_z, and accumulated kinetic energy. The peak electromagnetic repulsion reaches just above 1 N, resulting in a final relative separation velocity of 0.33 m/s, or approximately 0.165 m/s per satellite, satisfying the minimum dispersal velocity requirement derived in earlier deployment analyses.

Table 6.3: Disengagement Model Simulation Parameters

Parameter	Value
Total Capacitance	3 F
Total ESR	0.08 Ω
Circuit Resistance	0.01Ω
Coil Resistance	0.196 Ω
Coil Inductance	55.7 µH
Number of turns	36
Pulse Width	100 ms
Operating Voltage	5.3 V
Magnet Offset	0.65 mm
Mass	0.25 kg
Temperature	20 °C

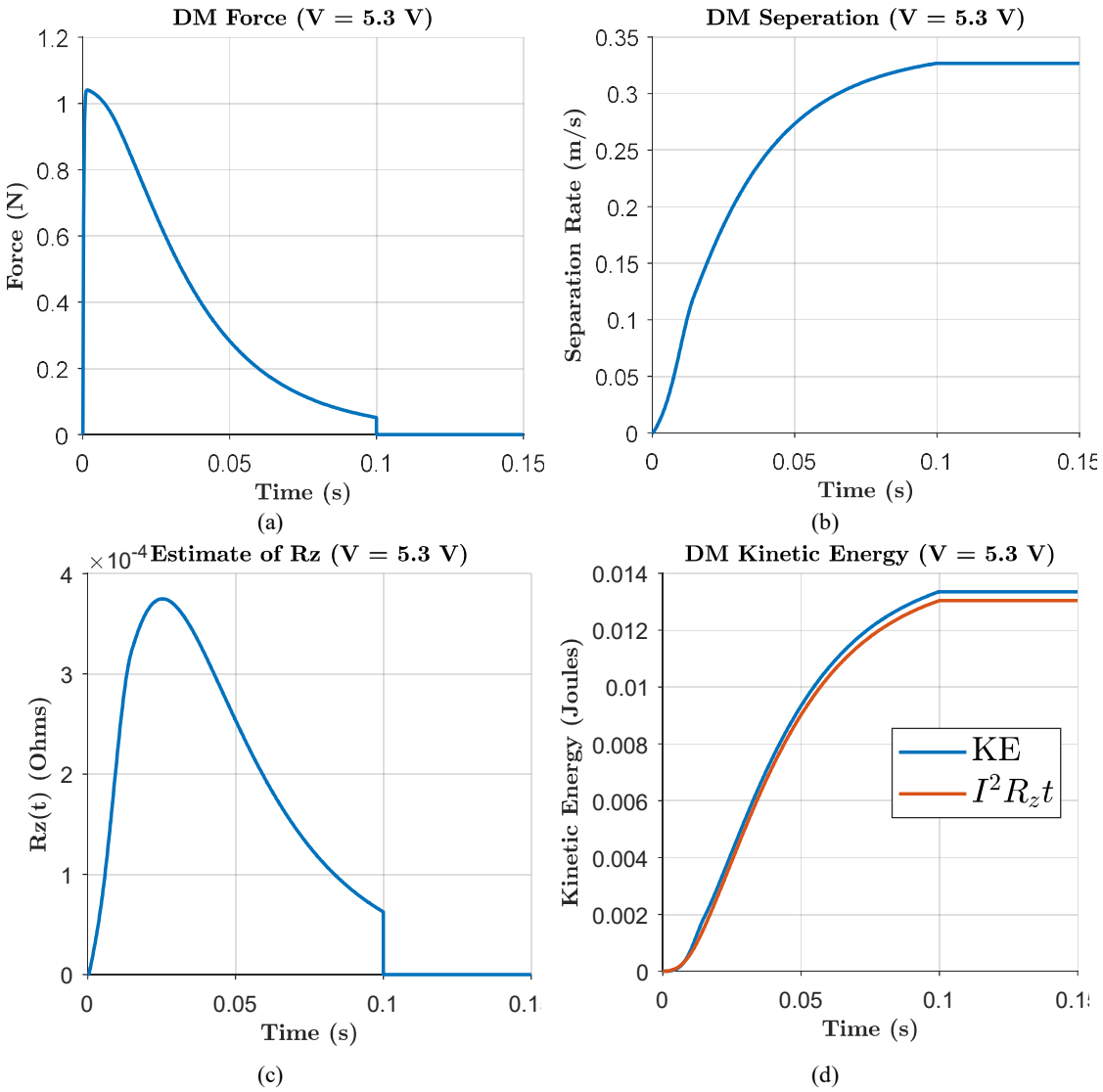

Figure 6.9: Evolution of disengagement output:
(a) Force, (b) Velocity, (c) Analogous resistance $\mathbf{R_z}$ (d) Kinetic Energy

The model also confirms that the dynamic resistance term R_z, representing the mechanical load in the electrical domain, remains significantly smaller than the coil and circuit resistance throughout the pulse duration. This observation validates the simplifying assumption made in the earlier analytical formulation to neglect R_z in the circuit model. The slight discrepancy between the energy dissipated through R_z and the total kinetic energy, as shown in Figure 6.9(d), is attributed to the contribution of the mechanical springs, which provide additional impulse but are not captured by R_z.

The total translational kinetic energy generated during the disengagement event is 13.3 mJ, derived from the electrical energy stored in the supercapacitor bank. This value does not account for the eddy current losses quantified in the previous section, which amount to 1.9 mJ. The relative magnitude of this loss indicates that eddy currents

constitute a non-negligible portion of the total energy budget and must be considered when assessing the mechanism's overall efficiency and output Δv.

Figure 6.10 splits the total axial force into its constituent components, including the electromagnetic coil repulsion, spring-assisted force, and opposing magnetic attraction. The net repulsive force remains positive throughout the disengagement event, with a peak margin of approximately 0.7 N over the opposing magnetic force. Frictional forces, estimated based on lateral misalignment and structural contact with guide pins, were found to be negligible and did not meaningfully influence the outcome.

Thermal effects were also evaluated under worst-case assumptions, namely, that no heat is dissipated into the surrounding PCB during the disengagement pulse. As shown in Figure 6.11, the coil temperature increases from 20 °C to approximately 21.5 °C over the 100-ms actuation period. Due to the brevity of the pulse and the thermal mass of the coil, the net temperature rise remains modest and well within safe operating limits.

The torque resulting from an off-centre mass distribution by 0.1 mm was also evaluated. Figure 6.12 illustrates the time-dependent torque and resulting angular displacement due to the asymmetry in the satellite's moment of inertia. The simulation yields a peak torque of 1.05 mNm about the y-axis and 0.65 mNm about the x-axis, resulting in a peak rotation of approximately 18°. This level of angular motion is within the correction capability of the onboard ADCS, which can stabilise the satellite within roughly 7 seconds using its available control authority [17].

The sensitivity of the mechanism to input parameters was also examined. Figure 6.13 presents the effect of varying pulse width and capacitor charge voltage on the resulting separation velocity. Figure 6.13(a) shows an exponential relationship between pulse duration and final Δv, while Figure 6.13(b) demonstrates a near-linear dependence on input voltage. This confirms that both parameters offer viable tuning mechanisms to adjust separation performance based on mission-specific requirements.

The full velocity range predicted by the model spans from 0.16 m/s to 0.33 m/s, corresponding to a specific impulse range between 0.16 kgm/s and 0.33 kgm/s for the PQ1 satellite. While the mechanism does not reach the upper threshold of 0.4 m/s defined in Chapter 5.2, it exceeds the minimum requirement of 0.2 m/s by an acceptable, thereby ensuring the feasibility of the deployment scenario. The shortfall relative to the maximum reflects a minor deviation from the optimal phasing condition, but does not compromise the functionality or validity of the proposed deployment strategy.

Considering a maximum synchronisation error of 12.5 ns introduced by the use of unsynchronised microcontroller clock sources, the resultant discrepancy is negligible, amounting to less than one-thousandth of a per cent deviation from the ideal synchronised scenario. Even when the synchronisation error is intentionally increased, the system exhibits only a 0.1% deviation at 350 µs and a 0.4% deviation at 1 ms. These results demonstrate that the selected synchronisation approach offers sufficient accuracy for the intended application. The negligible impact at the nanosecond scale and the modest error at the microsecond scale confirm the method's robustness and reliability under both nominal and degraded timing conditions.

Additionally, the simulation was conducted across a range of initial temperatures, from –40 °C to 40 °C, to evaluate the effect on peak coil current and resulting separation rates, as illustrated in Figure 6.14a and 7.14b, respectively. The highest peak current, 22.3 A, was observed at –40 °C, attributable to the reduced coil resistance at lower temperatures. In contrast, the lowest peak current of 17.5 A occurred at 40 °C, where higher resistance limited current flow. The separation rates followed a similar trend: at –40 °C, the peak separation velocity reached 0.4 ms^{-1}, while at 40 °C, it was limited to 0.3 ms^{-1}. These values correspond to a capacitor voltage of 5.3 V. In both cases, the currents remain within the safe operating area of the driver circuitry.

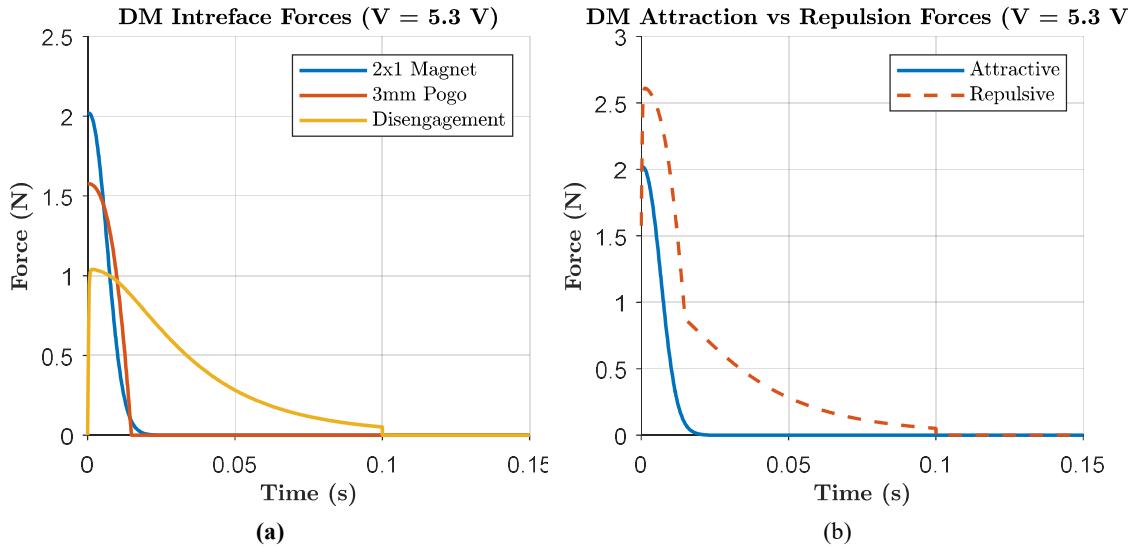

(a) (b)

Figure 6.10: Interface Forces: (a) Individual, (b) Combined

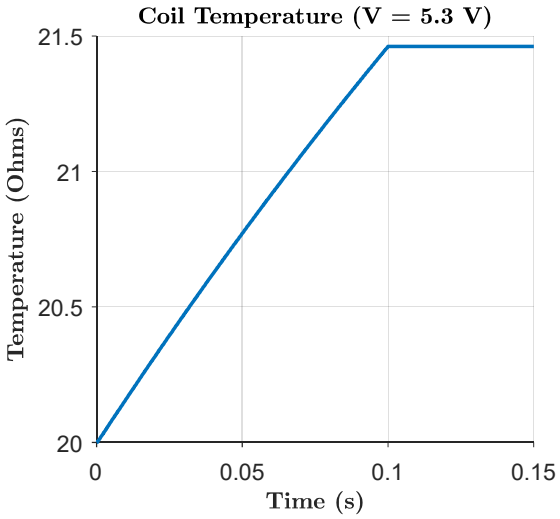

Figure 6.11: Coil temperature during disengagement

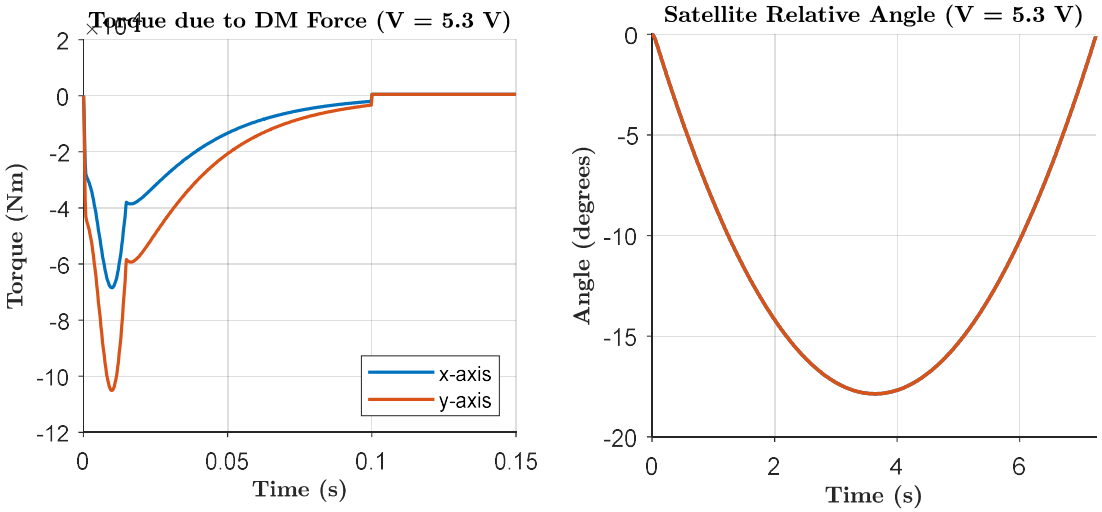

Figure 6.12: (a) Torque , (b) Induced rotation due to non-symmetric inertia matrix

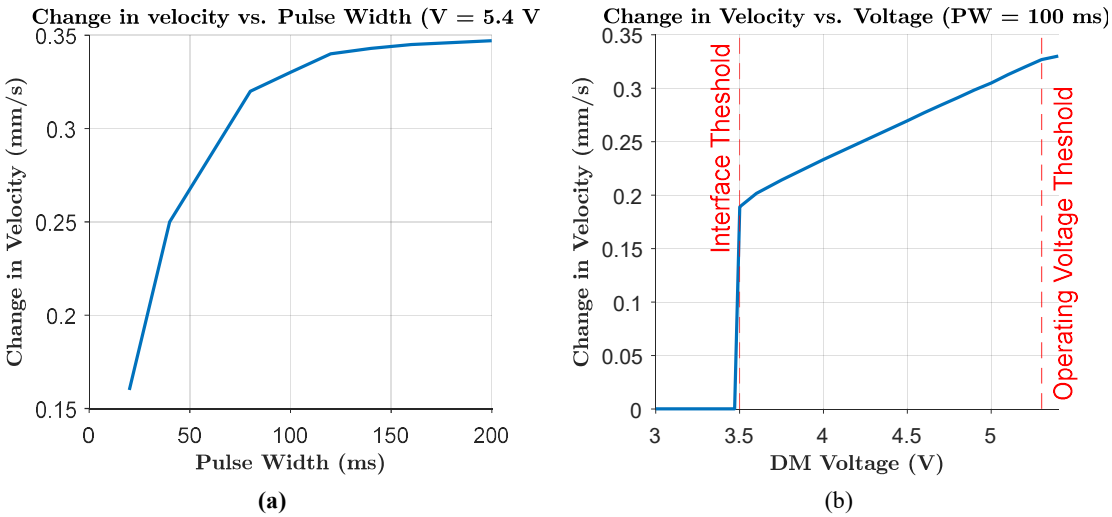

Figure 6.13: Control input response: (a) Pulse Width and (b) Voltage

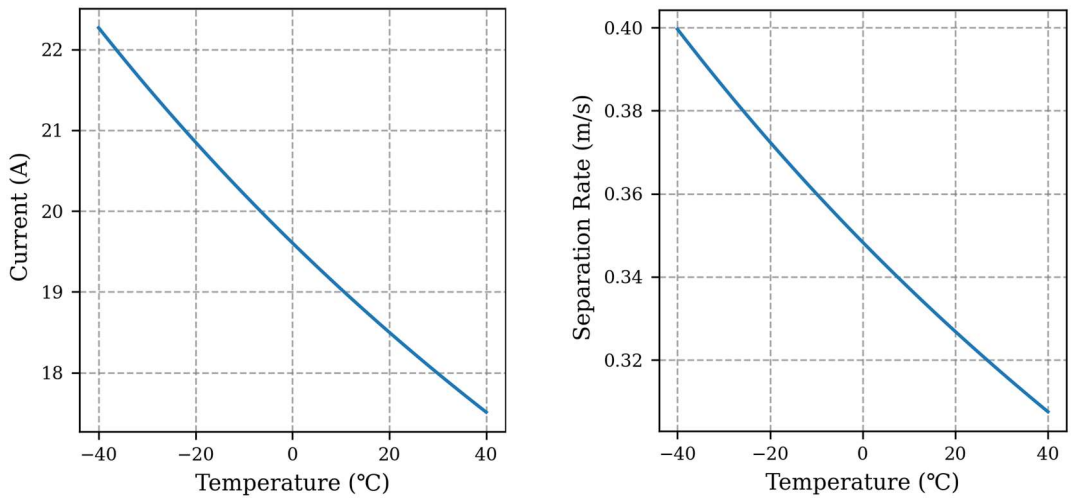

Figure 6.14: Response to different initial Temperatures : (a) Current and (b) Separation Rates

6.3 Bench-level Circuit Testing

To validate the functionality of the disengagement circuit under real operating conditions, a series of benchtop experiments were conducted. These tests evaluated the performance of the series/parallel switching circuit, the H-Bridge gate driver, the coil discharge behaviour, and energy consumption during disengagement.

The first test examined the series/parallel capacitor configuration. Figure 7.15 presents an oscilloscope capture of the high-side capacitor during operation. The circuit was charged to 2.7 V and then transitioned into series mode. Due to a deliberate overcharge of the bottom capacitor, used to compensate for the Schottky diode drop, the output reaches approximately 5.4 V, as expected. This confirms the correct sequencing and functionality of the switching logic.

Subsequent tests evaluated disengagement at four voltage levels: 3.3 V, 3.5 V, 4.5 V, and 5.4 V, each using a 100 ms pulse. For each test, oscilloscope traces were recorded for the bootstrap gate voltage (Figure 7.16), coil voltage (Figure 7.17), and capacitor voltage (Figure 7.18).

The bootstrap gate voltage exhibits behaviour consistent with the LTSpice simulations. At the onset of the pulse, the gate voltage rises to the sum of the bootstrap capacitor voltage (4.1 V) and the source voltage across the coil. Although the voltage decays gradually during the pulse, the high-side MOSFET remains fully enhanced throughout, confirming that saturation is maintained for the duration of the pulse.

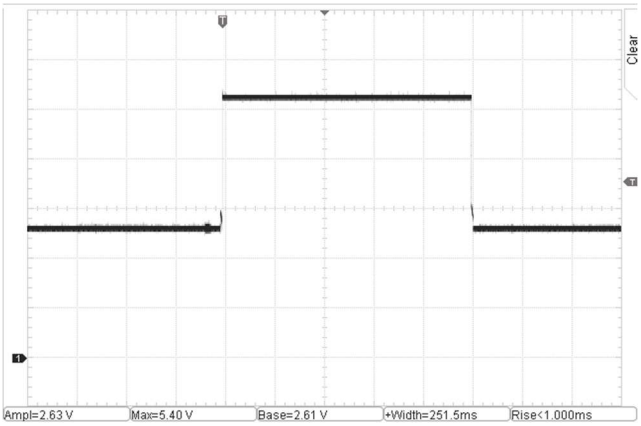

Figure 6.15: Series/parallel Switch at 2.7 V Charge Voltage (1 V/div)

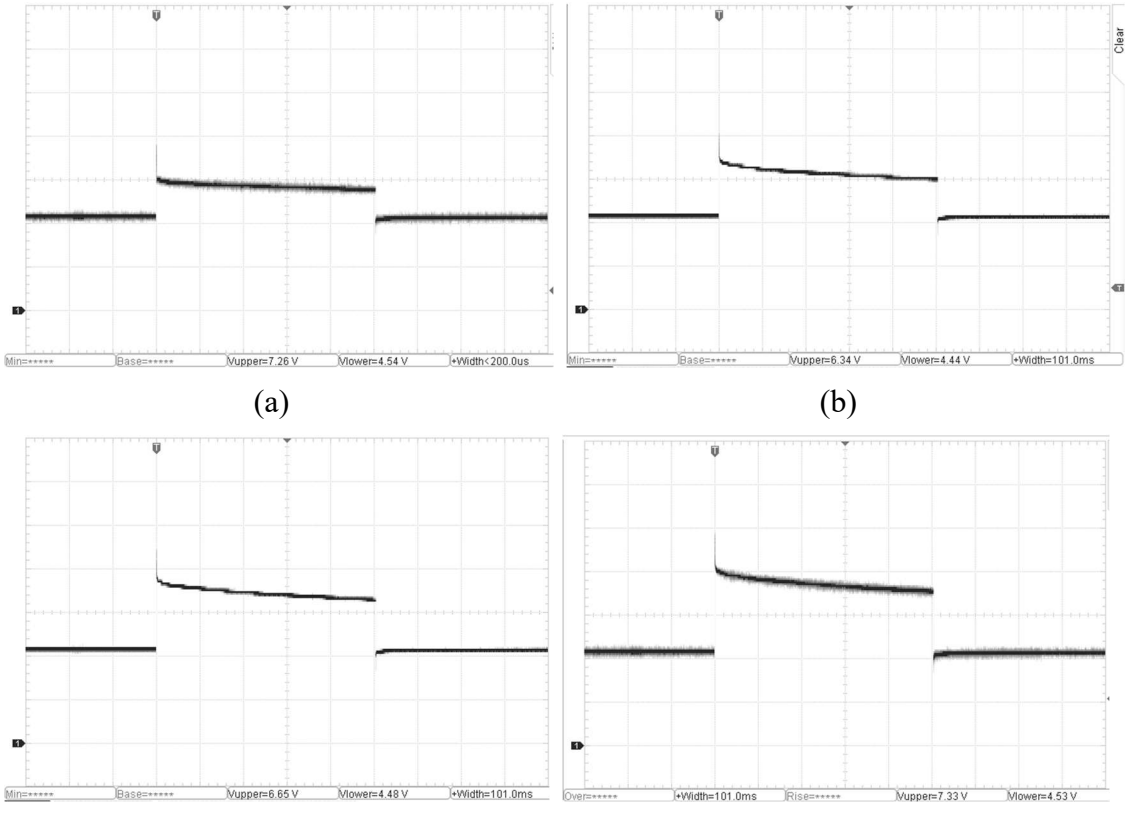

Figure 6.16: Bootstrap Voltage with a V_{DM} of: (a) 3.3 V, (b) 3.8 V, (c) 4.5 V, (d) 5.4 V (2 V/div)

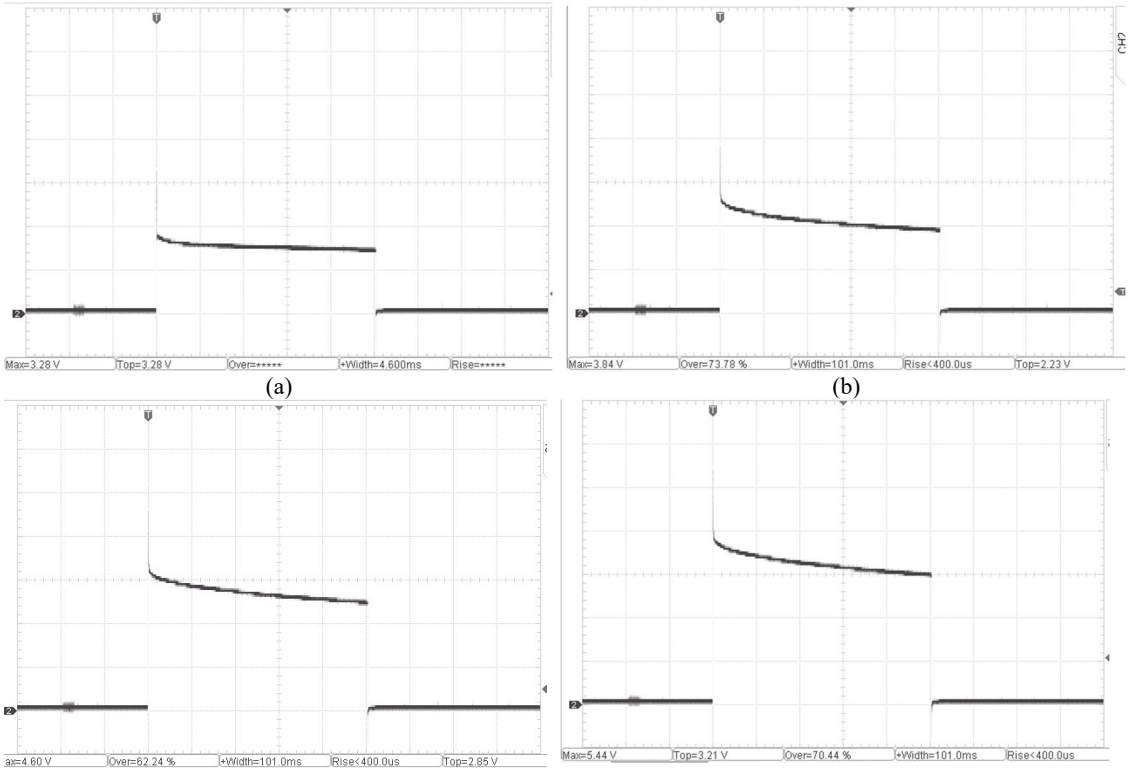

(a) (b)

(c) (d)

Figure 6.17: Coil Voltage with a V_{DM} of: (a) 3.3 V, (b) 3.8 V, (c) 4.5 V, (d) 5.4 V (1 V/div)

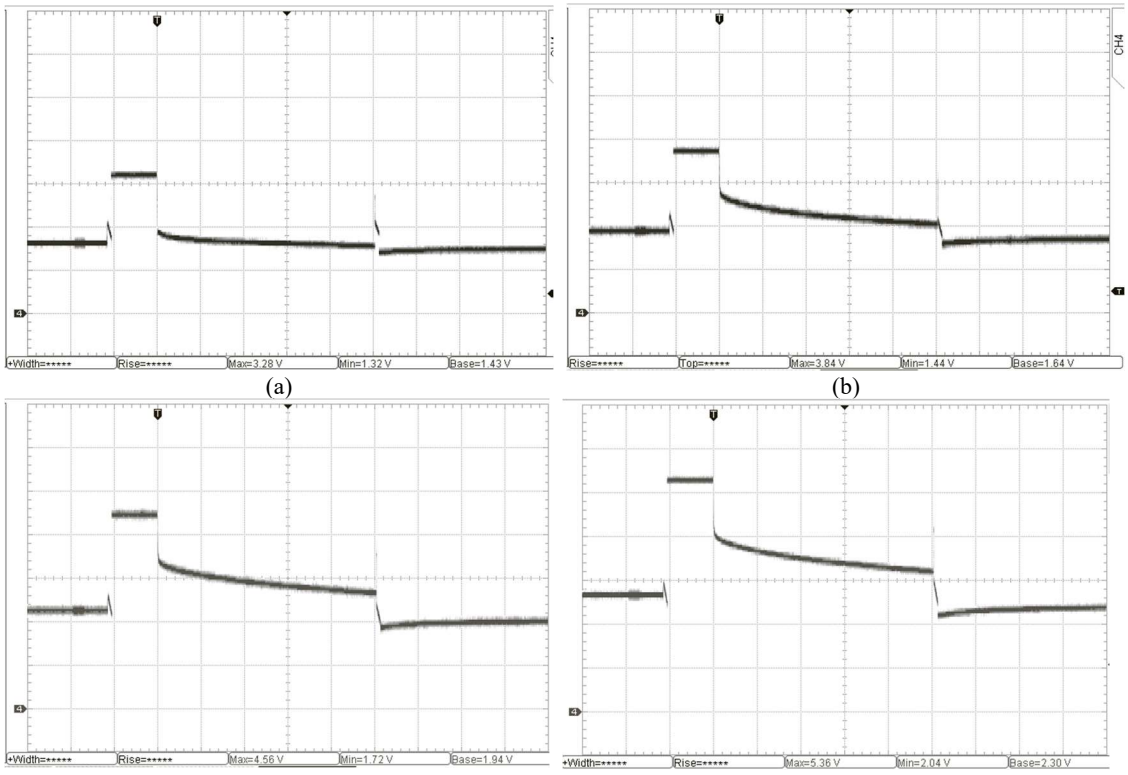

(a) (b)

(c) (d)

Figure 6.18: Capacitor Voltage with a V_{DM} of: (a) 3.3 V, (b) 3.8 V, (c) 4.5 V, (d) 5.4 V (1 V/div)

The coil current was extrapolated from the measured voltage profiles and compared against the analytical model of the circuit. Figure 6.19 illustrates the results for the 5.4 V disengagement case. The measured data shows a higher peak current during the initial transient, followed by a steady-state current estimation error of approximately 4 %. Integration of the voltage–current product yields a total transferred energy of 5.96 J, which is 2.7 % lower than the value obtained from the analytical model.

The capacitor voltage profiles before and after disengagement exhibit a consistent voltage drop of approximately 0.6 V across all tests. This corresponds to an energy dissipation ranging from approximately 5.4 J at the lowest test voltage (3.3 V) to 9.1 J at the highest (5.4 V). In the latter case, comparison with the current profile shown in Figure 6.15 indicates that approximately 66% of the available energy is transferred to the coils, with the remaining 34% dissipated within the circuit. Given that the disengagement mechanism comprises two identical circuits operating in parallel, both the total energy input and the energy delivered to the coils are effectively doubled.

Although this energy conversion is notably inefficient, the system still achieves the required separation velocity. Moreover, since disengagement occurs at the beginning of the mission, when battery state-of-charge is high and solar cell output exceeds demand due to end-of-life design margins, the energy is effectively “free.” Consequently, despite its low efficiency, the method remains practical and viable for the intended application.

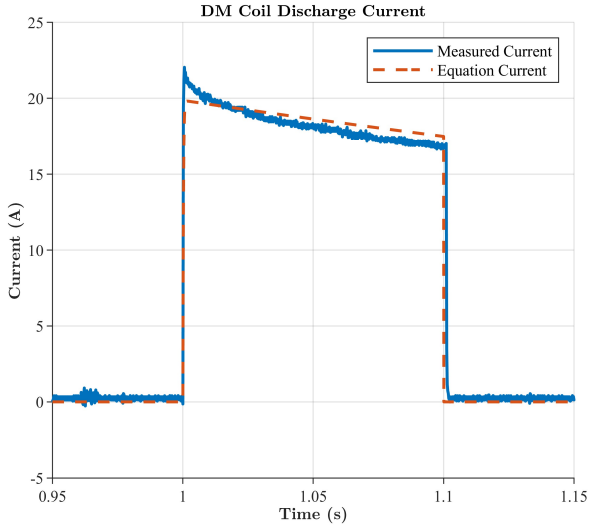

Figure 6.19: Analytical and measured coil currents

The bench-level tests confirmed the correct operation of all major subcircuits in the disengagement mechanism. The series/parallel switching produced the expected outputs, validating the reconfiguration logic. Bootstrap gate voltages remained stable throughout the pulse duration, ensuring reliable high-side MOSFET conduction. Coil voltage profiles matched both LTSpice and analytical models, confirming the accuracy of current predictions. Capacitor voltage drops indicated energy losses of 10.8 - 18.2 J per disengagement event across both circuits. Although the system exhibits low electrical-to-kinetic conversion efficiency, the achieved separation velocities meet mission requirements, and the energy expenditure is acceptable within the mission context.

6.4 Uncertainty Analysis of Simulation Outputs

The simulations presented in Section 7.3 yield a nominal separation velocity for the disengagement mechanism of 334 mm/s. However, this result is subject to a range of uncertainties that arise from both electrical and mechanical tolerances within the model. These uncertainties stem from component-level variations, measurement limitations, and integration-dependent factors, and they collectively influence the final predicted separation velocity.

These sources include component tolerances in capacitor parameters, analogue-to-digital converter (ADC) accuracy for charge voltage, pogo-pin spring and magnet force variation, MOSFET drain-source resistance, and mechanical alignment offsets. The complete set of error margins, representing both best-case and worst-case scenarios, is summarised in Table 6.4. The resulting uncertainty bounds correspond to a separation velocity range of 309 mm/s to 345 mm/s, equating to a total uncertainty of +11% / –7% relative to the nominal value.

These values are derived using a combination of methods. For the electromagnetic (EM) force, the margins are obtained through simulation. Only negative deviations are considered to prevent the model from overestimating performance. For the pogo pins and permanent magnets, although manufacturer-specified tolerances may be wider, the integration process requires force-matched components. Only those with force deviations within ± 5 % across the operational separation distance are accepted. A similar approach was applied to the coil windings, where only coils within the specified dimensional tolerances were integrated, and the margins reported reflect the resolution of the measurement equipment used during inspection.

The most significant contributions to the overall uncertainty originate from the coil resistance and the coil centre offset, which explains the asymmetric error margins (larger positive than negative deviation). Both of these contributors can be further mitigated through stricter component selection and alignment control during assembly. Ultimately, these findings highlight the importance of precision in component matching and mechanical integration to minimise uncertainty and ensure consistent separation performance.

Table 6.4: Simulation Model Margins of Error (at 20 ºC)

Source	Min Error	Max Error
Coil Resistance	- 6 mΩ	+ 6 mΩ
Charge Voltage	- 10 mV	+ 10 mV
Drain-Source	0	+4 mΩ
EM Force	- 2 %	0
Spring Force	- 5 %	+ 5 %
Magnet Force	- 5 %	+ 5 %
Magnet Offset	- 0.1 mm	0
Coil Centre Offset	- 0.1 mm	+ 0.1 mm

The margins reported in Table 6.4 were defined using conservative, bounded estimates based on measurement data, component specifications, and manufacturing tolerances. Electrical parameters such as coil resistance and spring and magnet forces were assigned limits based on measured minimum and maximum values across available samples. The charge voltage margin reflects the effective resolution and accuracy of the onboard ADC, while the drain–source resistance bound was derived from manufacturer datasheet specifications. The electromagnetic force uncertainty was obtained from finite element analysis by comparing analytical and FEA-derived force predictions. Geometric offsets, including magnet protrusion and coil centring, were bounded using achievable manufacturing and assembly tolerances.

6.5 Pendulum Tests

To validate the accuracy of the dynamic disengagement model, a physical test method is required that captures the interaction between the time-varying electromagnetic force output and the resulting mechanical motion. Up to this point, model validation has assumed a quasi-static approximation, wherein the static force generated by the coils is sampled at discrete time steps and numerically integrated to yield velocity and

displacement. While this approach offers computational simplicity, it inherently neglects the coupling and feedback between force application and mechanical response, particularly during transient events.

A pendulum-based test provides a real-time experimental platform to investigate this coupling. By allowing the test mass to move freely in response to the disengagement force, it becomes possible to assess whether the simulated force profiles accurately reflect the actual dynamics of the system under realistic boundary conditions. This method enables the direct measurement of key parameters such as swing amplitude, separation velocity, and induced rotation, while preserving the fidelity of the disengagement force profile and its temporal characteristics.

Two pendulum configurations were developed explored. The first configuration employed a rigid-arm pendulum to isolate and assess translational behaviour in a controlled, single degree-of-freedom system. The second configuration used a string-based pendulum with a full-scale satellite model, enabling free translation and rotation and more closely approximating on-orbit conditions. The insights gained from these tests were critical in evaluating the limitations of the quasi-static model, identifying system sensitivities, particularly to mass asymmetry, and refining both hardware and modelling approaches.

6.5.1 Rigid Arm Pendulum Configuration

The initial experimental setup employed a rigid arm pendulum to provide a controlled environment for testing the disengagement mechanism. In this configuration, the test body, representing a satellite or sub-satellite assembly, was mounted at the end of a non-flexible, one meter pendulum arm, which was suspended from a flexure pivot bearing at its top, as shown in Figure 6.20. The use of a flexure pivot eliminated static and kinetic friction from the system and replaced them with a well-defined torsional spring constant. This simplified the dynamic model of the pendulum while preserving essential mechanical realism.

The pendulum constrained motion to a single plane and suppressed rotational degrees of freedom, allowing the experiment to isolate and evaluate translational separation dynamics such as timing accuracy, release symmetry, and consistency in applied force. Although the flexure pivot introduces geometric nonlinearity and hysteresis

due to elastic deformation, these effects are well characterised in the manufacturer's datasheet and were accounted for in the simulation.

At the swinging end of the pendulum arm, a simplified satellite model containing the disengagement mechanism and associated circuitry was mounted. A second, identical model was fixed to the base to replicate the PQ8 alignment. Although both satellites would separate in orbit, only one was free to swing, and the simulation was adjusted to reflect this asymmetry. To minimise eddy current losses, both models used 3D-printed plastic frames in place of aluminium, and their internal configurations were limited to the EPS PCB and a stacked control board. The setup also ensured sufficient spacing from the aluminium test rig to prevent magnetic field attenuation from surrounding conductive materials.

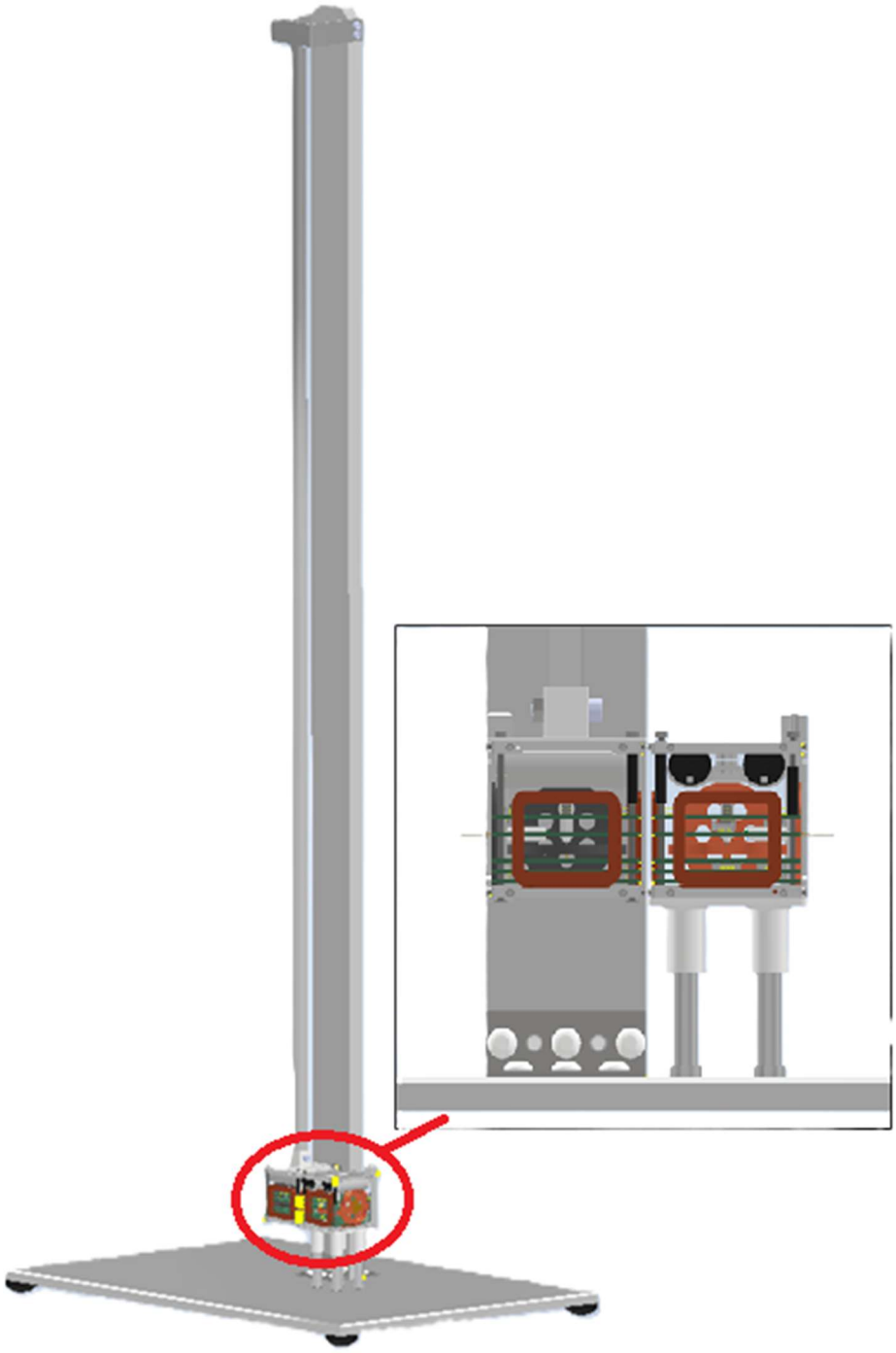

Figure 6.20: Rigid pendulum test setup

Data acquisition was performed using a high-resolution camera aligned parallel to the axis of the swing. The camera was positioned to eliminate parallax and recorded the entire disengagement sequence at 60 frames per second. The footage was processed frame by frame to extract angular displacement over time, which was then used to derive velocity and compare measured dynamics to those predicted by the simulation.

Due to the non-negligible mass of the pendulum arm, the system behaves as a compound pendulum. The calibration process, between the test setup and simulation, thus

focused on identifying the correct effective centre of mass and moment of inertia. These parameters were tuned using the measured oscillation period, which is independent of the disengagement force, to bring the simulated and experimental dynamics into alignment.

Once calibrated, the amplitude of the swing, governed by the impulse imparted during disengagement, was used to validate the simulated force model. The simulation was configured with the same physical parameters as the experiment, as listed in Table 6.5.

Table 6.5: Rigid pendulum test parameters

Parameter	Value
Operating Voltage	5.3 V
Pulse Width	200 ms
Mass of Satellite Model	50 g
Mass of Rod	100 g
Centre of Mass (From pivot)	0.675
Flexure Pivot Torsion	$8\times10^{-5}\ \theta$
Initial Pendulum Angle, $\theta_{initial}$	0 °
Moment of Inertia	0.0859 kg.m^2

Figure 6.21 shows the setup before and during disengagement, while Figure 6.22 compares the simulated angular displacement of the pendulum to that extracted from the experimental video. The curves show strong agreement, both in peak amplitude and in the shape of the trajectory. The mean absolute error (MAE) was 0.3 °, and the root mean squared error (RMSE) was 0.4 °, with a maximum deviation of 1 °. These discrepancies are attributed primarily to the limited temporal resolution of the video recording, which affects tracking accuracy at higher angular velocities.

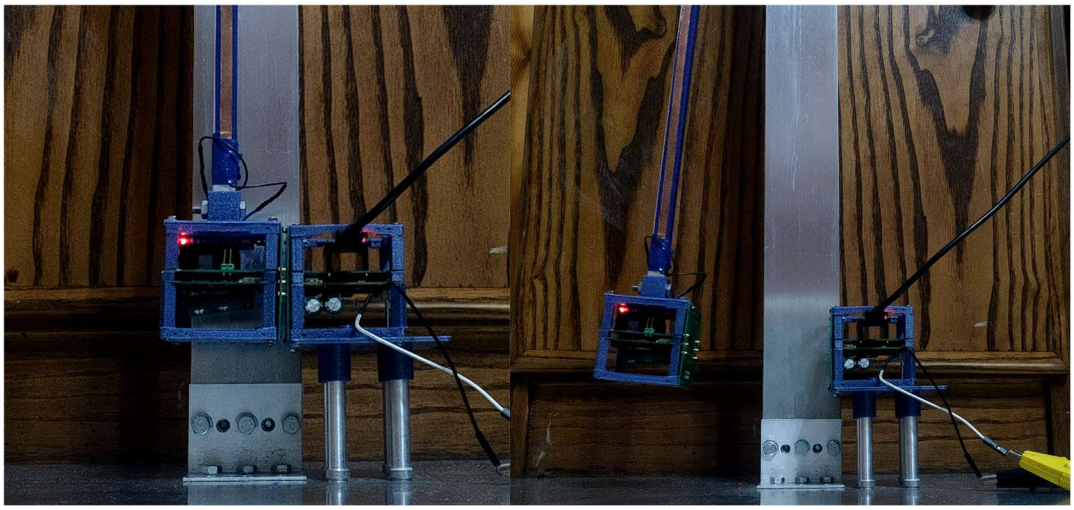

Figure 6.21: Photo of rigid-pendulum experimental setup.

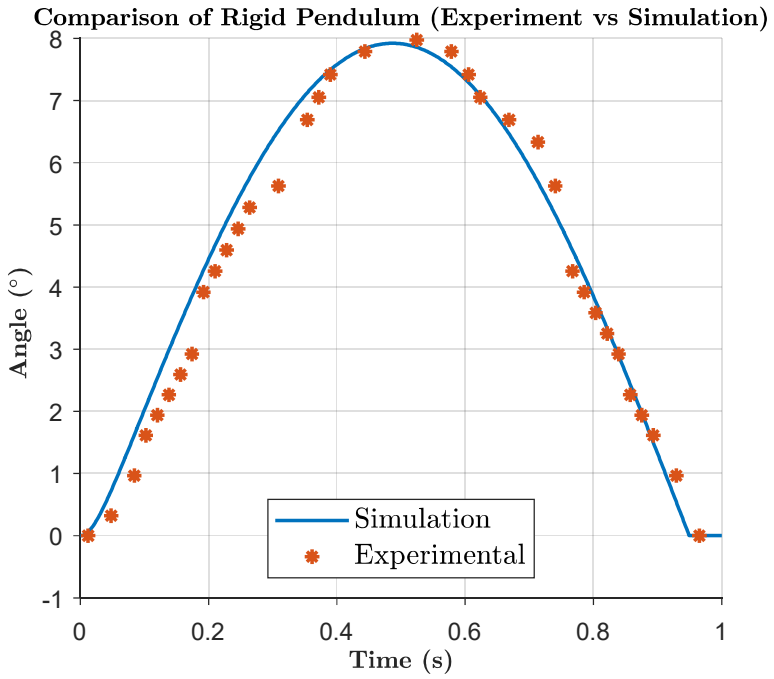

Figure 6.22: Comparison of results from rigid pendulum simulation and experiment

Despite these limitations, the close match between simulated and observed pendulum motion demonstrates that the modelled force profile accurately captures the dynamics of the real system. This result validates the use of the force model for simulating translational separation in a constrained configuration. It supports the applicability of the static formulation for dynamic motion when rotational dynamics are absent or suppressed.

6.5.2 Second Configuration: Free-swing Pendulum

To emulate the whole dynamics of an in-orbit separation event, including both translational and rotational motion, a second experimental configuration was implemented using a flexible string pendulum. This setup was designed to overcome the planar motion constraints of the rigid arm test and allow the satellite model to move with six degrees of freedom, more closely replicating post-disengagement conditions in space.

The satellite model used in this configuration was structurally representative of flight hardware, including the full aluminium frame and internal PCBs to reflect realistic mass and inertia distributions. Modifications were made to accommodate test instrumentation, that is, reaction wheels and magnetorquers not relevant to the test axis were removed to free space for Bluetooth modules, SD card data logging, and switching circuitry. These changes preserved critical mass properties along the axis of interest while enabling onboard data acquisition.

The satellites were suspended from a five meter long string, resulting in an extended oscillation period and improved temporal resolution. This change also eliminated torsional stiffness in the suspension, allowing the system to exhibit both translational and rotational motion. However, this configuration made precise angular tracking difficult, as the camera's field of view had to span a large vertical region, which was not practically feasible. Consequently, the analysis focused on the linear displacement of the satellite model. The test setup is illustrated in Figure 6.23.

Given the extended length of the string and the relatively small swing angles involved, the arc of motion closely approximates a straight line. This allows the pendulum's motion to be considered as linear in the direction of the swing, simplifying the analysis without significantly compromising accuracy. Under these small-angle conditions, the arc length s can be approximated as the linear displacement x, and the angular velocity can be similarly approximated using:

$$x(t) \approx L\theta(t), \qquad for\ small\ \theta$$

where L is the length of the string and $\theta(t)$ is the angular displacement. This small-angle approximation is valid for the low-amplitude swings observed during testing and aligns with the goal of measuring the translational separation velocity imparted by the disengagement mechanism.

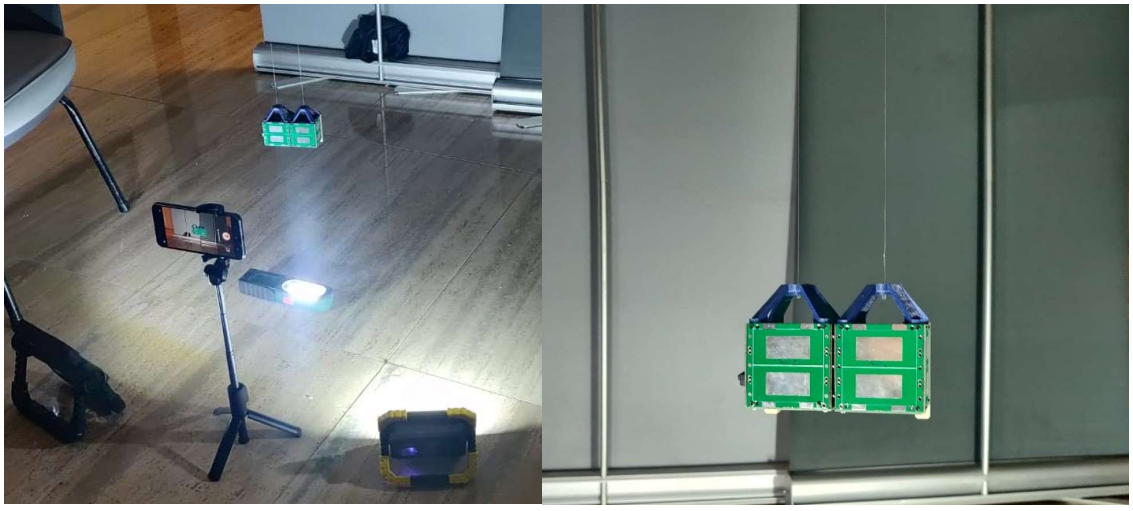

Figure 6.23: Photos of free-swing pendulum experiment setup.

The data acquisition system was also upgraded. The original 60 frames-per-second camera used in the rigid-arm tests was replaced with a high-speed 240 frames-per-second camera. This upgrade enabled finer resolution of high-speed motion immediately following the release event.

The key experimental parameters used in the simulation and testing are listed in Table 6.6. The primary test objective was to assess whether the mechanism could deliver a post-release relative velocity of at least 0.2 m/s, which corresponds to the minimum mission requirement for adequate clearance and proper phasing between satellites.

Table 6.6: Free-swing pendulum experiment parameters

Parameter	Value
Operating Voltage	3.6 V
Pulse Width	100 ms
Mass of Satellite Model	156 g
Pendulum Length	5 m

6.5.2.1 First Attempt and Lessons Learned

The first test run using this configuration was unsuccessful. Instead of clean translational motion, the satellites exhibited rapid rotational motion immediately following disengagement. This unexpected behaviour caused the satellites to spin about their axes uncontrollably upon release. As they swung back toward one another, a collision occurred, which arrested the rotational motion and resulted in a wide linear separation. Repeated tests with the same setup yielded the same behaviour.

Although the tests did not produce the intended linear response, they revealed several important lessons:

1. The setup accurately reflects the actual dynamics of the system, including undesired effects, which is critical for realistic validation.
2. The disengagement modules functioned reliably in the full-scale test setup, confirming electrical and mechanical integration.
3. The imbalance in the satellite's centre of mass had a substantial adverse effect on the post-release motion, inducing rotation and degrading the effectiveness of the separation.

This outcome particularly highlighted the sensitivity of the mechanism to mass asymmetries and the need for precise balancing to avoid rotational coupling. To address this, a balancing procedure was introduced, which is covered in the following subsection.

6.5.2.2 Balancing the Satellites

Following the unexpected rotational behaviour observed during the first test attempt, a systematic mass-balancing process was undertaken to minimise torque-induced rotation during disengagement. The objective was to ensure that the disengagement force acted through the satellite's centre of mass, thereby reducing the generation of angular momentum.

The experimental setup, Figure 6.24, included an onboard accelerometer and gyroscope, enabling real-time measurement of the satellite's attitude. A Kalman filter was implemented to generate estimates of the pitch and roll angles, whilst improving the signal-to-noise ratio of the raw sensor data. To ensure accuracy, the Kalman filter output was calibrated against measurements from a digital spirit level, which provided an independent angular reference with a known accuracy of $\pm$ 0.5 ° over the relevant range.

The satellites were suspended across the disengagement axis, as illustrated in Figure 21, so that balancing efforts directly addressed moments about the axis responsible for inducing unwanted rotation. A set of test masses was then incrementally added to various locations on the structure. By observing the static equilibrium orientation of the satellite and comparing the pitch and roll angles to zero reference, the magnitude and position of the compensating mass could be iteratively refined.

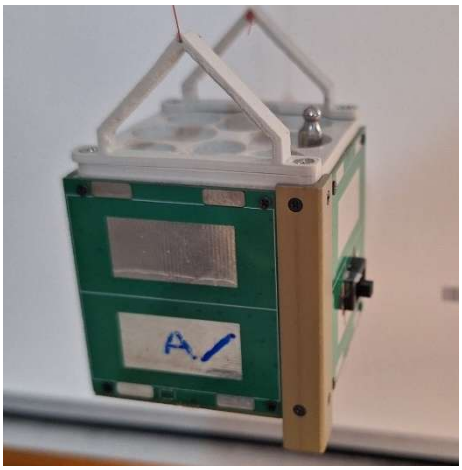

Figure 6.24: PQ1 Balancing Exercise

This iterative procedure resulted in a configuration where the satellite remained level and stable when suspended along the disengagement axis, indicating that the applied force would act through the centre of mass with minimal off-axis torque. Achieving this condition was critical for the second test attempt. Even slight residual imbalances at the moment of release were found to induce noticeable rotational motion.

6.5.2.3 Second Attempt

The free-swing pendulum experiment was repeated using the parameters listed in Table 6.5, this time incorporating the balancing corrections described in the previous section. The aim was to minimise torque-induced rotation and achieve clean translational separation along the disengagement axis.

The results showed a marked improvement in linear motion following actuation. Although some residual rotation remained, it was substantially reduced compared to the initial attempt. The satellite models demonstrated symmetric translational movement away from one another, more closely approximating the desired in-orbit behaviour. While a perfectly rotation-free separation was not achieved, the test was deemed successful, as it captured the essential system dynamics and yielded usable data for validating the force model and estimating the separation velocity.

To quantify the separation, the video footage was processed using colour-based blob detection and frame-by-frame tracking to extract the positions of the satellites over time. From these trajectories, the relative displacement and its derivative (i.e., separation velocity) were calculated. The blob masks used in the analysis are shown in Figures 7.22 and 7.23, for the initial and maximum swings, respectively. The resulting maximum and minimum observed amplitude and velocity profiles are presented in Figures 7.26a and 7.26b, respectively, along with a comparison to the simulated response in Figure 6.27.

The largest source of deviation in the results was due to parallax errors. In the experimental coordinate frame, the disengagement axis corresponds to the x-axis, while the pendulum string defines the z-axis. The y-axis, perpendicular to both, lies along the camera's line of sight, and any motion along this direction introduces parallax error in the captured images, so care was taken to minimise and compensate for this effect.

Figure 6.25: PQ1 pendulum initial position

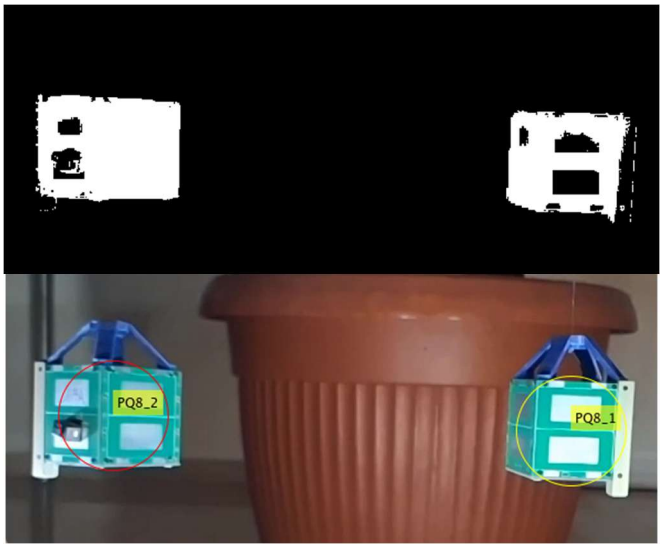

Figure 6.26: PQ1 pendulum max swing

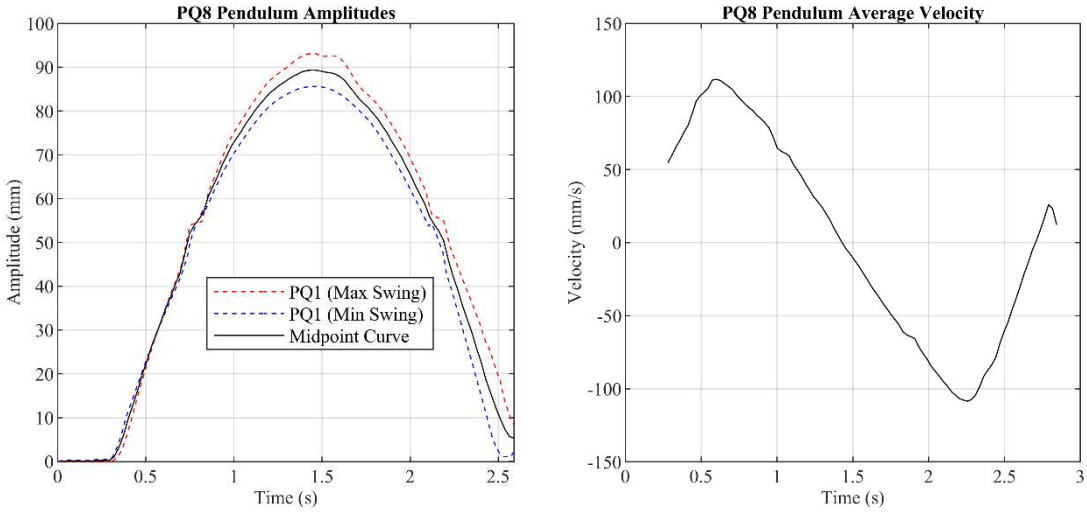

(a) (b)

Figure 6.27: Free-swing pendulum output: (a) Amplitudes, (b) Results

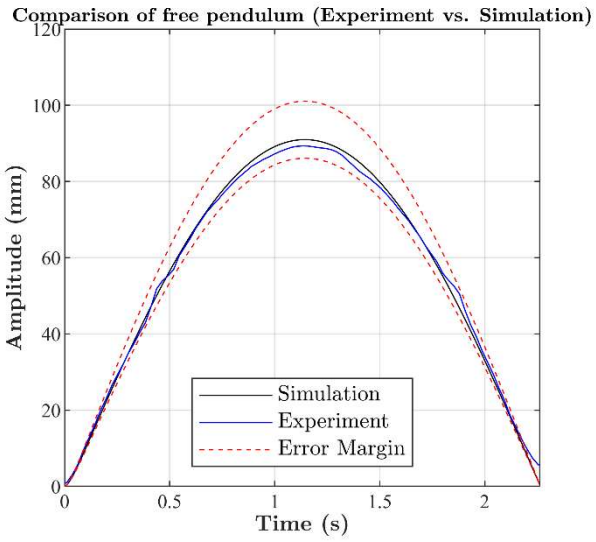

Figure 6.28: Comparison between experimental and simulation for the free-swing pendulum

Notably, one of the two satellites moves slightly towards the camera and the other away from it, resulting in a larger and smaller perceived swing, respectively. By averaging the data to obtain a mid-point curve, opposing parallax errors are approximately cancelled out, and a more representative result is obtained.

The model achieved a mean absolute error (MAE) of 1.2 mm and a root mean squared error (RMSE) of 1.3 mm, indicating strong agreement with experimental data. The observed trajectory error remained within 2.4%, supporting the validity of the force model under near-linear motion conditions. Additionally, the midpoint curve remains within the margins of error introduced by parameters described in Table 6.4.

Despite the improved balance, minor rotational motion persisted. This outcome reinforces the critical importance of precise mass balancing to ensure accurate disengagement. However, due to the limited availability of precision equipment during the experimental campaign, improving balance alignment further was not feasible. This remains a point for future refinement, potentially through the use of dedicated balancing rigs or moment-of-inertia characterisation systems.

6.6 Testing Methodology Justification and Limitations

The test campaign was intended as an initial feasibility demonstration of the disengagement concept, rather than a full qualification or environment-representative validation. The scope and limitations of the experimental setup are therefore primarily driven by bounding analyses and practical constraints.

Testing in a Helmholtz coil was not considered for this round of experiments for two main reasons. First, finite element analysis of the disengagement coils shows that the magnetic field strength generated locally during actuation is significantly larger than the ambient geomagnetic field. At the distances relevant to the disengagement event, the induced magnetic field exceeds the Earth's magnetic field magnitude by an order of magnitude. That is, values on the order of 11 to 110 mT compared to approximately 25 to 65 μT for the Earth's magnetic field at sea level. As a result, the influence of the Earth's magnetic field on the disengagement dynamics during actuation is expected to be negligible, and its inclusion would not materially affect the outcome of the test.

Secondly, practical and operational constraints limited the feasibility of Helmholtz testing. Access to a suitable Helmholtz cage would have required transporting relatively heavy experimental hardware between buildings, through high-traffic areas with limited environmental control. These constraints posed non-negligible risks to the hardware and significantly reduced the repeatability and controllability of the test conditions, making such testing impractical within the scope of this campaign.

As discussed in the limitations of the pendulum-based testing, repeatability issues were observed in the current setup. A meaningful Helmholtz-based test campaign, one aimed at quantifying the influence of the Earth's magnetic field, would require these repeatability issues to be resolved first. For this reason, combined Helmholtz and disengagement testing is deferred to future work, where improved experimental control can be ensured.

Testing of the full PQ8 configuration was similarly excluded from the present campaign as to isolate and validate the fundamental disengagement mechanism. Testing a reduced configuration allowed the dominant physical effects governing separation dynamics to be observed without introducing additional structural complexity or compounding sources of uncertainty. Extension to the full PQ8 assembly is therefore identified as a logical next step once the core mechanism has been fully experimentally explored.

Finally, a frictionless table was not considered due to the lack of available equipment and the constraints of both budget and development time. Designing and fabricating a suitable low-friction platform within the project timeframe was not feasible. The pendulum-based setup was therefore selected as a low-cost and rapidly deployable alternative. Despite its limitations, the pendulum configuration provides multiple degrees

of freedom and, if the identified repeatability issues are addressed, offers a promising analogue for in-orbit disengagement dynamics. In this respect, it may ultimately provide a more representative test environment than a planar frictionless surface, which inherently restricts motion to two dimensions.

Thermal-vacuum (TVAC) testing was not performed for the disengagement mechanism due to the unavailability of appropriate facilities during the research period. While the absence of TVAC testing limits direct experimental verification of performance under combined thermal and vacuum conditions, it does not materially reduce the assigned models Technology Readiness Level for this subsystem. The disengagement mechanism relies on electromagnetic actuation and passive mechanical elements whose functional behaviour is primarily governed by electrical input energy and geometric tolerances, rather than temperature-sensitive material properties.

Thermal effects were partially addressed through analytical estimates and simulations of coil resistive heating during the disengagement pulse, using conservative assumptions consistent with PocketQube thermal environments. These analyses indicate that expected temperature excursions remain within the operational limits of the selected materials and do not significantly compromise actuation margins. To mitigate the absence of TVAC testing, future work should include:

- thermal-vacuum cycling of the disengagement mechanism to verify repeatability across expected on-orbit temperature ranges,
- correlation of coil resistance and actuation timing with temperature,
- validation of thermal models against test data. T

These steps would support progression from design-level to qualification-level verification without requiring fundamental design changes.

6.7 Discussion on the Disengagement Mechanism

The disengagement mechanism developed in this work is characterised by a unique electromechanical architecture, with the primary output of interest being the impulse imparted during separation, or equivalently, the separation speed. All system parameters, from mechanical layout to electrical inputs, ultimately contribute to achieving this key performance metric. The analysis and modelling presented have focused on capturing this impulse accurately, evaluating its repeatability, sensitivity, and coupling with system-level constraints.

Experimental validation confirmed that the mechanism functions as intended and consistently delivers sufficient impulse to meet deployment objectives. However, the tests also revealed a crucial secondary effect, i.e. the introduction of rotational motion during separation. Despite deliberate efforts to centre the mass of the satellite models, the resulting torque was not eliminated. This demonstrates the high sensitivity of the system to small asymmetries, as even minor deviations between the applied force and the true centre of mass produce appreciable angular momentum. While the correction significantly reduced rotation, it remained non-negligible and highlights the critical role of mass balancing in such low-force, high-precision mechanisms. Addressing this issue should remain a priority in future work.

In this context, pendulum experiments proved useful in demonstrating the dynamic coupling between electrical actuation and physical motion. However, they are not well suited for the precise characterisation of the disengagement method, due to several limitations that impact repeatability and control. First, the initial configuration of the system (with two satellites joined as a compound pendulum) differs from the post-disengagement state, where each satellite becomes an independent pendulum with a shifted centre of mass and equilibrium point. This transition introduces minor rotational effects and a change in dynamics that complicate direct comparisons.

Second, the use of a flexible string introduces variability in pendulum length between trials. The string often becomes intertwined or twisted, an effect difficult to detect visually due to its length, resulting in inconsistencies between experiments that, although can be calibrated for, undermine experimental repeatability.

Third, the environmental conditions in the test facility are difficult to control. Identifying an appropriate space with a high ceiling, minimal air flow, and access control was a significant constraint. Additionally, the inability to adjust key environmental parameters such as temperature further limits the precision of the test campaign.

As a result of these factors, while the pendulum tests validate the general dynamic behaviour of the mechanism, they are insufficient for detailed performance characterisation. In future work, a dedicated experimental approach is required to systematically characterise the relationship between input parameters, including the disengagement voltage and pulse width, and the resulting Δv. The method should enable precise performance mapping and improved validation of the analytical model.

Two system parameters were found to dominate the mechanism's behaviour. First, the magnet offset, the extent to which magnets protrude from the solar panel PCB, substantially affects the required voltage and pulse width for activation. Second, current through the coils also plays a crucial role in force generation, though this is bounded by the match between the coils and the driving capacitors, as well as the electronic system's power handling capabilities.

The system presented here was modelled without idealising assumptions wherever possible. Rigid body motion is justified by the structure's design, and symmetry was assumed only for components such as the magnets and pogo-pins, which can be matched and aligned during assembly. While eddy currents were not included in the initial analytical formulation, their effects were later quantified using FEA and incorporated into the final energy analysis, ensuring their contribution was accounted for.

Direct analogues to this disengagement mechanism are scarce. Compared to more traditional systems, this design offers simplicity, both in its circuitry and its motion dynamics. Each part of the mechanism is relatively simple to model and build, although the complexity arises from their interaction rather than from any individual subsystem. It also exhibits strong repeatability, with one caveat: coil resistance is temperature-dependent, but this variability can be monitored and compensated using onboard temperature sensors already available on the satellite.

From a performance perspective, the force delivery is predictable and sufficient for the application. The design boasts a minimal mass and volume footprint, with no dead weight post-disengagement; the coils double as magnetorquers and the supercapacitors as auxiliary energy storage, giving the mechanism excellent functional integration. Control is also versatile, allowing tuning through both voltage and pulse width.

The mechanism is inherently scalable, with larger satellites requiring larger coils and more energy, both of which scale naturally with available onboard resources. It integrates cleanly with the PQ8 satellite platform. However, testing can be challenging due to the miniaturised nature of the work and the need to isolate the system from external forces, a persistent difficulty when evaluating low-force actuators.

Post-disengagement, rotational correction is required, and therefore the ADCS must be capable of handling the imparted angular momentum. This places additional design constraints on both ADCS performance and the accuracy of the centre-of-mass balancing process.

While the modelling approach was comprehensive, a few limitations remain. Primarily, the lack of experimental validation using a completely balanced system, which would help quantify how effectively torque can be minimised in the best-case configuration.

Although the modelling and evaluation focused primarily on mechanical and electromagnetic behaviour, eddy current losses within the system were found to be a significant source of inefficiency. In particular, copper ground planes or large copper pours on nearby PCBs are a considerable source of energy loss. In this work, no specific precautions were taken to mitigate these effects, and the resulting energy losses directly reduced the available impulse delivered by the mechanism. Addressing this issue in future designs of all subsystems is essential. Imposing geometric or layout constraints, such as removing copper in critical areas, shaping ground planes, or defining keep-out zones, can substantially reduce eddy current paths and improve both the efficacy and predictability of the mechanism.

A promising future avenue lies in the shaping of the current pulse used to activate the coils. The current implementation relies on a near-square pulse, which delivers strong force initially but quickly loses effectiveness as the satellites move apart. Suppose the pulse waveform could be tailored, for example, to extend the duration or shift power delivery. In that case, it may be possible to maintain a more consistent force profile, leading to a more efficient impulse. While the practical implementation of this idea remains uncertain, it is a compelling direction for future exploration.

Finally, the design of the mechanism is not isolated. It is tightly coupled with other subsystems. In particular, the coil design and drive electronics were constrained by the ADCS requirements, including desired magnetic moments and allowable control voltages. This resulted in a compromise on coil wire diameter, shifting from an ideal 0.8 mm to 0.65 mm to satisfy both magnetic and electrical design goals. This underscores a broader point to the developed of this space systems: even small design choices in one part of the system can ripple through the entire satellite architecture, making integrated, cross-disciplinary thinking essential.

6.8 Repeatability of Experiments

The experimental campaign prioritised dynamic validation of the disengagement force model rather than high-volume statistical characterisation. Each experimental configuration was therefore performed under nominally identical electrical inputs to verify qualitative repeatability and consistency of the resulting motion. For the rigid-arm pendulum, these tests produced near-identical angular trajectories, with observed deviations dominated by video frame quantisation and tracking resolution rather than stochastic system behaviour.

In the free-swing configuration, repeatability was constrained by environmental sensitivity, variability in string geometry, and residual mass imbalance, which introduced scatter primarily in peak displacement and velocity rather than in the overall separation behaviour. Consequently, statistical confidence is expressed through bounded error envelopes derived from parameter uncertainty propagation, as listed in Table 6.4, and experimentally observed maximum and minimum responses, rather than through confidence intervals. This approach was considered appropriate given the low-force, highly coupled nature of the system and the limited controllability of the test environment.

Table 6.7 lists the demonstrative experiments performed, together with their limitations in terms of repeatability and sources of error. Although the experiments provide sufficient confidence to demonstrate feasibility, these repeatability issues are outlined for further work, where full characterisation of the disengagement mechanism becomes more important.

Table 6.7: Experiment Repeatability Summary

Experiment	Measured Quantity	Dominant Error Sources	Repeatability Assessment	Margin / Uncertainty Treatment
Rigid-arm pendulum	Angular displacement	Video frame rate, pixel quantisation, Pendulum parameter measurement	High. Showing consistent trajectories across trials	Measurement-resolution limited. MAE and RMSE reported
Free-swing pendulum (unbalanced)	Linear displacement	Mass asymmetry, rotational coupling, parallax	Poor. Showing rotational motion dominates response	Used diagnostically. No quantitative margins claimed.
Free-swing pendulum (balanced)	Linear displacement, Separation velocity	Parallax, Residual Rotation, Pendulum geometry variability	Moderate. Showing peak amplitudes consistent within a few percent	Envelope defined by observed bounds and simulation uncertainty. MAE and RMSE reported

6.9 Conclusion

This chapter presented the simulation and validation of a dual-use disengagement mechanism designed for the PQ8 deployment architecture. The mechanism repurposes onboard magnetorquers to perform separation functions via electromagnetic repulsion, offering a compact, energy-efficient solution that aligns with the physical and operational constraints of small satellite missions.

System-level simulations were used to evaluate the disengagement dynamics, integrating electrical, mechanical, and thermal subsystems to predict current profiles, separation forces, and resulting satellite motion. These simulations confirmed that the mechanism can generate separation impulses consistent with mission requirements and that the dynamic load imposed on the electrical domain remains negligible throughout actuation.

Finite element analysis validated the use of the electromagnetic force expressions and quantified the influence of eddy current losses, which were subsequently incorporated into the complete kinematic model. Bench-level circuit testing confirmed that key subsystems, including the series/parallel switching circuitry, bootstrap drivers, and discharge path, behaved as expected and matched both analytical predictions and LTSpice simulations within acceptable margins.

Experimental validation through pendulum testing demonstrated the ability of the mechanism to generate clean translational motion when the satellite is well balanced, though some residual rotation persisted. Comparison of experimental and simulated pendulum trajectories showed strong agreement, validating the underlying force models. However, the tests also revealed significant challenges to repeatability due to limitations in environmental control, variability in pendulum geometry, and dynamic changes in the system's centre of mass post-disengagement.

While the tests effectively demonstrated the mechanism's functional behaviour, they were not suited for quantitative characterisation of its performance. Future work should focus on developing controlled experimental setups capable of systematically mapping the relationship between input parameters and the resulting Δv.

Despite these limitations, the simulation and validation campaign confirms that the mechanism achieves the required impulse delivery under realistic conditions and is suitable for integration into the PQ8 deployment system. All design requirements, as

outlined in Chapter 5, have been met. These include achieving the required impulse for clean separation, maintaining compatibility with power and ADCS constraints, and minimising the structural footprint.

The mechanism's simplicity, repeatability, and compact footprint, alongside the multi-functional reuse of its components as magnetorquers and energy storage, make it well-suited for resource-constrained missions. Despite the complexity of component interactions, the overall design remains analytically accurate and highly adaptable. Opportunities for further performance enhancement were identified, including shaping the actuation pulse to improve impulse efficiency across the separation trajectory.

Future work should focus on developing more reliable and repeatable methods for characterising the disengagement mechanism, particularly in terms of mapping input parameters to separation performance. This should then be followed by investigating pulse shaping strategies to optimise impulse delivery, conducting extended testing with precisely balanced systems, and evaluating long-term reliability under space-representative environmental conditions. Despite these remaining challenges, the current design demonstrates robust and consistent performance, with a clear path toward integration and further refinement for operational missions.

From a TRL perspective, the disengagement mechanism achieves a readiness level of 4, partially 5, having been validated and verified through both simulation and experimentation. The system does not reach TRL5 completely as the model was not tested under a thermal-vacuum environment, although simulations indicate improved performance under these conditions.

7 CONCLUSIONS & FUTURE WORK

7.1 Summary of Conclusions

7.1.1 Background & Literature Review

There is growing interest in satellite constellations for both commercial and research purposes. Large-scale initiatives such as OneWeb and Starlink aim to deliver global internet coverage, while companies like Planet Labs leverage constellations for Earth observation and data analytics. These are just a few of the many emerging applications of constellation-based technologies. However, despite increasing demand, the high costs and logistical complexity of constellation deployment continue to present significant barriers to entry. Notably, research into alternative deployment strategies remains limited.

This study began with a literature review spanning four foundational domains: (1) small satellites and their constellations, (2) standards and specifications for satellite structures, (3) disengagement mechanisms, and (4) passive constellation dispersal methods. Each section concluded by identifying the limitations of current approaches in relation to the PQ8 Architecture concept. These limitations were then distilled into a set of requirements to guide the design and development of the proposed system.

The central contribution of this research is the introduction of the PQ8 Architecture, a novel framework for deploying large-scale PocketQube constellations. The literature review contextualised the motivation behind this architecture by assessing the PocketQube platform's benefits and limitations as an affordable satellite class. The following key challenges motivated the need for a new deployment model:

- Rising costs of CubeSats and PocketQubes: Increased adoption, especially of CubeSats, in commercial and academic contexts has driven up costs across the small satellite sector.
- Limited PocketQube launch volume: The original PocketQube concept envisioned replacing a single 1U CubeSat with eight 1P PocketQubes, thereby achieving an eightfold cost reduction per satellite. In practice, limitations in miniaturising deployers meant that only half of these savings were realised.
- Logistical complexity: Deploying pico- and nanosatellite constellations typically relies on securing rideshare slots, which introduces significant uncertainties in scheduling, testing requirements for multiple vehicles, prolonged deployment timelines, and fluctuating launch costs.

These factors led to the conceptualisation of the PQ8 Architecture, an approach aimed at restoring the 1:8 mass/volume ratio between CubeSats and PocketQubes. The goal is to reduce per-satellite launch costs, and the total number of launches required to deploy a constellation. To achieve this, the PQ8 Architecture needed to demonstrate:

1. The structural feasibility of aggregating eight PocketQubes into a single unit.
2. A reliable mechanism for in-orbit disengagement.
3. A method for passively dispersing the satellites to form the intended constellation.

The next literature review focused on satellite structures. Given the practical emphasis of this component, the review prioritised standards, specifications, and launch vehicle user manuals over academic publications to align with industrial practices. While scholarly literature often concentrates on niche structural analyses, standards documents provide comprehensive requirements, test methodologies, and acceptance criteria. Key references included:

- ECSS Standards.
- CubeSat Specifications,
- Several launch vehicle user manuals: Falcon 9, Ariane 5/6, Ariane Vega C

Subsequently, disengagement mechanisms were examined. As the many-in-one satellite concept has limited precedence, the review concentrated on existing deployables and related mechanisms. A widely adopted framework categorising deployment systems into restraint, guidance, and actuation components was used to structure the review. The following gaps were identified in the existing literature and technology:

- No comprehensive disengagement system currently satisfies all PQ8 requirements
- Mechanisms requiring precise synchronisation of multiple identical triggers have yet to be demonstrated.,
- No actuator has been implemented that uses synchronised electromagnetic pulses to produce a coordinated repulsive force across multiple separation interfaces.

Finally, passive methods for constellation dispersal were reviewed. This analysis focused on the fundamental physics underlying approaches such as differential drag and nodal precession, both considered as potential dispersal techniques for the PQ8 system. The following research gaps were identified:

- Existing constellation deployment models assume individual satellite deployment, with initial conditions defined by relative position and velocity. The case of deployment from a single, combined unit has not been adequately explored.
- Consequently, dispersal algorithms do not account for disengagement velocity as a tunable control parameter, and its effect on phasing timelines remains largely unaddressed.

7.1.2 The PQ8 Architecture: Overview

The project presented in this thesis is a systems-level design study and therefore spans a broad range of topics. This chapter focused on the structural design and power requirements of the proposed system. Its primary objectives were to establish the mass and power budgets of the satellite, both of which are critical parameters for the design of the dispersal method and disengagement mechanism. Additionally, the chapter finalised the structural design and validated it through both NASTRAN simulations and physical testing.

The structural design was based on the CubeSat standard and developed using an iterative process to balance mass and volume constraints against the need to withstand launch loads. The design adhered to the safety factors defined in ECSS standards and various launch vehicle user manuals. The final structure passed modal, linear static, sinusoidal-equivalent vibration, and shock response spectrum analyses for the Ariane 5, Ariane 6, and Falcon 9 launch vehicles. However, the structure did not meet the shock load requirements of the Vega-C vehicle.

The satellite structure exhibited a first modal frequency of 860 Hz in isolation, which reduced to 183.5 Hz when subsystems were included, both exceeding the minimum 100 Hz requirement. Shock response analysis showed that a safety factor of 1.15 was achieved for the Falcon 9 and Ariane 5/6 vehicles. Linear static analysis yielded substantially higher safety factors, exceeding the ECSS minimum of 2. These elevated margins indicate an overengineered structure, primarily due to modifications introduced to satisfy shock response requirements.

Finally, the structural design was validated through physical testing in accordance with ECSS standards. These tests confirmed the satellite's ability to withstand both sinusoidal-equivalent vibration and shock environments for the Falcon 9 launch vehicle.

7.1.3 The Dispersal Method

The dispersal methodology developed in this project is notable for its generality, it extends beyond the PQ8 Architecture and can be applied to other many-in-one satellite systems. In this context, the chapter adapted a proven in-orbit dispersal approach, demonstrated initially by Planet Labs, to accommodate deployment scenarios consistent with the PQ8 Architecture.

A generalised dispersal strategy was proposed, treating the disengagement-induced Δv as a control variable. Two algorithms were introduced, which, for a given constellation topology of n satellites, output the required Δv and the corresponding disengagement timings needed to achieve optimal phasing intervals. These results enable the design of the separation event to produce a desired constellation geometry without requiring active propulsion after deployment.

The analysis demonstrated that dispersing PQ8 satellites without deployable panels is technically feasible; however, it results in significantly prolonged phasing times, approaching the duration of the mission itself. The chapter concluded that while the proposed dispersal method is valid for the PQ8 Architecture, it is also scalable to larger satellite configurations. To enhance the practical viability of the PQ8 design, particularly in reducing phasing duration, the inclusion of at least one deployable panel is recommended. Specifically, the analysis showed that for the presented case studies, the disengagement mechanism must deliver a Δv in the range of 0.2 to 0.4 m/s to achieve the desired constellation geometry at a perigee altitude of 500 km and eccentricity of 0.001.

7.1.4 The Disengagement Mechanism: Background

This chapter introduced the topology of the disengagement mechanism, outlining its functional requirements and key constraints. A central source of these constraints was the need for a dual-purpose coil design, in which the existing magnetorquer coils are repurposed to function as actuators within the disengagement mechanism. The chapter concluded by presenting an overview of the design methodology adopted for the mechanism's development. This approach followed a structured approach, beginning with an analysis of the static force equations, followed by the development of a dynamic disengagement model, the design of the driver circuit, verification of the design through simulation, and final validation through experimental testing.

7.1.5 The Disengagement Mechanism: Analysis & Design

Building on the requirements and constraints outlined in the background chapter on disengagement mechanisms, a comprehensive MATLAB model was developed to capture the mechanisms governing the conversion of electrical energy, stored in the supercapacitors, into kinetic energy by the disengagement mechanism. The model incorporates the circuit behaviour, thermal effects, mechanical interface interactions, friction, and both linear and rotational kinetic energy components.

This model was then used in conjunction with a short-list of candidate capacitor banks to identify the optimal coil-capacitor pairing for achieving the desired disengagement velocity. The subsequent design of the driver circuits presented a significant challenge: balancing stringent size constraints and power requirements while relying exclusively on COTS component.

The chapter concluded with a theoretical failure mode analysis and corresponding risk mitigation strategies. These included proposed modifications to the circuitry and operational procedures aimed at reducing both the likelihood and impact of potential failure modes.

7.1.6 The Disengagement Mechanism: Testing

The testing and validation campaign assessed the performance of the PQ8 disengagement mechanism through a combination of circuit-level verification and dynamic system experiments. At the circuit level, bench tests confirmed correct operation of the series/parallel switching network, bootstrap drivers, and H-Bridge discharge circuit. Experimental results across multiple discharge voltages aligned closely with analytical predictions and LTSpice simulations, validating current profiles, switching behaviour, and energy losses.

System-level simulations were conducted to evaluate the complete disengagement model, integrating the electrical and kinematic domains. Using the designed circuitry and an optimised coil-capacitor pairing constrained by available volume and mechanical interface requirements, the simulations predict a Δv range of 0.16 m/s to 0.33 m/s. The selected charge voltage and pulse width drive this range. While the mechanism does not reach the theoretical maximum Δv required for optimal phasing, it comfortably exceeds the minimum threshold of 0.2 m/s, confirming the feasibility of the approach for the intended mission.

Dynamic testing was performed using two pendulum configurations to assess the coupling between actuation and mechanical response. The rigid pendulum enabled controlled evaluation of translational motion, with experimental angular displacements tracking simulation within 0.4° RMSE. A flexible string pendulum was subsequently employed to emulate in-orbit disengagement conditions with five degrees of freedom. While initial tests revealed excessive rotation due to mass imbalance, satellite rebalancing led to improved separation behaviour and enabled estimation of imparted Δv.

However, the pendulum experiments were not suitable for characterising performance. Shifts in the centre of mass post-separation, variability in string length due to twisting, and uncontrolled environmental conditions introduced inconsistencies that undermined repeatability. While these tests confirmed that the disengagement dynamics

function as expected, they cannot reliably quantify system performance across the full input range.

Future efforts should prioritise developing a repeatable and controlled test method to characterise the relationship between disengagement voltage, pulse width, and imparted Δv. This will enable complete performance mapping of the mechanism and support optimisation for specific mission requirements.

7.2 Significance of the PQ8 Architecture

This research contributes more than a novel constellation architecture, it also introduces new ways in which very small satellite constellations can be deployed, operated, and integrated using existing launch and regulatory ecosystems. These benefits are further outlined as follows:

1. Lowering the barrier to access for PocketQube missions:

By packaging eight PocketQubes within a single 1U CubeSat-equivalent volume, the PQ8 architecture allows PocketQube-class missions to access established CubeSat rideshare opportunities without requiring dedicated deployers or bespoke launch interfaces. This directly reduces both launch cost and launch integration complexity for PocketQube missions. Compared with CubeSat deployers, PocketQube deployers were shown to have lower volumetric efficiency, which translates into higher launch costs. In addition, although PocketQube missions do have access to rideshare opportunities, those opportunities are typically less numerous than for CubeSats. For the small satellite community, this means that:

- PocketQube missions can leverage the same commercial rideshare pipelines as CubeSats,
- Launch opportunities become more frequent and predictable, and
- Mission planning is less constrained by deployer availability.

2. Enabling independent rideshares within a single deployer slot:

The PQ8 concept enables a new form of ridesharing, in which each PocketQube can represent a completely independent mission, potentially from different institutions or organisations, while sharing a single launch slot. Unlike traditional multi-payload deployers, where satellites are already separated at deployment, PQ8 performs controlled post-deployment separation.

This enables:

- Multiple stakeholders to share one CubeSat-class launch opportunity,
- Cost-sharing between independent mission owners, and
- Launch of mixed missions with different objectives and operational timelines.

This model is particularly attractive for universities, start-ups, and early-stage technology demonstrations that cannot individually justify the cost of current deployment methods.

3. Extending the viability of PocketQube Constellations:

Historically, PocketQube constellation concepts have been constrained by the cost and integration overhead associated with deploying multiple small satellites individually. The PQ8 Architecture mitigates this by launching multiple PocketQube-class satellites as a single integrated unit that is later dispersed on orbit. This clustered deployment model improves launch-volume utilisation and simplifies integration, making multi-satellite PocketQube missions, including constellations, technology demonstration campaigns, and distributed experiments, significantly more practical.

4. Demonstrating a transferable architecture for satellite constellation deployment:

Although developed for PocketQubes, the PQ8 architecture demonstrates principles that are transferable to other small satellite classes:

- Multi-unit clustered launch,
- Post-deployment disengagement, and
- Passive constellation phasing.

These concepts are directly relevant to future satellite constellations, as they enable multiple spacecraft to be efficiently integrated within a single launch volume and subsequently dispersed in orbit. In this sense, the project contributes not only a specific hardware solution but also a systems-level design philosophy for deploying large numbers of very small satellites safely, cheaply, and flexibly within existing launch infrastructures.

7.3 Achievement of Aims and Objectives

The work presented in this thesis has contributed to the PQ8 Architecture, bringing it from a concept to a technology with proven feasibility. Being a systems engineering project, the work was divided into three sections: satellite structure, dispersal

method and disengagement mechanism. Each contributes to the PQ8 Architecture concept, and each has been developed to different technology readiness levels.

In terms of satellite structure, the main objectives were to design, simulate and test the structure to verify and validate the design for the launch environment. A TRL of 7 was set during the initial phases of the project. In this regard, the PQ1 structure and its subsystems have met the level, having successfully demonstrated their capabilities to withstand launch loads within the launch provider's safety factors. The PQ8 structure was not tested, however, leaving its TRL at 5, having undergone analytical validation. The inclusion of a deployable panel, as proposed in Chapter 4, needs to be considered and is addressed in the future work section.

For the dispersal method, an initial TRL target of 3 was established, focusing on orbit-level simulations to evaluate the deployment and phasing sequence. This objective was met through simulation-based analysis, establishing a robust framework for differential-drag-based phasing in many-in-one architectures. Advancement beyond TRL 3 was not feasible due to the absence of specific orbit parameters and the lack of in-orbit validation. Moreover, the strategy is contingent on the use of deployable panels for drag modulation, a feature yet to be realised.

For the disengagement mechanism, a TRL of 4 was targeted, with the aim of designing the release circuitry and modelling the dynamic separation process. These goals were achieved through a combination of circuit-level validation via simulation and bench-top testing, and the development of a comprehensive multi-domain simulation. This model captured magnetic and electromagnetic forces, thermal influences, electrical behaviour, and mechanical spring dynamics. Its accuracy was substantiated through pendulum experiments, with measured results falling well within expected error margins. As such, the mechanism reaches TRL 4, with partial attainment of TRL 5, pending demonstration in a representative orbital environment.

In summary, the integrated development of these subsystems validates the overall feasibility of the PQ8 Architecture. While individual subsystems have reached different maturity levels, the system as a whole meets the objectives set at the outset of the project and demonstrates compliance with both ECSS and CDS. The system currently stands at an overall TRL of 3, with a clear pathway for future development and refinement.

7.4 Technology Readiness Level Assignment

The assignment of Technology Readiness Levels to each subsystem is based on the type and maturity of verification activities performed. The PQ1 structural subsystem was assigned TRL 7 based on qualification-level structural analyses and physical testing, including modal, quasi-static, and shock/response testing representative of the launch environment and compliant with applicable ECSS safety factors, thereby demonstrating system-level performance in a relevant operational environment.

The dispersal method was assigned TRL 3, as its feasibility was demonstrated analytically through orbit-level simulations that establish proof-of-concept for differential-drag-based deployment and phasing, without experimental validation or demonstration in a representative environment.

The disengagement mechanism was assigned TRL 4, supported by component- and breadboard-level validation through circuit simulations, benchtop electrical testing, and experimentally validated multi-physics modelling of the separation dynamics. Collectively, these activities provide a traceable and standards-consistent basis for the TRL assignments reported for each subsystem.

7.5 Future Work

As a systems-level project spanning multiple engineering domains, including mechanical design, electromagnetic modelling, circuit design, thermal analysis, and orbital dynamics, this work has necessarily adopted a broad and interdisciplinary approach. The development and validation of the PQ8 architecture demanded extensive cross-domain integration and experimental groundwork, yet several areas remain where further investigation is both possible and necessary. Given the complexity and interdependence of the subsystems, future research will be essential to refine individual components, enhance overall performance, and ensure robustness under real mission conditions. The following points outline key areas where additional modelling, optimisation, or experimental validation would significantly strengthen and advance the PQ8 deployment concept:

1. Structural Enhancements for Accelerated Dispersal: Although the structural design has reached a sufficient level of maturity for the PQ8 system, there remains an opportunity to reduce constellation phasing times through the integration of deployable panels. Such deployables are well-established in CubeSat and

PocketQube development, having been successfully demonstrated across numerous missions, and pose no particular technical challenge. Moreover, the current mass and volume margins comfortably accommodate their inclusion. Future iterations of the platform could explore various deployment geometries to maximise cross-sectional area and improve differential drag control.

2. Cross-Validation of the Dispersal Model: The dispersal modelling conducted in this work utilised MATLAB's Aerospace Toolbox, which integrates built-in perturbation models and space weather data to estimate differential drag-driven phase separation. However, two key limitations remain. First, the model was not cross-validated using alternate software such as GMAT or Ansys STK, due to the absence of appropriate atmospheric models in GMAT (i.e., NRLMSISE-00) and licensing limitations for STK. Second, and more critically, the model has not been validated through actual orbital deployment. A future in-orbit demonstration of the PQ8 dispersal sequence would be the definitive test of its accuracy and viability.
3. Coefficient of Drag Estimate: In this work, the drag coefficient (Cd) used in the dispersal model was derived from well-established analytical equations found in literature, which were based on years of empirical observations of satellite behaviour in low Earth orbit. While these models provide a solid baseline, they still rely on simplifying assumptions, most notably regarding the ratio of quasi-specular to diffuse reflections from the satellite surface. To reduce uncertainties in phase-time predictions and improve the fidelity of the dispersal model, future work should involve computational fluid dynamics (CFD) simulations in the free-molecular flow regime and tailored to the PQ8 geometry and materials. Such simulations would enable a more precise characterisation of drag behaviour under varying orientations and thermal conditions, ultimately enhancing the accuracy of differential drag-based control.
4. Incorporation of ADCS Performance in Dispersal Modelling: While this work included a sensitivity analysis of ADCS performance in applying differential drag, the study was based on generalised assumptions rather than specific actuator performance data. The actual accuracy of the ADCS unit used in the PQ8 system was not available during modelling, limiting the fidelity of this evaluation. A more detailed future study should incorporate the real-world control authority, pointing accuracy, and slew rate limitations of the flight hardware to more accurately simulate dispersal outcomes and delta-v allocation.

5. Post-Dispersal Constellation Maintenance: The current deployment model terminates simulation once the satellites achieve their target orbital spacing. In practice, however, drag perturbations continue to act on the system and necessitate periodic adjustments to maintain relative positioning. This challenge grows with constellation size, demanding coordinated control strategies across all units. Future work should focus on developing and testing decentralised or cooperative algorithms for station-keeping using differential drag, possibly leveraging inter-satellite communication or onboard autonomy.
6. Redundancy Optimisation and Radiation Tolerance in DM Circuitry: The disengagement mechanism circuit design was concluded with a failure mode analysis and risk mitigation strategy. An analysis of the subsystems on the PQ8 Satellite should be undertaken to see which redundancies can be removed to make space for rad-hard components. This may add more space for rad-hard replacements of key elements in the disengagement mechanism.
7. Thermal Modelling of the PQ8 System and Disengagement Mechanism: Thermal modelling was not undertaken in this work, representing a key gap in the system-level analysis of the PQ8 architecture. Given that the disengagement mechanism includes components whose performance may vary significantly with temperature, understanding the thermal environment is essential for defining safe and reliable operating limits. Future work should involve detailed thermal simulations of the satellite under various orbital conditions, accounting for solar exposure, eclipse durations, and internal power dissipation. These results could then inform thermal design measures, such as insulation, heat spreading, or active regulation, and enable validation of the mechanism's functionality across the full expected temperature range.
8. Expanded System-Level Testing of the Disengagement Mechanism: A significant limitation of this work is the restricted experimental characterisation of the disengagement mechanism as an integrated system. This shortcoming arose from limited access to high-fidelity testing facilities capable of replicating microgravity conditions and isolating individual variables. Two complementary approaches are proposed for future testing:
    a. Parabolic Flight Experiments: A compelling, albeit expensive, solution is to perform disengagement experiments aboard a parabolic flight. These flights offer repeated periods of microgravity, approximating the actual orbital environment. However, constraints include limited test repetitions,

a steep learning curve for microgravity handling, and the need for precise onboard inertial measurement systems to track motion.

b. Precision Test Jig for Axis-Isolated Characterisation: Alternatively, a dedicated test jig could be developed to isolate and measure rotation and translation along individual axes. This setup would need to be calibrated to very fine tolerances, given the small forces involved in disengagement, and ideally be compact enough to operate within a thermal chamber. This would allow for the characterisation of the mechanism across a range of temperatures, improving confidence in its reliability and repeatability under space-like conditions.

In addition to refinements of the current PQ8 system, the architecture itself opens the door to further research in several promising directions. Its compact, modular, and deployer-independent design makes it a strong candidate for a broader range of missions, both in Earth orbit and beyond. Key directions include:

- Scalability by Size: Apply the PQ8 deployment and dispersal methodology to larger satellite classes, to assess how mechanical forces, drag dynamics, and system complexity scale with mass and volume.
- Scalability by Quantity: Increase the number of satellites per many-in-one deployment or chain multiple deployments to form larger constellations. This would require deeper analysis of coordination strategies, cumulative dispersion control, and mission operations at scale.
- Planetary Deployment Models: Adapt the PQ8 system for use in the orbits of other planetary bodies. Its minimal deployer requirements, high integration density, and low mass make it an excellent candidate for missions to Mars or other planets with a gaseous atmosphere, where small constellations could provide distributed sensing, communications, or surface mapping.

7.6 Publications

Patent: *Cumbo, D. Azzopardi, MA. "Satellite, satellite assembly and method of deploying satellites from a satellite assembly". (US-20240391610-A1), 28/11/2024.*

Cumbo, D.; Azzopardi, M.A. Modeling and Analysis of Staged Constellation Deployment from a Single-Unit System. Aerospace 2025, 12, 586. https://doi.org/10.3390/aerospace12070586

REFERENCES

[1] Fong, C.-J., Shiau, W.-T., Lin, C.-T., Kuo, T.-C., Chu, C.-H., Yang, S.-K., Yen, N. L., Chen, S.-S., Kuo, Y.-H., Liou, Y.-A., and Chi, S., "Constellation Deployment for the FORMOSAT-3/COSMIC Mission," *IEEE Transactions on Geoscience and Remote Sensing*, Vol. 46, No. 11, 2008, pp. 3367–3379. https://doi.org/10.1109/TGRS.2008.2005202

[2] SpaceX, "Capabilities & Services," 2025. Retrieved 18 December 2025. https://www.spacex.com/assets/media/Capabilities&Services.pdf

[3] Kim, M. J., "Counting Stars and Costs: An Empirical Examination of Space Launch Cost Trend at NASA," *Acta Astronautica*, Vol. 232, 2025, pp. 633–639. https://doi.org/https://doi.org/10.1016/j.actaastro.2025.04.011

[4] Planet Labs PBC, "Planet Imagery Product Specifications," 2023.

[5] SpaceX, "Smallsat Rideshare Program," https://www.spacex.com/rideshare/?utm_source=chatgpt.com, May 18 2025.

[6] Alba Orbital, "Alba Launch," https://www.albaorbital.com/launch, May 18 2025.

[7] Crisp, N. H., Smith, K., and Hollingsworth, P., "Launch and Deployment of Distributed Small Satellite Systems," *Acta Astronautica*, Vol. 114, 2015, pp. 65–78. https://doi.org/10.1016/j.actaastro.2015.04.015

[8] Di Pasquale, G., Sanjurjo-Rivo, M., and Pérez Grande, D., "Optimization of Constellation Deployment Using On-Board Propulsion and Earth Nodal

Regression," *Advances in Space Research*, Vol. 70, No. 11, 2022, pp. 3281–3300. https://doi.org/https://doi.org/10.1016/j.asr.2022.09.019

[9] J. Twiggs, "ESA Vega Maiden Flight First Workshop," 2008.

[10] The CubeSat Program, "CubeSat Design Specification Rev. 14.1."

[11] ESA, "Technology Readiness Levels (TRL)," https://www.esa.int/Enabling_Support/Space_Engineering_Technology/Shaping_the_Future/Technology_Readiness_Levels_TRL, May 27 2025.

[12] Cachia, D., "Design of a Pico-Satellite Platform," 2017.

[13] Cachia, D., Camilleri, J., Azzopardi, M. A., Angling, M., and Sammut, A., "FEASIBILITY STUDY OF A POCKETQUBE PLATFORM TO HOST AN IONOSPHERIC IMPEDANCE PROBE."

[14] Camilleri, J., Cachia, D., and Azzopardi, M., "A Miniaturized Impedance Probe for Ionospheric Sensing," 2016.

[15] Belazi, M. El, "Distributed Electrical Power Supply for a Picosatellite," 2020.

[16] De Battista, D., "Design of an Attitude Determination and Control System for the UoMBSat1 Pico-Satellite," 2019.

[17] Denise Baldacchino, D. D. R. R. D. C. M. A. A. S. G. F. and M. K. B., "Review and Feasibility of Active Attitude Control and Detumbling for the UoMBSat-1 PocketQube," IEEE, Valletta, 2017.

[18] Vassallo, O., "Design of a Software Radio Hardware Platform for a PicoSatellite," 2018.

[19] J. Puig-Suari, C. T. W. A., "Development of the Standard CubeSat Deployer and a CubeSat Class Pico-Satellite," *Proceedings of the IEEE Aerospace Conference*, 2001, pp. 1–9.

[20] Johnstone, A., "CubeSat Design Specification Rev. 14.1," San Luis Obispo, CA, July 2022.

[21] Swartwout M., "The First One Hundred CubeSats: A Statistical Look," *Journal of Small Satellite*, Vol. 2, 2013, pp. 213–233.

[22] Kulu, E., "Nanosats Database," https://www.nanosats.eu/, Nov 18 2024.

[23] Puig-Suari, J., Turner, C., and Twiggs, R. J., “CubeSat: The Development and Launch Support Infrastructure for Eighteen Different Satellite,” 2001.

[24] Lee, S., Toorian, A., Clemens, N., Puig-Suari, J., and Twiggs, B., “Cal Poly Coordination of Multiple CubeSats on the DNEPR Launch Vehicle,” Vol. 1, 2015, pp. 18.

[25] Spremo, S., Crocker, A., and Panontin, T., “Small Spacecraft Overview.”

[26] Twiggs, R. J., Jernigan, J. G., Cominsky, L. R., Malphrus, B. K., Silverman, B. S., Zack, K., McNeil, S., and Roach-Barrett, W., “The PocketQube Concept ,” 2014.

[27] Kramer, A., Bangert, P., and Schilling, K., “UWE-4: First Electric Propulsion on a 1U CubeSat—In-Orbit Experiments and Characterization,” *Aerospace*, Vol. 7, No. 7, 2020. https://doi.org/10.3390/aerospace7070098

[28] Alba Orbital, “Democratizing Space: A Beginner’s Guide to Open Source PocketQubes,” https://www.albaorbital.com/open-source-pocketqube, May 20 2025.

[29] Bouwmeester, J., Radu, S., Uludag, M. S., Chronas, N., Speretta, S., Menicucci, A., and Gill, E. K. A., “Utility and Constraints of PocketQubes,” *CEAS Space Journal*, Vol. 12, No. 4, 2020, pp. 573–586. https://doi.org/10.1007/s12567-020-00300-0

[30] “IADC Space Debris Mitigation Guidelines,” March 2020.

[31] Twiggs, R. J., Zucherman, A. P., Bujold, E., Counts, N. E., Colman, C., Garcia, J., Diddle, A., and Zhirkina, P., “The ThinSat Program: Flight Opportunities for Education, Research and Industry,” 2018.

[32] Radu, S. ; U. M. S. ; S. S. ; B. J. ; D. A. ; W. T. ; K. D. C. P. L. ; C. C., “PocketQube Standard Issue 1 - Published,” June 2018.

[33] California Polytechnic State University, “Poly Picosatellite Orbital Deployer Mk. III Rev. E Guide.”

[34] Alba orbital, “AlbaPod: The Most Advanced Space-Proven PocketQube Deployer,” https://connectivity.esa.int/news/albapod-most-advanced-spaceproven-pocketqube-deployer, Nov 30 2020.

[35] Hoang, H., Røed, · K, Bekkeng, T. A., Moen, J. I., Clausen, · L B N, Trondsen, · E, Lybekk, · B, Strøm, · H, Bang-Hauge, · D M, Pedersen, · A, Nokes, · C D A,

Cupido, · C, Mann, · I R, Ariel, · M, Portnoy, · D, and Sagi, · E, “The Multi-Needle Langmuir Probe Instrument for QB50 Mission: Case Studies of Ex-Alta 1 and Hoopoe Satellites.”

[36] Kılıç, Ç., Scholz, T., and Asma, C., “Deployment Strategy Study of QB50 Network of CubeSats,” 2013. https://doi.org/10.1109/RAST.2013.6581349

[37] Cairns, I. H., Charles, C., Dempster, A. G., Funamoto, J., Cheong, J. W., Peacock, W., Lam, J., Osborne, B., Andrew, W., Croston, T., Southwell, B., Boswell, R. W., Monger, A. G., Betters, C. H., Leon-Saval, S. G., Bland-Hawthorn, J., Khachan, J., Wu, X., Manidis, S., Tsifakis, D., and Maj, R., “The INSPIRE-2 CubeSat for the QB50 Project,” *Space Science Reviews*. 3. Volume 216. https://doi.org/10.1007/s11214-020-00659-w

[38] Franzese, V., “PocketQube Picosatellites: Survey of Missions and Technologies,” *CEAS Space Journal*, Vol. 17, No. 6, 2025, pp. 1007–1018. https://doi.org/10.1007/s12567-025-00603-0

[39] Fernandez, J., “FossaSat-1, First Steps Into Space,” 2019.

[40] Tapley, B., Bettadpur, S., Watkins, M., and Reigber, C., “The Gravity Recovery and Climate Experiment: Mission Overview and Early Results,” *Geophysical Research Letters*, Vol. 31, 2004, p. 4 PP. https://doi.org/10.1029/2004GL019920

[41] Ching, B. K., Hickman, D. R., and Straus, J. M., “Effects of Atmospheric Winds and Aerodynamic Lift on the Inclination of the Orbit of the S3-1 Satellite,” *Journal of Geophysical Research (1896-1977)*, Vol. 82, No. 10, 1977, pp. 1474–1480. https://doi.org/https://doi.org/10.1029/JA082i010p01474

[42] Killough, R., Scherrer, J., Rose, R., Brody, A., Redfern, J., Smith, K., Ruf, C. S., and Yee, T., “CYGNSS Launch and Early Ops: Parenting Octuplets.”

[43] Patel, B., Schroll, S., and Lewin, A., “On-Orbit Performance of the ORBCOMM Spacecraft Constellation,” 1999.

[44] Foster, C., Mason, J., Vittaldev, V., Leung, L., Beukelaers, V., Stepan, L., and Zimmerman, R., “Constellation Phasing with Differential Drag on Planet Labs Satellites,” *Journal of Spacecraft and Rockets*, Vol. 55, No. 2, 2017, pp. 473–483. https://doi.org/10.2514/1.A33927

[45] Gangestad, J. W., Hardy, B. S., and Hinkley, D. A., “Operations, Orbit Determination, and Formation Control of the AeroCube-4 CubeSats,” 2013.

[46] Jeon, S., Park, S. Y., and Kim, G. N., “Relative Orbit Control Algorithms and Scenarios for the Inertial Alignment Hold Demonstration Mission by CubeSat Formation Flying,” *MDPI Aerospace*, Vol. 11, No. 2, 2024. https://doi.org/10.3390/aerospace11020135

[47] Bussy-Virat, C. D., Ridley, A. J., Masher, A., Nave, K., and Intelisano, M., “Assessment of the Differential Drag Maneuver Operations on the CYGNSS Constellation,” *IEEE Journal of Selected Topics in Applied Earth Observations and Remote Sensing*, Vol. 12, No. 1, 2019, pp. 7–15. https://doi.org/10.1109/JSTARS.2018.2878158

[48] Maclay, T. D., and Tuttle, C., “Satellite Station Keeping of the ORBCOMM Constellation via Active Control of Atmospheric Drag: Operations, Constraints, and Performance (AAS 05-152),” *Advances in the Astronautical Sciences*, Vol. 120, No. 1, 2005, p. 763.

[49] eoPortal, “AeroCube-4 CubeSats,” https://www.eoportal.org/satellite-missions/aerocube-4#aerocube-4, May 20 2025.

[50] Sin, E., Arcak, M., and Packard, A., “Small Satellite Constellation Separation Using Linear Programming Based Differential Drag Commands,” 2018. https://doi.org/10.23919/ACC.2018.8431408

[51] Bakhtiari, M., Panahyazdan, A., and Abbasali, E., “Finite-Time Control for Satellite Formation Reconfiguration and Maintenance in LEO: A Nonlinear Lyapunov-Based SDDRE Approach,” *MDPI Aerospace*, Vol. 12, No. 3, 2025. https://doi.org/10.3390/aerospace12030201

[52] Falcone, G., Willis, J. B., and Manchester, Z., “Propulsion-Free Cross-Track Control of a LEO Small-Satellite Constellation with Differential Drag,” arXiv.org, Ithaca, 2023. Retrieved 14 April 2025. http://arxiv.org/abs/2306.13844

[53] Ivanov, D., Monakhova, U., Guerman, A., and Ovchinnikov, M., “Decentralized Control of Nanosatellite Tetrahedral Formation Flying Using Aerodynamic Forces,” *MDPI Aerospace*, Vol. 8, No. 8, 2021. https://doi.org/10.3390/aerospace8080199

[54] Chernov, K., Monakhova, U., Mashtakov, Y., Biktimirov, S., Pritykin, D., and Ivanov, D., “Decentralized Differential Aerodynamic Control of Microsatellites

Formation with Sunlight Reflectors," *MDPI Aerospace*, Vol. 10, No. 10, 2023. https://doi.org/10.3390/aerospace10100840

[55] Moe, M. M., and Wallace, S. D., "Improved Satellite Drag Coefficient Calculations from Orbital Measurements of Energy Accommodation," 2003.

[56] Ballance, J. 0, "NASA TECHNICAL MEMORANDUM WAKE AND INTERREFLECTION EFFECTS IN THE CALCULATION OF FREE MOLECULAR FLOW DRAG COEFFIC IENTS Marsh& W653 Ju'v65 Spme Flight Center (ACCESSION NUMBER) (THRU)," 1967.

[57] Senda, Y., "Theoretical Analysis of Vacuum Evacuation in Viscous Flow and Its Applications," 2010.

[58] Cook, G. E., "Satellite Drag Coefficients," 1965.

[59] Sherdan L. Phillip, "Graduate Theses, Dissertations, and Problem Reports Updates and Improvements to the Satellite Drag Coefficient Updates and Improvements to the Satellite Drag Coefficient Response Surface Modeling Toolkit Response Surface Modeling Toolkit Recommended Citation Recommended Citation," 2021.

[60] Gregory, J. C. P. P. N., "A Measurement of the Angular Distribution of 5 EV Atomic Oxygen Scattered off a Solid Surface in Earth Orbit," 1986.

[61] Moe, K., and Moe, M. M., "Gas-Surface Interactions and Satellite Drag Coefficients," *Planetary and Space Science*, Vol. 53, No. 8, 2005, pp. 793–801. https://doi.org/10.1016/j.pss.2005.03.005

[62] Moe, K., Moe, M. M., and Wallace, S. D., "Improved Satellite Drag Coefficient Calculations from Orbital Measurements of Energy Accommodation," *Journal of Spacecraft and Rockets*, Vol. 35, No. 3, 1998, pp. 266–272. https://doi.org/10.2514/2.3350

[63] Goodman, F. O., "Three-Dimensional Hard Spheres Theory of Scattering of Gas Atoms from a Solid Surface I. Limit of Large Incident Speed," *Surface Science*, Vol. 7, No. 3, 1967, pp. 391–421. https://doi.org/https://doi.org/10.1016/0039-6028(67)90029-5

[64] Jan A. King; Neal J. Beidleman, "United States Patent: Method And Apparatus For Deploying a Satellite Network," 2019.

[65] Leppinen, H., “Deploying a Single-Launch Nanosatellite Constellation to Several Orbital Planes Using Drag Maneuvers,” *Acta Astronautica*, Vol. 121, 2016, pp. 23–28. https://doi.org/https://doi.org/10.1016/j.actaastro.2015.12.036

[66] Varma, S., and Kumar, K., “Multiple Satellite Formation Flying Using Differential Solar Radiation Pressure,” *AIAA/AAS Astrodynamics Specialist Conference*, American Institute of Aeronautics and Astronautics, 2010. https://doi.org/doi:10.2514/6.2010-7960

[67] Chase, J. P., Chow, N., Gralla, E. L., and Kasdin, N. J., “LEO Constellation Design Using the Lunar L1 Point,” 2004.

[68] Sauder, J., Gebara, C., Reddy, N. H., and García-Mora, C. J., “A Framework for Small Satellite Deployable Structures and How to Deploy Them Reliably,” *Communications Engineering*. 1. Volume 3. https://doi.org/10.1038/s44172-024-00210-7

[69] Bhattarai, S., Go, J. S., and Oh, H. U., “Experimental Cansat Platform for Functional Verification of Burn Wire Triggering-Based Holding and Release Mechanisms,” *Aerospace*, Vol. 8, No. 7, 2021. https://doi.org/10.3390/aerospace8070192

[70] Kailaje, A. P., Tapadia, P., Ganti, H., Brindavan, M., Paliva, A., Thakurta, V., and Kumar, A. A., “Implementation of Wire Burn Deployment Mechanism Using COTS Resistors and Related Investigations,” 2019. https://doi.org/10.1109/AERO.2019.8741776

[71] Thurn, A., Huynh, S., Koss, S., Oppenheimer, P., Butcher, S., Schlater, J., and Hagan, P., “A Nichrome Burn Wire Release Mechanism for CubeSats,” 2012.

[72] Bortoluzzi, D., Mäusli, P. A., Antonello, R., and Nellen, P. M., “Modeling and Identification of an Electro-Mechanical System: The LISA Grabbing Positioning and Release Mechanism Case,” *Advances in Space Research*, Vol. 47, No. 3, 2011, pp. 453–465. https://doi.org/10.1016/j.asr.2010.09.004

[73] Vertegaal, C., Alidjan, K., Pourshaghaghi, H. R., and Bentum, M., “Self-Deploying Antennas for Proof-of-Concept Radio Astronomy Science Satellite,” 2023. https://doi.org/10.1109/AERO55745.2023.10115784

[74] Lan, X., Liu, L., Pan, C., Hou, G., Li, F., Liu, Z., Dai, W., Zhang, F., Sun, J., Yue, H., Liu, Y., Leng, J., Zhong, X., and Tang, Y., “Smart Space Deployable Truss

Based on Shape-Memory Releasing Mechanisms and Actuation Laminates," *Journal of Spacecraft and Rockets*, 2023, pp. 1–15. https://doi.org/10.2514/1.A35649

[75] Xing Yun New Materials Ltd., "When Was Shape Memory Alloys Discovered?," https://www.nitinol.vip/when-was-shape-memory-alloys-discovered/, May 21 2012.

[76] Oh, H.-U., and Lee, M.-J., "Development of a Non-Explosive Segmented Nut-Type Holding and Release Mechanism for Cube Satellite Applications," *TRANSACTIONS OF THE JAPAN SOCIETY FOR AERONAUTICAL AND SPACE SCIENCES*, Vol. 58, 2015, pp. 1–6. https://doi.org/10.2322/tjsass.58.1

[77] Kingston, J., Hobbs, S., Roberts, P., Juanes-Vallejo, C., Robinson, F., Sewell, R., Snapir, B., Virgili Llop, J., and Patel, M., "Use of CYPRES^{TM} Cutters with a Kevlar Clamp Band for Hold-down and Release of the Icarus De-Orbit Sail Payload on TechDemoSat-1," *Acta Astronautica*, Vol. 100, 2014, pp. 82–93. https://doi.org/10.1016/j.actaastro.2014.03.014

[78] Oh, H.-U., Jeon, S.-H., and Kwon, seong-cheol, "Structural Design and Analysis of 1U Standardized STEP Cube Lab for On-Orbit Verification of Fundamental Space Technologies," *International Journal of Materials, Mechanics and Manufacturing*, Vol. 2, 2014, pp. 239–244. https://doi.org/10.7763/IJMMM.2014.V2.135

[79] Dowen, D., Christiansen, S. S., and Peffer, A., "Development of a Reusable, Low-Shock Clamp Band Separation System for Small Spacecraft Release Applications," 2001.

[80] Liu, J., Walmer, M., and Jasinski, M., "Modern Sm-Co Permanent Magnets," *Modern Permanent Magnets*, edited by J. Croat and J. Ormerod, Woodhead Publishing, 2022, pp. 113–134. https://doi.org/https://doi.org/10.1016/B978-0-323-88658-1.00001-7

[81] Khentov, A. A., "On Permanent Rotation of an Equatorial Satellite in the Geomagnetic Field," *Radiophysics and Quantum Electronics*, Vol. 15, No. 3, 1972, pp. 303–313. https://doi.org/10.1007/BF02210670

[82] Alsup, K. P., Anantachaisilp, F., Komma, J. L., Lobo, K. B., Lovdahl, B. L., Shapiro, J. R., Rhatigan, J. L., Romano, M., and Virgili-Llop, J., "Drag-Enhancing

Deorbit Devices for Mid-Sized Spacecraft Self-Disposal," 2019. https://doi.org/10.1109/AERO.2019.8741759

[83] Bhattarai, S., Go, J. S., and Oh, H. U., "Experimental Cansat Platform for Functional Verification of Burn Wire Triggering-Based Holding and Release Mechanisms," *Aerospace*, Vol. 8, No. 7, 2021. https://doi.org/10.3390/aerospace8070192

[84] Bridges, C., Taylor, B., Horri, N., Underwood, C., Kenyon, S., Barrera-Ars, J., Pryce, L., and Bird, R., "STRaND-2: Visual Inspection, Proximity Operations & Nanosatellite Docking," 2013. https://doi.org/10.1109/AERO.2013.6497348

[85] Mopidevi, O., Redah, A., Paudel, S., Pathak, M., and Athawle, C., "Design and Development of an Active Magnetic Docking System for Small Satellites," 2024.

[86] Yunhan, H., Zhaokui, W., and Yulin, Z., "The Electromagnetic Separation System for the Small Spherical Satellite Q-SAT," *Acta Astronautica*, Vol. 184, 2021, pp. 180–192. https://doi.org/https://doi.org/10.1016/j.actaastro.2021.03.026

[87] European Cooperation for Space Standardization (ECSS), "Space Engineering Structural General Requirements," 2008.

[88] European Cooperation for Space Standardization (ECSS), "Space Engineering Spacecraft Mechanical Loads Analysis Handbook," 2013.

[89] European Cooperation for Space Standardization (ECSS), "Space Engineering Structural Factors of Safety for Spaceflight Hardware," 2019.

[90] Larson, W. J., and Wertz, J. R., "Space Mission Analysis and Design," Kluwer Academic Publishers, Dordrecht, 1992.

[91] arianespace, "Vega C User's Manual Issue 0 Revision 0," May 2018.

[92] Scott, A. D., "AN ANALYSIS OF SPACECRAFT DYNAMIC TESTING AT THE VEHICLE LEVEL," MONTEREY, CALIFORNIA, 1996.

[93] arianespace, "ARIANE 6 User's Manual Issue 2 Revision," February 2021.

[94] SpaceX, "Flacon 9 Launch Vehicle: Payload User's Guide," 2009.

[95] Kulu, E., "CubeSats & Nanosatellites-2024 Statistics, Forecast and Reliability," 2024.

[96] Grech, R., “Structural Integrity of Pod-Mounted Pico-Satellites during Launch Conditions,” University of Malta, Msida, 2025.

[97] Franzese, V., Kanavouras, K., Rosete, C. B., Sajjad, N., Alandihallaj, M., Gouvalas, S., Herasimenka, A., and Hein, A. M., “POQUITO: The First Satellite Mission of the University of Luxembourg,” Vol. 13546, edited by M. Petrozzi-Ilstad, 2025, pp. 135463W. https://doi.org/10.1117/12.3062670

[98] Uludağ, M., and Speretta, S., “Delfi-PQ: In-Orbit Performance and Lessons Learned in Developing a 3P PocketQube,” 2025. https://doi.org/10.52202/083084-0062

[99] Sentman, L. H., “Free Molecule Flow Theory and Its Application to The Determination of Aerodynamic Forces,” 1961.

[100] Schamberg, R., “A New Analytic Representation of Surface Interaction for Hyperthermal Free Molecule Flow with Applications to Neutral-Particle Drag Estimates of Satellites,” 1959.

[101] Sinpetru, L. A., Crisp, N. H., Mostaza-Prieto, D., Livadiotti, S., and Roberts, P. C. E., “ADBSat: Methodology of a Novel Panel Method Tool for Aerodynamic Analysis of Satellites,” *Computer Physics Communications*, Vol. 275, 2022, p. 108326. https://doi.org/https://doi.org/10.1016/j.cpc.2022.108326

[102] Sinpetru, L. A., Crisp, N. H., Roberts, P. C. E., Sulliotti-Linner, V., Hanessian, V., Herdrich, G. H., Romano, F., Garcia-Almiñana, D., Rodríguez-Donaire, S., and Seminari, S., “ADBSat: Verification and Validation of a Novel Panel Method for Quick Aerodynamic Analysis of Satellites,” *Computer Physics Communications*, Vol. 275, 2022, p. 108327. https://doi.org/https://doi.org/10.1016/j.cpc.2022.108327

[103] Mesalles-Ripoll, P., Rositani, R., and Duncan, M., “Low-Earth Orbit Prediction Accuracy Review of Modern Empirical Atmospheric Models and Space Weather Data Sources,” 2023.

[104] eoPortal, “Alba Orbital Unicorn PocketQubes,” https://www.eoportal.org/satellite-missions/alba-orbital#references, May 12 2025.

[105] Akins, K., Healy, L., Coffey, S., and Picone, J., “Comparison of MSIS and Jacchia Atmospheric Density Models for Orbit Determination and Propagation,” 2003.

[106] Grover, F. W., “Methods for the Derivation and Expansion of Formulas for the Mutual Inductance of Coaxial Circles and for the Inductance of Single-Layer Solenoids,” *Bureau of Standards Journal of Research*, Vol. 1, 1928, p. 487. https://api.semanticscholar.org/CorpusID:59325314

[107] Babic, S., Akyel, C., Ren, Y., and Chen, W., “Magnetic Force Calculation between Circular Coils of Rectangular Cross Section with Parallel Axes for Superconducting Magnet,” *PIER B*, Vol. Vol 37, 2012. https://doi.org/10.2528/PIERB11110508

[108] Rosa, E. B., and Cohen, L., “The Mutual Inductance of Two Circular Coaxial Coils of Rectangular Section,” 1906.

[109] Grover, F. W., “Inductance Calculations,” Instrument Society of America, 1981.

[110] ARRL Inc., “The ARRL Handbook for Radio Communications 2017,” 2016.

[111] Vishay, “Si8851EDB Datasheet,” May 2018.

[112] onsemi, “NTTFD2D8N03P1E Datasheet Rev.4,” June 2022.

[113] Bonnici, M., “Analysis and Design for the ASTREA Project,” 2017.

[114] Alasdair Allan, “FossaSat-1, an Open Source Satellite for the Internet of Things,” https://www.hackster.io/news/fossasat-1-an-open-source-satellite-for-the-internet-of-things-7f31cab00ef5, 2019.

APPENDIX A: STRUCTURE DRAWINGS

Chassis Top Frame Drawing

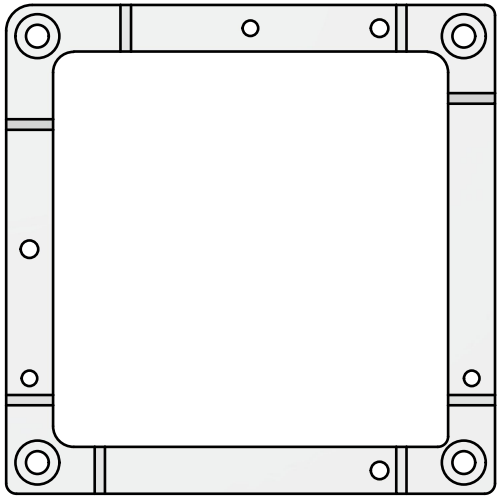

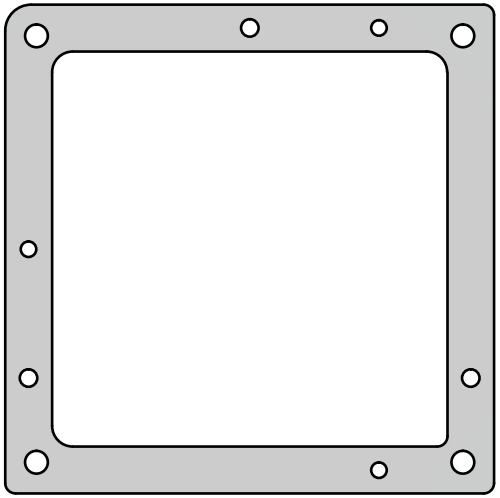

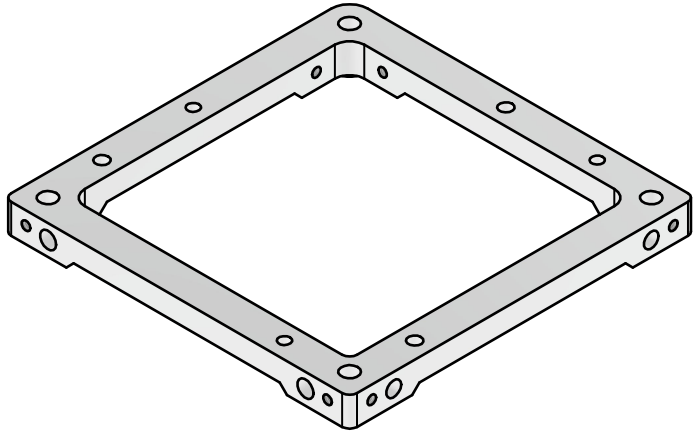

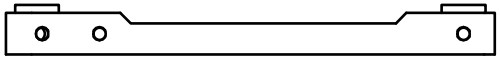

Side C

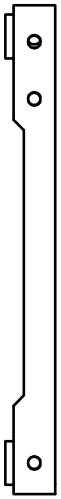

Side D

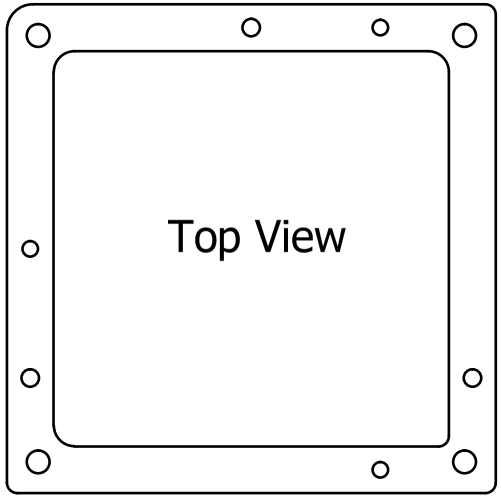

Top View

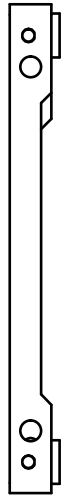

Side B

Side A

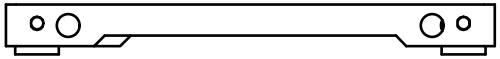

Notes:

- Units: mm
- Material: Aluminium 6061

DRAWN Daniel	31/03/2023	L-Università ta' Malta	University of Malta	
CHECKED DC		TITLE	Chassis Top Frame	
QA				
MFG				
APPROVED DC		SIZE B	DWG NO Chassis_Top_v5	REV 1
		SCALE 2 : 1	SHEET 1 OF 5	

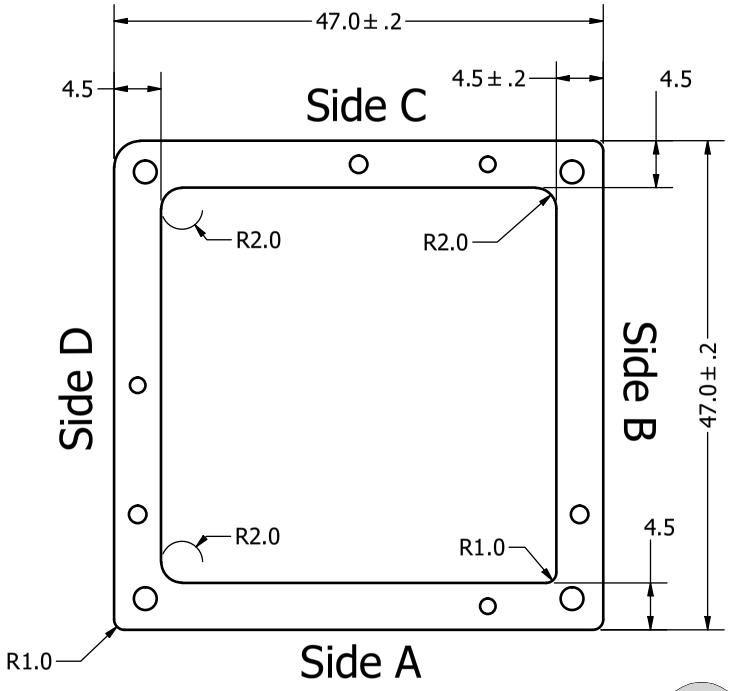

Holes:

A = Ø2.2
B = Ø1.5
C = Ø1.7

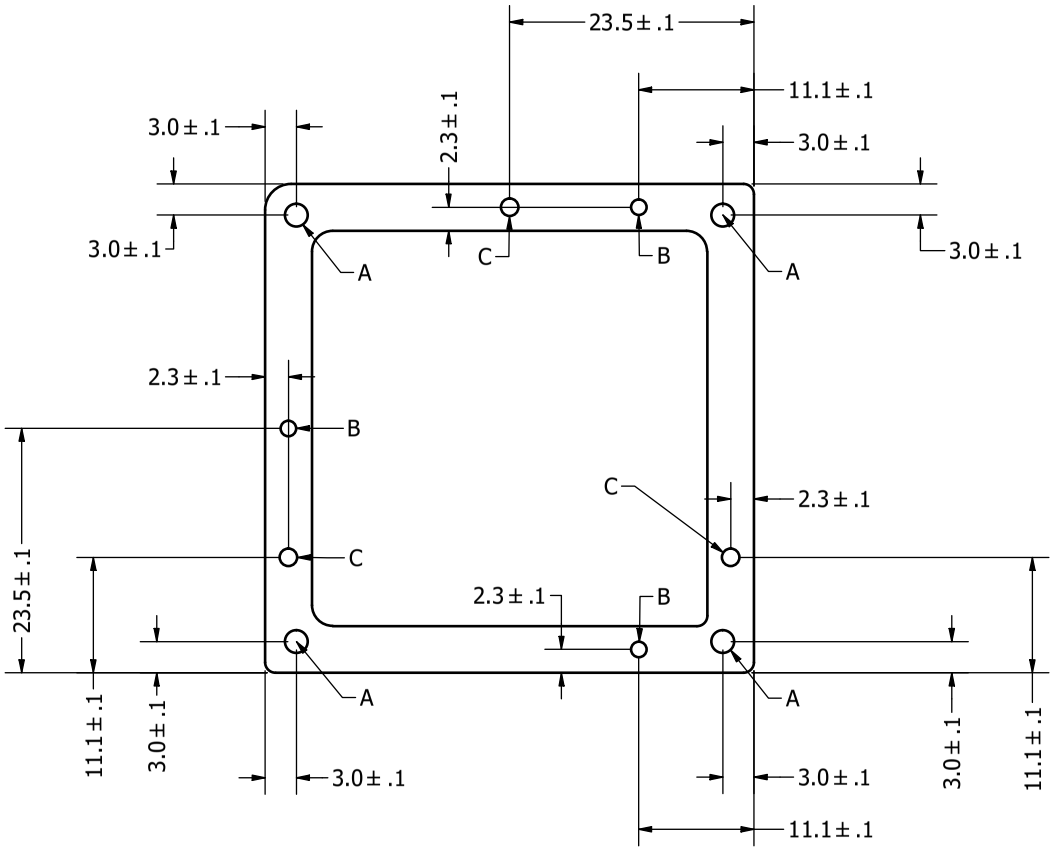

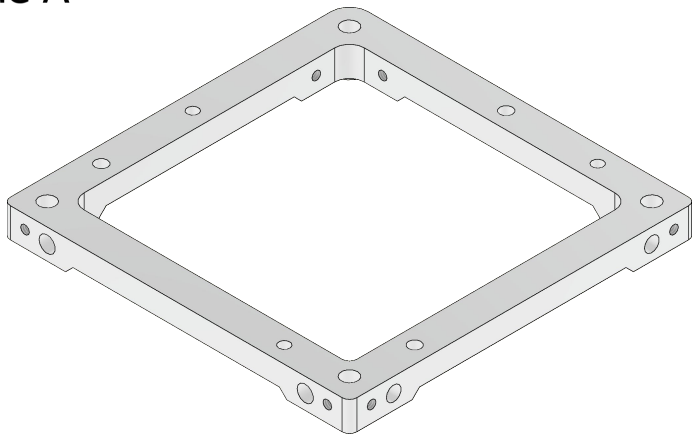

Notes:

- Units: mm
- Material: Aluminium 6061
- Tolerance: ISO 2768 – Medium unless specified

DRAWN Daniel	31/03/2023	L-Università ta' Malta	University of Malta	
CHECKED DC		TITLE	Chassis Top Frame	
QA				
MFG				
APPROVED DC		SIZE B	DWG NO Chassis_Top_v5	REV 1
		SCALE 2 : 1	SHEET 2 OF 5	

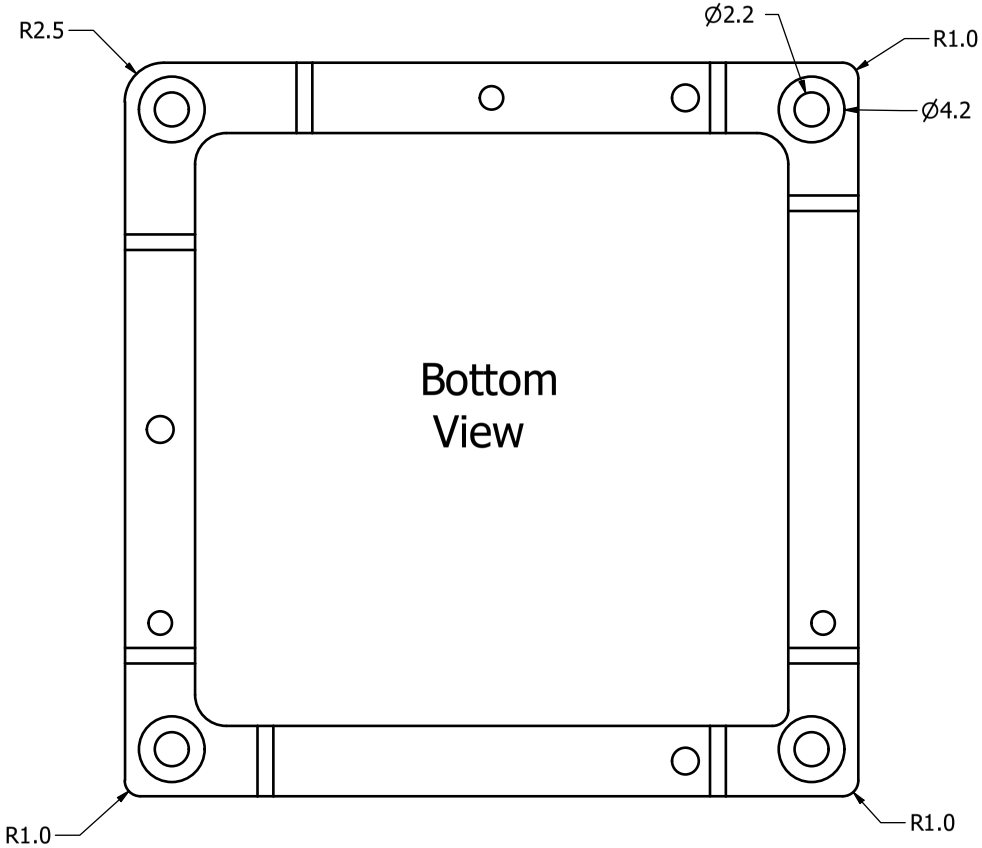

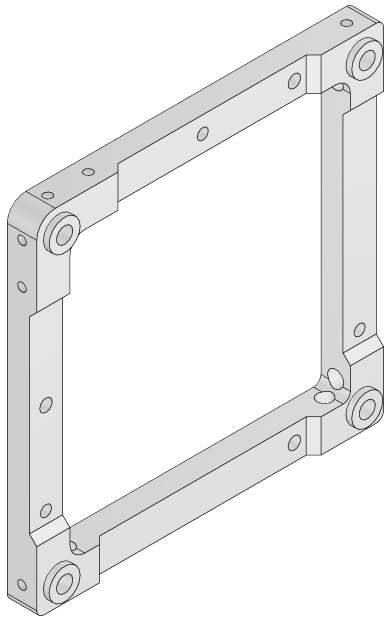

Notes:

- Units: mm
- Material: Aluminium 6061
- Tolerance: ISO 2768 – Medium unless specified

DRAWN Daniel	31/03/2023	L-Università ta' Malta	University of Malta	
CHECKED DC		TITLE	Chassis Top Frame	
QA				
MFG				
APPROVED DC		SIZE B	DWG NO Chassis_Top_v5	REV 1
		SCALE 2 : 1	SHEET 3 OF 5	

Side A:

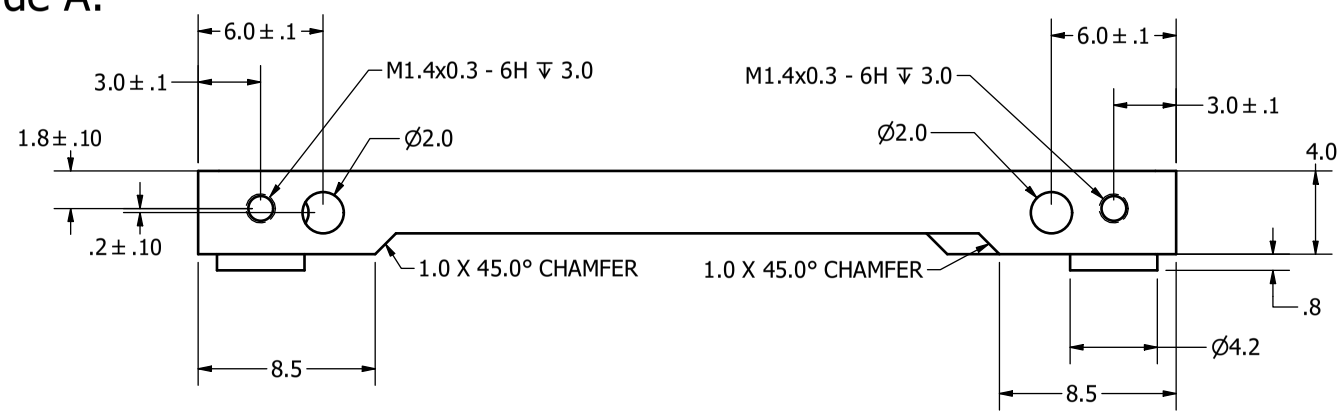

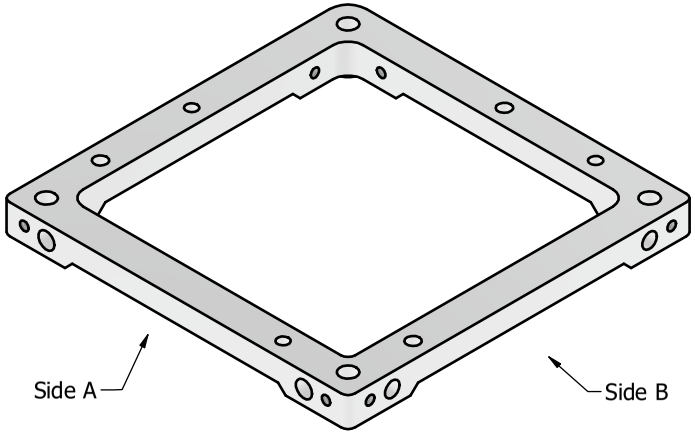

Side B:

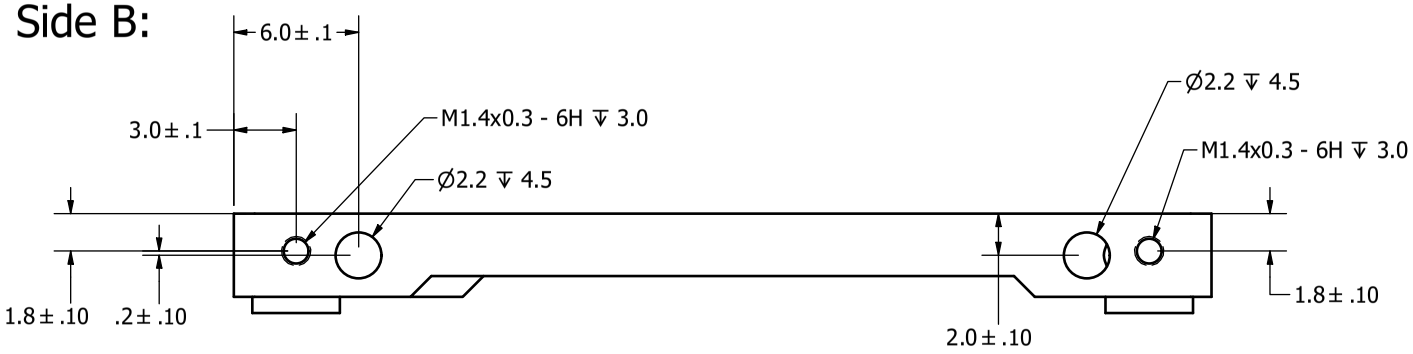

Notes:

- Units: mm
- Material: Aluminium 6061
- Tolerance: ISO 2768 – Medium unless specified

DRAWN Daniel	31/03/2023	L-Università ta' Malta	University of Malta	
CHECKED DC		TITLE	Chassis Top Frame	
QA				
MFG				
APPROVED DC		SIZE B	DWG NO Chassis_Top_v5	REV 1
		SCALE 4 : 1	SHEET 4 OF 5	

Side D:

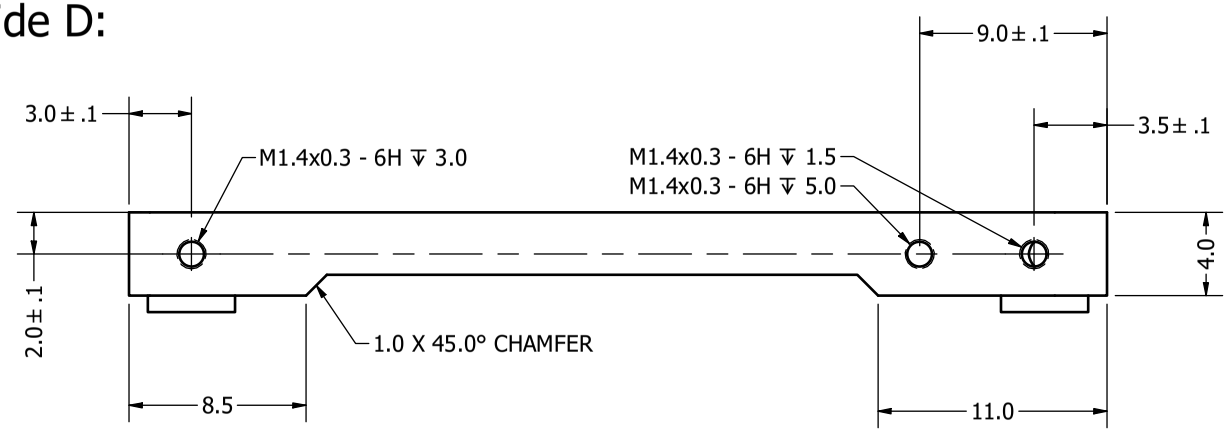

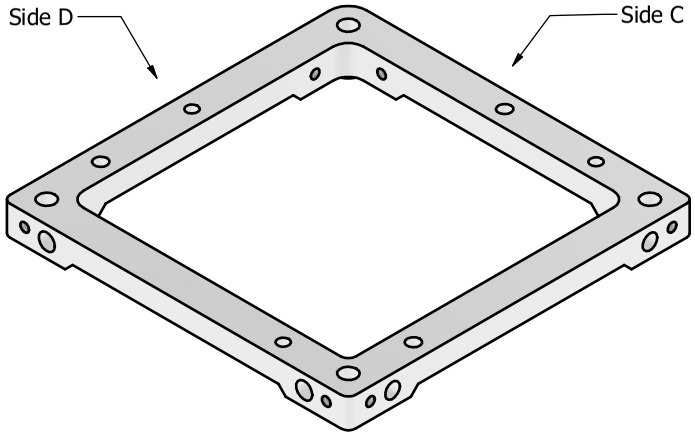

Side C:

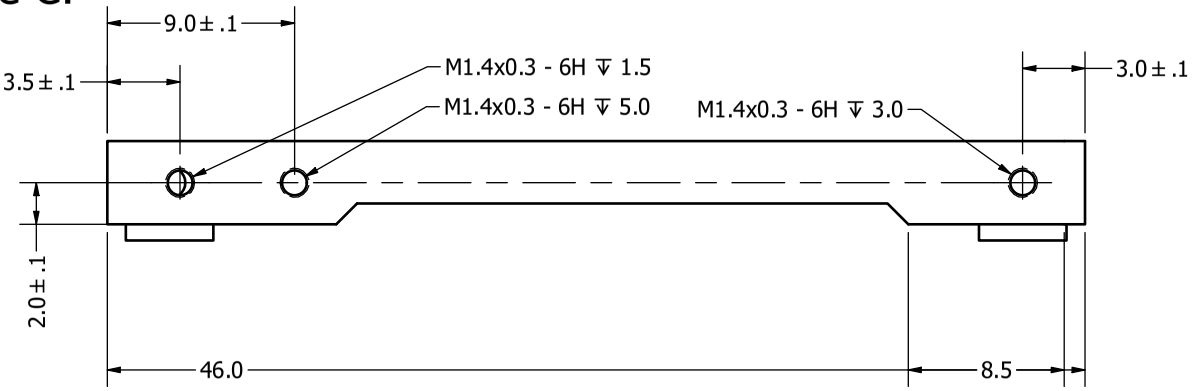

Notes:

- Units: mm
- Material: Aluminium 6061
- Tolerance: ISO 2768 – Medium unless specified

DRAWN Daniel	31/03/2023	L-Università ta' Malta	University of Malta	
CHECKED DC		TITLE	Chassis Top Frame	
QA				
MFG				
APPROVED DC		SIZE B	DWG NO Chassis_Top_v5	REV 1
		SCALE 4 : 1	SHEET 5 OF 5	

Chassis Bottom Frame Drawing

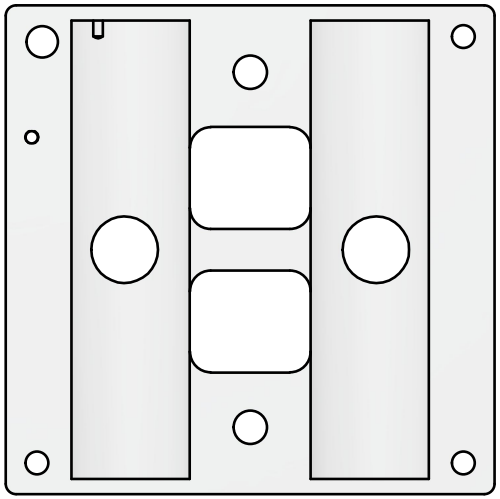

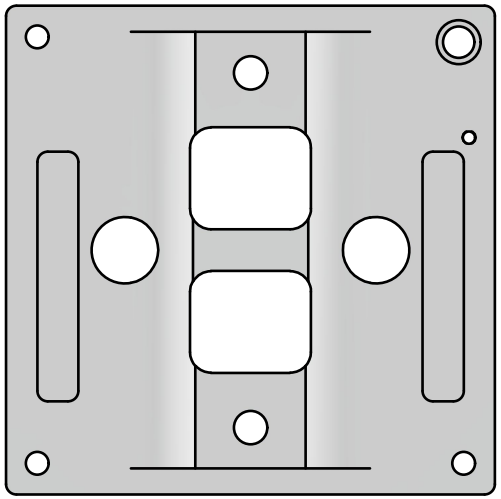

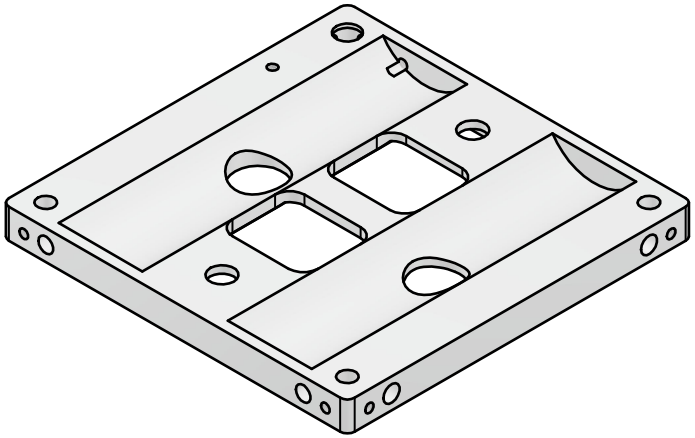

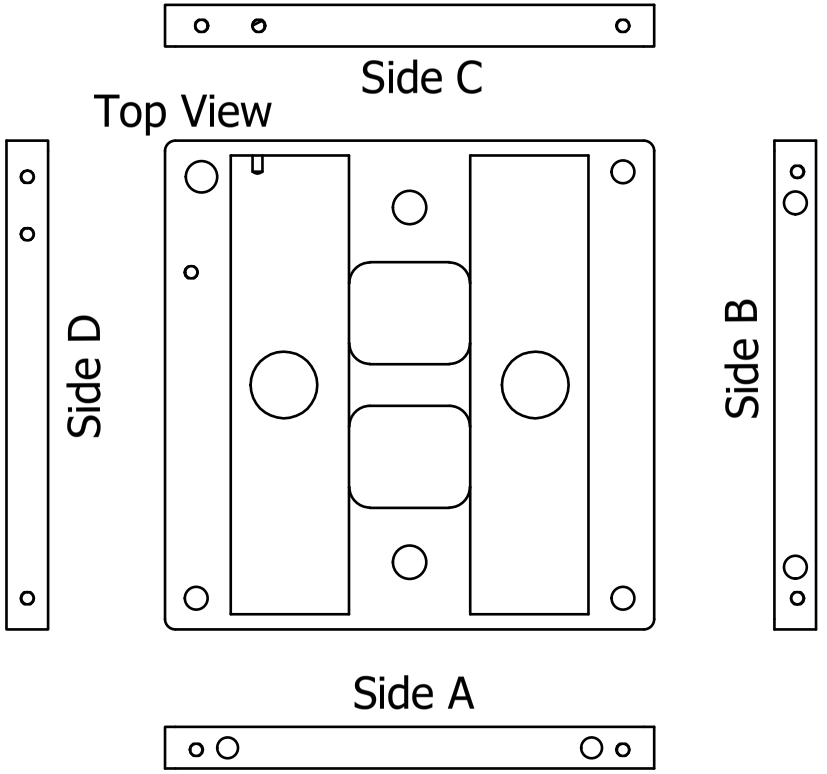

Notes:

- Units: mm
- Material: Aluminium 6061
- Tolerance: ISO 2768 – Medium unless specified

DRAWN Daniel	03/04/2023	L-Università ta' Malta	University of Malta	
CHECKED		TITLE	PQ8 Bottom Frame	
QA				
MFG				
APPROVED		SIZE B	DWG NO Chassis_Bottom_v7	REV 1
		SCALE 2 : 1		SHEET 1 OF 5

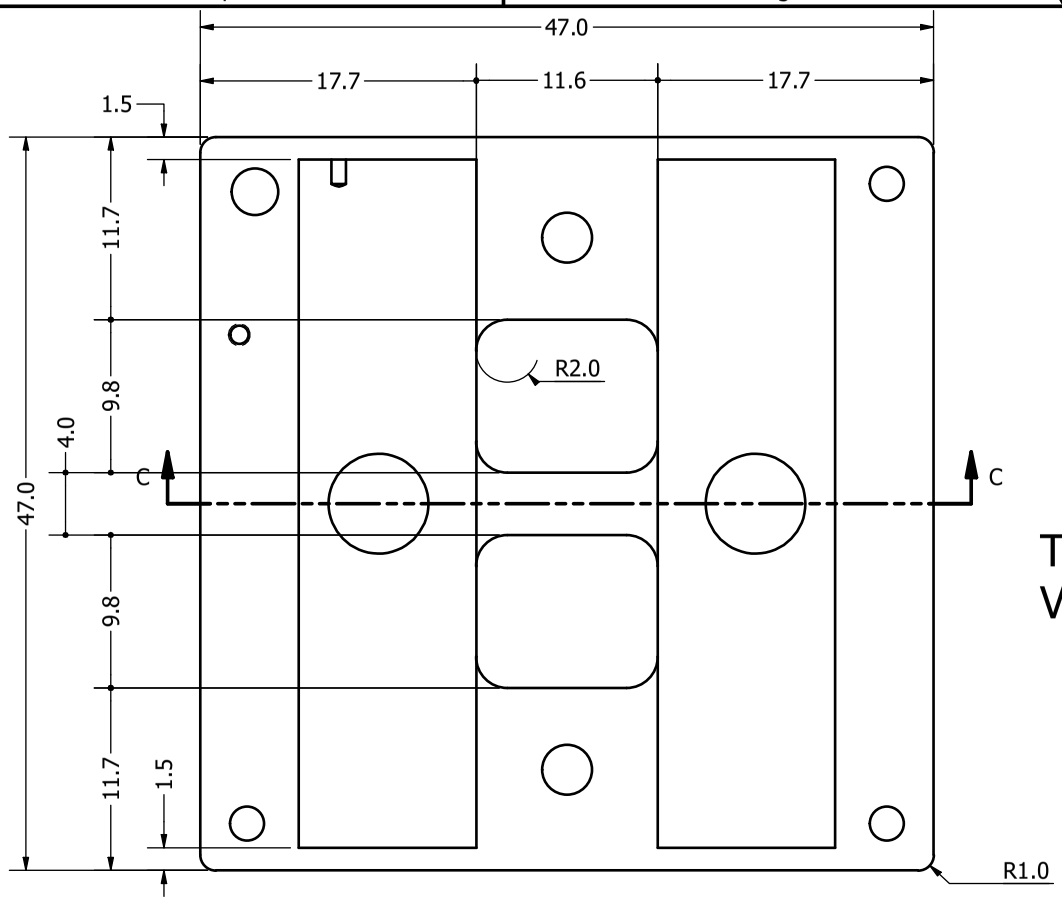

Top View

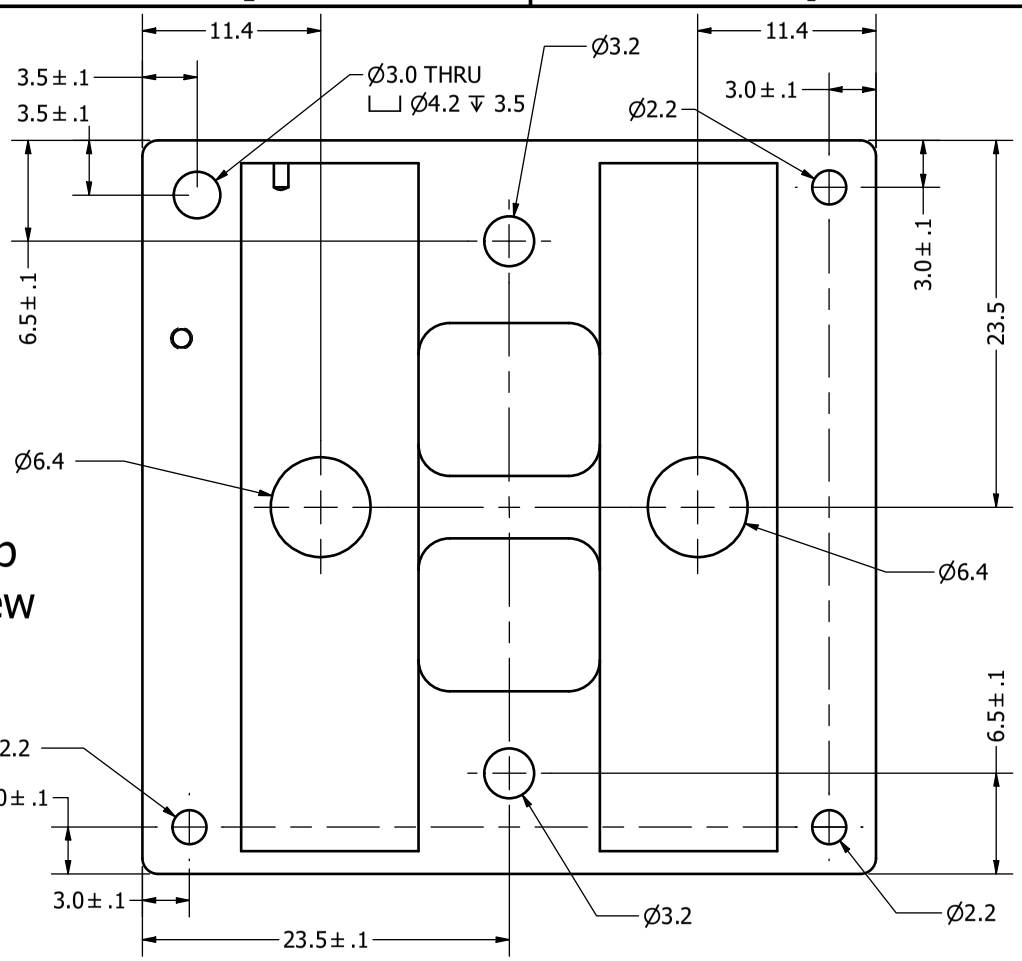

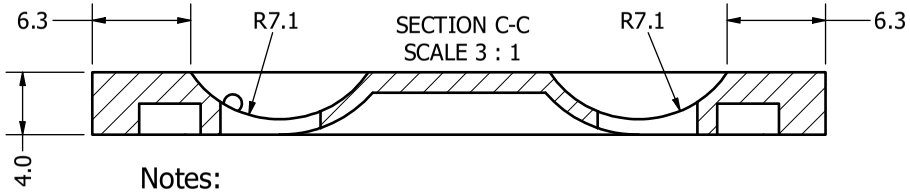

Notes:

- Units: mm
- Material: Aluminium 6061
- Tolerance: ISO 2768 – Medium unless specified

DRAWN Daniel	03/04/2023	L-Università ta' Malta	University of Malta
CHECKED		TITLE	PQ8 Bottom Frame
QA			
MFG			
APPROVED			
		SIZE B	DWG NO Chassis_Bottom_v7
		SCALE 3 : 1	REV 1
			SHEET 2 OF 5

SECTION D-D
SCALE 3 : 1

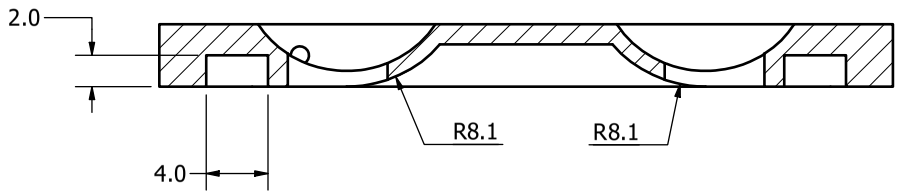

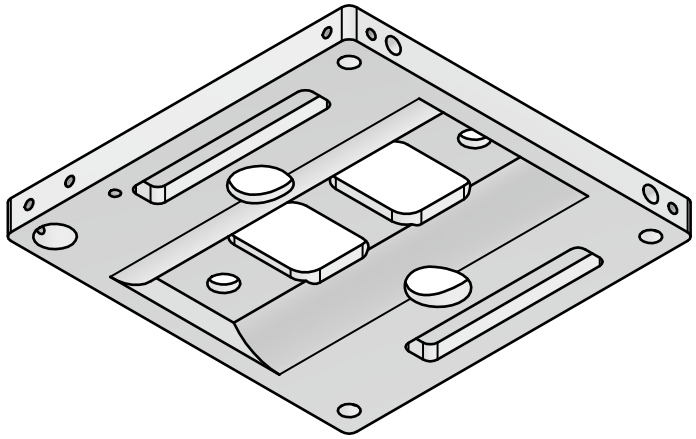

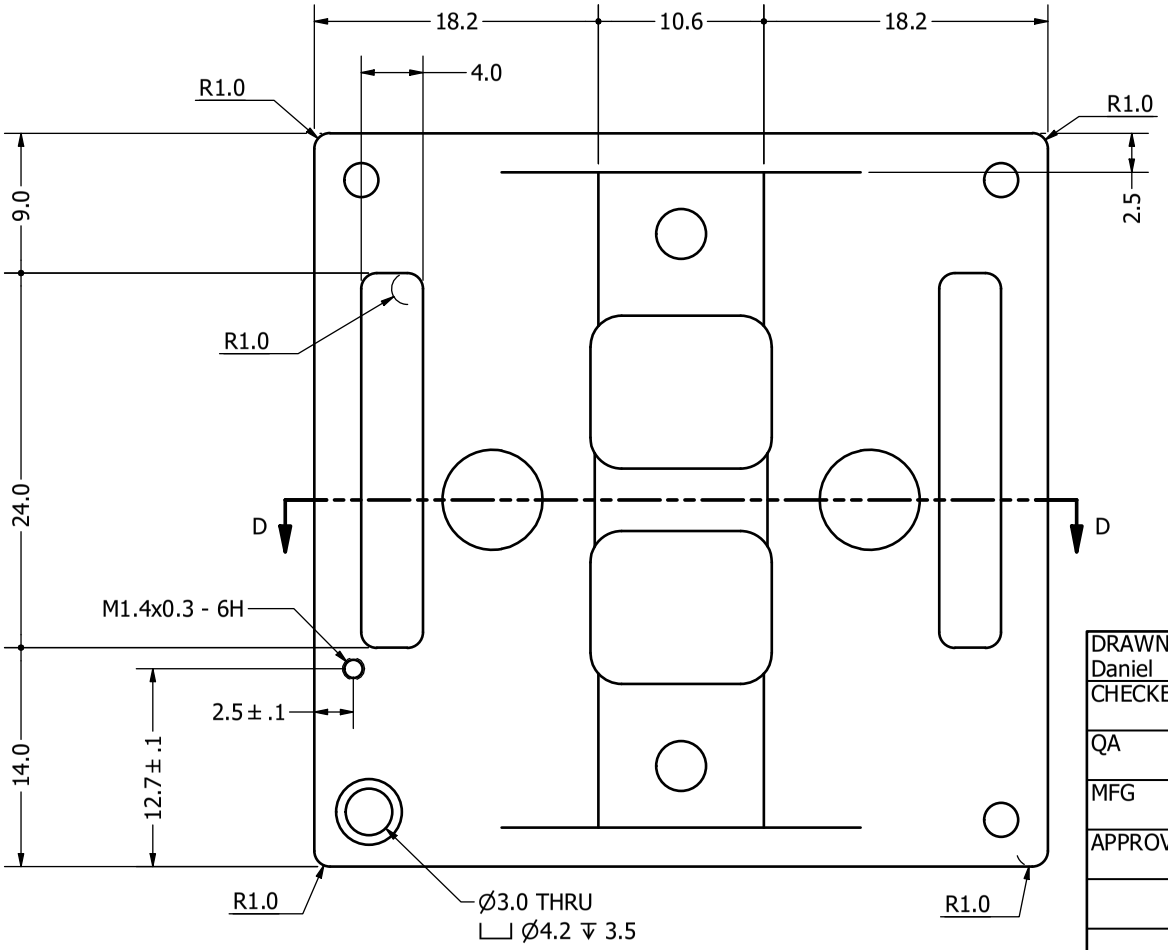

Notes:

- Units: mm
- Material: Aluminium 6061
- Tolerance: ISO 2768 – Medium unless specified

DRAWN Daniel	03/04/2023	L-Università ta' Malta	University of Malta	
CHECKED		TITLE	PQ8 Bottom Frame	
QA				
MFG				
APPROVED		SIZE B	DWG NO Chassis_Bottom_v7	REV 1
		SCALE 3 : 1	SHEET 3 OF 5	

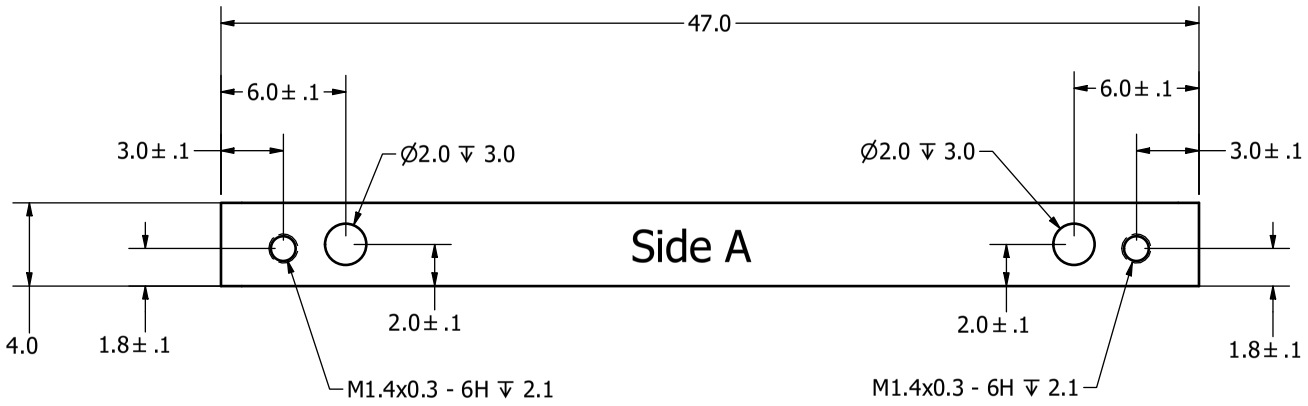

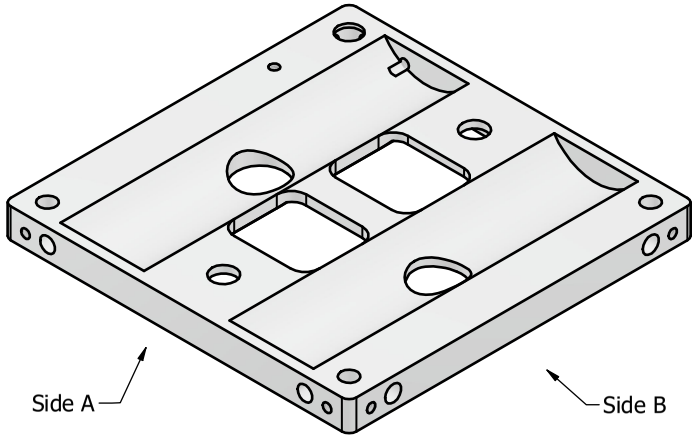

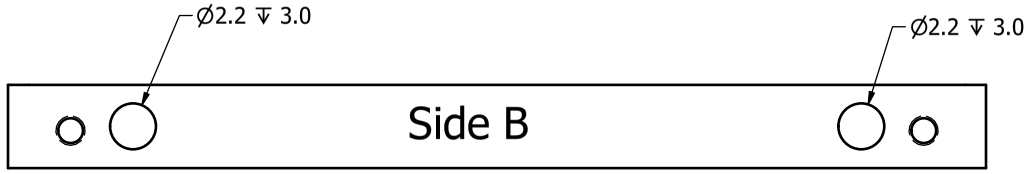

Notes:

- Units: mm
- Material: Aluminium 6061
- Tolerance: ISO 2768 – Medium unless specified

DRAWN Daniel	03/04/2023	L-Università ta' Malta	University of Malta	
CHECKED		TITLE	PQ8 Bottom Frame	
QA				
MFG				
APPROVED		SIZE B	DWG NO Chassis_Bottom_v7	REV 1
		SCALE 4 : 1	SHEET 4 OF 5	

Side D:

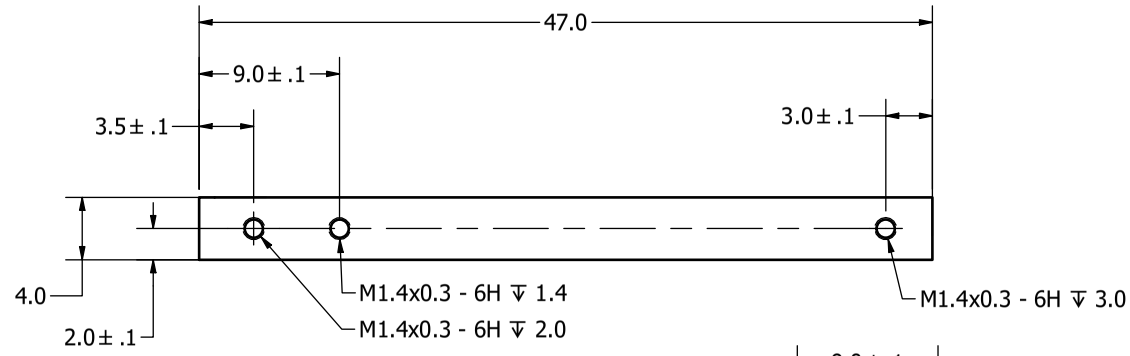

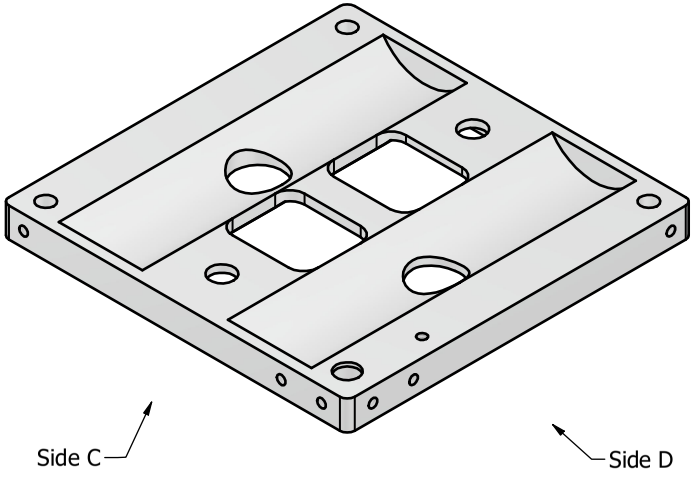

Side C:

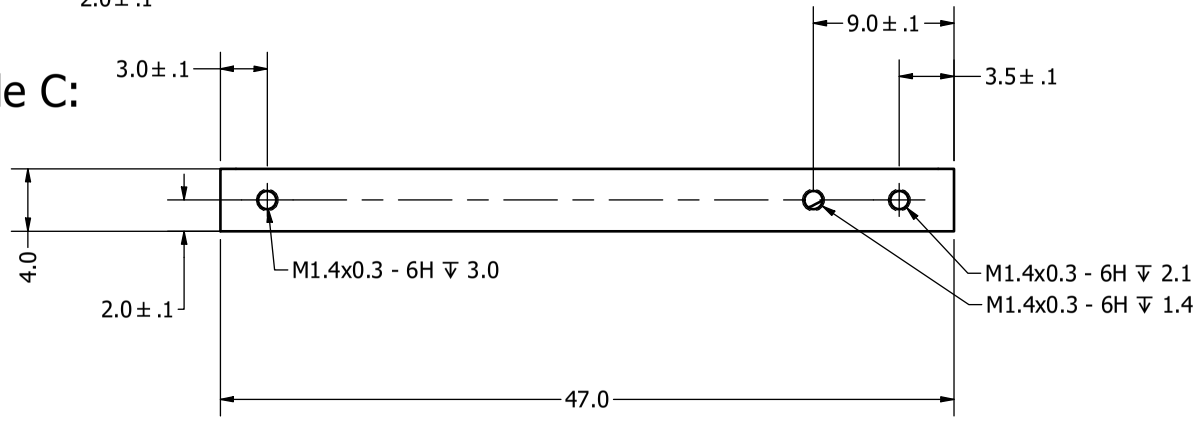

Notes:

- Units: mm
- Material: Aluminium 6061
- Tolerance: ISO 2768 - Medium unless specified

DRAWN Daniel	03/04/2023	L-Università ta' Malta	University of Malta	
CHECKED		TITLE	PQ8 Bottom Frame	
QA				
MFG				
APPROVED		SIZE B	DWG NO Chassis_Bottom_v7	REV 1
		SCALE 3 : 1	SHEET 5 OF 5	

Chassis Rail Drawing

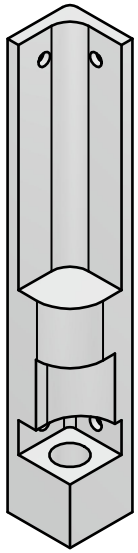

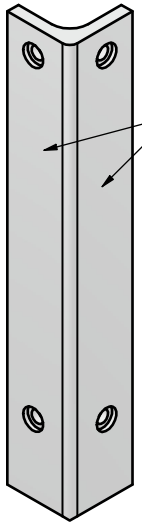

These two sides require < 1.6 um roughness.

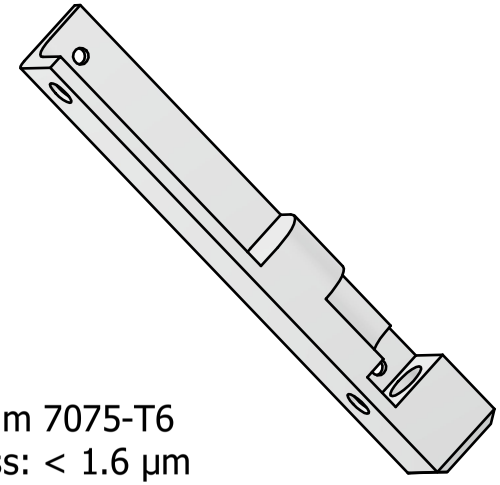

Top View

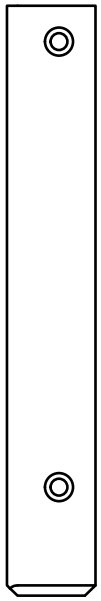

Side A

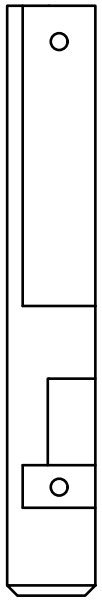

Side B

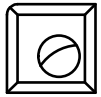

Bottom View

Notes:

- Units: mm
- Material: Aluminium 7075-T6
- Sufrace Roughness: < 1.6 µm
- Surface Finish: Anodized
- Tolerance: ISO 2768 - Medium unless specified

DRAWN Daniel	02/04/2023	L-Università ta' Malta	University of Malta
CHECKED		TITLE	PQ8 Rail
QA			
MFG		SIZE B	DWG NO Chassis_Rail_v5_1
APPROVED			REV 1
		SCALE 2 : 1	SHEET 1 OF 3

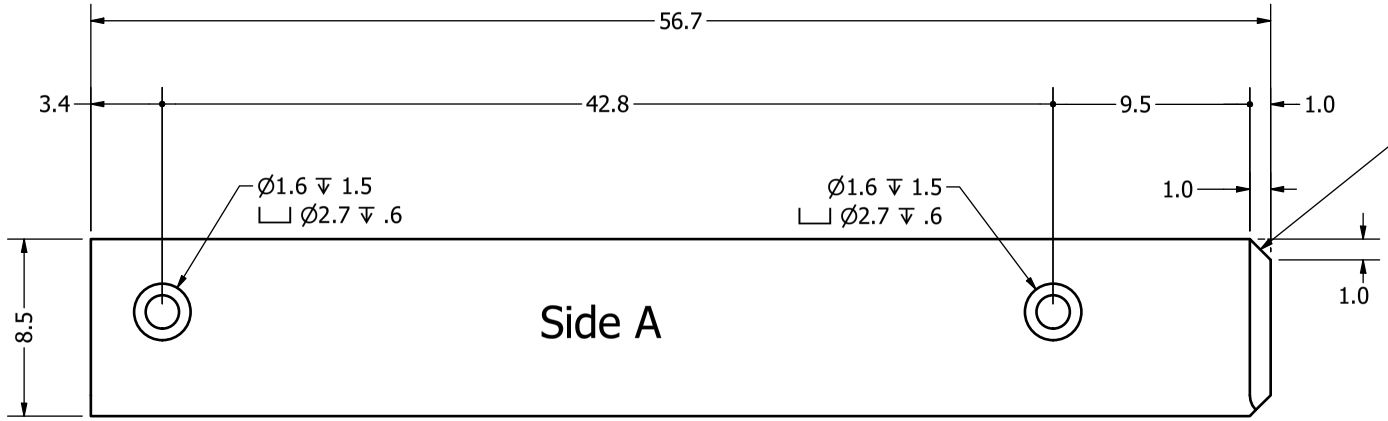

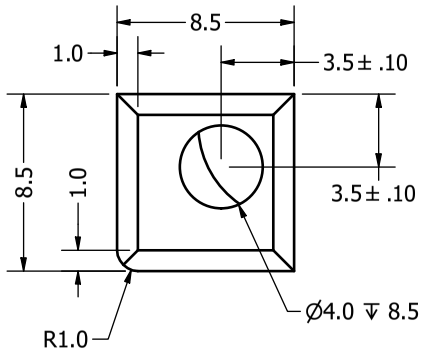

Bottom View

Top View

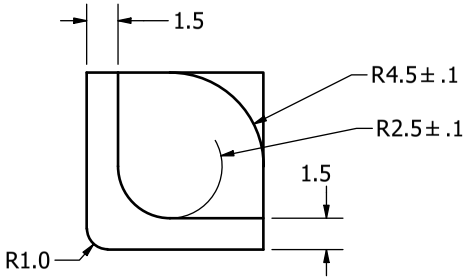

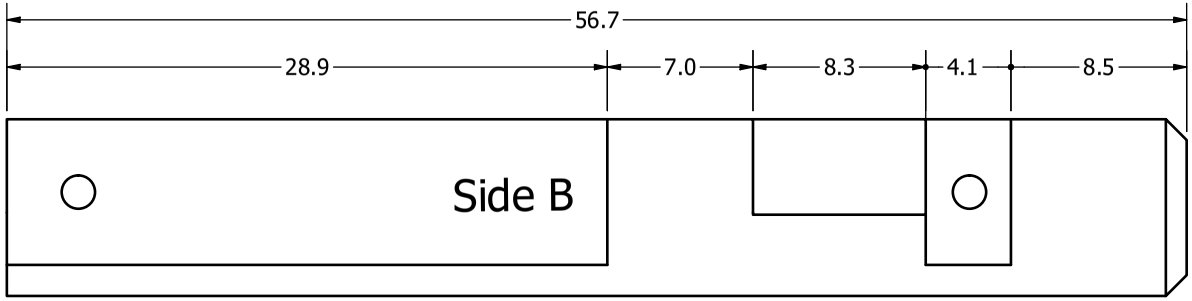

Notes:

- Units: mm
- Material: Aluminium 7075-T6
- Sufrace Roughness: < 1.6 µm
- Surface Finish: Anodized
- Tolerance: ISO 2768 - Medium unless specified

DRAWN Daniel	02/04/2023	L-Università ta' Malta	University of Malta
CHECKED		TITLE	PQ8 Rail
QA			
MFG			
APPROVED		SIZE B	DWG NO Chassis_Rail_v5_1
		SCALE 4 : 1	REV 1
			SHEET 2 OF 3

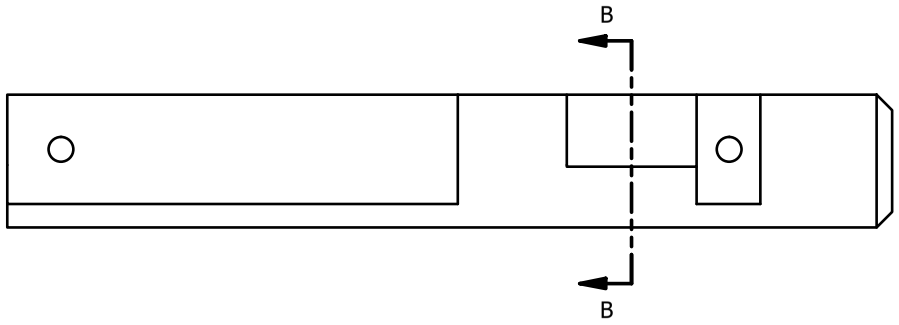

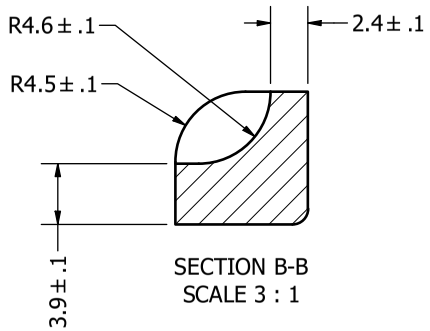

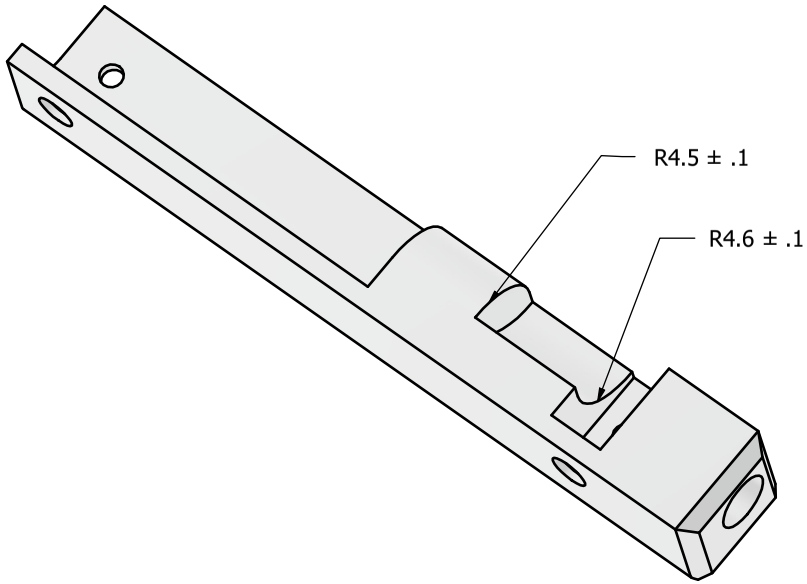

Notes:

- Units: mm
- Material: Aluminium 7075-T6
- Sufrace Roughness: < 1.6 µm
- Surface Finish: Anodized
- Tolerance: ISO 2768 - Medium unless specified

DRAWN Daniel	02/04/2023	L-Università ta' Malta	University of Malta	
CHECKED		TITLE	PQ8 Rail	
QA				
MFG				
APPROVED		SIZE B	DWG NO Chassis_Rail_v5_1	REV 1
		SCALE 3 : 1	SHEET 3 OF 3	

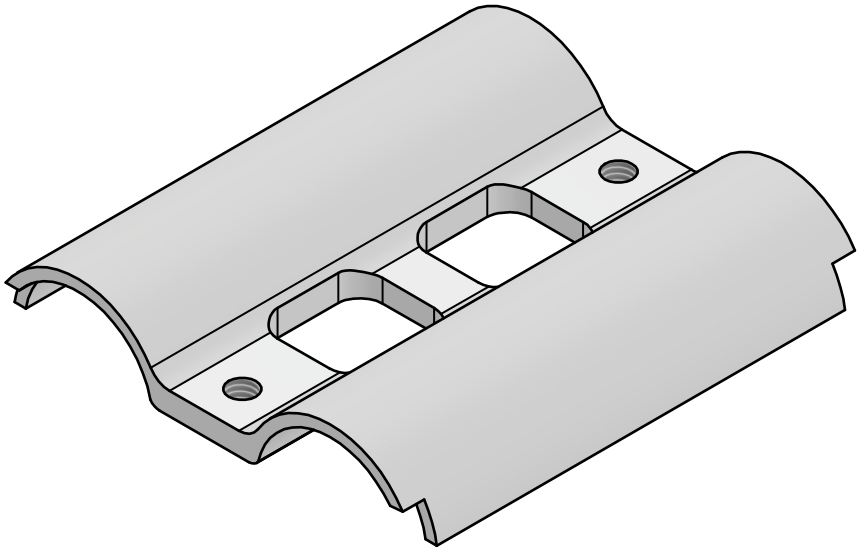

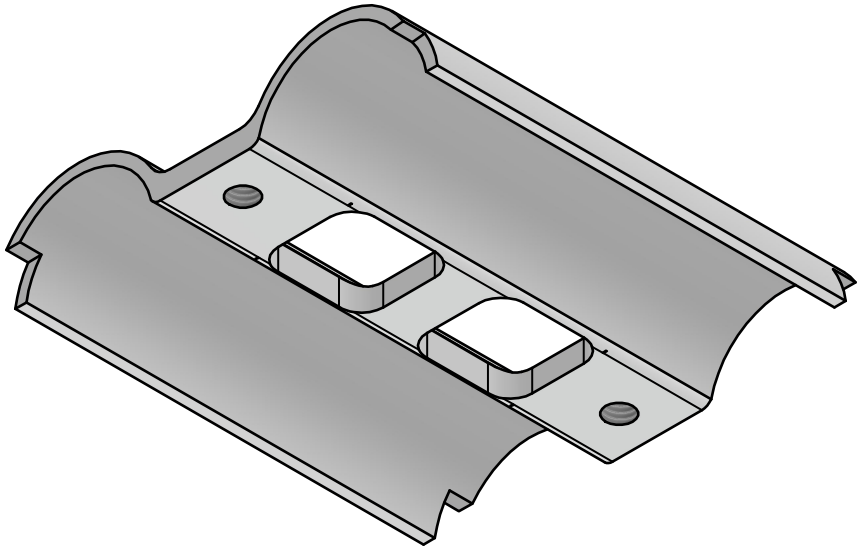

Notes:

- Units: mm
- Material: Aluminium 6061
- Tolerance: ISO 2768 - Medium unless specified

DRAWN Daniel	02/04/2023	L-Università ta' Malta	University of Malta	
CHECKED		TITLE	PQ8 Battery Clamp	
QA				
MFG				
APPROVED		SIZE B	DWG NO Battery_Clamp_v2	REV 1
		SCALE 3 : 1	SHEET 1 OF 3	

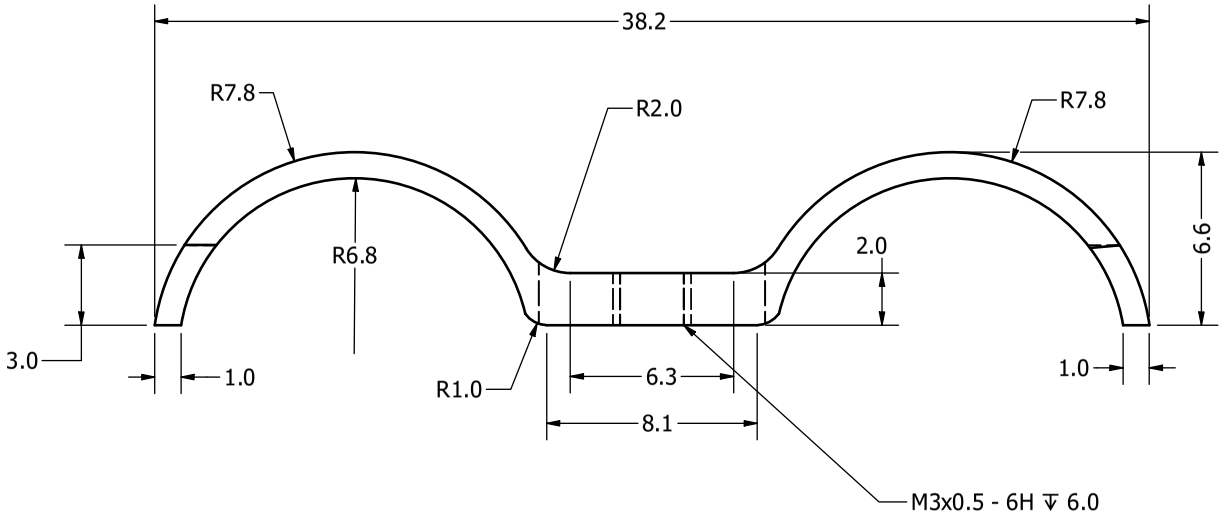

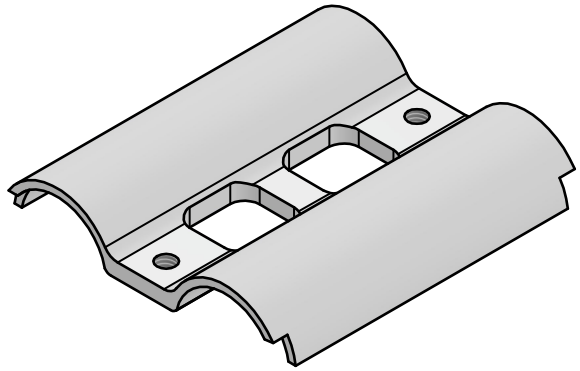

Notes:

- Units: mm
- Material: Aluminium 6061
- Tolerance: ISO 2768 - Medium unless specified

DRAWN Daniel	02/04/2023	L-Università ta' Malta	University of Malta
CHECKED		TITLE	PQ8 Battery Clamp
QA			
MFG			
APPROVED			
		SIZE B	DWG NO Battery_Clamp_v2
		SCALE 5 : 1	SHEET 2 OF 3
			REV 1

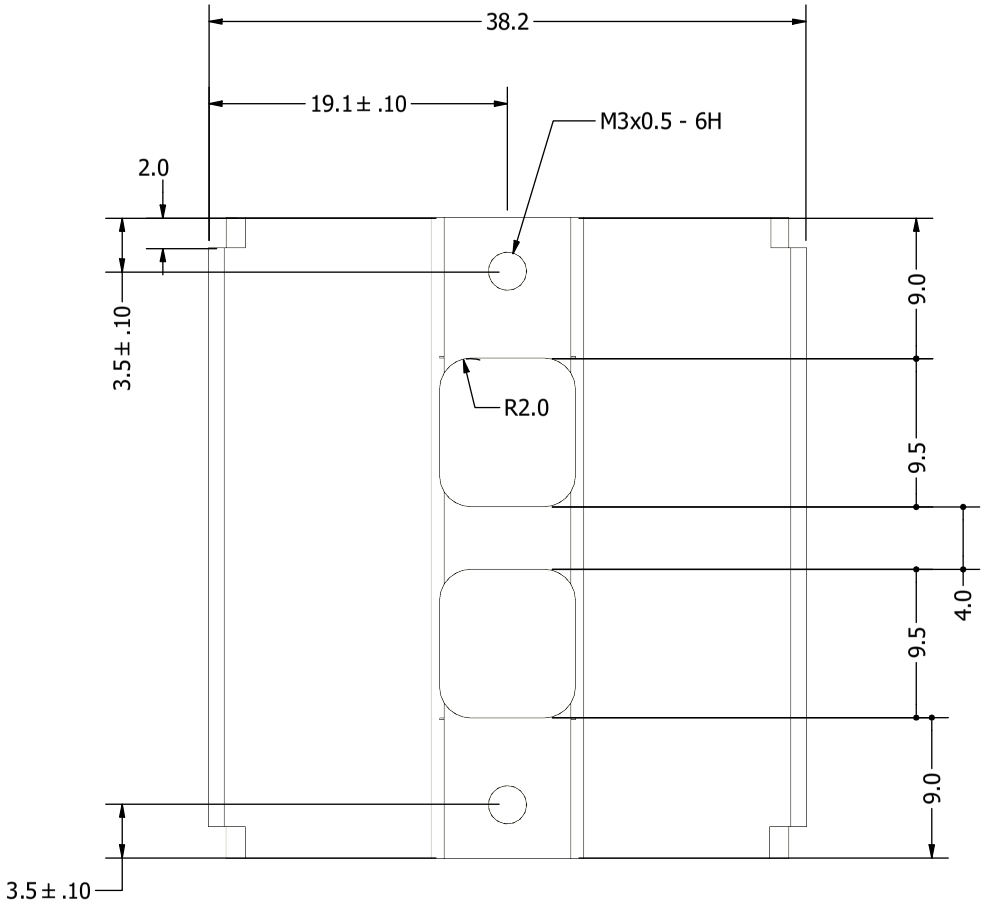

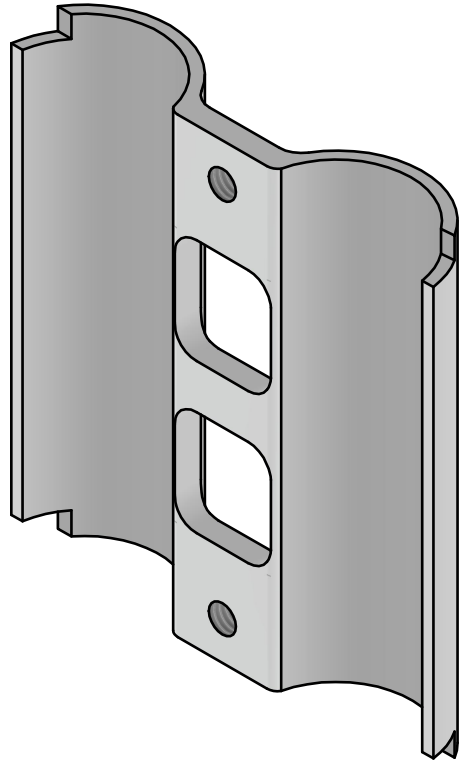

Notes:

- Units: mm
- Material: Aluminium 6061
- Tolerance: ISO 2768 - Medium unless specified

DRAWN Daniel	02/04/2023	L-Università ta' Malta	University of Malta	
CHECKED		TITLE	PQ8 Battery Clamp	
QA				
MFG				
APPROVED		SIZE B	DWG NO Battery_Clamp_v2	REV 1
		SCALE 3 : 1	SHEET 3 OF 3	

APPENDIX B: DISENGAGEMENT MECHANISM SCHEMATICS

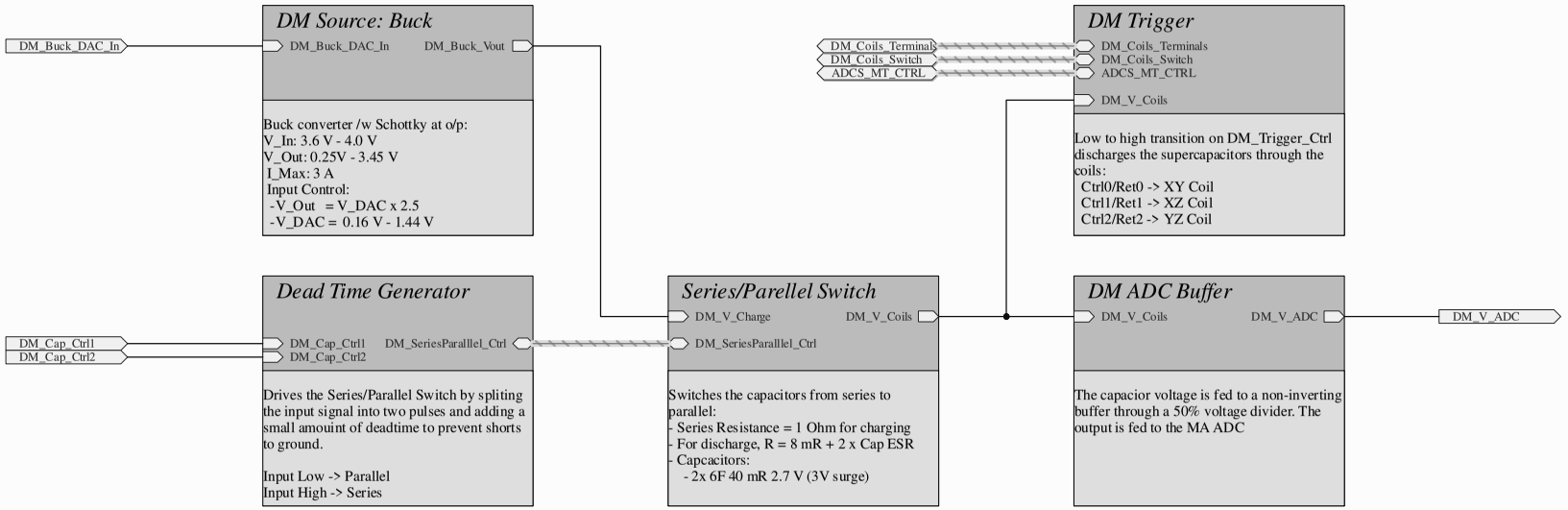

Title: PQ8 Disengagement Circuitry	
Project Name: PQ8 EPS Subsystem	
Designer: Daniel Cumbo	*Release Date* 01/03/2022
Revision: 2	*Page No:* 21

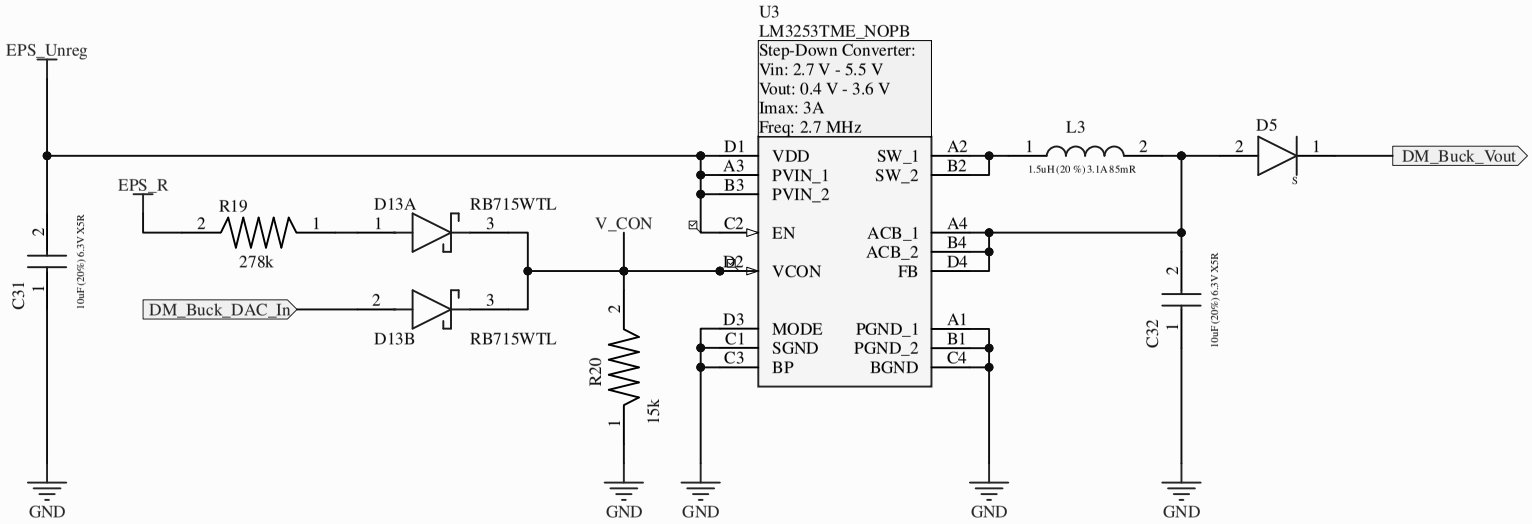

Title: DM Buck Converter	
Project Name: PQ8 EPS Subsystem	
Designer: Daniel Cumbo	*Release Date* 03/04/2022
Revision: 1	*Page No:* 22

Input Ports

Control Inputs (Source: MA)

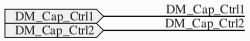

DM_Cap_Ctrl:
-> Input Low = Parallel
-> Input High = Series

Output Ports

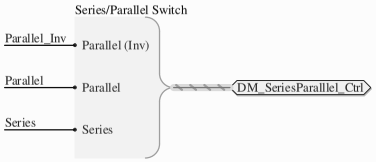

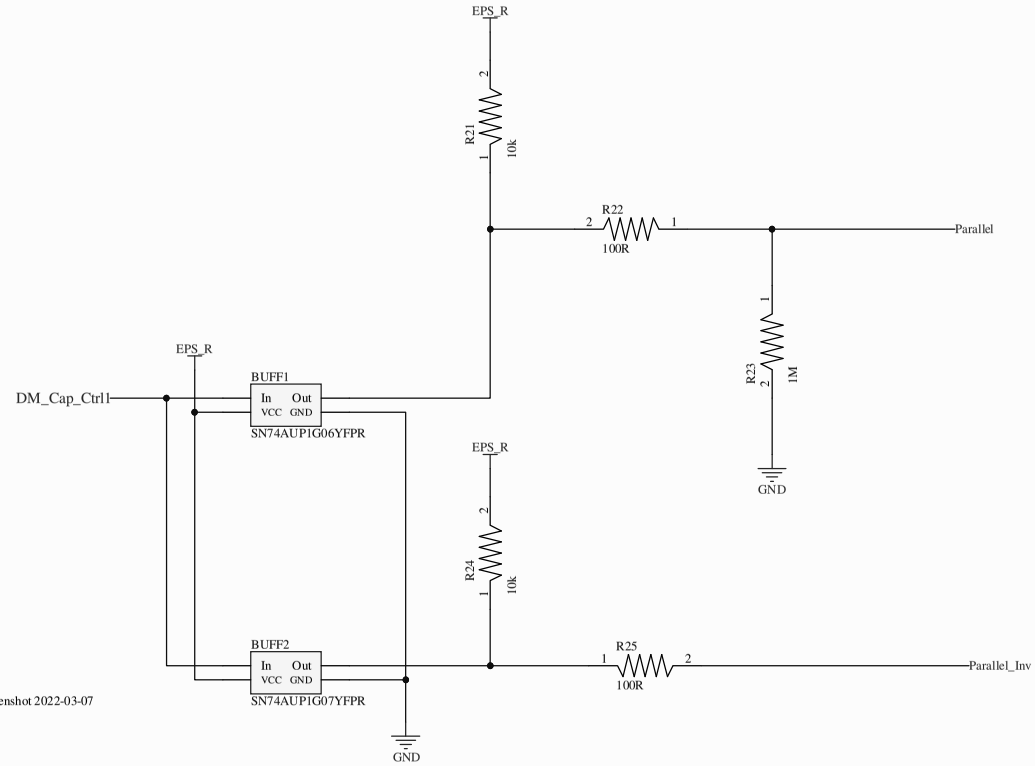

Cannot open file E:\Altium\Projects\PQ8\PQ8_EPS\PQ8_EPS_Rev2\PQ8_EPS_Rev2\Screenshot 2022-03-07 103851.png. File does not exist.

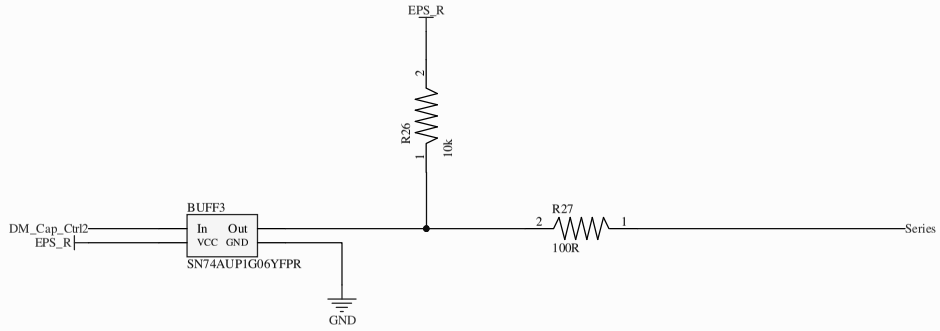

Title: DM Deadtime Generation	
Project Name: PQ8 EPS Subsystem	
Designer: Daniel Cumbo	*Release Date* 03/06/2022
Revision: 1	*Page No:* 23

Input Ports

Control Inputs (Source: Deadtime Circuit)

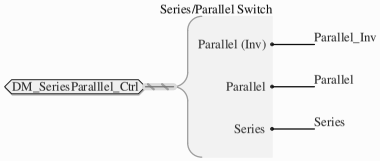

Input Voltage (Source: DM Buck)

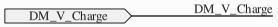

Output Ports

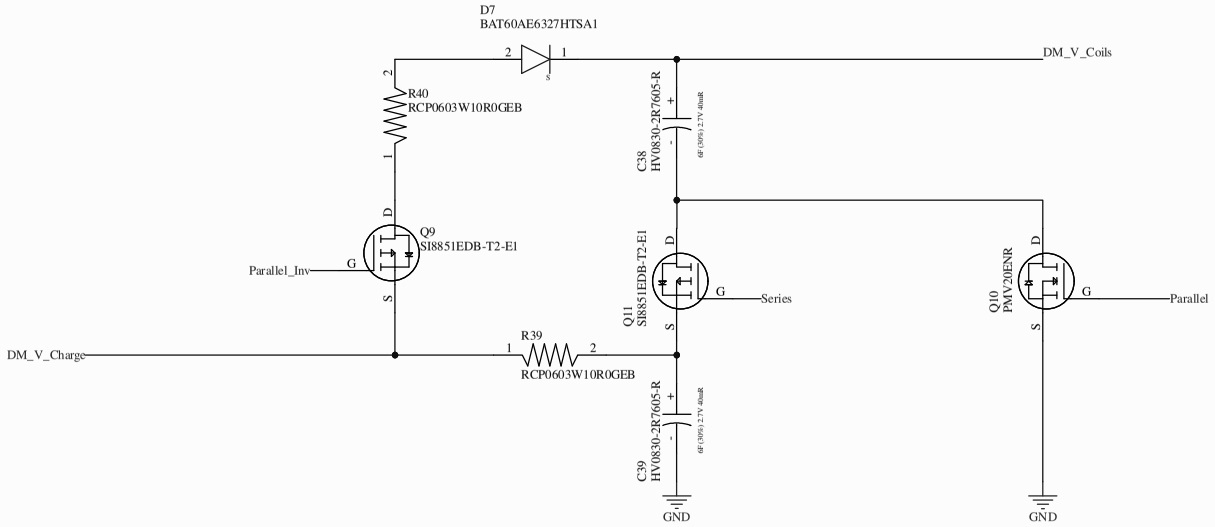

Title: Series/Parallel Capacitor Switch	
Project Name: PQ8 EPS Subsystem	
Designer: Daniel Cumbo	*Release Date* 03/04/2022
Revision: 1	*Page No:* 24

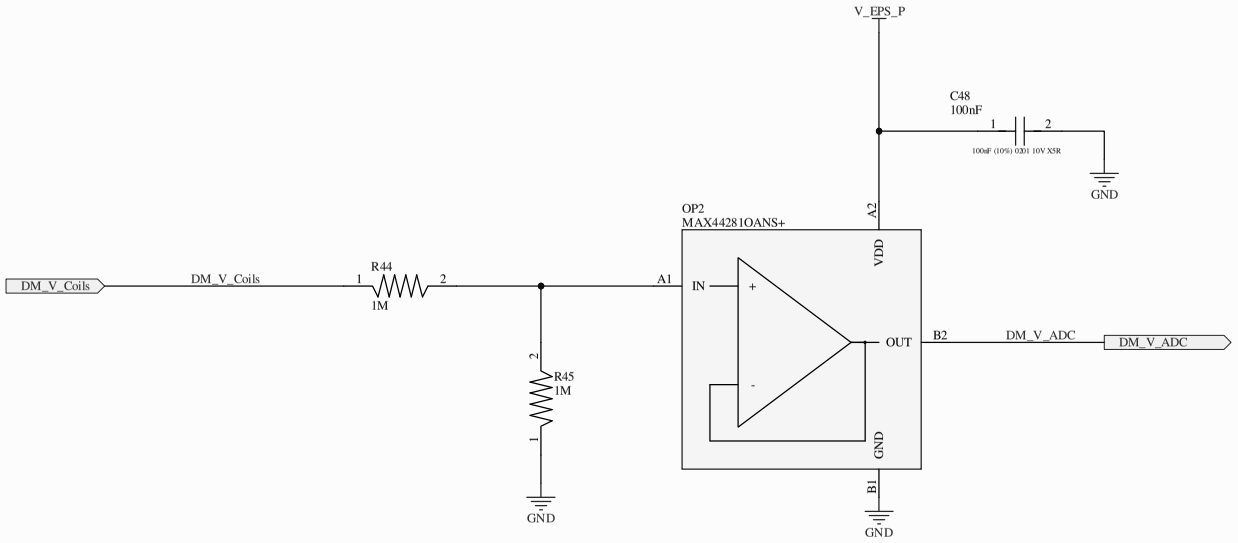

Title: PQ8 DM ADC Buffer	
Project Name: PQ8 EPS Subsystem	
Designer: Daniel Cumbo	*Release Date* 07/03/2022
Revision: 1	*Page No:* 25

Input Ports

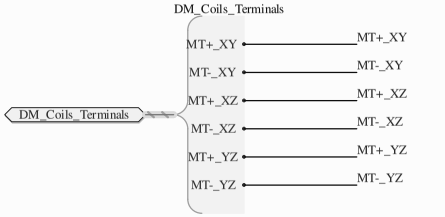

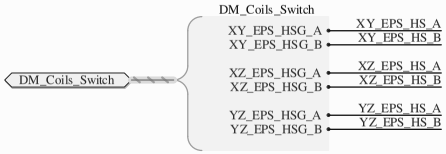

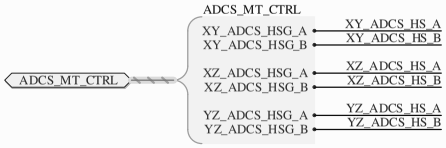

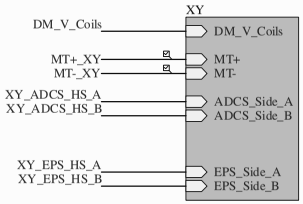

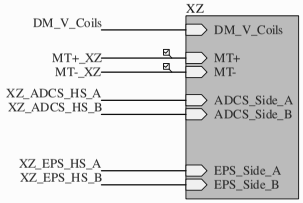

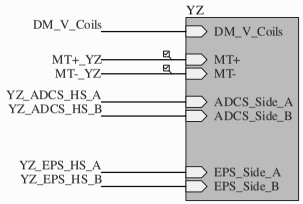

Title: PQ8 DM Trigger	
Project Name: PQ8 EPS Subsystem	
Designer: Daniel Cumbo	*Release Date* 07/03/2022
Revision: 1	*Page No:* 26

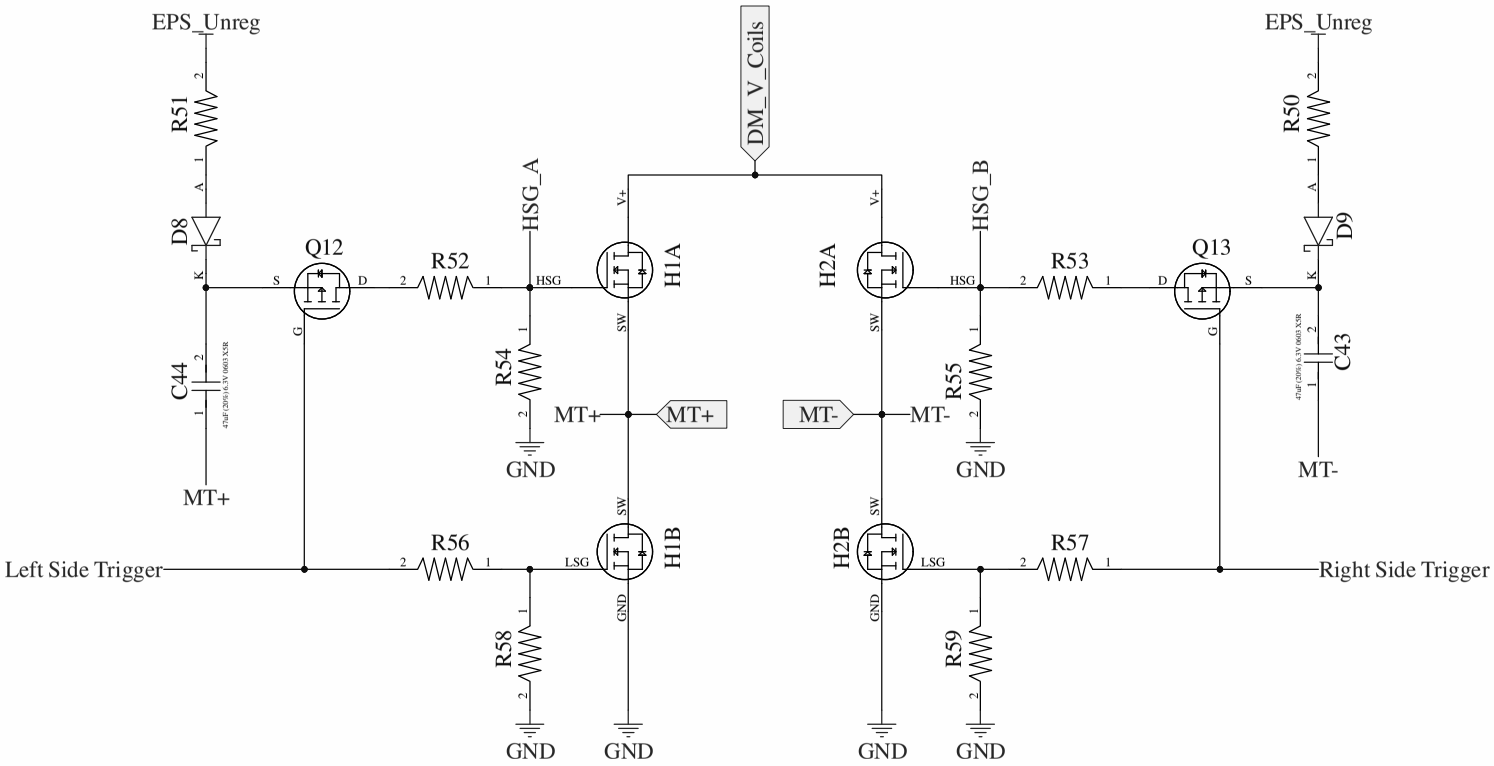

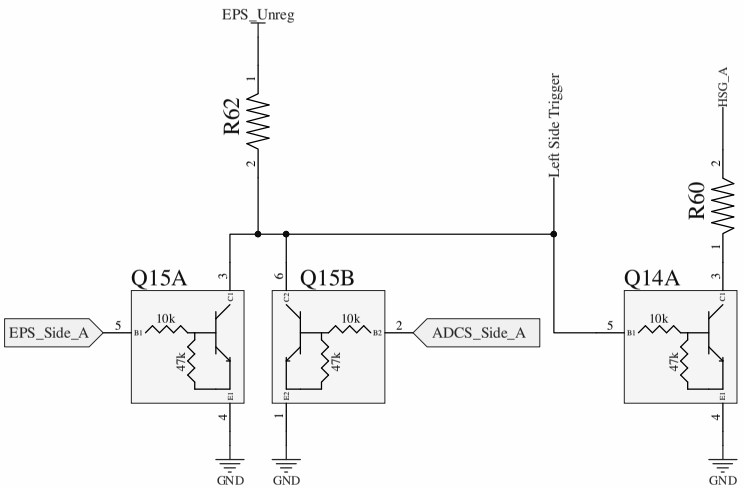

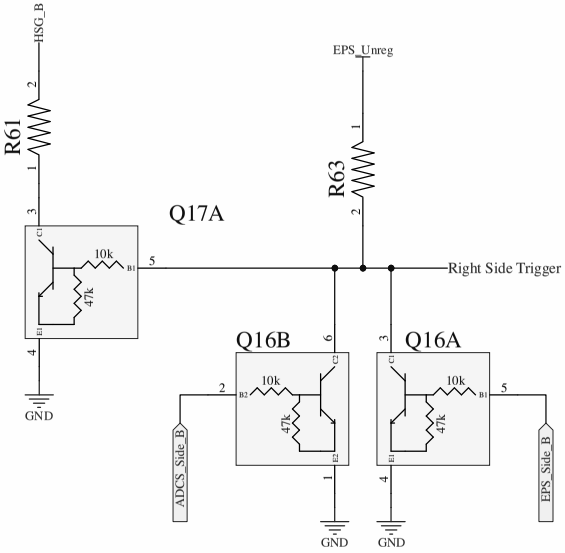

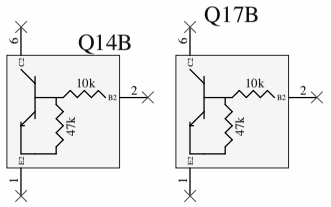

Title: DM Trigger H-Bridge	
Project Name: PQ8 EPS Subsystem	
Designer: Daniel Cumbo	*Release Date* 18/03/2021
Revision: 1	*Page No:* 27

APPENDIX C: PQ8 SPECIFICATIONS AND REQUIREMENTS

Requirement Number	Requirement	Source	Compliance?	Comment
MECH_1	CubeSats which incorporate any deviation from the CDS will submit a DAR and adhere to the waiver process (see Section 1.3 and Appendix A).	CubeSat Specs (Rev 14.1)	TBD	May be required due to mass and materials
MECH_2	All parts shall remain attached to the CubeSats during launch, ejection and operation. No additional space debris will be created.	CubeSat Specs (Rev 14.1)	Yes	
MECH_3	No pyrotechnics shall be permitted.	CubeSat Specs (Rev 14.1)	Yes	
MECH_4	Any propulsion systems shall be designed, integrated, and tested in accordance with AFSPCMAN 91-710 Volume 3.	CubeSat Specs (Rev 14.1)	Yes	No propulsion
MECH_5	Propulsion systems shall have at least 3 inhibits to activation.	CubeSat Specs (Rev 14.1)	Yes	
MECH_6	Total stored chemical energy will not exceed 100 Watt-Hours.	CubeSat Specs (Rev 14.1)	Yes	Total Watt-hours of all batteries does not exceed 50 W-Hours
MECH_7	CubeSat hazardous materials shall conform to AFSPCMAN 91-710, Volume 3.	CubeSat Specs (Rev 14.1)	Yes	Hazards include: flammability, combustibility, toxicity, contact compatibility, electrostatic build-up near fuel.
MECH_8	CubeSats materials shall have a Total Mass Loss (TML) < 1.0 %	CubeSat Specs (Rev 14.1)	Yes	
MECH_9	CubeSat materials shall have a Collected Volatile Condensable Material (CVCM) < 0.1%	CubeSat Specs (Rev 14.1)	Yes	
MECH_10	As a general guideline, it is advised to limit magnetic field outside the CubeSat static envelope to 0.5 Gauss above Earth's magnetic field.	CubeSat Specs (Rev 14.1)	Yes	

MECH_11	The CubeSat shall be designed to accommodate ascent venting per ventable volume/area < 2000 inches	CubeSat Specs (Rev 14.1)	TBD	
MECH_12	The CubeSat shall use the coordinate system as defined in Appendix B in the CubeSat specifications for the appropriate size.	CubeSat Specs (Rev 14.1)	Yes	All reports should reference as per Appendix
MECH_13	The CubeSat configuration and physical dimensions shall be per the appropriate section of Appendix B in the CubeSat specifications	CubeSat Specs (Rev 14.1)	Yes	
MECH_14	The –Z face of the CubeSat will be inserted first into the P-POD	CubeSat Specs (Rev 14.1)	Yes	-Z axis and +Z axis are identical, interchangeable
MECH_15	No components on the green and yellow shaded sides shall exceed 6.5 mm normal to the surface.	CubeSat Specs (Rev 14.1)	Yes	
MECH_16	Deployables shall be constrained by the CubeSat, not the P-POD.	CubeSat Specs (Rev 14.1)	Yes	
MECH_17	Rails shall have a minimum width of 8.5mm.	CubeSat Specs (Rev 14.1)	Yes	
MECH_18	Rails will have a surface roughness less than 1.6 µm.	CubeSat Specs (Rev 14.1)	Yes	
MECH_19	The edges of the rails will be rounded to a radius of at least 1 mm	CubeSat Specs (Rev 14.1)	Yes	
MECH_20	The ends of the rails on the +/- Z face shall have a minimum surface area of 6.5 mm x 6.5 mm contact area for neighbouring CubeSat rails (as per Figure 6).	CubeSat Specs (Rev 14.1)	Yes	
MECH_21	At least 75% of the rail will be in contact with the P-POD rails. 25% of the rails may be recessed and no part of the rails will exceed the specification.	CubeSat Specs (Rev 14.1)	Yes	Around 80 % is in contact. 20 % recessed
MECH_22	The maximum mass of a 1U CubeSat shall be 2 kg	CubeSat Specs (Rev 14.1)	Yes	

MECH_23	The CubeSat centre of gravity shall be located within 2 cm from its geometric centre in the X, Y and Z directions	CubeSat Specs (Rev 14.1)	Yes	The CoG will be at the centre by default
MECH_24	Aluminium 7075, 6061, 5005, and/or 5052 will be used for both the main CubeSat structure and the rails.	CubeSat Specs (Rev 14.1)	Yes	
MECH_25	The CubeSat rails and standoff, which contact the P-POD rails and adjacent CubeSat standoffs, shall be hard anodized aluminium to prevent any cold welding within the P-POD.	CubeSat Specs (Rev 14.1)	Yes	Requirement during manufacturing
MECH_26	The 1U, 1.5U, and 2U CubeSats shall use separation springs to ensure adequate separation.	CubeSat Specs (Rev 14.1)	Yes	Space for these is included
MECH_27	The CubeSat must be tested for quasi-static and dynamic loads for qualification, taking into consideration the launch vehicle and appropriate safer factors	Design Requirements	Yes	Passed
MECH_28	The PQ8 Architecture is to form a single rigid structure whin CubeSat formation	Design Requirements	Yes	The satellite will use magnets and guide pins for this purpose
MECH_29	The PQ8 Architecture must not use the P-POD as a form of structural support	Design Requirements	Yes	The satellite will use magnets and guide pins for this purpose
MECH_30	Movable metal parts, such as guide pins, in contact with other metal parts must be anodized to prevent cold welding.	Design Requirements	Yes	Requirement during manufacturing
MECH_31	The following metals must not be used in order to prevent whiskering: tin, some tin alloys, zinc, cadmium, indium, antimony, silver, other materials prone to whiskering .	Design Requirements	Yes	
MECH_32	The total mass of a PQ8-S satellite is not exceed 250 g.	Design Requirements	Yes	See Mass budget

MECH_33	The total mass of any subsystem is to comply with the mass budget	Design Requirements	Yes	Compliant subsystems: EPS, ADCS, OBC, COMMS, Payload
MECH_34	Each PQ8-S satellite must incorporate a disengagement mechanism	Design Requirements	Yes	
MECH_35	The disengagement mechanism should provide enough separation as to create a 1 m margin at time of closest approach during orbit.	Design Requirements	Yes	
MECH_36	The circuitry for the disengagement mechanism must be incorporated on the EPS board	Design Requirements	Yes	
ELEC_1	The CubeSat power system shall be at a power off state to prevent CubeSat from activating any powered functions while integrated in the P-POD from the time of delivery to the LV through on-orbit deployment	CubeSat Specs (Rev 14.1)	Yes	
ELEC_2	The CubeSat shall have, at a minimum, one deployment switch on a rail standoff, per Figure 7.	CubeSat Specs (Rev 14.1)	Yes	
ELEC_3	In the actuated state, the CubeSat deployment switch shall electrically disconnect the power system from the powered functions; this includes real time clocks (RTC).	CubeSat Specs (Rev 14.1)	Yes	
ELEC_4	The deployment switch shall be in the actuated state at all times while integrated in the PPOD.	CubeSat Specs (Rev 14.1)	Yes	
ELEC_5	In the actuated state, the CubeSat deployment switch will be at or below the level of the standoff.	CubeSat Specs (Rev 14.1)	Yes	

ELEC_6	If the CubeSat deployment switch toggles from the actuated state and back, the transmission and deployable timers shall reset to t=0.	CubeSat Specs (Rev 14.1)	Yes	
ELEC_7	The RBF pin and all CubeSat umbilical connectors shall be within the designated Access Port locations, green shaded areas shown in Appendix B.	CubeSat Specs (Rev 14.1)	Yes	
ELEC_8	The CubeSat shall include an RBF pin.	CubeSat Specs (Rev 14.1)	Yes	
ELEC_9	The RBF pin shall cut all power to the satellite once it is inserted into the satellite	CubeSat Specs (Rev 14.1)	Yes	
ELEC_10	The RBF pin shall be removed from the CubeSat after integration into the P-POD.	CubeSat Specs (Rev 14.1)	Yes	
ELEC_11	The RBF pin shall protrude no more than 6.5 mm from the rails when it is fully inserted into the satellite.	CubeSat Specs (Rev 14.1)	Yes	
ELEC_12	CubeSats shall incorporate battery circuit protection for charging/discharging to avoid unbalanced cell conditions.	CubeSat Specs (Rev 14.1)	Yes	
ELEC_13	The CubeSat will have one RF inhibit and RF power output of no greater than 1.5W at the transmitting antenna's RF input.	CubeSat Specs (Rev 14.1)	Yes	
ELEC_14	The minimum efficiency of the EPS from extraction to distribution should not be below 70 %	Design Requirements	Yes	
ELEC_15	All subsystems are to comply with the power budget	Design Requirements	Yes	
ELEC_16	The average power per orbit shall not exceed 288 mW	Design Requirements	Yes	
ELEC_17	The EPS must provide a regulated voltage of 3.3 V to each subsystem	Design Requirements	Yes	
ELEC_18	The EPS must provide an unregulated voltage to each subsystem	Design Requirements	Yes	

ELEC_19	Each supply line provided by the EPS should be protected for latch-up, short circuit and reverse voltage.	Design Requirements	Yes	
OPER_1	Operators will obtain and provide documentation of proper licenses for use of radio frequencies.	CubeSat Specs (Rev 14.1)	TBD	
OPER_2	CubeSats will comply with their country's radio license agreements and restrictions	CubeSat Specs (Rev 14.1)	TBD	
OPER_3	CubeSats mission design and hardware shall be in accordance with NPR 8715.6 to limit orbital debris.	CubeSat Specs (Rev 14.1)	Yes	
OPER_4	Any CubeSat component shall re-enter with energy less than 15 Joules.	CubeSat Specs (Rev 14.1)	Yes	
OPER_5	Developers will obtain and provide documentation of approval of an orbital debris mitigation plan from the FCC (or NOAA if imager is present).	CubeSat Specs (Rev 14.1)	TBD	
OPER_6	All deployables such as booms, antennas, and solar panels shall wait to deploy a minimum of 30 minutes after the CubeSat's deployment switch(es) are activated from PPOD ejection.	CubeSat Specs (Rev 14.1)	Yes	
OPER_7	No CubeSats shall generate or transmit any signal from the time of integration into the PPOD through 45 minutes after on-orbit deployment from the P-POD. However, the CubeSat can be powered on following deployment form the P-POD.	CubeSat Specs (Rev 14.1)	Yes	
OPER_8	Cal Poly will conduct a minimum of one fit check in which developer hardware will be inspected and integrated into the P-POD or Test POD. A final fit check will be conducted prior to launch.	CubeSat Specs (Rev 14.1)	TBD	